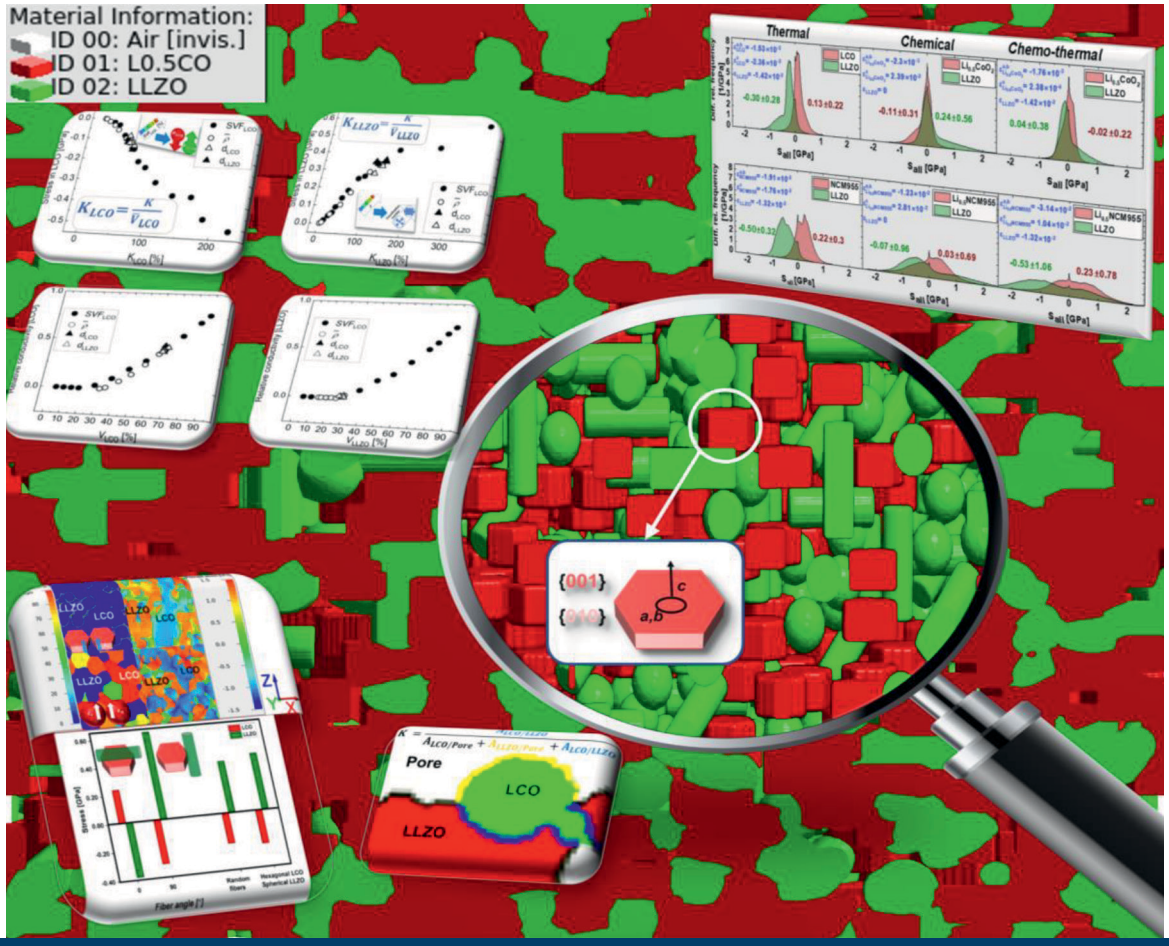

Material design and stability of All-Solid-State Lithium batteries

Fadi Hasan Al-Jaljouli

Energie & Umwelt / Energy & Environment
Band / Volume 720
ISBN 978-3-95806-951-0

Mitglied der Helmholtz-Gemeinschaft

JÜLICH
Forschungszentrum

Schriften des Forschungszentrums Jülich
Reihe Energie & Umwelt / Energy & Environment Band / Volume 720

Forschungszentrum Jülich GmbH
Institute of Energy Materials and Devices (IMD)
Werkstoffsynthese und Herstellungsverfahren (IMD-2)

Material design and stability of All-Solid-State Lithium batteries

Fadi Hasan Al-Jaljouli

Schriften des Forschungszentrums Jülich
Reihe Energie & Umwelt / Energy & Environment Band / Volume 720

ISSN 1866-1793 ISBN 978-3-95806-951-0

Bibliografische Information der Deutschen Nationalbibliothek.
Die Deutsche Nationalbibliothek verzeichnet diese Publikation in der
Deutschen Nationalbibliografie; detaillierte Bibliografische Daten
sind im Internet über http://dnb.d-nb.de abrufbar.

Herausgeber und Vertrieb:	Forschungszentrum Jülich GmbH Zentralbibliothek, Verlag 52425 Jülich Tel.: +49 2461 61-5368 Fax: +49 2461 61-6103 zb-publikation@fz-juelich.de www.fz-juelich.de/zb
Umschlaggestaltung:	Grafische Medien, Forschungszentrum Jülich GmbH
Druck:	Grafische Medien, Forschungszentrum Jülich GmbH
Copyright:	Forschungszentrum Jülich 2026

Schriften des Forschungszentrums Jülich
Reihe Energie & Umwelt / Energy & Environment, Band / Volume 720

D 82 (Diss. RWTH Aachen University, 2026)

ISSN 1866-1793
ISBN 978-3-95806-950-3 (Print)
ISBN 978-3-95806-951-0 (E-Book)

Vollständig frei verfügbar über das Publikationsportal des Forschungszentrums Jülich (JuSER)
unter www.fz-juelich.de/zb/openaccess.

Acknowledgments

First and foremost, I would like to sincerely thank Prof. Dr. Olivier Guillon for granting me the precious opportunity to pursue my PhD research in the field of battery research within the modeling team at the Institute of Energy Materials and Devices (IMD-2). I am deeply grateful for his mentorship, his profound and insightful scientific discussions, and his valuable guidance regarding my work. I also greatly appreciate the time and effort he devoted to reviewing my manuscripts and this thesis, as well as the opportunity he gave me to present my results at international conferences.

His support extended far beyond the scientific domain. He has set an exceptional example of leadership, from which one can learn immensely—even without direct interaction—through his discipline, attention to detail, and outstanding time management. His patience, honesty, willingness to help, respect and sense of humor have been invaluable in easing the challenges I faced as a fresh PhD student during my meetings with him. It has truly been an honor to be one of his students, and it is of great significance to me to receive my degree under his supervision, as I believe that one essential factor in defining the quality of a PhD is the person who confers it.

I would also like to extend my sincere thanks to my scientific advisor, Dr. Robert Mücke, for his constant support and commitment during my PhD journey. He created a collaborative and welcoming working environment, where I was encouraged to develop and reshape my own ideas through open discussion. His door was always open for numerous meetings in which he carefully listened, challenged my thoughts with constructive feedback, and shared his expertise generously. I am especially appreciative of his careful attention to my manuscripts and the many skills I acquired under his supervision.

Beyond the scientific realm, I am grateful for the many personal conversations we shared, which, together with his sense of humor, broadened my perspective on life. He also made my stay in Germany much easier, supporting me in many practical and administrative matters that would have been far more challenging as a foreigner. His generosity went even further by welcoming me into his home and introducing me to his family and friends, making me feel part of a second family here. For this kindness, I also wish to warmly thank his wife, Ines. I can truly say that I regard him as more than a mentor, but also as a brother, and it has been a privilege to work alongside him.

I would also like to thank my colleagues in the modeling team. My heartfelt gratitude goes to Dr. Dijana Milosavljević for her remarkable support and encouragement throughout my work. I am

especially thankful for her friendship, for always being someone I could rely on, and for her contribution to this thesis by preparing the figure of the layered oxide material despite her busy schedule. I also wish to thank Dr. Kai Wilkner for his time, assistance, and continuous support during my research.

I would also like to thank my colleagues at IMD-2 who contributed to the success of this thesis. I am grateful to Dr. Christoph Roitzheim and Dr. Martin Finsterbusch from the electrochemical department for their efforts in reviewing my manuscripts and for the many valuable discussions we had. Their contributions are deeply appreciated. I also thank Dr. Yoo Jung Sohn for her support with training and for facilitating the experimental work, which was essential for the progress of my research.

I would like to take this opportunity to thank my beloved family in Palestine. I am especially grateful to my late father, who unfortunately passed away before I could complete this work. I deeply miss him, particularly during the difficult moments of my PhD journey, and I wish he were here to share this achievement with me. I will always cherish his unwavering encouragement and support, and I pray that he rests in peace.

My heartfelt thanks also go to my mother, whose constant belief in me and encouragement pushed me beyond my limits. Her daily morning calls to check on me were a source of comfort and strength throughout these years. I am also indebted to my sister, Dr. Mariam Al-Jaljouli, for her continuous support and, in particular, for her generous financial help during challenging times. Finally, I sincerely thank my brother for his ongoing care and encouragement, which meant a great deal to me.

I would also like to thank my friend Jalal for his valuable connections and constant encouragement. My gratitude extends to Khalil for the insightful discussions we shared and for his generous financial support during challenging times. A very special thanks goes to Dr. Abdalhalim Abuawad, whose true friendship and unwavering support have accompanied me throughout this journey.

I am also grateful to the Palestinian-German Science Bridge (PGSB) for enabling me to pursue my PhD at Forschungszentrum Jülich. My special thanks go to Dr. Caitlin Morgan from the German side for her continuous support and valuable advice throughout this journey.

Finally, I would like to thank those who placed obstacles in my path. Without these challenges, I would not have been able to achieve what I have accomplished today.

Declaration on publications

This thesis comprises the related articles that have been published in international journals.

Publication 01: **Fadi Al-Jaljouli**, Robert Mücke, Payam Kaghazchi, Yoo Jung Sohn, Martin Finsterbusch, Dina Fattakhova-Rohlfing, Olivier Guillon: Microstructural parameters governing the mechanical stress and conductivity of all-solid-state lithium-ion-battery cathodes: Journal of Energy Storage, 68 (2023) 107784: https://doi.org/10.1016/j.est.2023.107784.

Publication 02: **Fadi Al-Jaljouli**, Robert Mücke, Christoph Roitzheim, Yoo Jung Sohn, Najma Yaqoob, Martin Finsterbusch, Payam Kaghazchi, Olivier Guillon: Chemo-thermal stress in all-solid-state batteries: Impact of cathode active materials and microstructure: Journal of Power Sources, 644 (2025) 237136: https://doi.org/10.1016/j.jpowsour.2025.237136.

Publication 03: **Fadi Al-Jaljouli**, Robert Mücke, Martin Finsterbusch, Payam Kaghazchi, Olivier Guillon: Modeling chemo-thermal mechanical stresses in all-solid-state lithium Batteries: Influence of grain morphology and alignment: Journal of Power Sources, 653 (2025) 237539: https://doi.org/10.1016/j.jpowsour.2025.237539.

Publication 04: Robert Mücke, Najma Yaqoob, Martin Finsterbusch, **Fadi Al-Jaljouli,** Payam Kaghazchi, Dina Fattakhova-Rohlfing, Olivier Guillon: Modelling electro-chemically induced stresses in all-solid-state batteries: screening electrolyte and cathode materials in composite cathodes: Journal of Materials Chemistry A, 2023,11, 18801-18810: https://doi.org/10.1039/D3TA01729J.

Presentation of the work in the conferences

The following talks were presented at conferences, and the related abstracts were published in the conference proceedings.

46th International Conference & Exposition on Advanced Ceramics & Composites (ICACC2022) – January 23 – 28, 2022. (Online).

F. Al-Jaljouli (Talk), R. Mücke, O. Guillon,

Material design and stability of all-solid-state lithium ion battery cathodes.

49th International Conference & Exposition on Advanced Ceramics & Composites (ICACC2025) – January 26 – 31, 2025, Daytona beach, USA.

F. Al-Jaljouli (Talk), R. Mücke, P. Kaghazchi, C. Roitzheim, Y. Sohn, M. Finsterbusch, O. Guillon, Microstructure based modelling ceramic composite cathodes for all-solid-state lithium-ion batteries.

New Perspectives in solid-state and materials research –from fundamentals to applications– February 3 – 5, 2025, Max Planck Institute for Solid State Research, Stuttgart, Germany.

F. Al-Jaljouli (Talk), R. Mücke, O. Guillon, Material design and stability of all-solid-state batteries.

Kurzfassung

Festkörper-Lithium-Batterien (All-Solid-State Batteries, ASSBs) gelten aufgrund ihrer hohen Sicherheit und Energiedichte als vielversprechende Batterietechnologie der Zukunft. Allerdings unterliegen sie während des Lade-/Entladebetriebs mechanischer Ermüdung, verursacht durch mechanische Spannungen, die infolge von Volumenänderungen der Elektroden-Aktivmaterialien entstehen, welche durch den festen Elektrolyten mechanisch eingeschränkt sind.

Diese Arbeit basiert auf computerunterstütztem Materialdesign (GeoDict), um eine experimentelle Mikrostruktur einer Komposit-Kathode bestehend aus $LiCoO_2$ und $Li_7La_3Zr_3O_{12}$ (LCO/LLZO) zu rekonstruieren. Anschließend wurde diese Struktur unter Variation mikrostruktureller Designparameter erneut generiert: dem Feststoffvolumenanteil von LCO (SVF_{LCO}), der relativen Dichte ($\bar{\rho}$) sowie den Korngrößen von LCO und LLZO (d_{LCO} bzw. d_{LLZO}). Jeder dieser Parameter wurde einzeln variiert, während die übrigen konstant gehalten wurden. Für jede Variation wurden die elektrochemisch mechanischen induzierten Spannungen während eines Zyklus sowie die relativen elektronischen und ionischen Leitfähigkeiten berechnet. Diese Methodik ermöglicht eine systematische Untersuchung des Einflusses mikrostruktureller Designparameter auf die mechanische Spannungsverteilung und die relativen Leitfähigkeiten – auch für Konfigurationen, die experimentell schwer zugänglich sind.

Es wurde festgestellt, dass sowohl die mechanischen Spannungen als auch die Leitfähigkeiten in linearer Beziehung zu SVF_{LCO} stehen und eine progressive Abhängigkeit zur relativen Dichte ($\bar{\rho}$) aufweisen, während die Korngrößen von LCO und LLZO nur einen vernachlässigbaren Einfluss zeigen. Zur Beschreibung der maßgeblichen Einflussgröße auf die induzierte mechanische Spannung wurde eine neue dimensionslose Kenngröße eingeführt, der Faktor $\boldsymbol{K_n}$, definiert als das Verhältnis der relativen Grenzflächen zwischen den festen Phasen der Kompositkathode zur Volumenfraktion dieser Phasen (n = LCO oder LLZO). Die elektronischen bzw. ionischen Leitfähigkeiten werden hingegen vorrangig durch die jeweiligen Volumenanteile von LCO bzw. LLZO bestimmt.

Zur Verbesserung der Spannungsprognose in ASSBs wurde ein „chemo-thermomechanisches Spannungsmodell“ entwickelt, das den thermischen Eigenspannungszustand nach dem Sinterprozess mit den chemischen Spannungen infolge der (De-)Lithiation koppelt. Dieser ganzheitliche Ansatz zeigt, dass die thermischen Spannungen einen signifikanten Einfluss auf die Netto-Spannung (chemo-thermisch) im Aktivmaterial haben. Für LCO beispielsweise kompensiert die thermische Eigenspannung einen Teil der chemischen Spannung während der

Delithiation, was zu einer Reduktion der Gesamtspannung um etwa 43 % führt. Im Gegensatz dazu verstärken thermische Eigenspannungen die chemisch induzierten Spannungen in $Li_{0.5}$NCM955 und $Li_{0.1}$NCM955 um ca. 42 % bzw. 15 %.
Zudem zeigen die Ergebnisse, dass LCO unter den untersuchten Kathodenmaterialien (CAMs) das vorteilhafteste mechanische Verhalten aufweist, was auf die niedrigeren Gesamtspannungen und das Überwiegen von Druckspannungen zurückzuführen ist – ein entscheidender Faktor zur Vermeidung von Versagen in spröden oxidbasierten Materialien.
Abschließend wurde der Einfluss der Kornmorphologie der Kathode auf die induzierten chemo-thermomechanischen Spannungen untersucht. Dabei wurden vier Systemkonfigurationen simuliert: sphärisches LCO–sphärisches LLZO, sphärisches LCO–faserförmiges LLZO, hexagonales LCO–sphärisches LLZO sowie hexagonales LCO–faserförmiges LLZO. Die Ergebnisse zeigen, dass faserförmiges LLZO in Kombination mit texturiertem, hexagonalem LCO die induzierten mechanischen Spannungen um 11,0 % in LCO und 9,0 % in LLZO reduziert. Im Gegensatz dazu führt der Einsatz von zufällig orientiertem sphärischem LCO zu einer Erhöhung der Spannungen in beiden Phasen. Die Ausrichtung der faserförmigen LLZO-Partikel beeinflusst die Spannungsverteilung entscheidend über facettenspezifische Kontaktflächen und unterstreicht die Bedeutung mikrostruktureller Optimierung zur Verbesserung der mechanischen Zuverlässigkeit von ASSBs.

Abstract

All-solid-state lithium batteries (ASSBs) are considered a promising future battery technology due to their high safety and energy density. However, they are suffering from mechanical fatigue during cycling, caused by induced mechanical stresses by volume changes in the electrode active materials which is constrained by the solid electrolyte. This research is based on computer-aided material design (Geodict), to reconstruct an experimental microstructure of composite cathode consisting of $LiCoO_2$/$Li_7La_3Zr_2O_{12}$ (LCO/LLZO), followed by regenerating this structure while varying its microstructural design parameters (solid volume fraction of LCO – SVF_{LCO}, relative density – $\bar{\rho}$ and grain sizes of LCO and LLZO – d_{LCO}, d_{LLZO} respectively). Where each variation occurred while fixing the other parameters. We calculated the electrochemical stresses during cycle and relative conductivities (electronic and ionic) for each variation. This methodology enables systematic investigation of the impact of microstructural design parameters on mechanical stress distribution and relative conductivities, including configurations not easily accessible experimentally. We found that mechanical stresses and conductivities exhibit a linear relationship with the variation of SVF_{LCO} and a progressive relation with variation of $\bar{\rho}$, while the grain sizes of LCO and LLZO show negligible influence. A new dimensionless parameter, $\boldsymbol{K_n}$, defined as the ratio of relative interface area between solid contents of composite cathode to the volume ratio of these contents (n = LCO or LLZO), was introduced as a governing factor of the induced mechanical stress. On the other hand, the electronic and ionic conductivities are primarily governed by the volume fractions of LCO and LLZO, respectively.

To further enhance stress prediction in ASSBs, we developed a "chemo-thermal stress" model that integrates residual thermal stress after sintering with chemical stress induced during (de)lithiation. This holistic approach demonstrates that thermal stress has a significant impact on the net stress values (chemo-thermal) in active materials. For LCO, thermal stress mitigates the chemical stress during delithiation, reducing total chemo-thermal stress by approximately 43%. In contrast, residual stress amplifies chemical stress in $Li_{0.5}$NCM955 and $Li_{0.1}$NCM955 by around 42% and 15%, respectively. Moreover, our results revealed that among the studied cathode active materials (CAMs), LCO exhibits superior mechanical behavior due to lower overall stress and a predominance of compressive stress, reducing failure risk in brittle oxide materials.

Finally, we investigated the influence of cathode grain morphology on induced chemo-thermal mechanical stress, focusing on systems combining spherical or hexagonal LCO with spherical or

fiber-shaped LLZO. Modeled microstructures of four configurations—spherical LCO–spherical LLZO, spherical LCO–fiber LLZO, hexagonal LCO–spherical LLZO, and hexagonal LCO–fiber LLZO—were analyzed. Results show that fiber-shaped LLZO combined with textured hexagonal LCO reduces mechanical stress by 11.0% in LCO and 9.0% in LLZO. while, randomly oriented spherical LCO increases induced stresses in both phases. The alignment of fiber LLZO critically affects the stress distribution through facet-specific contact interfaces, emphasizing the importance of microstructural engineering to enhance the mechanical reliability of ASSBs.

Table of Contents

Table of Contents 1
List of Figures xiii
List of Abbreviation xiv
Chapter 1 Motivations and Objectives 1
1.2. Motivations 1
1.2. Objectives 3
Chapter 2 Fundamentals 5
2.1. Fundamentals of Batteries 5
2.1.1. Definition of Batteries 5
2.1.2. History of Batteries 6
2.1.3. Components of Batteries 6
2.1.4. Parameters of Batteries Performance 8
2.1.5. All-Solid-State Batteries 10
2.2. Cathode Active Materials 13
2.2.1. Layered Oxide Cathodes 13
2.3. Solid Electrolyte 23
2.3.1. Garnet-Type 23
2.3.2. Sulfide type 25
2.3.3. Lithium Phosphorus Oxynitride 27
2.4. Mechanical Stress in Solids 30
2.4.1. Definition of Mechanical Stress 30
2.4.2. Definition of Strain 30
2.4.3. Hooke's Law 31
2.4.4. Principal Stresses 33
2.4.5. Tensile and Compressive Stress 33
2.5. Representative Volume Element 35
2.5.1. Definition of the Representative Volume Element 35
2.5.2. Conditions for Representativeness 35
2.5.3. Boundary Conditions and Homogenization 36
2.5.4. Microstructure Generation Techniques 37
2.6. Voxel-Based Mechanical Stress Solvers 38
2.6.1. Definition of Voxel 38
2.6.2. Principles of Image-Based Mechanical Simulation 39
2.6.3. Periodic Boundary Conditions and Fourier-Based Formulation 40

2.6.4. Limitations 40

References 42

Chapter 3 Research Papers 54

3.1. Paper I: Microstructural parameters governing the mechanical stress and conductivity of All-solid-state lithium-ion-battery cathodes 54

3.2. Paper II: Chemo-Thermal Stress in All-Solid-State Batteries: Impact of Cathode Active Materials and Microstructure 88

3.3. Paper III: Modeling Chemo-Thermal Mechanical Stresses in All-Solid-State Lithium Batteries: Influence of Grain Morphology and Alignment 117

3.4. Paper IV: Modelling Electro-Chemically Induced Stresses in All-Solid-State Batteries: Screening Electrolyte and Cathode Materials in Composite Cathodes 143

Chapter 4 Conclusions and Outlook 172

List of Figures

Figure 1. Global electric vehicle sales and market share from 2015 to 2024, (BEV : battery electric vehicle; PHEV : plug-in hybrid vehicle). Adapted from ref [1]. 1
Figure 2. a) Objects discovered at Khuyut Rabboua (near Baghdad) in 1936, commonly referred to as the 'Baghdad Battery'. Adapted from ref [19] b) Sketch of modeled Baghdad battery. Adapted from ref [20]. 6
Figure 3. Composite cathode microstructure generated by Geodict software, illustrating the major components of composite cathode: CAM in red and SE in yellow. 11
Figure 4. Crystal structure of layered oxides generated by VESTA software. 13
Figure 5. Crystal structure of LCO. Adapted from ref [75]. 14
Figure 6. Structural variation of LCO from hexagonal to monoclinic with anisotropic lattice parameters variation after delithiation. Adapted from ref [84]. 15
Figure 7. Lattice parameters variation of LCO a) a-axis, b) c-axis c) volume of the unit cell of LCO as a function of lithium concentration. Adapted from ref [80]. 15
Figure 8. TEM images illustrate cracks within LCO particles obtained from cycled cathode. Adapted from ref [88]. 16
Figure 9. Crystal structure of NCM. Where, the transition metal layer consists of Ni and Co (gray and blue respectively), while O and Mn are in red and purple respectively. Adapted from ref [95]. 17
Figure 10. Lattice parameter variation of NCM111 due to delithiation (white circles) and lithiation (black circles) processes a) a-axis, b) c-axis. c) the net unit cell volume change. Adapted from ref [101]. 18
Figure 11. Variation of lattice parameters of NCM811 as a function of cell voltage during a single charge–discharge cycle. Adapted from ref [119]. 19
Figure 12. SEM image with high-magnification illustrating the impact of cycling (500 cycles) on NCM811. Adapted from ref [118]. 19
Figure 13. Variation of lattice parameters of NCM955 in a) a-axis, and b) in c-axis as a function of cell voltage. Adapted from ref [122]. 20
Figure 14. Crystal structures of LMO, where the Li and O are in green and red respectively, while Mn positions are enclosed by the polyhedral. Adapted from ref [131]. 21
Figure 15. Lattice variation in LMO as a function of Li concentration during a) delithiation and b) lithiation process. Adapted from ref [130]. 21
Figure 16. Crystal structure of LLZO in its two phases: a) cubic phase and b) tetragonal phase. Adapted from ref [145]. 24
Figure 17. Conduction channel pathway of Li-ion in LLZO. Adapted from ref [146]. 24
Figure 18. Crystal structures of LPS, LGPS, and LPSX. Adapted from ref [55]. 26
Figure 19. Crystal structure of LiPON generated by AIMD. Adapted from ref [161]. 27
Figure 20. Illustration of boundary conditions: a) periodic and b) symmetric. Adapted from ref [191]. 37
Figure 21. Schematic of voxilized microstructure illustrating the voxel. 38
Figure 22. Finite element meshing. 39

List of Abbreviation

µCT	Micro-computed tomography
Ah	Ampere-hours
AIMD	Ab initio molecular dynamics
BEV	Battery electric vehicle
PHEV	Plug-in hybrid vehicle
BMS	Battery management systems
CE	Coulombic efficiency
EV	Electric vechicles
FE	Finite element
FEA	Finite element analysis
FFT	Fast fourier transform
FIB-SEM	Focused ion beam scanning electron microscopy
GEN_PRVE	Generated representative volume element
HRTEM	High-resolution transmission electron microscopy
KUBC	Kinematic uniform boundary conditions
LGPS	$Li_{10}GeP_2S_{12}$
LIB	Lithium-ion batteriey
LCO	Lithium cobalt oxide
LiPON	Lithium phosphorus oxynitride
LLZO	Lithium lanthanum zirconium oxide
LMO	$LiMn_2O_4$
NCM	Nickel manganese cobalt oxide
PBC	Periodic boundary conditions
PE	Polyethylene

PM_{10}	Particulate matter with a diameter of 10 micrometers or smaller
$PM_{2.5}$	Particulate matter with a diameter of 2.5 micrometers or smaller
PP	Polypropylene
$R\bar{3}m$	Rhombohedral space group
Redox	Reduction-oxidation
RVE	Representative volume element
SBC	Symmetric boundary condition
SE	Solid electrolyte
SEI	Solid electrolyte interphase
SEM	Scanning electron microscope
SUBC	Static uniform boundary conditions
SVF	Solid volume fraction
TEM	Transmission electron microscopy
TM	Transition metal
XCT	X-ray computed tomography
XRD	X-ray diffraction
α-$NaFeO_2$	Alpha-sodium ferrite

Chapter 1 Motivations and Objectives

1.2. Motivations

The past decades have seen remarkable technological progress, transforming industries and lifestyles with innovations such as autonomous drones, electric vehicles (EVs), and advanced robotics. These emerging technologies demand unprecedented levels of portable and reliable energy storage. For example, EV adoption is accelerating worldwide where, global EV sales surpassed 17 million units in 2024, accounting for more than 20% of new car sales (Figure 1) [1]. Similarly, drone technology is expanding beyond hobbyist use into logistics, precision agriculture, surveillance, and emergency response, all requiring compact, high-energy batteries for sustained and autonomous operation.

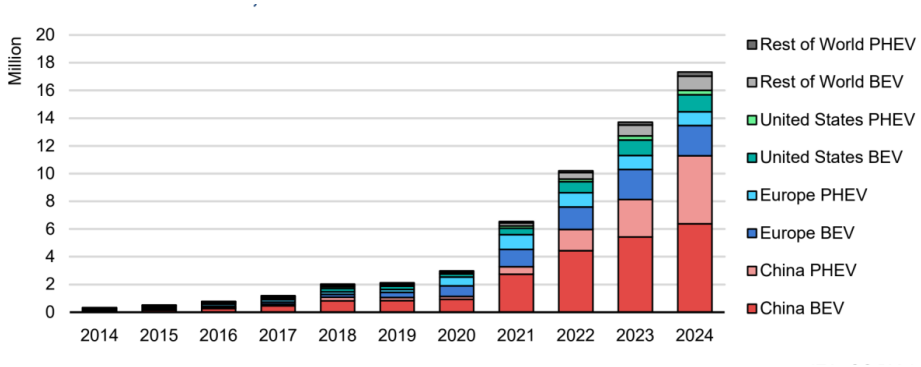

Figure 1. Global electric vehicle sales and market share from 2015 to 2024, (BEV : battery electric vehicle; PHEV : plug-in hybrid vehicle). Adapted from ref [1].

At the same time, the global energy landscape faces critical challenges. Although fossil fuels still dominate the supply chain, their extraction and combustion release substantial amounts of airborne pollutants, including nitrogen oxides, sulfur oxides, and fine particulate matter ($PM_{2.5}$), all of which pose serious threats to public health and environmental quality [2]. These pollutants have immediate and measurable impacts, contributing to over 6.7 million premature deaths globally each year and incurring heavy economic costs due to increased healthcare demand and reduced labor productivity [2].

Recent studies confirm that increasing EV penetration has tangible environmental benefits in terms of air quality. In cities like Beijing, Shanghai, and Shenzhen, replacing internal

combustion vehicles with EVs between 2019 and 2021 led to significant reductions in $PM_{2.5}$, NO_2, SO_2, CO, and PM_{10} concentrations, with public health benefits already observable [3]. A similar trend has been documented in Southern California, where modeled EV adoption scenarios predict up to 30% drops in NO_2 and 14% reductions in $PM_{2.5}$, especially in urban and low-income neighborhoods [4]. These outcomes support the case for rapid electrification—for immediate air pollution mitigation and health impact reduction.

To address both the raising demand for portable power and the environmental impact of fossil energy, there is a growing worldwide shift toward electrification supported by renewable energy integration. Renewable sources such as solar and wind are being deployed at an unprecedented pace. However, their intermittent and location-dependent nature presents a major challenge to energy reliability and calls for the deployment of advanced energy storage systems (ESS) to buffer and stabilize supply. Among available technologies, electrochemical storage—particularly lithium-ion batteries (LIBs)—remains the most scalable and efficient option, offering round-trip efficiencies approaching 95% along with high energy and power densities [7].

Yet the operational demands of next-generation applications—ultra-fast charging, high current density cycling, and mechanical resilience—are beginning to expose the limitations of current LIB designs. High-nickel cathode materials, solid-state configurations, and extreme load conditions introduce complex chemo-mechanical phenomena, including particle fracture, interfacial delamination, and internal stress accumulation, which undermine battery longevity and safety. These issues are particularly critical for autonomous aerial vehicles, heavy-duty electric trucks, and grid storage systems, where failures carry high operational and economic costs.

Developing high-energy, durable, and safe battery systems capable of withstanding variable loads and repeated cycling is therefore a pressing research frontier. This work is driven by the need to enhance the structural integrity and long-term performance of battery materials under realistic operating stresses, ultimately enabling the portable and sustainable energy solutions that future mobility and energy infrastructures increasingly demand.

1.2. Objectives

The transition from conventional lithium-ion batteries towards all-solid-state lithium batteries (ASSBs) include various benefits starting from high energy density, reducing the size of the battery, and finally increasing safety by avoiding the usage of liquid electrolytes and hence preventing the formation of short circuits. However, in spite of previous advantages, ASSBs are still facing challenges hindering its wide-spread production. Among these challenges is the formation of high induced mechanical stresses in the components of the composite cathode. This ascribed to the constrains on the CAM's volume change by the rigid solid electrolyte (SE) during the cycling process, which in turn lead to formation of cracks in the system causing a drop in the capacity.

The main objective of this PhD thesis is to investigate the capability of reducing the induced mechanical stress in the system while improving or maintaining the electronic and ionic conductivities of the CAMs and SEs, respectively. A numerical simulation method that evaluates the stress state in clearly defined microstructures with varying microstructural parameters shall be developed, starting with an obtain representative volume element (RVE) that reproduce an experimental microstructure. The following objectives shall be addressed:

- **Computational reconstruction of experimental microstructures**
  The first goal in this study is to achieve an accurate digital reconstruction of the experimental microstructure by implementing a systematic generation approach and by defining quantitative metrices to assess the degree of similarity between the experimental structure and the reproduced.
- **Defining the realistic mechanical stress state in the composite cathode**
  Establish the most realistic mechanical stress state in the composite cathode by integrating both manufacturing and electrochemical effects. This includes evaluating the residual stress generated during the cooling down after sintering (thermal stress) and combining it with the stress induced by the delithiation process (chemical stress). The goal is to introduce and analyze the resulting chemo-thermal mechanical stress as a comprehensive representation of the stress state in the composite cathode.
- **Quantifying the impact of microstructural design parameters on the durability and performance of composite cathodes**
  Define the microstructural design parameters (solid volume fraction of CAM –SVF_{CAM}, relative density–$\bar{\rho}$, and grain sizes of CAM and LLZO–d_{CAM} and d_{LLZO}, respectively) and

investigate their influence on two properties: (1) durability, by analyzing the induced mechanical stresses in both the CAM and LLZO, and (2) performance, by evaluating the electronic and ionic conductivities of the CAM and LLZO, respectively.

- **Identifying the governing factors of mechanical stress and conductivity in composite cathodes**

  This part of research aims to define the governing factor of the induced mechanical stresses of CAM and SE of the composite cathode, by identifying microstructural parameters that directly define the stress state in the system. Furthermore, it aims to define the governing factors of the electronic and ionic conductivities of CAM and SE, respectively.

- **Comparing stress behavior in different CAMs**

  The aim of this part of the research is to compare different types of layered CAMs coupled with LLZO as SE under comparable conditions through variation of the same microstructural design parameters exploring thermal, chemical, and chemo-thermal stresses.

- **Understanding the effect of LCO and LLZO grain morphologies and alignment on stress distribution in composite cathodes**

  This section shall be dedicated to investigate the impact of morphologies and alignments of grains of LCO and LLZO on the induced mechanical stresses. it should elucidate the effect of adjacent different facet combinations on the stresses. Moreover, it shall examine the effect of randomly orientated LCO grains which is present when using spherically-shaped LCO on the stresses.

Chapter 2 Fundamentals

2.1. Fundamentals of Batteries

2.1.1. Definition of Batteries

A battery is a device that stores and electrochemically converts chemical energy into electrical energy through redox reactions [5-7]. This conversion occurs due to a series of chemical reactions which generate a flow of charged particles, driven by differences in chemical potential, which in turn produce an electric current required to power external load [8, 9]. The thermodynamic driving force for the redox reaction is the change in Gibbs free energy (ΔG) of the full-cell electrochemical reaction, expressed as:

$$\Delta G = -nFE_{cell} \quad (1)$$

where n is the number of transferred electrons, F represents Faraday constant (96485 C/mol), and E_{cell} is the cell potential (V). The negative sign indicates a spontaneous reaction, where no external energy source is needed [10, 11]. The cell potential E_{cell} is defined as the difference between the electrode potentials of the cathode and anode:

$$E_{cell} = E_{cathode} - E_{anode} \quad (2)$$

Nernst equation governs the voltage under non-standard conditions:

$$E_{cell} = E^0_{cell} - \frac{RT}{nF}\ln Q \quad (3)$$

where E^0_{cell} is the standard electrode potential, R is the ideal gas constant (8.314 J/mol·K), T is the temperature (in K), and Q is the reaction quotient [10, 12].

Batteries vary widely in scale, from delivering nanowatt/hour to support miniature devices like sensors to providing megawatt/hours for large-scale operations such as grid energy storage, showcasing their adaptability across applications [13, 14]. They are integral to modern technologies, enabling the operation of consumer electronics like smartphones and laptops, supporting industrial systems by stabilizing renewable energy sources such as solar and wind, and powering transportation innovations including electric vehicles (EVs) and aerospace equipment, where their lightweight and efficient energy delivery is vital [15, 16]. The utility of batteries lies in their self-contained nature, eliminating the need for continuous fuel input unlike traditional generators, with ongoing advancements in electrochemical design enhancing their energy efficiency, power output, and environmental sustainability, making them a cornerstone of energy solutions in both every day and specialized contexts [10, 12].

2.1.2. History of Batteries

The origins of battery technology are traced to the enigmatic “Baghdad Battery”, discovered near Baghdad and dated between 250 BCE and 250 CE, a clay vessel with a copper cylinder and iron rod (Figure 2) hypothesized to have served as an early electrochemical power source though its purpose is still debated [17, 18].

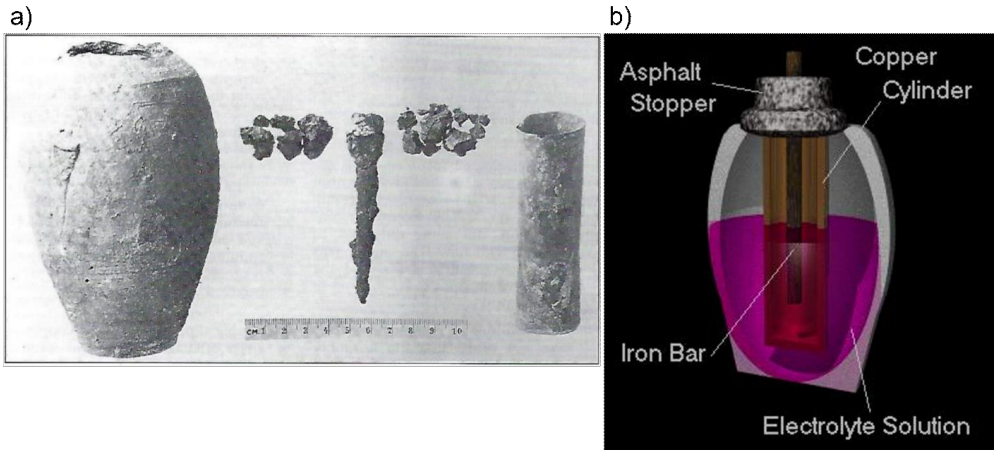

Figure 2. a) Objects discovered at Khuyut Rabboua (near Baghdad) in 1936, commonly referred to as the ‘Baghdad Battery’. Adapted from ref [19] b) Sketch of modeled Baghdad battery. Adapted from ref [20].

The modern era of batteries started with the invention of the Voltaic Pile in 1800 by Alessandro Volta. A stack of zinc and copper disks separated by brine-soaked material that generated a steady electric current, marking the birth of the first true battery [5, 21]. Followed by several improvements, until 1991 when Sony commercialized the lithium-ion batteries which transformed portable electronics with high energy density, illustrating a progression fueled by scientific discovery and practical demand [5, 21, 22].

2.1.3. Components of Batteries

A conventional Li-ion battery consists of several fundamental components that determine its performance and efficiency.

1. Electrodes

Electrodes are the components in a battery that serve as the sites for storing and releasing electrical energy. In principle, there are two types of electrodes, defined by their roles during battery operation, as follows:

2. Cathode

The positive electrode derived from Greek "kathodos" (κάθοδος), meaning "downward path" (from "kata" [κατά], "down," and "hodos" [ὁδός], "path"), coined by William Whewell in 1834 [23]. During the redox operation, the cathode serves as the source which ions started to release toward the electrolyte during the charge process of the battery [14, 24]. This in turn leads to consider the cathode as the main influencer on the battery's voltage and energy storage capacity, while its stability under varying conditions impacts safety and age, making it a main part for performance optimization [25, 26]. Furthermore, the selection of the cathode material plays a great role determining the performance and the durability of the battery.

3. Anode

The negative electrode, derived from Greek "Anodos" (ἄνοδος), meaning "upward path" (from "ana" [ἀνά], "up," and "hodos" [ὁδός], "path"), coined by William Whewell in 1834 [23]. During the redox operation, the anode serves as a receptor which store the ions during charging the battery until releasing them during the discharge process [25, 26]. The storage service of the anode make it play a key role in determining the battery's charge-holding ability and its performance over repeated cycles, with its efficiency in ion exchange being essential for operational effectiveness.

4. Electrolyte

The electrolyte functions as the ionic conductive medium that permits the transportation of the ions between the cathode and anode during cycling, enabling the battery's electrochemical reactions while preventing electron flow within the cell to avoid short circuits [5, 27]. It must exhibit high ionic conductivity ($>10^{-3}$ S cm^{-1}), a wide electrochemical stability window (typically 2.5 – 4.5 V vs. Li^+/Li), and compatibility with electrode interfaces to ensure efficient energy transfer and safety under operational [28, 29]. The electrolyte's properties, such as its resistance to degradation or thermal runaway, are vital for maintaining performance and extending the battery's operational life [27, 30].

5. Separator

The separator is a thin porous electrically insulating membrane positioned between the cathode and anode in systems with liquid electrolytes. For liquid-base batteries, the separator considered an essential part which insure both safety and efficiency. Typical materials include: Polyethylene (PE), Polypropylene (PP) and Tri-layer PP/PE/PP composites [5, 6]. It requires mechanical strength to prevent dendrite penetration, and thermal resilience to stop ion transport during thermal runway by melting in high temperature (PE melts at ~135 °C) in order to

withstand operational conditions and prevent failures like short circuits [16, 31]. It is worth to mention that failure of the separator can lead to internal short circuits, rapid heat generation, and catastrophic battery failure [32, 33]. On other hand, in all-solid-state batteries the separator is replaced by the solid electrolyte.

6. Current Collectors

Current collectors are conductive layers that support the electrodes and facilitate electron flow to and from the external circuit, ensuring efficient energy transfer [5, 6]. Positioned at the cathode (copper foil ~10–20 µm – stable at low potential) and anode (aluminum foil ~15–25 µm – resistant to corrosion at high voltage), they provide a pathway for electrons, requiring high conductivity and compatibility with the electrodes' operating conditions [33, 34]. Their design impacts the battery's power delivery and structural integrity, making them integral to overall performance [7, 35]. The harmony among these components is essential to define the battery's electrochemical capabilities, with research continually improving their integration to enhance efficiency, safety, and longevity [5, 14, 30].

2.1.4. Parameters of Batteries Performance

Battery performance is evaluated through a comprehensive set of parameters that quantify energy storage, delivery, durability, and operational limits, each critical for determining suitability across applications such as consumer electronics, renewable energy systems, electric vehicles (EVs), and aerospace. These metrics provide a holistic assessment of a battery's capabilities, guiding design optimization and real-world deployment decisions [5, 22, 36].

a) Capacity (Q)

Capacity measures the total electrical charge a battery can deliver, expressed in ampere-hours (Ah), and serves as the foundational metric for assessing how long a battery can power a device under a given load [5, 7]. It is calculated as:

$$Q = \int_0^t I \, dt \tag{4}$$

where I is the discharge current, and t is time [8, 35]. For example, a 3 Ah battery can supply 3 A for 1 hour under ideal conditions. Lithium-ion batteries range from a few Ah in small cells to hundreds of Ah in large packs, indicating their scalability [30, 37, 38]. However, the capacity is a dynamic value affected by several parameters. For example, high discharge rates reduce the capacity due to internal resistance limiting ion transport, while aging degrades it through mechanisms like solid electrolyte interphase (SEI) growth or electrode material breakdown [14, 39]. Temperature extremes exacerbate this behavior, as low temperatures reduce ion mobility

(e.g., 20-30% capacity loss at -20°C), while on other hand, heat accelerates side reactions (e.g., electrolyte decomposition above 40°C) [5, 25, 39]. Furthermore, the cycling patterns, such as frequent deep discharges, also shorten lifespan, while shallow cycles preserve capacity [22, 36]. Hence, capacity is considered as a critical parameter for sizing batteries and predicting service life, often requiring battery management systems (BMS) to optimize usage and mitigate degradation [30, 38].

b) Energy Density

Energy density quantifies the energy a battery stores per unit volume (Wh/l) or mass (Wh/kg). It determines value of energy can be stored relative to the battery's size or weight, where it can be approximated as:

$$E = \frac{U_{avg} \times Q}{X} \quad (5)$$

where U_{avg} is the average operating voltage, Q is the capacity and X represents either the mass (m, in kg) for gravimetric energy density or the volume (V, in l) for volumetric energy density [7, 37]. The importance of energy density relies on the fact that it is a key factor for portability and range in compact or mobile applications [5, 40].

c) Power Density

Power density measures the rate at which energy can be delivered, in watts per either liter (W/l) or kilogram (W/kg). It is calculated as:

$$P = \frac{U \times I}{X} \quad (6)$$

where U is voltage, I is current, reflecting instantaneous power output and X represents either the mass (m, in kg) for gravimetric power density or the volume (V, in l) for volumetric power density [6, 41]. Power density is crucial for applications requiring rapid energy bursts like EV acceleration or power tools [5, 8]. Lithium-ion batteries reach up to 2000 W/kg [7, 21, 38]. However, several conditions are required to have high power density, for example low internal resistance and thin porous electrode structures in order to facilitate faster ion transport. High power compromises energy density as dense electrodes slow down diffusion [24, 37, 42] and high-rate materials enhance power density but may lower capacity leading to required tailored design optimization [5, 14, 38]. Moreover, power density is sensitive towards temperature, where cold temperatures reduce conductivity and power output (e.g., up to 50% power loss at −20°C), while elevated temperatures enhance conductivity and power density but at the cost of increased degradation and thermal instability [25, 43].

d) C-rate

C-rate is defined as the charging/discharging (cycling) speed relative to capacity, by linking current to capacity [7, 44]. Where 1C equals full discharge (or charge) in an hour [5, 6].
It is calculated by

$$C = \frac{Q}{I} \quad (7)$$

where I is the applied current, and Q is the capacity. High C-rates (e.g., 5C, charging in 12 minutes) enable fast-charging EVs or power tools, but reduce capacity via polarization and heat, while low C-rates (e.g., 0.1C), on other hand, maximize capacity for uses like backup power [5, 38, 45]. Several factors affect the C-rate, for example, thinner electrode and high temperature increase the C-rate [26, 43, 46]. Hence, C-rate can be considered as a key link between performance and durability which guide in turn the design of charging/discharging strategy [5, 37]. On other hand, it is worth to mention that excessive rates lead to lithium plating or thermal stress [22, 36]. Therefore, a battery management system (BMS) limits C-rates (e.g., to 2C) to balance rapid charging with long-term cell health [14, 16, 38].

e) Coulombic Efficiency

Coulombic efficiency (CE) is a percentage ratio of discharged to charged capacity, in lithium-ion battery after initial cycles, measuring charge reversibility [5, 8]. It can be calculated by:

$$\eta = {Q_{out}}/{Q_{in}} \times 100\% \quad (8)$$

where Q_{out} is discharged capacity and Q_{in} is charged capacity [6, 47].
Coulombic efficiency is also considered as a tracking indicator of efficiency and durability of the battery [5, 38]. Where lower values of coulombic efficiency indicate for a health concerns of the battery like plating [13, 36, 37, 42].

2.1.5. All-Solid-State Batteries

All-solid-state batteries (ASSBs) represent a transformative advancement in electrochemical energy storage, offering potential improvements over conventional lithium-ion batteries (LIBs) that utilize liquid electrolytes. ASSBs employ solid electrolytes (SEs) to facilitate ion transport between the anode and cathode, eliminating flammable liquid components and enabling enhanced safety, higher energy density, and broader operating temperature ranges [44, 48].

- **Advantages of All-Solid-State Batteries**

ASSBs offer several advantages over conventional LIBs. First, the replacement of flammable liquid electrolytes with non-flammable SEs significantly enhances battery safety, reducing the

risk of thermal runaway and fire hazards [6, 22]. Second, ASSBs enable the use of lithium metal anodes, which can increase energy density to over 500 Wh kg^{-1}, compared to 250–300 Wh kg^{-1} for conventional LIBs [49, 50]. Third, SEs may exhibit wider electrochemical stability windows, allowing operation at higher voltages and temperatures [26, 51]. Finally, the mechanical stability of SEs can in principle suppress dendrite growth, potentially improving cycle life and coulombic efficiency [27, 52].

- **Challenges in All-Solid-State Battery Development**

Despite their promise, ASSBs face significant challenges that hinder commercialization. A primary issue is the high interfacial resistance between the solid electrolyte and electrodes, which arises from poor physical contact and chemical instability [53, 54]. For instance, sulfide-based SEs can react with lithium metal to form undesirable interphases, reducing ionic conductivity [55, 56]. Another challenge is the low ionic conductivity of many SEs compared to liquid electrolytes, particularly at room temperature [57, 58]. Additionally, the mechanical brittleness of ceramic SEs complicates large-scale manufacturing and cycling stability [59, 60]. Finally, dendrite formation remains a concern, as high current density or defects in SEs can still promote lithium penetration [61, 62].

- **Composite Cathodes in All-Solid-State Batteries**

Composite cathodes have emerged as a critical strategy to enhance the performance of ASSBs by addressing the limitations of traditional cathode designs, particularly poor ionic and electronic conductivity within the cathode layer.

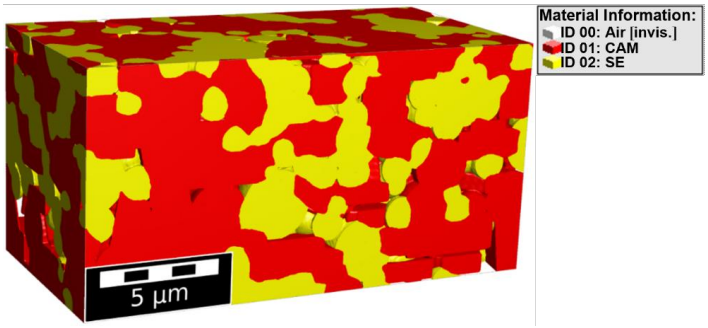

Figure 3. Composite cathode microstructure generated by Geodict software, illustrating the major components of composite cathode: CAM in red and SE in yellow.

Unlike conventional cathodes, which rely solely on active materials, the absence of a liquid electrolyte renders it essential to provide ionic conductance in close proximity to the active materials. Therefore, composite cathodes integrate active materials with SEs (Figure 3). Furthermore, conductive additives such as carbon black, carbon nanotubes, or graphene are

incorporated to form a mixed ionic–electronic conducting network [63, 64]. This design improves charge transport pathways and reduces interfacial resistance by surrounding active material particles with solid electrolyte, thereby facilitating efficient lithium-ion transfer across interfaces. Simultaneously, the incorporation of conductive additives establishes continuous electron conduction networks, thereby mitigating electronic transport limitations and enhancing the overall electrochemical performance [63]. However, the development of composite cathodes faces several challenges. The optimization of the component ratios is critical, as excessive SE content can reduce the active material loading and lower energy density, while insufficient SE content limits ionic conductivity [65, 66]. Additionally, chemical compatibility between the active material and SE is essential to prevent side reactions that degrade performance [67, 68].

2.2. Cathode Active Materials

Cathode active material (CAM) are considered as the basic element in the lithium-ion battery (LIB) technology. It is the element which dictates several performance parameters of the LIB such as energy density, voltage profile, and cycle life. Over the past three decades, tremendous progress has been made in developing and optimizing a wide range of CAMs to meet the increasing demands of portable electronics, electric vehicles, and grid storage applications. These materials can be systematically categorized by their crystallographic structures into layered oxides, spinels, olivines, and polyanionic/NASICON-type materials. Each class possesses unique structural, electrochemical, and mechanical characteristics that influence lithium-ion transport, electronic conductivity, structural stability, and interfacial reactivity which are more pronounced in the field of all solid-state battery (ASSB) systems that employ garnet-type electrolytes such as $Li_7La_3Zr_2O_{12}$ (LLZO) [15, 69, 70].

2.2.1. Layered Oxide Cathodes

Layered oxides have the general formula $LiMO_2$ (where M includes Co, Ni, Mn, or combinations). They are crystallizing in the α-$NaFeO_2$ structure with $R\bar{3}m$ symmetry. Layered oxides are characterized by their two-dimensional structure, consisting of alternating layers of lithium and transition metal (TM) ions separated by oxygen layers (Figure 4). They feature a hexagonal layered structure that facilitates the diffusion of lithium-ions along the planes during cycling which in turn, leads to high energy densities rendering them the favorable candidates for the commercial LIBs [71, 72].

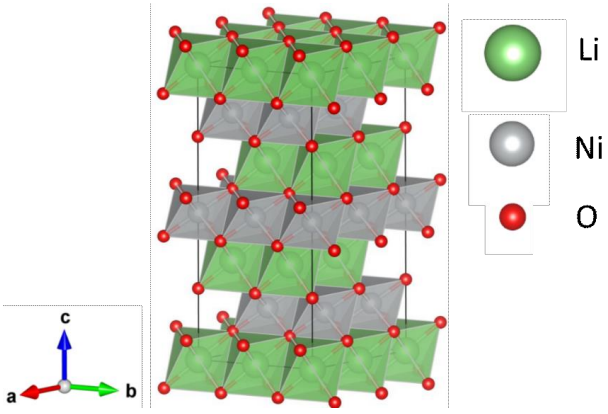

Figure 4. Crystal structure of layered oxides generated by VESTA software.

- **Lithium Cobalt Oxide**

Lithium cobalt oxide ($LiCoO_2$, LCO) was initially developed and first reported as a promising cathode in 1980 by Goodenough's group, marking a milestone in the development of rechargeable lithium-ion batteries [40, 69, 70]. It became the first commercially successful cathode material in Sony's 1991 lithium-ion battery [73].

LCO adopts a trigonal layered structure α-$NaFeO_2$ structure with rhombohedral symmetry (space group $R\bar{3}m$), in which Li ions occupy octahedral 3b sites and Co ions are located in octahedral 3a sites, forming alternating Li and Co layers separated by close-packed oxygen [69, 74] (Figure 5). This structure provides two-dimensional Li-ion diffusion pathways predominantly within the interlayer space (*ab*-plane) [40, 74].

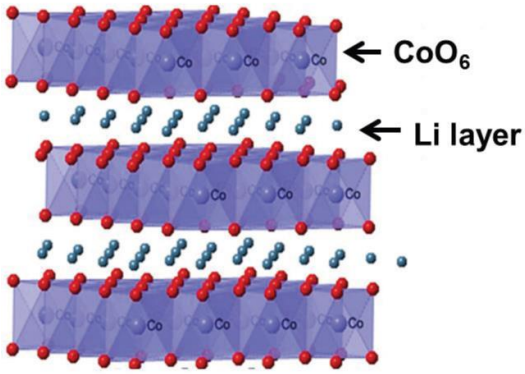

Figure 5. Crystal structure of LCO. Adapted from ref [75].

LCO has a theoretical capacity of 274 mAh g^{-1}, however, only ~140–150 mAh g^{-1} is practically extracted since beyond this limit, the material undergoes a sequence of irreversible phase transitions (H1 → M1 → H2 → O1) at high states of delithiation (>0.5 Li extraction) accompanied by oxygen evolution, cation migration, and lattice collapse [10, 11]. Furthermore, LCO has a cycle life of 500-1000 cycles [76]. The material's high density and compact structure also make it advantageous in terms of volumetric energy density. Electronic conductivity of LCO is relatively high, reaching up to 10^{-2} S cm^{-1} attributed to partial Co^{3+}/Co^{4+} redox participation during charge [77-79]. It is, however, characterized by low ionic conductivity, with Li^+ diffusion coefficient in the range of 10^{-9} and 10^{-12} cm^2 s^{-1}, decreasing significantly near full delithiation [74, 78].

The typical lattice parameters of pristine LCO are a ≈ 2.82 Å and c ≈ 14.05 Å [80-83]. During the delithiation process, the structure of LCO changes from hexagonal lattice structure to monoclinic (Figure 6), which in turn induces anisotropic lattice strains. The initial removal of lithium results in expansion of the *c*-axis due to increased electrostatic repulsion between adjacent CoO_2 layers when operated below 4.2 V (Figure 7b). On the other hand, *a* and *b*-axes contract under similar condition (Figure 7a). As a result, LCO exhibits modest volume changes during delithiation to $Li_{0.5}CoO_2$ (~2% expansion) (Figure 7c).

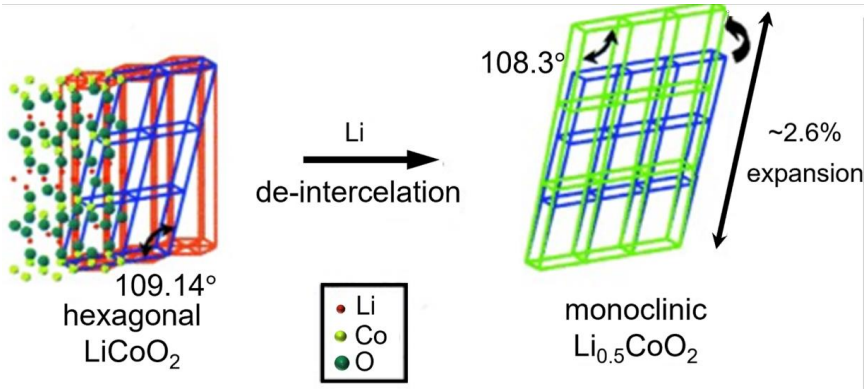

Figure 6. Structural variation of LCO from hexagonal to monoclinic with anisotropic lattice parameters variation after delithiation. Adapted from ref [84].

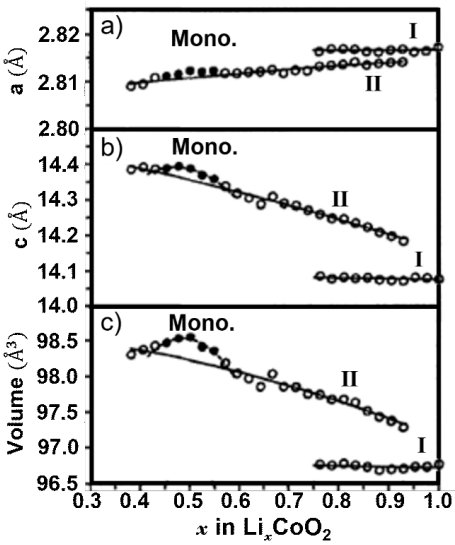

Figure 7. Lattice parameters variation of LCO a) *a*-axis, b) *c*-axis c) volume of the unit cell of LCO as a function of lithium concentration. Adapted from ref [80].

This structural evolution is largely reversible, contributing to its exceptional cycling stability helps preserve particle integrity and minimize mechanical degradation [85]. However, further delithiation causes structural contraction and oxygen rearrangement. At higher voltages (>4.5 V), LCO may undergo irreversible phase transformations to spinel- or rock-salt-like phases, accompanied by lattice oxygen release and capacity fading [35, 85, 86], which can lead to particle cracking, as observed by HRTEM (Figure 8) [74, 87, 88].

Experimental techniques such as in situ XRD confirm that mechanical degradation from anisotropic lattice strain is a leading cause of capacity fade in LCO-based systems [89-91].

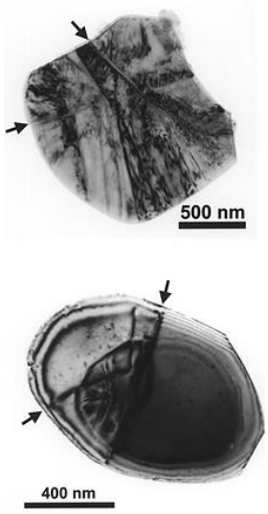

Figure 8. TEM images illustrate cracks within LCO particles obtained from cycled cathode. Adapted from ref [88].

LCO is particularly notable for its thermal and chemical stability in contact with solid electrolytes, especially garnet-type LLZO ($Li_7La_3Zr_2O_{12}$). Studies show that LCO can be co-sintered with LLZO at temperatures above 900-1085 °C with minimal formation of interfacial degradation products [85, 92], with trace formation of $LaCoO_3$ or $LiCoO_2$ secondary phases under extreme conditions [86]. Its thermal expansion coefficient is closely matched with LLZO, further reducing the risk of delamination or interfacial stress during processing or operation [92]. Unlike Mn- or Ni-rich systems, cobalt-based interfaces generate less oxygen activity and minimal Li transfer, maintaining high ionic conductivity at the interface. This stability renders

LCO one of the most favorable cathode candidates for all-solid-state battery configurations, despite cobalt's high cost and toxicity.

- **Nickel Manganese Cobalt Oxides (NCM)**

NCM cathodes, have the general formula of $Li[Ni_xCo_yMn_z]O_2$ (x + y + z = 1), these materials were first reported in 2001 as a Co-reduced alternative to LCO [93]. They crystallize in the same $R\bar{3}m$ α-$NaFeO_2$-type layered structure as $LiCoO_2$, but with transition metal (TM) ions Ni, Co, and Mn which are combined randomly in varying ratios occupying the TM layers [94] and lithium positioned in octahedral sites between the layers (Figure 9).

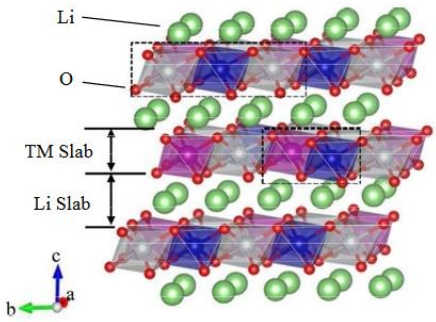

Figure 9. Crystal structure of NCM. Where, the transition metal layer consists of Ni and Co (gray and blue respectively), while O and Mn are in red and purple respectively. Adapted from ref [95].

Different derivatives of NCM can be achieved by varying the ratios (x, y, and z), such as NCM111, NCM811 (8:1:1), and NCM955 (0.9:0.05:0.05). They are considered the most commercially relevant layered oxide materials due to their tunable energy density, structural stability and reduced reliance on cobalt [93].

NCM111 was introduced to reduce cobalt content and improve thermal safety [96]. Its structure remains layered ($R\bar{3}m$), but the presence of Mn^{4+} improves lattice stability, while Co^{3+} enhances electronic conductivity and Ni^{2+} participates in redox reactions [97, 98]. NCM111 offers practical capacities of 150–165 mAh g^{-1} at 3.75 V with improved cost-effectiveness. However, Ni^{2+}/Li^{+} disorder and surface reconstruction limit long-term cycling [99, 100]. NCM111 exhibits a moderate volume contraction (~2%) during cycling (Figure 10c).

During delithiation, the *a*-axis contracts uniformly (Figure 10a), whereas the *c*-axis expands until roughly half delithiation and subsequently contracts with further lithium removal (Figure 10b) [101, 102].

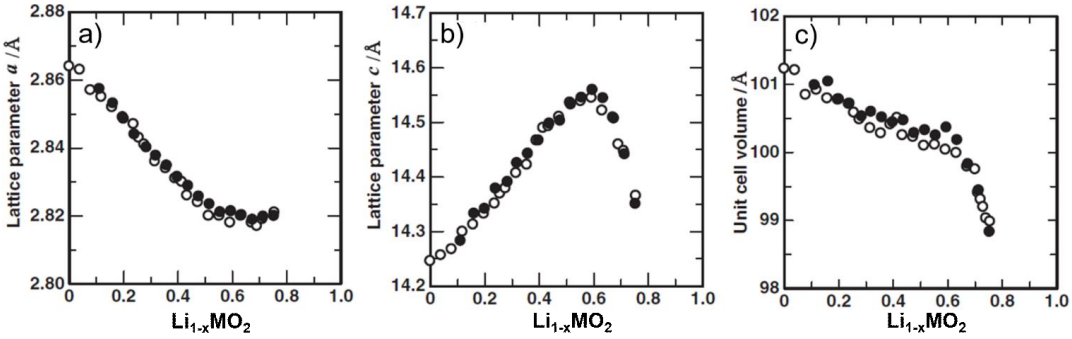

Figure 10. Lattice parameter variation of NCM111 due to delithiation (white circles) and lithiation (black circles) processes a) *a*-axis, b) *c*-axis. c) the net unit cell volume change. Adapted from ref [101].

On other hand, NCM111 exhibits moderate electronic conductivity typically around 10^{-6} to 10^{-5} S cm^{-1}, which improves significantly with Ni content (up to ~10^{-4} to 10^{-3} S cm^{-1}), while the ionic conductivity remains similar to LCO in the range of 10^{-10} to 10^{-12} S cm^{-1} [78, 103].

However, NMC111 shows limited stability with LLZO when sintered at high temperatures (>700 °C), often forming La-based mixed oxides or resistive interphases such as $LaNiO_3$ or $LaMnO_3$ [104]. Nevertheless, researches showed a reduction of interface reactions when applying Li_3PO_4 as surface coatings [105-108].

NCM811, a high-Ni layered oxide, offers capacities exceeding 200 mAh g^{-1} due to the higher proportion of electrochemically active Ni^{2+} [77, 109-111]. It is widely studied for EV applications due to its high energy density [112]. The increased Ni content improves specific capacity and electronic conductivity (~10^{-2} S cm^{-1}), but also renders the structure prone to severe cation mixing and phase transitions [113, 114].

NCM811 exhibits anisotropic volume change this can reach up to ~5.1%, particularly along the *c*-axis, where contraction exceeds 3% during deep delithiation, while the *a*-axis contracts more steadily (Figure 11) [74, 115-117]. Such strain induces internal cracking (Figure 12), which in turn degrades electrical connectivity and reduces cycle life [118].

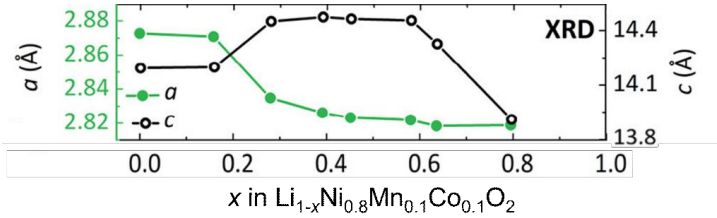

Figure 11. Variation of lattice parameters of NCM811 as a function of cell voltage during a single charge–discharge cycle. Adapted from ref [119].

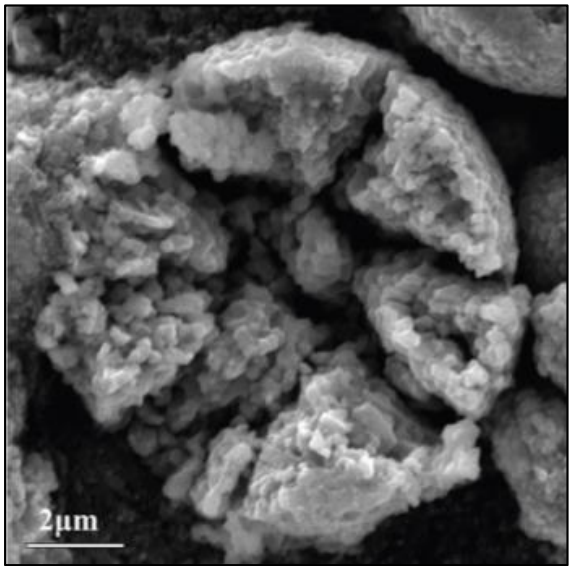

Figure 12. SEM image with high-magnification illustrating the impact of cycling (500 cycles) on NCM811. Adapted from ref [118].

NMC955 is an extremely Ni-rich composition (~95% Ni) designed to minimize cobalt use while pushing the theoretical capacity limits above 220 mAh g^{-1} [120]. However, the high Ni content introduces pronounced structural and electrochemical instability, where cation mixing becomes severe, which in turn leads to a significant impairing Li-ion mobility [121]. The material undergoes a considerable anisotropic lattice strain, with expansion of the *c*-axis in early stages followed by contraction at high delithiation levels (Figure 13b), while *a*-axis undergoes to a continuous contraction (Figure 13a) which hence leads to total volume changes of about 15% [122].

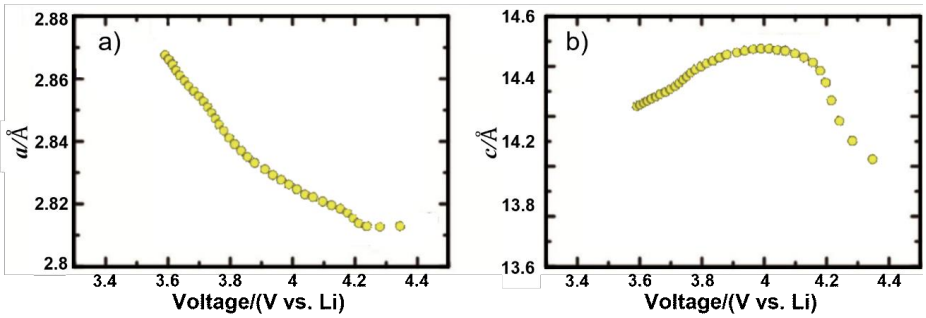

Figure 13. Variation of lattice parameters of NCM955 in a) *a*-axis, and b) in *c*-axis as a function of cell voltage. Adapted from ref [122].

For interfaces between LLZO and Ni-rich NCM (NCM811 and NCM955), studies reveal intense interfacial reactions leading to decomposition of LLZO, forming phases like $La_2Zr_2O_7$, NiO, and Li_2CO_3 or another carbonate. This, in turn, increases impedance and, hence, reduces the performance of the cell [123-125].

- **Spinel Oxide Cathodes**

Spinel oxide cathodes are a class of CAMs which characterized by a cubic close-packed oxygen framework with a three-dimensional lithium diffusion network. They crystallize in the spinel structure (space group $Fd\bar{3}m$), where lithium ions occupy tetrahedral sites while the transition metal cations reside in octahedral positions. This structural arrangement enables fast lithium-ion transport, contributing to excellent rate capability and thermal stability [126]. Lithium manganese oxide ($LiMn_2O_4$ – LMO) is considered as a famous member of this family (Figure 14). It was proposed by Thackeray in 1983 [127] and gained traction due to its low-cost, cobalt-free cathode material [127-129]. It operates at an average voltage of 3.0–4.2 V, delivering a practical capacity of 100–120 mAh g^{-1}.

LMO exhibits isotropic lattice behavior during cycling (Figure 15), with moderate volume change (~6–7%) that helps maintain mechanical stability over moderate cycling regimes [130].

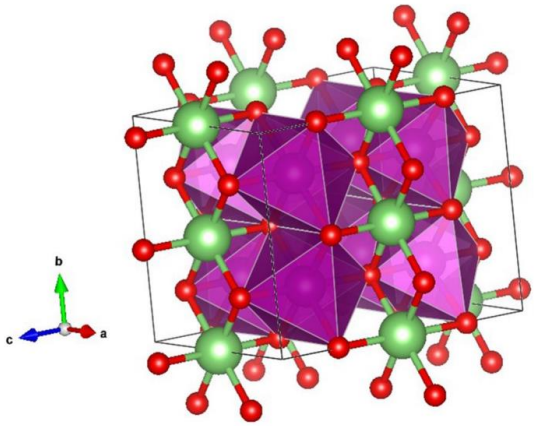

Figure 14. Crystal structure of LMO, where the Li and O are in green and red respectively, while Mn positions are enclosed by the polyhedral. Adapted from ref [131].

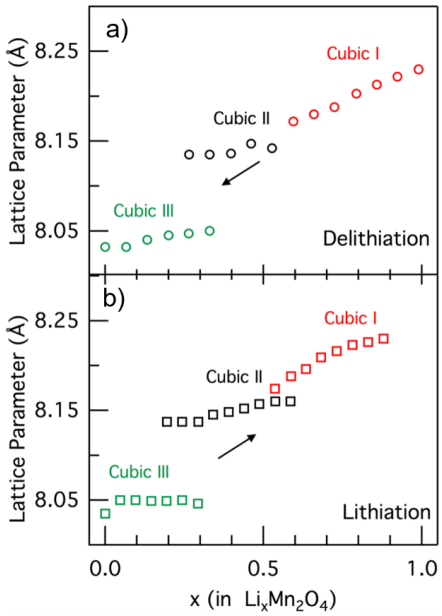

Figure 15. Lattice variation in LMO as a function of Li concentration during a) delithiation and b) lithiation process. Adapted from ref [130].

On other hand, LMO is featured with a relatively low electronic conductivity (~10^{-6} to 10^{-5} S cm^{-1}). However, this limitation can be improved through doping (e.g., with Ni, Cr, or Fe) and the use of conductive coatings [132, 133], which in turn increases the cost of this material.

LMO is considered moderately stable regarding chemical compatibility with LLZO [134]. High-temperature processing above ~900°C leads to partial interdiffusion, which further leads to form a secondary phase such as $LaMnO_3$ or Mn_3O_4 at the interface, especially if no buffer layer is applied. These interphases are resistive and impede charge transfer [134, 135]. Nonetheless, LMO is generally considered more LLZO-compatible than Ni-rich layered oxides, especially when sintered below the solid-state reaction threshold or combined with interlayers like Li_3PO_4 or Al_2O_3 to suppress side reactions in order to maintain interfacial stability [136].

A major challenge for LMO is its tendency to experience **Jahn-Teller distortion** associated with Mn^{3+} ions, particularly during cycling below 3 V. This distortion results in elongation of Mn–O bonds and hence, a reduction in symmetry of the lattice, triggering micro strain, lattice collapse, and capacity fading. Combined with disproportionation of Mn^{3+} ($2Mn^{3+} \rightarrow Mn^{2+} + Mn^{3+}$), which yields dissolution of Mn^{2+} in the electrolyte, subsequently limiting the cycle life [137-139].

2.3. Solid Electrolyte

Solid electrolytes are critical components in all-solid-state lithium-ion batteries (ASSBs), offering a safer and more stable alternative to flammable liquid electrolytes [58]. These materials facilitate lithium-ion (Li^+) transport between electrodes while maintaining high ionic conductivity (>10^{-4} S cm^{-1} at room temperature), negligible electronic conductivity, and wide electrochemical stability windows to support high-voltage cathodes and low-potential anodes [140, 141]. By eliminating risks like dendrite formation and leakage, solid electrolytes enable higher energy densities and improved thermal stability [58].

2.3.1. Garnet-Type

Garnet-type solid electrolytes play a crucial role in the development of all-solid-state lithium-ion batteries (ASSBs), offering a compelling combination of high ionic conductivity, wide electrochemical stability windows, and compatibility with lithium metal anodes—addressing the intrinsic safety limitations of conventional liquid electrolytes [3]. Among these, Lithium lanthanum zirconium oxide ($Li_7La_3Zr_2O_{12}$, LLZO), first reported in 2007, has emerged as one of the most promising candidates due to its superior properties including high room-temperature ionic conductivity, wide electrochemical stability window, low electronic conductivity, and excellent chemical stability against lithium metal [141, 142].

The performance of LLZO is deeply dominated by its crystal structure, which exists in two polymorphic forms: tetragonal ($I4_1/acd$) and cubic (Ia-3d) [141, 143]. The tetragonal phase is characterized by ordered lithium-ion occupancy at the 8a, 16f, and 32g sites, which restricts lithium mobility [141] (Figure 16b). In contrast, the cubic phase exhibits disordered lithium distribution across the 24d and 96h sites—with an occupancy of approximately 60%—enabling significantly higher ionic conductivity [141, 143] (Figure 16a). The structural transition from the tetragonal to cubic phase occurs around 645 °C, driven by lithium sublattice disorder, with a thermal hysteresis observed near 625 °C [143]. The cubic phase offers 120 possible sites of which 56 are typically occupied, which provide a greater number of diffusion vacancies that enhance lithium-ion transport [141, 144]. Furthermore, the structure comprises interconnected ZrO_6 octahedra and LaO_8 dodecahedra, which in turn, leads to formation of a robust three-dimensional conduction network [141] (Figure 17).

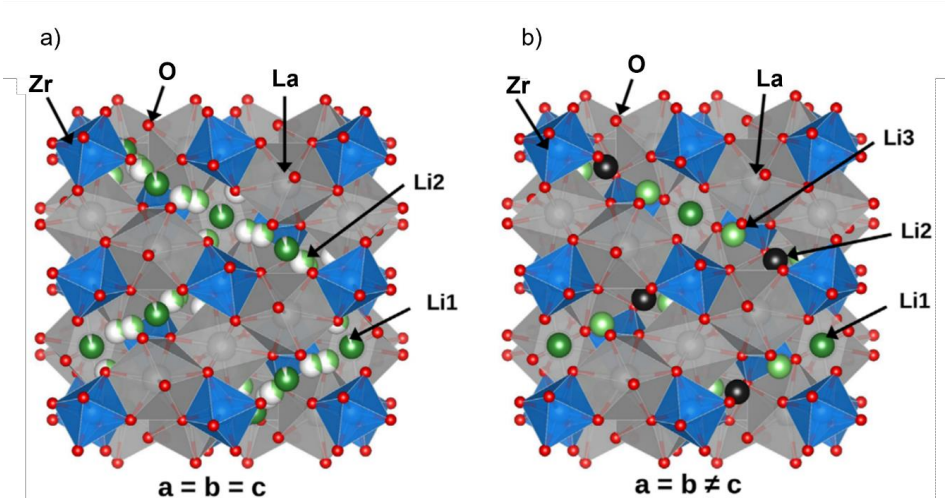

Figure 16. Crystal structure of LLZO in its two phases: a) cubic phase and b) tetragonal phase. Adapted from ref [145].

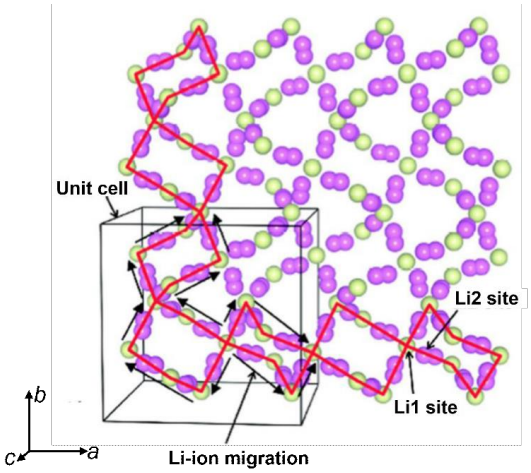

Figure 17. Conduction channel pathway of Li-ion in LLZO. Adapted from ref [146].

Computational studies estimate the cubic lattice constant to be approximately 12.97 Å, which reduces both structural tetragonality and migration energy barriers by widening Li-ion transport channels [147].

The ionic conductivity of LLZO is highly phase-dependent, with the cubic form being essential for practical applications in ASSBs. At room temperature, cubic LLZO can achieve ionic conductivities up to 3×10^{-4} S cm^{-1}, which is 100 times higher than the value of the tetragonal

phase under similar conditions (~10^{-6} S cm^{-1}) [142]. Enhancements through Al doping and the addition of Al_2O_3 have led to dense LLZO ceramics reaching 4×10^{-4} S cm^{-1}, attributed to improved grain connectivity [148]. Studies showed that with optimized doping strategies, conductivities up to 10^{-3} S cm^{-1} are possible—rivaling those of liquid electrolytes [2]. For example, Ga-doped variants such as $Li_{6.25+x}Ga_{0.25}La_{3-x}Sr_xZr_2O_{12}$ have achieved conductivities as high as 1.62×10^{-3} S cm^{-1} [141]. Substitution at Zr sites with Nb or Ta for example $Li_{6.4}La_3Zr_{1.4}Ta_{0.6}O_{12}$, yields promising conductivity (6.04×10^{-4} S cm^{-1}) [141]. Density functional theory (DFT) simulations have guided dopant site selection, suggesting that Al substitution at Li sites and Ta at Zr sites most effectively reduce defect formation energies [149]. Multi-doping approaches involving elements such as Y, Sc, and Sb have achieved conductivity levels around 7.7×10^{-4} S cm^{-1} [141]. It is worth to mention that the importance of the dopant strategy relies not only on their enhancement of the ionic conduction but also on their suppression of electronic conductivity, which is vital for preventing short circuits [150, 151]. On other hand, excessive or incompatible doping may lead to secondary phase formation (e.g., $La_2Zr_2O_7$), which, in turn, negatively impacts on the overall performance [143, 150].

Despite its promising attributes, LLZO faces several significant challenges. Exposure to ambient moisture and CO_2 causes lithium loss and the formation of $Li_{7-x}H_xLa_3Zr_2O_{12}$ and Li_2CO_3 on the surface, which consequently results in severely diminished conductivity [58, 143]. Moreover, high interfacial resistance, particularly with cathodes, remains a bottleneck for power performance, which requires additional coating strategies [152, 153]. Mechanically, LLZO is characterized with a high Young's modulus (~150 GPa) which provides resistance to lithium dendrite penetration [154, 155].

2.3.2. Sulfide type

Sulfide-type solid electrolytes are pivotal to the advancement of all-solid-state batteries (ASSBs), attributed to their exceptional lithium-ion conductivity, mechanical flexibility, and compatibility with lithium metal [156]. Representative materials such as Li_2S–P_2S_5 glass-ceramics, $Li_{10}GeP_2S_{12}$ (LGPS), and argyrodite-type compounds like Li_6PS_5X (X = Cl, Br, I) exhibit conductivities comparable to those of liquid electrolytes, making them prime candidates for high-energy-density battery systems [157].

The structural diversity of sulfide electrolytes—ranging from amorphous to crystalline phases—(Figure18), enables tunable properties which directly impact ion transport behavior [156].

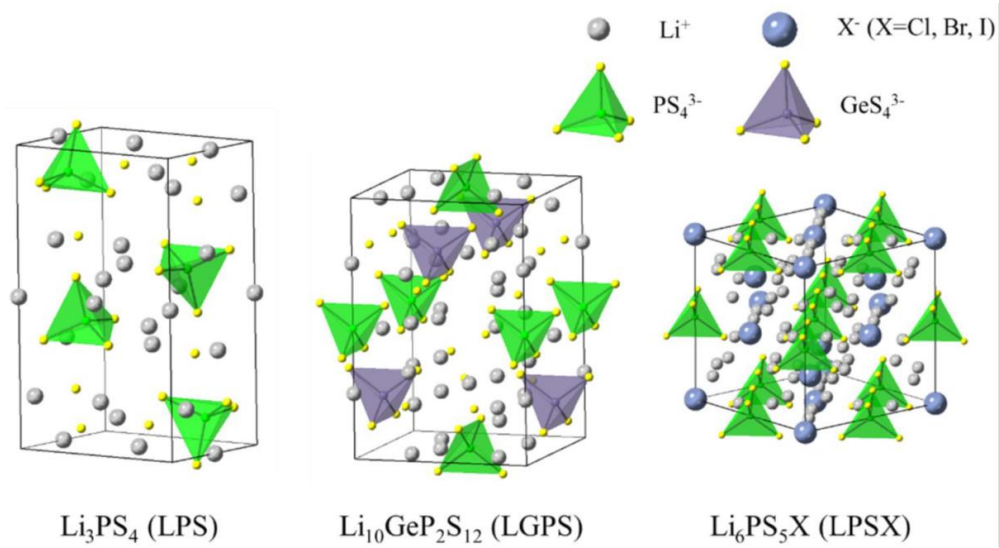

Figure 18. Crystal structures of LPS, LGPS, and LPSX. Adapted from ref [55].

In terms of ionic transport, sulfide electrolytes are among the best-performing solid-state conductors, often achieving room-temperature conductivities more than 10^{-3} S cm^{-1} [156]. LGPS, for example, exhibits a remarkable conductivity of 12 mS cm^{-1} and a low activation energy of approximately 0.25 eV, attributed to its one-dimensional lithium pathways [156]. On the other hand, argyrodite-type Li_6PS_5Br exhibits conductivities up to ~7 mS cm^{-1}, enhanced by halide-induced structural disorder [158]. $Li_7P_3S_{11}$ pushes the limits even further, achieving ~17 mS cm^{-1} through rapid lithium diffusion within its P_2S_7 framework [159]. The conductivity is governed by the lithium concentration by the following equation

$$\sigma = nq\mu \quad (9)$$

where σ is the conductivity, n is carrier concentration, q is the charge of the migrating ion and μ is ionic mobility. In case of sulfides, the high concentration of mobile lithium and their accessible diffusion pathways significantly boost the performance [156].

The practical advantages of sulfide electrolytes have been demonstrated across a variety of applications, particularly in high-performance ASSBs. LGPS-based batteries paired with $LiCoO_2$ cathodes have achieved capacities of approximately 120 mAh g^{-1} at 0.1C, delivering stable long-term cycling [156]. Argyrodite-type Li_6PS_5Cl cells retain more than 80% of their initial capacity after 100 cycles, attributed to their low interfacial resistance and good compatibility with electrode materials [158].

Despite these promising characteristics, sulfide electrolytes face significant barriers to commercialization. Their high reactivity with moisture results in the release of toxic hydrogen sulfide (H_2S) gas [156, 158]. Argyrodite-type materials are particularly vulnerable, exhibiting rapid conductivity loss upon air exposure, for instance, the ionic conductivity of Li_6PS_5Cl degrades from 1.8×10^{-3} to 8.7×10^{-4} S cm^{-1} after just 24 hours in humid conditions [158]. Electrochemical instability at the lithium metal interface also poses a major challenge, with the formation of resistive Li_2S-rich interphases which hinder ion transport [157]. Furthermore, LGPS is further limited by a narrow electrochemical window (~1.7–2.5 V), which restricts its compatibility with many cathode materials [156].

2.3.3. Lithium Phosphorus Oxynitride

Lithium Phosphorus Oxynitride (LiPON) is considered as an essential solid electrolyte for all-solid-state batteries (ASSBs), particularly in thin-film configurations, due to its remarkable interfacial stability with lithium metal, wide electrochemical window, and strong compatibility with microbattery architectures [160]. LiPON has an amorphous structure composed of a disordered network of PO_4 tetrahedra (Figure 19). Thanks to the incorporation of nitrogen, P–N and P=N bonds form, which partially replace oxygen and create cross-linked phosphate chains [160].

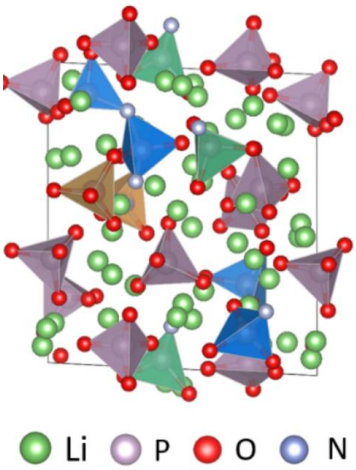

Figure 19. Crystal structure of LiPON generated by AIMD. Adapted from ref [161].

The amorphous nature of LiPON eliminates grain boundaries, which are the primary source of interfacial resistance in crystalline materials and inherently limit long-range ionic conductivity [160].

LiPON's ionic conductivity is relatively modest, typically ranging from 10^{-6} to 3×10^{-6} S cm^{-1} at room temperature, with an activation energy around 0.55 eV [160]. This conductivity is governed by equation (9). In this case, nitrogen incorporation enhances conductivity by stabilizing lithium-coordinating oxygen sites, thereby increasing n, and by opening the glass network, which improves μ [162]. Further improvement has been demonstrated in LiSiPON films, where ionic conductivity can approach ~4.8×10^{-6} S cm^{-1} through optimized silicon and nitrogen content [163]. Ultra-thin LiPON layers, such as 12 nm films, maintain conductivities around 2×10^{-7} S cm^{-1}, which render them suitable for high-conductance microbattery architectures [164]. Despite its lower ionic conductivity compared to other solid electrolytes, LiPON exhibits superior interfacial stability and its compatibility with thin-film geometries make it uniquely suited for micro-scale energy storage applications [160].

LiPON's outstanding electrochemical stability has made it a cornerstone material for powering microdevices such as medical implants and sensors [160]. Thin-film batteries employing LiPON as the electrolyte, together with $LiCoO_2$ cathodes and lithium metal anodes, can deliver areal capacities of approximately 100 μAh cm^{-2} while retaining over 90% of their initial capacity even after 1000 cycles [162]. Its wide electrochemical window (~0–5.5 V) supports the use of high-voltage cathodes, while its extremely low electronic conductivity minimizes self-discharge, which is a critical requirement for long-lifespan devices [160].

Multi-doping approaches that combine silicon and boron are being explored to simultaneously enhance conductivity and maintain electrochemical stability [162, 163, 165]. However, excessive dopant incorporation can lead to the formation of electrically insulating phases. The successful implementation of such doping strategies is essential for unlocking LiPON's full potential in microbattery systems [163, 164].

In addition to its low ionic conductivity which is considered as a major bottleneck, restricting its use to thin-film formats, the synthesis of LiPON is technically demanding and expensive, limiting scalability for broader applications [162]. During the fabrication of LiSiPON, lithium migration can degrade the film quality. Hence, advanced deposition techniques is required to

ensure uniformity and performance [163]. Furthermore, LiPON is also sensitive to ambient exposure; air contact can lead to the formation of surface Li_2CO_3 layers, which impedes conductivity and degrade interface quality [160].

2.4. Mechanical Stress in Solids

2.4.1. Definition of Mechanical Stress

In the field of continuum mechanics, stress is defined as the internal force transmitted per unit area within a material, arising in response to externally applied loads that tend to deform the material [166, 167]. It provides a measure of how internal forces are distributed across imaginary surfaces within the material. For simple uniaxial loading, normal stress is calculated as:

$$\sigma = F/A \tag{10}$$

where σ is the normal stress, F is the force applied perpendicular to a cross-sectional area A. To generalize this definition for three-dimensional solids, the internal force transmitted across an infinitesimal surface element within a continuous medium must be described [166-168]. This internal force per unit area is represented by the traction vector $\boldsymbol{t_i}$, which physically denotes the magnitude and direction of the stress acting on a specific plane within the material, linking the macroscopic loading conditions to the local stress state. While, the orientation of the surface is given by its unit normal $\boldsymbol{n_j}$. According to Cauchy's stress principle, the traction vector on an arbitrarily oriented surface passing through a point is determined entirely by the state of stress at that point, regardless of how the internal surface is oriented. This principle asserts that the traction vector is a linear function of the surface normal and is expressed using the Cauchy stress tensor $\boldsymbol{\sigma_{ij}}$ [166-168]:

$$\boldsymbol{t_i = \sigma_{ij} * n_j} \tag{11}$$

where σ_{ij} is a second-order tensor containing both **normal stresses** (diagonal terms, such as σ_{11}, σ_{22}, σ_{33},) and **shear stresses** (off-diagonal terms, σ_{ij} where $i \neq j$) [167, 169].

2.4.2. Definition of Strain

Strain is a measure of deformation representing the displacement between particles in the material body relative to a reference length [166, 168]. It describes the level of stretches, compresses, or distorts for a material under influenced applied forces. Strain captures the geometric change those forces produce. It can be caused by mechanical loading, thermal expansion, or phase transformations [168]. Normal strain measures the relative elongation or contraction of a material element under axial loading. In one-dimensional loading under the small displacement hypothesis, it is represented as:

$$\epsilon = {\Delta L}/{L_0} \tag{12}$$

where ΔL is the change in length and L_0 is the original length. This scalar measure reflects how much a material stretches or shortens in response to a mechanical load. However, in three-dimensional solids, normal strain generalizes to the diagonal terms of the strain tensor ϵ_{ij}, namely ϵ_{11}, ϵ_{22}, and ϵ_{33}, representing strain along the x, y, and z directions, respectively. These components are critical in evaluating dimensional changes and volumetric deformation under multi-axial loading [167, 168].

In the linear elasticity regime, small deformation refers to the condition where displacements and rotations are sufficiently small such that geometric nonlinearities can be neglected. Under this assumption, strain is small and reversible, and its characterization is essential for predicting structural response and failure [167]. The internal stress distribution within a solid lead to deformation, described by the concept of strain. For small, reversible (elastic) deformations, strain is quantified by the infinitesimal strain tensor [168] which can represented as:

$$\epsilon_{ij} = 0.5 \left[\frac{\partial u_i}{\partial x_i} + \frac{\partial u_j}{\partial x_j}\right] \quad (13)$$

where u_i is the component of the displacement vector field and *x* represents the spatial position vector. The strain tensor captures both normal and shear deformations and is symmetric for small deformations, where :

$\epsilon_{ij} = \epsilon_{ji}$,

implying that the strain tensor has only six independent components: three normal strains and three shear strains. The symmetry arises because rigid-body rotations are excluded in the derivation of the infinitesimal strain and because the relative displacement between adjacent points must be consistent regardless of the path taken between them. The symmetry simplifies both theoretical derivations and numerical implementations (for example, in finite element simulations) and ensures compatibility with the symmetric stiffness tensor of linear elasticity [167, 168].

2.4.3. Hooke's Law

- **One-Dimensional Elasticity**

In the linear elastic regime, Hooke's law characterizes the constitutive behavior of materials through a linear proportionality between uniaxial stress and strain [168]. This fundamental relationship is graphically represented in the stress–strain diagram, where the slope of the initial linear segment defines the material's Young's modulus (*E*), given by:

$$\sigma = E\epsilon \quad (14)$$

Young's modulus is considered as a material constant representing the stiffness or resistance to deformation. This relation remains for small, reversible deformations up to the material's proportional limit. As the applied stress increases beyond this proportional limit, the material enters the plastic deformation region, which is characterized by permanent, irreversible strain accumulation. In this region, Hooke's law no longer holds, and the material follows a nonlinear stress-strain path.

- **Three-Dimensional Isotropic Elasticity**

For isotropic materials, Hooke's law extends to three dimensions through a tensor formulation that relates stress and strain via the Lamé parameters. These constants, λ and μ characterize volumetric and shear deformation, respectively. The generalized form is expressed as:

$$\sigma_{ij} = \lambda\delta_{ij}\epsilon_{kk} + 2\mu\epsilon_{ij} \quad (15)$$

where δ_{ij} is the Kronecker delta and ϵ_{kk} is the trace of the strain tensor representing volumetric strain. This formula is valid for materials whose mechanical properties are direction-independent (isotropic)—an assumption that holds for many metals, polymers, and polycrystalline ceramics [167]. While, λ and μ can be derived by (16) and (17), respectively.

$$\lambda = \frac{E\nu}{(1+\nu)(1-2\nu)} \quad (16)$$

$$\mu = \frac{E}{2(1+\nu)} \quad (17)$$

where ν is the Poisson's ratio.

In matrix notation, the stress-strain relationship is written as:

$$\begin{bmatrix}\sigma_{11}\\ \sigma_{22}\\ \sigma_{33}\\ \sigma_{23}\\ \sigma_{13}\\ \sigma_{12}\end{bmatrix} = \begin{bmatrix}\lambda\,(\epsilon_{11}+\epsilon_{22}+\epsilon_{33}) + 2\mu\epsilon_{11}\\ \lambda\,(\epsilon_{11}+\epsilon_{22}+\epsilon_{33}) + 2\mu\epsilon_{22}\\ \lambda\,(\epsilon_{11}+\epsilon_{22}+\epsilon_{33}) + 2\mu\epsilon_{33}\\ 2\mu\epsilon_{23}\\ 2\mu\epsilon_{13}\\ 2\mu\epsilon_{12}\end{bmatrix} \quad (18)$$

This compact form, grounded in the assumptions of linear elasticity and isotropy, is widely used in analytical modeling and finite element analysis [170].

- **Anisotropic Elasticity**

In contrast to isotropic materials, **anisotropic materials** such as crystals and composites exhibit direction-dependent mechanical behavior. Hooke's law for anisotropic elasticity is expressed

using the fourth-order **stiffness tensor** $\boldsymbol{C_{ijkl}}$, which represents how stress responds to strain in each direction [171]:

$$\boldsymbol{\sigma_{ij}} = \boldsymbol{C_{ijkl}\epsilon_{kl}} \tag{19}$$

where *i, j, k, l* = 1, 2, 3.

Due to symmetry conditions, the 81 theoretical components of the tensor reduce to 21 independent terms for the most general anisotropic material. In computational mechanics, this tensor is expressed more conveniently using Voigt notation as a 6×6 matrix [171, 172]:

$$\begin{bmatrix}\sigma_{11}\\ \sigma_{22}\\ \sigma_{33}\\ \sigma_{23}\\ \sigma_{13}\\ \sigma_{12}\end{bmatrix} = \begin{bmatrix}C_{11} & C_{12} & C_{13} & C_{14} & C_{15} & C_{16}\\ C_{12} & C_{22} & C_{23} & C_{24} & C_{25} & C_{26}\\ C_{13} & C_{23} & C_{33} & C_{34} & C_{35} & C_{36}\\ C_{14} & C_{24} & C_{34} & C_{44} & C_{45} & C_{46}\\ C_{15} & C_{25} & C_{35} & C_{45} & C_{55} & C_{56}\\ C_{16} & C_{26} & C_{36} & C_{46} & C_{56} & C_{66}\end{bmatrix}\begin{bmatrix}\epsilon_{11}\\ \epsilon_{22}\\ \epsilon_{33}\\ 2\epsilon_{23}\\ 2\epsilon_{13}\\ 2\epsilon_{12}\end{bmatrix} \tag{20}$$

2.4.4. Principal Stresses

In the context of solid mechanics, principal stresses refer to the three normal stress components—maximum, intermediate, and minimum—at a given material point. These stresses are obtained by rotating the coordinate system to a unique orientation in which all shear stress components vanish, leaving only the purely normal stresses acting along the principal directions. Determining principal stresses involves solving:

$$\det\left(\sigma_{ij} - \lambda\delta_{ij}\right) = 0 \tag{21}$$

resulting in three eigenvalues $\sigma_1, \sigma_2, \sigma_3$, where $\sigma_1 \geq \sigma_2 \geq \sigma_3$. Corresponding eigenvectors define principal directions. Rotating axes to principal directions diagonalizes the stress tensor, removing shear stresses [172].

Principal stresses provide clear insights into the maximum tensile and compressive loads, forming the basis for applying common failure criteria like Tresca and von Mises. Evaluating principal stresses is essential for assessing structural safety, maintaining reliability, and optimizing material usage. In engineering practice, von Mises stress is typically used as the failure criterion for ductile materials such as metals, whereas principal stress evaluation is more appropriate for brittle materials such as ceramics, where failure is governed by the maximum normal stress [172].

2.4.5. Tensile and Compressive Stress

Tensile stress (positive) elongates materials by exerting axial forces that pull particles apart, promoting extension along the direction of loading. **Compressive stress** (negative) acts to

shorten materials by driving internal particles closer together. These two forms of normal stress originate from specific mechanical scenarios.

Both types of stress influence structural deformation, failure modes, and overall performance under load. The distinction between these stress types is essential, as each affects material behavior in fundamentally different ways [173]. For brittle materials such as ceramics, tensile stress elongates the material, stretching atomic bonds, increasing internal strain, and opening pre-existing microcracks and surface flaws, which precipitates premature catastrophic failure and significantly reduces fracture strength. In contrast, compressive stress compacts the material, closing flaws, retarding crack growth, and enabling a much higher fracture strength [173, 174].

2.5. Representative Volume Element

2.5.1. Definition of the Representative Volume Element

The Representative Volume Element (RVE) is a foundational concept in multiscale modeling and homogenization of heterogeneous materials [175]. It refers to the smallest volume over which a material property can be averaged to yield an effective value representative of the entire material.

The idea of the RVE is rooted in the physical necessity of simplifying the mathematical treatment of heterogeneous materials while preserving accuracy at the macroscale by replacing the complex details of the microstructure with an averaged response. This can be achieved by formulating the effective continuum models that represent the material's response under different conditions. The RVE must be large enough to incorporate a sufficient variety of microstructural features such as grains, pores, fibers, or inclusions. However, it must also remain small enough to qualify as a material point from the macroscopic perspective [176-178]. This balance defines its role in the hierarchy of multiscale modeling.

RVEs have become essential in multiscale modeling across a broad range of materials, including composites, polycrystals, porous media, biomaterials, and architected metamaterials. In composites, RVEs enable accurate prediction of the effective stiffness, stress distribution, and fracture behavior by accounting for the size, shape, distribution, and volume fraction of composite components [179, 180].

RVE modeling provides a powerful computational framework for virtual testing, optimization, and prediction of effective material behavior across length scales. It enables robust material design, reliability assessment, and performance-driven engineering by embedding microstructural realism into macroscopic simulations [180-182].

2.5.2. Conditions for Representativeness

To be considered representative, RVE must satisfy two fundamental criteria that reflect the statistical nature of the microstructure and its mechanical behavior under applied loads. These are:

1. Statistical Representativeness

A statistically representative RVE must capture the essential morphological features of the microstructure. These include volume fractions of different phases, grain or inclusion sizes and shapes, orientation distributions, and spatial correlations. The statistical descriptors used to

define these features should converge to those of the bulk material as the RVE size increases. This ensures that localized anomalies do not bias the overall effective response and that the RVE reflects the full variability of the microstructure [183, 184].

For complex microstructures with high heterogeneity—such as those involving multiple inclusions, irregular pores, or variant morphologies, significantly larger RVE domains are required in order to achieve the statistical convergence [178, 185] to ensure that the RVE represents both the average structure and its inherent variability [184, 186].

2. Mechanical Representativeness

Mechanical representativeness is evaluated by verifying that the RVE obeys the Hill–Mandel condition. This condition states that the volume-averaged microscopic mechanical power is equal to the mechanical power computed from the averaged stress and strain tensors. This requirement guarantees that the mechanical work done on the RVE is consistent with that experienced by the corresponding macroscopic material element [178, 183]. The condition is expressed mathematically as:

$$\langle \sigma : \epsilon \rangle = \langle \sigma \rangle : \langle \epsilon \rangle \qquad (22)$$

where σ is the microscopic stress tensor, and ϵ is the microscopic strain tensor within the RVE. The colon operator (:) denotes the scalar product between these second-order tensors, while, the angle brackets $\langle \quad \rangle$ indicate a volume average over the RVE domain. This formulation ensures energetic consistency between the micro and macroscopic scales by equating their virtual mechanical work.

2.5.3. Boundary Conditions and Homogenization

Boundary conditions are mathematical and physical constraints applied at the boundaries of the representative volume element.

Their role in RVE analysis is pivotal, where they dictate how it interacts with its surrounding material environment. They are essential in homogenization problems as they influence the computed response of the RVE under mechanical, thermal, or conductive loading [182, 187, 188]. These conditions specify the displacements, tractions, or continuity that must be satisfied on the RVE boundaries and are selected based on the symmetry, loading scenario, and morphology of the microstructure.

To satisfy the Hill–Mandel condition in numerical simulations, boundary conditions must be

carefully chosen. Among the most widely boundary conditions used are **Periodic Boundary Conditions (PBCs)** (Figure 20 a), which are preferred when feasible, especially for media that are approximately periodic or ergodic. **PBCs** ensure compatibility and equilibrium across opposite RVE faces, allowing more accurate and faster convergence of the effective material response [182, 187, 189]. In finite element (FE) modeling, periodicity in both geometry and mesh is required to apply **PBCs** correctly. Tools such as Gen_PRVE now automate the creation of periodic RVEs suitable for FE homogenization [190].

Another class of boundary conditions is **Symmetric Boundary Conditions (SBCs)** (Figure 20 b), which are particularly useful when the microstructure or loading exhibits mirror symmetry. **SBCs** constrain displacements normal to the symmetry plane while allowing tangential components, reducing the computational domain by half or more without significant loss of accuracy. Though **SBCs** do not enforce full periodicity, they are effective in many linear elasticity problems and are frequently used to exploit geometric or loading symmetry [182, 188].

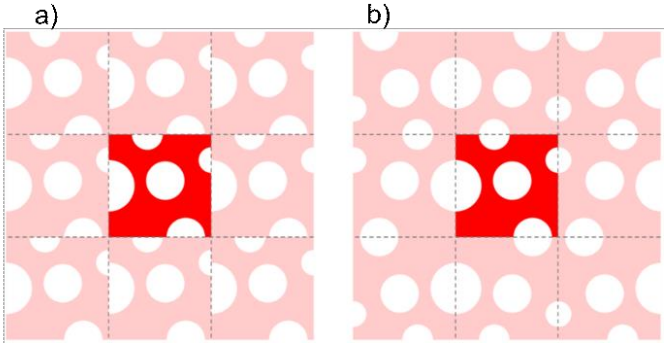

Figure 20. Illustration of boundary conditions: a) periodic and b) symmetric. Adapted from ref [191].

2.5.4. Microstructure Generation Techniques

Generating RVEs involves either reconstructing the material's microstructure from experimental data or synthesizing statistically equivalent geometries. Experimental reconstruction uses tools like X-ray computed tomography (XCT) or scanning electron microscopy (SEM) to build 3D voxel-based models. However, geometrical and statistical methods offer higher flexibility and control through theoretical generation. These include Voronoi tessellations, sphere packing algorithms, and field-based random media generators [181, 188].

2.6. Voxel-Based Mechanical Stress Solvers

2.6.1. Definition of Voxel

A voxel is defined as the smallest distinguishable volume in a three-dimensional digital model of a material's microstructure. It corresponds to a small cuboidal region (Figure 21) that carries local physical properties such as stiffness, phase identity, or density. It stands for volumetric pixel [192, 193]. These voxels are commonly extracted from high-resolution imaging techniques such as μCT or FIB-SEM [194-196], making it possible to transform physical microstructures directly into simulation-ready computational domains. In voxel-based FFT solvers, a representative volume element (RVE) is constructed as a periodic 3D array of voxels. This discretized domain serves as the basis for solving mechanical field equations, where each voxel reflects the heterogeneity of the material. The regularity of the voxel grid enables efficient computation and high fidelity in capturing local variations in material behavior [197, 198].

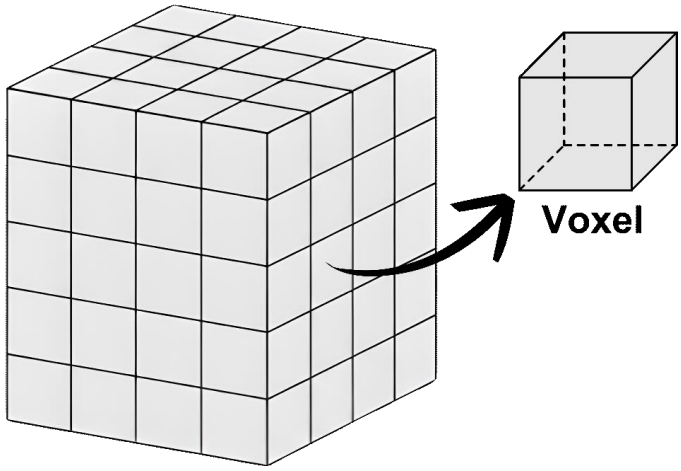

Figure 21. Schematic of voxilized microstructure illustrating the voxel.

GeoDict, developed by Math2Market GmbH, serves as a notable example of software that utilizes a voxel-based approach for both generating RVEs and characterizing mechanical stress. RVEs can be created using GeoDict's microstructure generation modules (e.g., **GrainGeo**), which allow precise control over grain size, shape, orientation, porosity, and component ratio, or derived directly from experimental voxel data [199]. Through its **ElastoDict** module, GeoDict evaluates the mechanical stress response of heterogeneous materials by discretizing the microstructure into a uniform grid of voxels. Each voxel represents a homogeneous region with

assigned constitutive properties, including Young's modulus, Poisson's ratio, and the stiffness tensor. The module computes local stress fields under applied boundary conditions, enabling evaluation of stress distribution and detailed local stress variations [200].

2.6.2. Principles of Image-Based Mechanical Simulation

Voxel-based FFT solvers represent a powerful approach for simulating the mechanical behavior of heterogeneous materials [197, 201]. They operate directly on regular voxel grids derived from 3D imaging data, where each voxel contains specific material properties [194, 195]. This approach bypasses the complex and time-consuming meshing process required in traditional finite element analysis (FEA) making it particularly suited for image-based modeling [194, 202]. By applying the Fast Fourier Transform (FFT), these solvers transform the governing field equations into the spectral domain, significantly accelerating computation and enabling full-field simulations on large microstructures [201, 203]. In contrast, FEA is a well-established method for solving solid mechanics problems by discretizing the simulation domain using structured or unstructured meshes composed of elements like tetrahedra or hexahedra [201, 202]. Each element contains nodes at which field variables such as displacement are computed (Figure 22). The method offers great flexibility for handling complex geometries, material nonlinearity, and boundary conditions. However, FEA often requires labor-intensive mesh generation and incurs high computational costs, especially for large-scale three-dimensional simulations [197, 203].

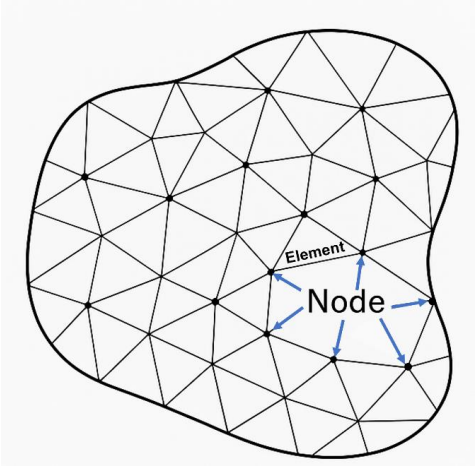

Figure 22. Finite element meshing.

2.6.3. Periodic Boundary Conditions and Fourier-Based Formulation

Voxel-based stress solvers typically assume periodic boundary conditions on the RVE. Physically, this means the microstructure is conceptually tiled to fill all space, so that opposite faces of the RVE have identical displacement and traction fields. Periodicity is a convenient choice because it eliminates boundary discontinuities and allows the use of Fourier series to represent field variables [197, 201]. Under periodic conditions, any field (e.g. stress or strain) can be expanded in a Fourier basis compatible with the unit-cell lattice. The benefit of the Fourier formulation is that the differential operator and the material heterogeneity become a convolution in real space, which is algebraically simpler in Fourier space. In particular, the **Lippmann–Schwinger equation** provides an integral equation reformulation of the elasticity problem [201]:

$$\epsilon(x) + \int_V \Gamma_0(x - x') : [C\ (x') - C_0] : \epsilon(x') dV = E \qquad (23)$$

where C_0 is a homogeneous reference stiffness and Γ_0 is its associated strain Green's function. The uniform applied (average) macroscopic strain is represented by E, while $\epsilon(x)$ is the local strain at the observation point x. The variable x' refers to positions within the integration volume V of RVE.

In practice, the convolution is evaluated efficiently by transforming to Fourier space, since convolution becomes element-wise multiplication in the frequency domain [195, 201].

2.6.4. Limitations

Despite their many strengths, voxel-based FFT solvers exhibit several important limitations that must be considered when applying them to microstructural simulations. One key constraint is the assumption of periodic boundary conditions. While mathematically convenient, this assumption may not align with all physical systems, particularly those with localized or non-repeating features, potentially introducing artificial interactions across the RVE boundaries [194, 201]. Another limitation arises from the voxelized geometry itself. Curved interfaces and fine structural features are approximated as stair-stepped surfaces within the voxel grid, which can lead to discretization artifacts [195]. Although increasing resolution helps mitigate these errors, it also substantially increases computational efforts. Furthermore, FFT solvers may encounter convergence issues in cases of high contrast or nonlinear material behavior. The standard fixed-point iteration scheme can converge slowly or even diverge unless advanced techniques, such as the augmented Lagrangian method or conjugate gradient acceleration, are employed [197, 203]. Finally, many FFT-based implementations are restricted to linear elastic

behavior. While extensions to handle plasticity, viscoelasticity, or damage have been proposed, they add complexity to the numerical framework and demand more computational effort [202].

References

[1] International Energy Agency. (2025). Global EV Outlook 2025. https://www.iea.org/reports/global-ev-outlook-2025.

[2] World Health Organization. (2024, August 29). Ambient (outdoor) air quality and health. https://www.who.int/news-room/fact-sheets/detail/ambient-(outdoor)-air-quality-and-health

[3] Y. Zhu, E. F. Choma, K.Wang, and H.Wang, Electric vehicle adoption delivers public health and environmental benefits, Eco-Environment & Health 2[4] (2023) 193-94. https://doi.org/10.1016/j.eehl.2023.07.008.

[4] S. Y. Chang, J. Huang, M. R. Chaveste, F.W. Lurmann, D. S. Eisinger, A. D. Mukherjee, G. B. Erdakos, M. Alexander, and E. Knipping, Electric vehicle fleet penetration helps address inequalities in air quality and improves environmental justice, Communications Earth & Environment 4[1] (2023) 135. https://doi.org/10.1038/s43247-023-00799-1.

[5] Y. Wu, Lithium-ion batteries: Fundamentals and Applications. CRC press, (2015).

[6] J. B. Goodenough and Y. Kim, Challenges for rechargeable Li batteries, Chemistry of materials 22[3] (2010) 587-603. https://doi.org/10.1021/cm901452z.

[7] J. Jiang and C. Zhang, Fundamentals and applications of lithium-ion batteries in electric drive vehicles. John Wiley & Sons, (2015).

[8] B. Scrosati and J. Garche, Lithium batteries: Status, prospects and future, Journal of Power Sources 195[9] (2010) 2419-30. https://doi.org/10.1016/j.jpowsour.2009.11.048.

[9] M. Armand and J. M. Tarascon, Building better batteries, Nature 451[7179] (2008) 652-57. https://doi.org/10.1038/451652a.

[10] A. J. Bard, L. R. Faulkner, and H. S. White, Electrochemical Methods: Fundamentals and Applications. Wiley, (2022).

[11] D. Linden and T. B. Reddy, Handbook of batteries 3 ed. amerika serikat: McGraw-Hill companies. in. Inc, 2002.

[12] Birke, K. P. (Ed.). (2019). Modern battery engineering: A comprehensive introduction. World Scientific.

[13] M. R. Palacín, Recent advances in rechargeable battery materials: a chemist's perspective, Chemical Society Reviews 38[9] (2009) 2565-75. https://doi.org/10.1039/B820555H.

[14] B. Dunn, H. Kamath, and J.-M. Tarascon, Electrical Energy Storage for the Grid: A Battery of Choices, Science 334[6058] (2011) 928-35. https://doi.org/10.1126/science.1212741.

[15] J. M. Tarascon and M. Armand, Issues and challenges facing rechargeable lithium batteries, Nature 414[6861] (2001) 359-67. https://doi.org/10.1038/35104644.

[16] A. S. Aricò, P. Bruce, B. Scrosati, J.-M. Tarascon, and W. van Schalkwijk, Nanostructured materials for advanced energy conversion and storage devices, Nature Materials 4[5] (2005) 366-77. https://doi.org/10.1038/nmat1368.

[17] W. König, Ein galvanisches Element aus der Partherzeit, Forschungen und Fortschritte 14[1] (1938) 8-9.

[18] G. Eggert, The Enigma of the "Battery of Baghdad." In 7th European Skeptics Conference, May.

[19] A. A. Mills, The "Baghdad Battery", Bull Sci Instrum Soc 68 (2001) 35-37.

[20] BooksFact, Baghdad Battery - Ancient Technology, (2012), https://www.booksfact.com/technology/ancient-technology/baghdad-battery.html.

[21] V. Etacheri, R. Marom, R. Elazari, G. Salitra, and D. Aurbach, Challenges in the development of advanced Li-ion batteries: a review, *Energy Environ. Sci.* 4[9] (2011) 3243-62. https://doi.org/10.1039/C1EE01598B.

[22] K. Xu, Electrolytes and Interphases in Li-Ion Batteries and Beyond, Chemical Reviews 114[23] (2014) 11503-618. https://doi.org/10.1021/cr500003w.

[23] W. E. Flood, The origins of chemical names, (No Title) (1963).

[24] J. W. Choi and D. Aurbach, Promise and reality of post-lithium-ion batteries with high energy densities, Nature Reviews Materials 1[4] (2016) 16013. https://doi.org/10.1038/natrevmats.2016.13.

[25] Z. Chen, D.-J. Lee,Y.-K. Sun, and K. Amine, Advanced cathode materials for lithium-ion batteries, MRS Bulletin 36[7] (2011) 498-505. https://doi.org/10.1557/mrs.2011.155.

[26] J. C. Bachman, S. Muy, A. Grimaud, H.-H. Chang, N. Pour, S. F. Lux, O. Paschos, F. Maglia, S. Lupart, P. Lamp, L. Giordano, and Y. Shao-Horn, Inorganic Solid-State Electrolytes for Lithium Batteries: Mechanisms and Properties Governing Ion Conduction, Chemical Reviews 116[1] (2016) 140-62. https://doi.org/10.1021/acs.chemrev.5b00563.

[27] C. Monroe and J. Newman, The Impact of Elastic Deformation on Deposition Kinetics at Lithium/Polymer Interfaces, Journal of The Electrochemical Society 152[2] (2005) A396. https://doi.org/10.1149/1.1850854.

[28] S.-T. Myung, F. Maglia, K.-J. Park, C. S. Yoon, P. Lamp, S.-J. Kim, and Y.-K. Sun, Nickel-Rich Layered Cathode Materials for Automotive Lithium-Ion Batteries: Achievements and Perspectives, ACS Energy Letters 2[1] (2017) 196-223. https://doi.org/10.1021/acsenergylett.6b00594.

[29] R. A. Huggins and R. A. Huggins, Energy storage: fundamentals, materials and applications. Springer, (2016).

[30] W.-J. Zhang, A review of the electrochemical performance of alloy anodes for lithium-ion batteries, Journal of Power Sources 196[1] (2011) 13-24. https://doi.org/10.1016/j.jpowsour.2010.07.020.

[31] L. Lu, X. Han, J. Li, J. Hua, and M. Ouyang, A review on the key issues for lithium-ion battery management in electric vehicles, Journal of Power Sources 226 (2013) 272-88. https://doi.org/10.1016/j.jpowsour.2012.10.060.

[32] K. Kang, Y. S. Meng, J. Bréger, C. P. Grey, and G. Ceder, Electrodes with High Power and High Capacity for Rechargeable Lithium Batteries, Science 311[5763] (2006) 977-80. https://doi.org/10.1126/science.1122152.

[33] P. G. Bruce, B. Scrosati, and J.-M. Tarascon, Nanomaterials for Rechargeable Lithium Batteries, Angewandte Chemie International Edition 47[16] (2008) 2930-46. https://doi.org/10.1002/anie.200702505.

[34] I. Kovalenko, B. Zdyrko, A. Magasinski, B. Hertzberg, Z. Milicev, R. Burtovyy, I. Luzinov, and G. Yushin, A Major Constituent of Brown Algae for Use in High-Capacity Li-Ion Batteries, Science 334[6052] (2011) 75-79. https://doi.org/10.1126/science.1209150.

[35] M. M. Thackeray, C. Wolverton, and E. D. Isaacs, Electrical energy storage for transportation—approaching the limits of, and going beyond, lithium-ion batteries, Energy & Environmental Science 5[7] (2012) 7854-63. https://doi.org/10.1039/C2EE21892E

[36] T.-H. Kim, J.-S. Park, S. K. Chang, S. Choi, J. H. Ryu, and H.-K. Song, The Current Move of Lithium Ion Batteries Towards the Next Phase, Advanced Energy Materials 2[7] (2012) 860-72. https://doi.org/10.1002/aenm.201200028.

[37] M. N. Obrovac and V. L. Chevrier, Alloy Negative Electrodes for Li-Ion Batteries, Chemical Reviews 114[23] (2014) 11444-502. https://doi.org/10.1021/cr500207g.

[38] N. Nitta, F. Wu, J. T. Lee, and G. Yushin, Li-ion battery materials: present and future, Materials Today 18[5] (2015) 252-64. https://doi.org/10.1016/j.mattod.2014.10.040.

[39] Y. Cao, M. Li, J. Lu, J. Liu, and K. Amine, Bridging the academic and industrial metrics for next-generation practical batteries, Nature Nanotechnology 14[3] (2019) 200-07. https://doi.org/10.1038/s41565-019-0371-8.

[40] M. S. Whittingham, Lithium Batteries and Cathode Materials, Chemical Reviews 104[10] (2004) 4271-302. https://doi.org/10.1021/cr020731c.

[41] M. Tatsumisago and A. Hayashi, Sulfide Glass-Ceramic Electrolytes for All-Solid-State Lithium and Sodium Batteries, International Journal of Applied Glass Science 5[3] (2014) 226-35. https://doi.org/10.1111/ijag.12084.

[42] K. Takada, Progress and prospective of solid-state lithium batteries, Acta Materialia 61[3] (2013) 759-70. https://doi.org/10.1016/j.actamat.2012.10.034.

[43] C. P. Grey and J. M. Tarascon, Sustainability and in situ monitoring in battery development, Nature Materials 16[1] (2017) 45-56. https://doi.org/10.1038/nmat4777.

[44] J. Janek and W. G. Zeier, A solid future for battery development, Nature Energy 1[9] (2016) 16141. https://doi.org/10.1038/nenergy.2016.141.
[45] D. Aurbach, E. Zinigrad, Y. Cohen, and H. Teller, A short review of failure mechanisms of lithium metal and lithiated graphite anodes in liquid electrolyte solutions, Solid State Ionics 148[3] (2002) 405-16. https://doi.org/10.1016/S0167-2738(02)00080-2.
[46] S. S. Zhang, Liquid electrolyte lithium/sulfur battery: Fundamental chemistry, problems, and solutions, Journal of Power Sources 231 (2013) 153-62. https://doi.org/10.1016/j.jpowsour.2012.12.102.
[47] J. B. Goodenough and K.-S. Park, The Li-Ion Rechargeable Battery: A Perspective, Journal of the American Chemical Society 135[4] (2013) 1167-76. https://doi.org/10.1021/ja3091438.
[48] T. Famprikis, P. Canepa, J. A. Dawson, M. S. Islam, and C. Masquelier, Fundamentals of inorganic solid-state electrolytes for batteries, Nature Materials 18[12] (2019) 1278-91. https://doi.org/10.1038/s41563-019-0431-3.
[49] P. Albertus, S. Babinec, S. Litzelman, and A. Newman, Status and challenges in enabling the lithium metal electrode for high-energy and low-cost rechargeable batteries, Nature Energy 3[1] (2018) 16-21. https://doi.org/10.1038/s41560-017-0047-2.
[50] D. Lin, Y. Liu, and Y. Cui, Reviving the lithium metal anode for high-energy batteries, Nature Nanotechnology 12[3] (2017) 194-206. https://doi.org/10.1038/nnano.2017.16.
[51] Z. Gao, H. Sun, L. Fu, F. Ye, Y. Zhang, W. Luo, and Y. Huang, Promises, Challenges, and Recent Progress of Inorganic Solid-State Electrolytes for All-Solid-State Lithium Batteries, Advanced Materials 30[17] (2018) 1705702. https://doi.org/10.1002/adma.201705702.
[52] F. Aguesse, W. Manalastas, L. Buannic, J. M. Lopez del Amo, G. Singh, A. Llordés, and J. Kilner, Investigating the Dendritic Growth during Full Cell Cycling of Garnet Electrolyte in Direct Contact with Li Metal, ACS Applied Materials & Interfaces 9[4] (2017) 3808-16. https://doi.org/10.1021/acsami.6b13925.
[53] S. Lou, F. Zhang, C. Fu, M. Chen, Y. Ma, G. Yin, and J. Wang, Interface Issues and Challenges in All-Solid-State Batteries: Lithium, Sodium, and Beyond, Advanced Materials 33[6] (2021) 2000721. https://doi.org/10.1002/adma.202000721.
[54] L. Xi, D. Zhang, X. Xu, Y. Wu, F. Li, S. Yao, M. Zhu, and J. Liu, Interface Engineering of All-Solid-State Batteries Based on Inorganic Solid Electrolytes, ChemSusChem 16[9] (2023) e202202158. https://doi.org/10.1002/cssc.202202158.
[55] Z. Wu, X. Li, C. Zheng, Z. Fan, W. Zhang, H. Huang, Y. Gan, Y. Xia, X. He, X. Tao, and J. Zhang, Interfaces in Sulfide Solid Electrolyte-Based All-Solid-State Lithium Batteries: Characterization, Mechanism and Strategy, Electrochemical Energy Reviews 6[1] (2023) 10. https://doi.org/10.1007/s41918-022-00176-0.
[56] T. K. Schwietert, V. A. Arszelewska, C. Wang, C. Yu, A. Vasileiadis, N. J. J. de Klerk, J. Hageman, T. Hupfer, I. Kerkamm, Y. Xu, E. van der Maas, E. M. Kelder, S. Ganapathy, and M. Wagemaker, Clarifying the relationship between redox activity and electrochemical stability in solid electrolytes, Nature Materials 19[4] (2020) 428-35. https://doi.org/10.1038/s41563-019-0576-0.
[57] Y. Kato, S. Hori, T. Saito, K. Suzuki, M. Hirayama, A. Mitsui, M. Yonemura, H. Iba, and R. Kanno, High-power all-solid-state batteries using sulfide superionic conductors, Nature Energy 1[4] (2016) 16030. https://doi.org/10.1038/nenergy.2016.30.
[58] F. Zheng, M. Kotobuki, S. Song, M.O.Lai, and L. Lu, Review on solid electrolytes for all-solid-state lithium-ion batteries, Journal of Power Sources 389 (2018) 198-213. https://doi.org/10.1016/j.jpowsour.2018.04.022.
[59] C. Chen, K. Wang, H. He, E. Hanc, M. Kotobuki, and L. Lu, Processing and Properties of Garnet-Type $Li_7La_3Zr_2O_{12}$ Ceramic Electrolytes, Small 19[12] (2023) 2205550. https://doi.org/10.1002/smll.202205550.
[60] X. Zhu, J. Wu, and J. Lu, Insight into Inorganic Solid-State Electrolytes: Ionic Transport and Failure Mechanisms, Advanced Functional Materials 34[49] (2024) 2409547. https://doi.org/10.1002/adfm.202409547.

[61] L. Porz, T. Swamy, B. W. Sheldon, D. Rettenwander, T. Frömling, H. L. Thaman, S. Berendts, R. Uecker, W. C. Carter, and Y.-M. Chiang, Mechanism of Lithium Metal Penetration through Inorganic Solid Electrolytes, Advanced Energy Materials 7[20] (2017) 1701003. https://doi.org/10.1002/aenm.201701003.

[62] C. Wang, K. Fu, S. P. Kammampata, D. W. McOwen, A. J. Samson, L. Zhang, G. T. Hitz, A. M. Nolan, E. D. Wachsman, Y. Mo, V. Thangadurai, and L. Hu, Garnet-Type Solid-State Electrolytes: Materials, Interfaces, and Batteries, Chemical Reviews 120[10] (2020) 4257-300. https://doi.org/10.1021/acs.chemrev.9b00427.

[63] Z. Zeng, J. Cheng, Y. Li, H. Zhang, D. Li, H. Liu, F.Ji,Q. Sun, and L. Ci, Composite cathode for all-solid-state lithium batteries: Progress and perspective, Materials Today Physics 32 (2023) 101009. https://doi.org/10.1016/j.mtphys.2023.101009.

[64] X. Yao, B. Huang, J. Yin, G. Peng, Z. Huang, C. Gao, D. Liu, and X. Xu, All-solid-state lithium batteries with inorganic solid electrolytes: Review of fundamental science, Chinese Physics B 25[1] (2016) 018802. https://doi.org/10.1088/1674-1056/25/1/018802.

[65] F. Al-Jaljouli, R. Mücke, P. Kaghazchi, Y. J. Sohn, M. Finsterbusch, D. Fattakhova-Rohlfing, and O. Guillon, Microstructural parameters governing the mechanical stress and conductivity of all-solid-state lithium-ion-battery cathodes, Journal of Energy Storage 68 (2023) 107784. https://doi.org/10.1016/j.est.2023.107784.

[66] M. Clausnitzer, R. Mücke, F. Al-Jaljouli, S. Hein, M. Finsterbusch, T. Danner, D. Fattakhova-Rohlfing, O. Guillon, and A. Latz, Optimizing the Composite Cathode Microstructure in All-Solid-State Batteries by Structure-Resolved Simulations, Batteries & Supercaps 6[11] (2023) e202300167. https://doi.org/10.1002/batt.202300167.

[67] T. Brahmbhatt, G. Yang, E. Self, and J. Nanda, Cathode–Sulfide Solid Electrolyte Interfacial Instability: Challenges and Solutions, Frontiers in Energy Research Volume 8 - 2020 (2020). https://doi.org/10.3389/fenrg.2020.570754.

[68] R. Koerver, I. Aygün, T. Leichtweiß, C. Dietrich, W. Zhang, J. O. Binder, P. Hartmann, W. G. Zeier, and J. Janek, Capacity Fade in Solid-State Batteries: Interphase Formation and Chemomechanical Processes in Nickel-Rich Layered Oxide Cathodes and Lithium Thiophosphate Solid Electrolytes, Chemistry of Materials 29[13] (2017) 5574-82. https://doi.org/10.1021/acs.chemmater.7b00931.

[69] K. Mizushima, P. C. Jones, P. J. Wiseman, and J. B. Goodenough, Li_xCoO_2 (0<x<-1): A new cathode material for batteries of high energy density, Materials Research Bulletin 15[6] (1980) 783-89. https://doi.org/10.1016/0025-5408(80)90012-4.

[70] A. Manthiram, A reflection on lithium-ion battery cathode chemistry, Nature Communications 11[1] (2020) 1550. https://doi.org/10.1038/s41467-020-15355-0.

[71] T. Ohzuku, A. Ueda, and M. Nagayama, Electrochemistry and Structural Chemistry of $LiNiO_2$ ($R\bar{3}m$) for 4 Volt Secondary Lithium Cells, Journal of The Electrochemical Society 140[7] (1993) 1862. https://doi.org/10.1149/1.2220730.

[72] R. Kanno and M. Murayama, Lithium Ionic Conductor Thio-LISICON: The Li_2S-GeS_2-P_2S_5 System, Journal of The Electrochemical Society 148[7] (2001) A742. https://doi.org/10.1149/1.1379028.

[73] Z. Dong, S. J. Kennedy, and Y. Wu, Electrospinning materials for energy-related applications and devices, Journal of Power Sources 196[11] (2011) 4886-904. https://doi.org/10.1016/j.jpowsour.2011.01.090.

[74] B. Strehle, Degradation Mechanisms of Layered Oxides Used as Cathode Active Materials in Lithium-Ion Batteries. in. Technische Universität München, 2022.

[75] C. Daniel, D. Mohanty, J. Li, and D. L. Wood, Cathode materials review, AIP Conference Proceedings 1597[1] (2014) 26-43. https://doi.org/10.1063/1.4878478.

[76] T. Ohzuku and A. Ueda, Solid-State Redox Reactions of $LiCoO_2$ ($R\bar{3}m$) for 4 Volt Secondary Lithium Cells, Journal of The Electrochemical Society 141[11] (1994) 2972. https://doi.org/10.1149/1.2059267.

[77] H.-J. Noh, S. Youn, C. S. Yoon, and Y.-K. Sun, Comparison of the structural and

electrochemical properties of layered $Li[Ni_xCo_yMn_z]O_2$ (x = 1/3, 0.5, 0.6, 0.7, 0.8 and 0.85) cathode material for lithium-ion batteries, Journal of Power Sources 233 (2013) 121-30. https://doi.org/10.1016/j.jpowsour.2013.01.063.

[78] L.-Y. Kuo, Effect of Substitution and Doping on Cathode Materials in Li-and Na-based Batteries: First-Principle Study. Freie Universität Berlin (Germany), (2021).

[79] Continuum Damage and Fracture Mechanics Andreas Öchsner: Springer, 2016 163 pages, ISBN 978-981-287-863-2, MRS Bulletin 41[9] (2016) 707-08. https://doi.org/10.1557/mrs.2016.202.

[80] J. N. Reimers and J. R. Dahn, Electrochemical and In Situ X-Ray Diffraction Studies of Lithium Intercalation in Li_xCoO_2, Journal of The Electrochemical Society 139[8] (1992) 2091. https://doi.org/10.1149/1.2221184.

[81] G. G. Amatucci, J. M. Tarascon, and L. C. Klein, CoO_2, The End Member of the Li_xCoO_2 Solid Solution, Journal of The Electrochemical Society 143[3] (1996) 1114. https://doi.org/10.1149/1.1836594.

[82] W. D. Johnston, R. R. Heikes, and D. Sestrich, The preparation, crystallography, and magnetic properties of the $Li_xCo_{(1-x)}O$ system, Journal of Physics and Chemistry of Solids 7[1] (1958) 1-13. https://doi.org/10.1016/0022-3697(58)90175-6.

[83] T. Ohzuku, A. Ueda, M. Nagayama, Y. Iwakoshi, and H. Komori, Comparative study of $LiCoO_2$, $LiNi_{12}Co_{12}O_2$ and $LiNiO_2$ for 4 volt secondary lithium cells, Electrochimica Acta 38[9] (1993) 1159-67. https://doi.org/10.1016/0013-4686(93)80046-3.

[84] J. Cho, Y. J. Kim, T.-J. Kim, and B. Park, Zero-Strain Intercalation Cathode for Rechargeable Li-Ion Cell, Angewandte Chemie International Edition 40[18] (2001) 3367-69. https://doi.org/10.1002/1521-3773(20010917)40:18.

[85] C. Roitzheim, Synthesis of optimized cathode materials for all-solid-state lithium batteries. Universitaet Duisburg-Essen (Germany), (2022).

[86] Y. Liu, Y. Zhu, and Y. Cui, Challenges and opportunities towards fast-charging battery materials, Nature Energy 4[7] (2019) 540-50. https://doi.org/10.1038/s41560-019-0405-3.

[87] E. Antolini, $LiCoO_2$: formation, structure, lithium and oxygen nonstoichiometry, electrochemical behaviour and transport properties, Solid State Ionics 170[3] (2004) 159-71. https://doi.org/10.1016/j.ssi.2004.04.003.

[88] H. Wang, Y. I. Jang, B. Huang, D. R. Sadoway, and Y. M. Chiang, TEM Study of Electrochemical Cycling-Induced Damage and Disorder in $LiCoO_2$ Cathodes for Rechargeable Lithium Batteries, Journal of The Electrochemical Society 146[2] (1999) 473. https://doi.org/10.1149/1.1391631.

[89] T. Ohnishi, K. Mitsuishi, and K. Takada, In Situ X-ray Diffraction of $LiCoO_2$ in Thin-Film Batteries under High-Voltage Charging, ACS Applied Energy Materials 4[12] (2021) 14372-79. https://doi.org/10.1021/acsaem.1c03046.

[90] Q. Xiang, L. Li, L. Wang, C. Zhou, D. Zhang, and Z. Li, Inhibiting degradation of $LiCoO_2$ cathode material by anisotropic strain during delithiation, Materials Research Express 7[2] (2020) 025501. https://doi.org/10.1088/2053-1591/ab6db2.

[91] B. Bal, B. Ozdogru, M. Wable, V. Murugesan, G. M. Veith, and Ö. Ö. Çapraz, Chemo-mechanical instabilities in lithium cobalt oxide at higher state-of-charge in Li-Ion batteries, Electrochimica Acta 508 (2024) 145223. https://doi.org/10.1016/j.electacta.2024.145223.

[92] Y. Qi, H. Guo, L. G. Hector, and A. Timmons, Threefold Increase in the Young's Modulus of Graphite Negative Electrode during Lithium Intercalation, Journal of The Electrochemical Society 157[5] (2010) A558. https://doi.org/10.1149/1.3327913.

[93] L. Li, L. Wang, X. Zhang, M. Xie, F. Wu, and R. Chen, Structural and Electrochemical Study of Hierarchical $LiNi_{1/3}Co_{1/3}Mn_{1/3}O_2$ Cathode Material for Lithium-Ion Batteries, ACS Applied Materials & Interfaces 7[39] (2015) 21939-47. https://doi.org/10.1021/acsami.5b06584.

[94] J. H. Yoon, H. J. Bang, J. Prakash, and Y. K. Sun, Comparative study of $Li[Ni_{1/3}Co_{1/3}Mn_{1/3}]O_2$ cathode material synthesized via different synthetic routes for asymmetric electrochemical capacitor applications, Materials Chemistry and Physics 110[2] (2008) 222-27. https://doi.org/10.1016/j.matchemphys.2008.01.032.

[95] H. Sun and K. Zhao, Electronic Structure and Comparative Properties of $LiNi_xMn_yCo_zO_2$ Cathode Materials, The Journal of Physical Chemistry C 121[11] (2017) 6002-10. https://doi.org/10.1021/acs.jpcc.7b00810.

[96] E. Lee and K. A. Persson, Revealing the coupled cation interactions behind the electrochemical profile of $Li_xNi_{0.5}Mn_{1.5}O_4$, Energy & Environmental Science 5[3] (2012) 6047-51. https://doi.org/10.1039/C2EE03068C.

[97] W. Li, E. M. Erickson, and A. Manthiram, High-nickel layered oxide cathodes for lithium-based automotive batteries, Nature Energy 5[1] (2020) 26-34. https://doi.org/10.1038/s41560-019-0513-0.

[98] D. Mohanty, A. Huq, E. A. Payzant, A. S. Sefat, J. Li, D. P. Abraham, D. L. Wood, III, and C. Daniel, Neutron Diffraction and Magnetic Susceptibility Studies on a High-Voltage $Li_{1.2}Mn_{0.55}Ni_{0.15}Co_{0.10}O_2$ Lithium Ion Battery Cathode: Insight into the Crystal Structure, Chemistry of Materials 25[20] (2013) 4064-70. https://doi.org/10.1021/cm402278q.

[99] J. Park, H. Zhao, S. D. Kang, K. Lim, C.-C. Chen, Y.-S. Yu, R. D. Braatz, D. A. Shapiro, J. Hong, M. F. Toney, M. Z. Bazant, and W. C. Chueh, Fictitious phase separation in Li layered oxides driven by electro-autocatalysis, Nature Materials 20[7] (2021) 991-99. https://doi.org/10.1038/s41563-021-00936-1.

[100] J.-H. Lim, H. Bang, K.-S. Lee, K. Amine, and Y.-K. Sun, Electrochemical characterization of Li_2MnO_3–$Li[Ni_{1/3}Co_{1/3}Mn_{1/3}]O_2$–$LiNiO_2$ cathode synthesized via co-precipitation for lithium secondary batteries, Journal of Power Sources 189[1] (2009) 571-75. https://doi.org/10.1016/j.jpowsour.2008.10.035.

[101] B. Xu, C. R. Fell, M. Chi, and Y. S. Meng, Identifying surface structural changes in layered Li-excess nickel manganese oxides in high voltage lithium ion batteries: A joint experimental and theoretical study, Energy & Environmental Science 4[6] (2011) 2223-33. https://doi.org/10.1039/C1EE01131F.

[102] K. Ishidzu, Y. Oka, and T. Nakamura, Lattice volume change during charge/discharge reaction and cycle performance of $Li[Ni_xCo_yMn_z]O_2$, Solid State Ionics 288 (2016) 176-79. https://doi.org/10.1016/j.ssi.2016.01.009.

[103] H. Komatsu, S. Banerjee, M. L. Holekevi Chandrappa, J. Qi, B. Radhakrishnan, S. Kuwata, K. Sakamoto, and S. P. Ong, Interfacial Stability of Layered $LiNi_xMn_yCo_{1-x-y}O_2$ Cathodes with Sulfide Solid Electrolytes in All-Solid-State Rechargeable Lithium-Ion Batteries from First-Principles Calculations, The Journal of Physical Chemistry C 126[41] (2022) 17482-89. https://doi.org/10.1021/acs.jpcc.2c05336.

[104] K. Kerman, A. Luntz, V. Viswanathan, Y.-M. Chiang, and Z. Chen, Review—Practical Challenges Hindering the Development of Solid State Li Ion Batteries, Journal of The Electrochemical Society 164[7] (2017) A1731. https://doi.org/10.1149/2.1571707jes.

[105] W. Zhang, L. Liang, F. Zhao, Y. Liu, L. Hou, and C. Yuan, Ni-rich $LiNi_{0.8}Co_{0.1}Mn_{0.1}O_2$ coated with Li-ion conductive Li_3PO_4 as competitive cathodes for high-energy-density lithium ion batteries, Electrochimica Acta 340 (2020) 135871. https://doi.org/10.1016/j.electacta.2020.135871.

[106] T. Sattar, S.-J. Sim, B.-S. Jin, and H.-S. Kim, Dual function Li-reactive coating from residual lithium on Ni-rich NCM cathode material for Lithium-ion batteries, Scientific Reports 11[1] (2021) 18590. https://doi.org/10.1038/s41598-021-98123-4.

[107] J. Zhu, Y. Li, L. Xue, Y. Chen, T. Lei, S. Deng, and G. Cao, Enhanced electrochemical performance of Li_3PO_4 modified $Li[Ni_{0.8}Co_{0.1}Mn_{0.1}]O_2$ cathode material via lithium-reactive coating, Journal of Alloys and Compounds 773 (2019) 112-20. https://doi.org/10.1016/j.jallcom.2018.09.237.

[108] P. Zou, Z. Lin, M. Fan, F. Wang, Y. Liu, and X. Xiong, Facile and efficient fabrication of Li_3PO_4-coated Ni-rich cathode for high-performance lithium-ion battery, Applied Surface Science 504 (2020) 144506. https://doi.org/10.1016/j.apsusc.2019.144506.

[109] F. Strauss, L. de Biasi, A. Y. Kim, J. Hertle, S. Schweidler, J. Janek, P. Hartmann, and T. Brezesinski, Rational Design of Quasi-Zero-Strain NCM Cathode Materials for Minimizing

Volume Change Effects in All-Solid-State Batteries, ACS Materials Letters 2[1] (2020) 84-88. https://doi.org/10.1021/acsmaterialslett.9b00441.

[110] C. Zhan, J. Lu, A. Jeremy Kropf, T. Wu, A. N. Jansen, Y.-K. Sun, X. Qiu, and K. Amine, Mn(II) deposition on anodes and its effects on capacity fade in spinel lithium manganate–carbon systems, Nature Communications 4[1] (2013) 2437. https://doi.org/10.1038/ncomms3437.

[111] Y. Duan, S.-P. Chen, L. Zhang, L. Guo, and F.-N. Shi, Review on Oxygen Release Mechanism and Modification Strategy of Nickel-Rich NCM Cathode Materials for Lithium-Ion Batteries: Recent Advances and Future Directions, Energy & Fuels 38[7] (2024) 5607-31. https://doi.org/10.1021/acs.energyfuels.3c04636.

[112] F. Wu, J. Tian, Y. Su, J. Wang, C. Zhang, L. Bao, T. He, J. Li, and S. Chen, Effect of Ni^{2+} Content on Lithium/Nickel Disorder for Ni-Rich Cathode Materials, ACS Applied Materials & Interfaces 7[14] (2015) 7702-08. https://doi.org/10.1021/acsami.5b00645.

[113] T. Li, X.-Z. Yuan, L. Zhang, D. Song, K. Shi, and C. Bock, Degradation Mechanisms and Mitigation Strategies of Nickel-Rich NMC-Based Lithium-Ion Batteries, Electrochemical Energy Reviews 3[1] (2020) 43-80. https://doi.org/10.1007/s41918-019-00053-3.

[114] J.-M. Lim, T. Hwang, D. Kim, M.-S. Park, K. Cho, and M. Cho, Intrinsic Origins of Crack Generation in Ni-rich $LiNi_{0.8}Co_{0.1}Mn_{0.1}O_2$ Layered Oxide Cathode Material, Scientific Reports 7[1] (2017) 39669. https://doi.org/10.1038/srep39669.

[115] B. Xu, D. Qian, Z. Wang, and Y. S. Meng, Recent progress in cathode materials research for advanced lithium ion batteries, Materials Science and Engineering: R: Reports 73[5] (2012) 51-65. https://doi.org/10.1016/j.mser.2012.05.003.

[116] Q. Wu, S. Mao, Z. Wang, Y. Tong, and Y. Lu, Improving $LiNi_xCo_yMn_{1-x-y}O_2$ cathode electrolyte interface under high voltage in lithium ion batteries, Nano Select 1[1] (2020) 111-34. https://doi.org/10.1002/nano.202000008.

[117] P. Liang, K. Qi, S. Chen, X. Ding, X. Wu, C. Wu, and Y. Zhu, Low-Electronegativity Cationic High-Entropy Doping to Trigger Stable Anion Redox Activity for High-Ni Co-Free Layered Cathodes in Li-Ion Batteries, Angewandte Chemie International Edition 63[10] (2024) e202318186. https://doi.org/10.1002/anie.202318186.

[118] G. Zha, C. Ouyang, S. Yin, K. Yao, S. Agarwal, N. Hu, and H. Hou, High Cycling Stability of the $LiNi_{0.8}Co_{0.1}Mn_{0.1}O_2$ Cathode via Surface Modification with Polyimide/Multi-Walled Carbon Nanotubes Composite Coating, Small 17[47] (2021) 2102981. https://doi.org/10.1002/smll.202102981.

[119] I. McClelland, S. G. Booth, N. N. Anthonisamy, L. A. Middlemiss, G. E. Pérez, E. J. Cussen, P. J. Baker, and S. A. Cussen, Direct Observation of Dynamic Lithium Diffusion Behavior in Nickel-Rich, $LiNi_{0.8}Mn_{0.1}Co_{0.1}O_2$ (NMC811) Cathodes Using Operando Muon Spectroscopy, Chemistry of Materials 35[11] (2023) 4149-58. https://doi.org/10.1021/acs.chemmater.2c03834.

[120] W. Li, B. Song, and A. Manthiram, High-voltage positive electrode materials for lithium-ion batteries, Chemical Society Reviews 46[10] (2017) 3006-59. https://doi.org/10.1039/C6CS00875E.

[121] B. K, M. Jareer, G. Lakshmi Sagar, P. Mukesh, A. A, D. Mandal, H. S. Nagaraja, and S. Shahgaldi, Advanced Electrolyte Additives for Lithium-Ion Batteries: Classification, Function, and Future Directions, The Journal of Physical Chemistry C 129[25] (2025) 11221-51. https://doi.org/10.1021/acs.jpcc.5c01331.

[122] H. Li, A. Liu, N. Zhang, Y. Wang, S. Yin, H. Wu, and J. R. Dahn, An Unavoidable Challenge for Ni-Rich Positive Electrode Materials for Lithium-Ion Batteries, Chemistry of Materials 31[18] (2019) 7574-83. https://doi.org/10.1021/acs.chemmater.9b02372.

[123] N. Zhang, X. Long, Z. Wang, P. Yu, F. Han, J. Fu, G. Ren, Y. Wu, S. Zheng, W. Huang, C. Wang, H. Li, and X. Liu, Mechanism Study on the Interfacial Stability of a Lithium Garnet-Type Oxide Electrolyte against Cathode Materials, ACS Applied Energy Materials 1[11] (2018) 5968-76. https://doi.org/10.1021/acsaem.8b01035.

[124] Y. Xiao, Y. Wang, S.-H. Bo, J. C. Kim, L. J. Miara, and G. Ceder, Understanding interface stability in solid-state batteries, Nature Reviews Materials 5[2] (2020) 105-26.

https://doi.org/10.1038/s41578-019-0157-5.
[125] N. B. Timusheva, A. A. Golubnichiy, A. V. Morozov, A. S. Burov, D. A. Aksyonov, A. A. Savina, R. G. Markopolskii, and A. M. Abakumov, Chemical compatibility at the interface of garnet-type Ga-LLZO solid electrolyte and high-energy Li-rich layered oxide cathode for all-solid-state batteries, Scientific Reports 15[1] (2025) 241. https://doi.org/10.1038/s41598-024-78927-w.
[126] M. M. Thackeray, A. de Kock, M. H. Rossouw, D. Liles, R. Bittihn, and D. Hoge, Spinel Electrodes from the Li-Mn-O System for Rechargeable Lithium Battery Applications, Journal of The Electrochemical Society 139[2] (1992) 363. https://doi.org/10.1149/1.2069222.
[127] M. M. Thackeray, W. I. F. David, P. G. Bruce, and J. B. Goodenough, Lithium insertion into manganese spinels, Materials Research Bulletin 18[4] (1983) 461-72. https://doi.org/10.1016/0025-5408(83)90138-1.
[128] J. C. Hunter, Preparation of a new crystal form of manganese dioxide: λ-MnO_2, Journal of Solid State Chemistry 39[2] (1981) 142-47. https://doi.org/10.1016/0022-4596(81)90323-6.
[129] K. Amine, H. Tukamoto, H. Yasuda, and Y. Fujita, Preparation and electrochemical investigation of $LiMn_{2-x}Me_xO_4$ (Me: Ni, Fe, and x = 0.5, 1) cathode materials for secondary lithium batteries, Journal of Power Sources 68[2] (1997) 604-08. https://doi.org/10.1016/S0378-7753(96)02590-6.
[130] Ö. Ö. Çapraz, S. Rajput, S. White, and N. R. Sottos, Strain Evolution in Lithium Manganese Oxide Electrodes, Experimental Mechanics 58[4] (2018) 561-71. https://doi.org/10.1007/s11340-018-0381-8.
[131] S. Patnaik, Overview of electrode advances in commercial Li-ion batteries, Ionics 30[6] (2024) 3069-90. https://doi.org/10.1007/s11581-024-05579-1.
[132] A.-H. Marincaş and P. Ilea, Enhancing Lithium Manganese Oxide Electrochemical Behavior by Doping and Surface Modifications, Coatings 11[4] (2021) 456. https://doi.org/10.3390/coatings11040456.
[133] Z.-J. Zhang, S.-L. Chou, Q.-F. Gu, H.-K. Liu, H.-J. Li, K. Ozawa, and J.-Z. Wang, Enhancing the High Rate Capability and Cycling Stability of $LiMn_2O_4$ by Coating of Solid-State Electrolyte $LiNbO_3$, ACS Applied Materials & Interfaces 6[24] (2014) 22155-65. https://doi.org/10.1021/am5056504.
[134] A. A. Delluva, J. Dudoff, G. Teeter, and A. Holewinski, Cathode Interface Compatibility of Amorphous $LiMn_2O_4$ (LMO) and $Li_7La_3Zr_2O_{12}$ (LLZO) Characterized with Thin-Film Solid-State Electrochemical Cells, ACS Applied Materials & Interfaces 12[22] (2020) 24992-99. https://doi.org/10.1021/acsami.0c03519.
[135] S. Zhang, D. Guan, Z. Xue, C. Shen, Y. Shen, G. Hu, Y. Cao, Z. Peng, W. Wang, Y. Ren, L. Kang, Z. Xue, and K. Du, Enhanced elevated-temperature performance of $LiMn_2O_4$ cathodes in lithium-ion batteries via a multifunctional electrolyte additive, Chemical Engineering Journal 503 (2025) 158219. https://doi.org/10.1016/j.cej.2024.158219.
[136] S. B. Riaz and M. Hassan, Mechanochemical Approaches for Advancing Lithium-Ion Battery Materials: Synthesis, Processing, and Performance Enhancement, Mechanics Exploration and Material Innovation 2[1] (2025) 49-58. https://doi.org/10.21776/ub.memi.2025.002.01.5
[137] C. Zuo, Z. Hu, R. Qi, J. Liu, Z. Li, J. Lu, C. Dong, K. Yang, W. Huang, C. Chen, Z. Song, S. Song, Y. Yu, J. Zheng, and F. Pan, Double the Capacity of Manganese Spinel for Lithium-Ion Storage by Suppression of Cooperative Jahn–Teller Distortion, Advanced Energy Materials 10[34] (2020) 2000363. https://doi.org/10.1002/aenm.202000363.
[138] A. B. Haruna, D. H. Barrett, C. B. Rodella, R. M. Erasmus, A. M. Venter, Z. N. Sentsho, and K. I. Ozoemena, Microwave irradiation suppresses the Jahn-Teller distortion in Spinel $LiMn_2O_4$ cathode material for lithium-ion batteries, Electrochimica Acta 426 (2022) 140786. https://doi.org/10.1016/j.electacta.2022.140786.
[139] W.-W. Liu, D. Wang, Z. Wang, J. Deng, W.-M. Lau, and Y. Zhang, Influence of magnetic ordering and Jahn–Teller distortion on the lithiation process of $LiMn_2O_4$, Physical Chemistry Chemical Physics 19[9] (2017) 6481-86. https://doi.org/10.1039/C6CP08324B.

[140] A. Manthiram, X. Yu, and S. Wang, Lithium battery chemistries enabled by solid-state electrolytes, Nature Reviews Materials 2[4] (2017) 16103. https://doi.org/10.1038/natrevmats.2016.103.

[141] M. M. Raju, F. Altayran, M. Johnson, D. Wang, and Q. Zhang, Crystal Structure and Preparation of $Li_7La_3Zr_2O_{12}$ (LLZO) Solid-State Electrolyte and Doping Impacts on the Conductivity: An Overview, Electrochem 2[3] (2021) 390-414. https://doi.org/10.3390/electrochem2030026.

[142] R. Murugan, V. Thangadurai, and W. Weppner, Fast lithium ion conduction in garnet-type $Li_7La_3Zr_2O_{12}$, Angewandte Chemie-International Edition in English- 46[41] (2007) 7778. https://doi.org/10.1002/anie.200701144.

[143] G. Larraz, A. Orera, and M. L. Sanjuán, Cubic phases of garnet-type $Li_7La_3Zr_2O_{12}$: the role of hydration, Journal of Materials Chemistry A 1[37] (2013) 11419-28. https://doi.org/10.1039/C3TA11996C.

[144] H. Buschmann, J. Dölle, S. Berendts, A. Kuhn, P. Bottke, M. Wilkening, P. Heitjans, A. Senyshyn, H. Ehrenberg, A. Lotnyk, V. Duppel, L. Kienle, and J. Janek, Structure and dynamics of the fast lithium ion conductor "$Li_7La_3Zr_2O_{12}$", Physical Chemistry Chemical Physics 13[43] (2011) 19378-92. https://doi.org/10.1039/C1CP22108F.

[145] Y.-Y. Ting, R. Ye, E. Dashjav, Q. Ma, S. Taminato, D. Mori, N. Imanishi, M. Finsterbusch, M. H. Eikerling, O. Guillon, P. Kaghazchi, and P. M. Kowalski, Thermodynamic and structural characterization of high-entropy garnet electrolytes for all-solid-state battery, Frontiers in Energy Research Volume 12 - 2024 (2024). https://doi.org/10.3389/fenrg.2024.1393914.

[146] J. Awaka, A. Takashima, K. Kataoka, N. Kijima, Y. Idemoto, and J. Akimoto, Crystal Structure of Fast Lithium-ion-conducting Cubic $Li_7La_3Zr_2O_{12}$, Chemistry Letters 40[1] (2010) 60-62. https://doi.org/10.1246/cl.2011.60.

[147] N. Bernstein, M. D. Johannes, and K. Hoang, Origin of the Structural Phase Transition in $Li_7La_3Zr_2O_{12}$, Physical Review Letters 109[20] (2012) 205702. https://doi.org/10.1103/PhysRevLett.109.205702.

[148] E. Yuniarti, S. Priyono, S. Sindhu Hendradjaja, J. Setiawan, K. Prijono, and B. Femlee R, Structural Evolution and Ionic Conductivity of Al_2O_3-Doped LLZO via Single Heat Treatment, Jurnal Ilmu Fisika,17[2] (2025) 157-70. https://doi.org/10.25077/jif.17.2.157-170.2025.

[149] L. J. Miara, W. D. Richards, Y. E. Wang, and G. Ceder, First-Principles Studies on Cation Dopants and Electrolyte Cathode Interphases for Lithium Garnets, Chemistry of Materials 27[11] (2015) 4040-47. https://doi.org/10.1021/acs.chemmater.5b01023.

[150] D. Rettenwander, G. Redhammer, F. Preishuber-Pflügl, L. Cheng, L. Miara, R. Wagner, A. Welzl, E. Suard, M. M. Doeff, M. Wilkening, J. Fleig, and G. Amthauer, Structural and Electrochemical Consequences of Al and Ga Cosubstitution in $Li_7La_3Zr_2O_{12}$ Solid Electrolytes, Chemistry of Materials 28[7] (2016) 2384-92. https://doi.org/10.1021/acs.chemmater.6b00579.

[151] Y. Song, L. Yang, L. Tao, Q. Zhao, Z. Wang, Y. Cui, H. Liu, Y. Lin, and F. Pan, Probing into the origin of an electronic conductivity surge in a garnet solid-state electrolyte, Journal of Materials Chemistry A 7[40] (2019) 22898-902. https://doi.org/10.1039/C9TA10269H.

[152] A. J. Samson, K. Hofstetter, S. Bag, and V. Thangadurai, A bird's-eye view of Li-stuffed garnet-type $Li_7La_3Zr_2O_{12}$ ceramic electrolytes for advanced all-solid-state Li batteries, Energy & Environmental Science 12[10] (2019) 2957-75. https://doi.org/10.1039/C9EE01548E.

[153] T. Thompson, S. Yu, L. Williams, R. D. Schmidt, R. Garcia-Mendez, J. Wolfenstine, J. L. Allen, E. Kioupakis, D. J. Siegel, and J. Sakamoto, Electrochemical Window of the Li-Ion Solid Electrolyte $Li_7La_3Zr_2O_{12}$, ACS Energy Letters 2[2] (2017) 462-68. https://doi.org/10.1021/acsenergylett.6b00593.

[154] S. Yu, R. D. Schmidt, R. Garcia-Mendez, E. Herbert, N. J. Dudney, J. B. Wolfenstine, J. Sakamoto, and D. J. Siegel, Elastic Properties of the Solid Electrolyte $Li_7La_3Zr_2O_{12}$ (LLZO), Chemistry of Materials 28[1] (2016) 197-206. https://doi.org/10.1021/acs.chemmater.5b03854.

[155] T. Yu, Y. Liu, H. Li, Y. Sun, S. Guo, and H. Zhou, Ductile Inorganic Solid Electrolytes for All-Solid-State Lithium Batteries, Chemical Reviews 125[6] (2025) 3595-662. https://doi.org/10.1021/acs.chemrev.4c00894.

[156] J. Lau, R. H. DeBlock, D. M. Butts, D. S. Ashby, C. S. Choi, and B. S. Dunn, Sulfide Solid Electrolytes for Lithium Battery Applications, Advanced Energy Materials 8[27] (2018) 1800933. https://doi.org/10.1002/aenm.201800933.
[157] M. Tatsumisago, M. Nagao, and A. Hayashi, Recent development of sulfide solid electrolytes and interfacial modification for all-solid-state rechargeable lithium batteries, Journal of Asian Ceramic Societies 1[1] (2013) 17-25. https://doi.org/10.1016/j.jascer.2013.03.005.
[158] M. A. Kraft, S. P. Culver, M. Calderon, F. Böcher, T. Krauskopf, A. Senyshyn, C. Dietrich, A. Zevalkink, J. Janek, and W. G. Zeier, Influence of Lattice Polarizability on the Ionic Conductivity in the Lithium Superionic Argyrodites Li_6PS_5X (X = Cl, Br, I), Journal of the American Chemical Society 139[31] (2017) 10909-18. https://doi.org/10.1021/jacs.7b06327.
[159] K. Mori, K. Enjuji, S. Murata, K. Shibata, Y. Kawakita, M. Yonemura, Y. Onodera, and T. Fukunaga, Direct Observation of Fast Lithium-Ion Diffusion in a Superionic Conductor: $Li_7P_3S_{11}$ Metastable Crystal, Physical Review Applied 4[5] (2015) 054008. https://doi.org/10.1103/PhysRevApplied.4.054008.
[160] J. B. Bates, N. J. Dudney, B. Neudecker, A. Ueda, and C. D. Evans, Thin-film lithium and lithium-ion batteries, Solid State Ionics 135[1] (2000) 33-45. https://doi.org/10.1016/S0167-2738(00)00327-1.
[161] M. A. T. Marple, T. A. Wynn, D. Cheng, R. Shimizu, H. E. Mason, and Y. S. Meng, Local Structure of Glassy Lithium Phosphorus Oxynitride Thin Films: A Combined Experimental and Ab Initio Approach, Angewandte Chemie International Edition 59[49] (2020) 22185-93. https://doi.org/10.1002/anie.202009501.
[162] J. Li, C. Ma, M. Chi, C. Liang, and N. J. Dudney, Solid Electrolyte: the Key for High-Voltage Lithium Batteries, Advanced Energy Materials 5[4] (2015) 1401408. https://doi.org/10.1002/aenm.201401408.
[163] R. Bianchini Nuernberg, A.-K. Landry, F. Le Cras, and B. Pecquenard Le Cras, Enhancing ionic conductivity of LiSiPON thin films electrolytes: Overcoming synthesis challenges related to Li-migration in the precursor target, Solid State Ionics 418 (2024) 116723. https://doi.org/10.1016/j.ssi.2024.116723.
[164] S. Nowak, F. Berkemeier, and G. Schmitz, Ultra-thin LiPON films – Fundamental properties and application in solid state thin film model batteries, Journal of Power Sources 275 (2015) 144-50. https://doi.org/10.1016/j.jpowsour.2014.10.202.
[165] M. Nisula, Y. Shindo, H. Koga, and M. Karppinen, Atomic Layer Deposition of Lithium Phosphorus Oxynitride, Chemistry of Materials 27[20] (2015) 6987-93. https://doi.org/10.1021/acs.chemmater.5b02199.
[166] M. E. Gurtin, An introduction to continuum mechanics, Vol. 158. Academic press, (1982).
[167] A. C. Ugural and S. K. Fenster, Advanced Mechanics of Materials and Applied Elasticity. Pearson Education, (2011).
[168] L. E. Malvern, Introduction to the mechanics of a continuous medium, [Nachdr.] ed. Prentice-Hall: Englewood Cliffs, NJ, (2007).
[169] L. E. Malvern, Introduction to the Mechanics of a Continuous Medium. Prentice-Hall, (1969).
[170] Theory of Elasticity (Third Edition). Edited by E. M. Lifshitz, A. M. Kosevich, andL. P. Pitaevskii. Butterworth-Heinemann, Oxford, 1986.
[171] T. C. T. Ting, Anisotropic Elasticity: Theory and Applications. Oxford University Press, (1996).
[172] M. H. Sadd, Elasticity: Theory, Applications, and Numerics. Academic Press, (2009).
[173] J. Kim, Tensile Fracture Behavior and Characterization of Ceramic Matrix Composites, Materials 12[18] (2019) 2997. https://doi.org/10.3390/ma12182997.
[174] D. J. Green, An Introduction to the Mechanical Properties of Ceramics, pp. 348, (1998).
[175] R. Hill, Elastic properties of reinforced solids: Some theoretical principles, Journal of the Mechanics and Physics of Solids 11[5] (1963) 357-72. https://doi.org/10.1016/0022-5096(63)90036-X.
[176] W. J. Drugan and J. R. Willis, A micromechanics-based nonlocal constitutive equation and estimates of representative volume element size for elastic composites, Journal of the Mechanics

and Physics of Solids 44[4] (1996) 497-524. https://doi.org/10.1016/0022-5096(96)00007-5.
[177] J. Cugnoni and M. Galli, Representative Volume Element Size of Elastoplastic and Elastoviscoplastic Particle-Reinforced Composites with Random Microstructure, Computer Modeling in Engineering & Sciences 66[2] (2010) 165--86. https://doi.org/10.3970/cmes.2010.066.165.
[178] T. Kanit, S. Forest, I. Galliet, V. Mounoury, and D. Jeulin, Determination of the size of the representative volume element for random composites: statistical and numerical approach, International Journal of Solids and Structures 40[13] (2003) 3647-79. https://doi.org/10.1016/S0020-7683(03)00143-4.
[179] M. Ostoja-Starzewski, Material spatial randomness: From statistical to representative volume element, Probabilistic Engineering Mechanics 21[2] (2006) 112-32. https://doi.org/10.1016/j.probengmech.2005.07.007.
[180] M. M. Shahzamanian, S. S. Akhtar, A. F. M. Arif, W. J. Basirun, K. S. Al-Athel, M. Schneider, N. Shakelly, A. S. Hakeem, A. A. Abubakar, and P. D. Wu, Thermo-mechanical properties prediction of Ni-reinforced Al_2O_3 composites using micro-mechanics based representative volume elements, Scientific Reports 12[1] (2022) 11076. https://doi.org/10.1038/s41598-022-14685-x.
[181] M. G. D. Geers, V. G. Kouznetsova, and W. A. M. Brekelmans, Multi-scale computational homogenization: Trends and challenges, Journal of Computational and Applied Mathematics 234[7] (2010) 2175-82. https://doi.org/10.1016/j.cam.2009.08.077.
[182] C. Miehe, J. Schröder, and J. Schotte, Computational homogenization analysis in finite plasticity Simulation of texture development in polycrystalline materials, Computer Methods in Applied Mechanics and Engineering 171[3] (1999) 387-418. https://doi.org/10.1016/S0045-7825(98)00218-7.
[183] I. M. Gitman, H. Askes, and L. J. Sluys, Representative volume: Existence and size determination, Engineering Fracture Mechanics 74[16] (2007) 2518-34. https://doi.org/10.1016/j.engfracmech.2006.12.021.
[184] S. Ghosh, K. Lee, and S. Moorthy, Multiple scale analysis of heterogeneous elastic structures using homogenization theory and voronoi cell finite element method, International Journal of Solids and Structures 32[1] (1995) 27-62. https://doi.org/10.1016/0020-7683(94)00097-G.
[185] T. I. Zohdi and P. Wriggers, An Introduction to Computational Micromechanics. Springer Berlin Heidelberg, (2008).
[186] M. May and S. Kilchert, Image Based Statistical Analysis of Composite Microstructure for RVE Simulations, in ASME 2025 Aerospace Structures, Structural Dynamics, and Materials Conference.
[187] J. C. Michel, H. Moulinec, and P. Suquet, A computational scheme for linear and non-linear composites with arbitrary phase contrast, International Journal for Numerical Methods in Engineering 52[1-2] (2001) 139-60. https://doi.org/10.1002/nme.275.
[188] J. C. Michel, H. Moulinec, and P. Suquet, Effective properties of composite materials with periodic microstructure: a computational approach, Computer Methods in Applied Mechanics and Engineering 172[1] (1999) 109-43. https://doi.org/10.1016/S0045-7825(98)00227-8.
[189] S. Bargmann, B. Klusemann, J. Markmann, J. E. Schnabel, K. Schneider, C. Soyarslan, and J. Wilmers, Generation of 3D representative volume elements for heterogeneous materials: A review, Progress in Materials Science 96 (2018) 322-84. https://doi.org/10.1016/j.pmatsci.2018.02.003.
[190] A. Elbana, A. Khennane, and P. J. Hazell, Multiscale modelling of particulate composites with spherical inclusions, Engineering with Computers 40[5] (2024) 3087-113. https://doi.org/10.1007/s00366-024-01954-8.
[191] H. Math2Market Gmb, ElastoDict User Guide: GeoDict release 2022, (2022). https://doi.org/10.30423/userguide.geodict2022-elastodict.
[192] R. A. Lebensohn, A. D. Rollett, and P. Suquet, Fast fourier transform-based modeling for the determination of micromechanical fields in polycrystals, JOM 63[3] (2011) 13-18.

https://doi.org/10.1007/s11837-011-0037-y.
[193] C. Mareau and C. Robert, Different composite voxel methods for the numerical homogenization of heterogeneous inelastic materials with FFT-based techniques, Mechanics of Materials 105 (2017) 157-65. https://doi.org/10.1016/j.mechmat.2016.12.002.
[194] E. Maire and P. J. Withers, Quantitative X-ray tomography, International Materials Reviews 59[1] (2014) 1-43. https://doi.org/10.1179/1743280413y.0000000023.
[195] M. D. Uchic, M. A. Groeber, D. M. Dimiduk, and J. P. Simmons, 3D microstructural characterization of nickel superalloys via serial-sectioning using a dual beam FIB-SEM, Scripta Materialia 55[1] (2006) 23-28. https://doi.org/10.1016/j.scriptamat.2006.02.039.
[196] L. Gélébart, A modified FFT-based solver for the mechanical simulation of heterogeneous materials with Dirichlet boundary conditions, Comptes Rendus. Mécanique 348[8-9] (2020) 693-704. https://doi.org/10.5802/crmeca.54.
[197] X. Li, Z. Liu, S. Cui, C. Luo, C. Li, and Z. Zhuang, Predicting the effective mechanical property of heterogeneous materials by image based modeling and deep learning, Computer Methods in Applied Mechanics and Engineering 347 (2019) 735-53. https://doi.org/10.1016/j.cma.2019.01.005.
[198] P. Eisenlohr, M. Diehl, R. A. Lebensohn, and F. Roters, A spectral method solution to crystal elasto-viscoplasticity at finite strains, International Journal of Plasticity 46 (2013) 37-53. https://doi.org/10.1016/j.ijplas.2012.09.012.
[199] GRAINGEO User Guide, GeoDict release 2024 (2024). https://doi.org/10.30423/userguide.geodict.
[200] ELASTODICT User Guide, GeoDict release 2024 [10.30423/userguide.geodict] (2024). https://doi.org/10.30423/userguide.geodict.
[201] J. Besson, M. Blétry, G. Cailletaud, J. L. Chaboche, and S. Forest, Non-Linear Mechanics of Materials. Springer Netherlands, (2009).
[202] T. I. Zohdi, Rapid Voxel-Based Digital-Computation for Complex Microstructured Media, Archives of Computational Methods in Engineering 26[5] (2019) 1379-94. https://doi.org/10.1007/s11831-018-9284-1.
[203] H. Moulinec and P. Suquet, A numerical method for computing the overall response of nonlinear composites with complex microstructure, Computer Methods in Applied Mechanics and Engineering 157[1] (1998) 69-94. https://doi.org/10.1016/S0045-7825(97)00218-1.

Chapter 3 Research Papers

3.1. Paper I: Microstructural parameters governing the mechanical stress and conductivity of All-solid-state lithium-ion-battery cathodes

Authors	**Fadi Al-Jaljouli**, Robert Mücke, Payam Kaghazchi, Yoo Jung Sohn, Martin Finsterbusch, Dina Fattakhova-Rohlfing and Olivier Guillon
Journal	Journal of energy storage
Volume	68
Pages	107784
Published on	September 2023
DOI	10.1016/j.est.2023.107784

The following constitute my sole contributions:

- Reproducing the experimental structure.
- Set up the validation parameters.
- Generation of microstructures while varying the microstructural design parameters.
- Mechanical and electronic characterization of the regenerated samples.
- Explaining the impact of microstructural design parameters on mechanical stresses and conductivities.
- Proposing the governing factor of the mechanical stresses.
- Writing the entire manuscript
- Authoring the complete supporting information.
- Creation of all figures in the manuscript and supporting information except for Figure 4.

Microstructural parameters governing the mechanical stress and conductivity of All-solid-state lithium-ion-battery cathodes

Fadi Al-Jaljouli [a,b], Robert Mücke [a], Payam Kaghazchi [a], Yoo Jung Sohn [a], Martin Finsterbusch [a], Dina Fattakhova-Rohlfing [a, c] and Olivier Guillon [a,b]

[a] *Forschungszentrum Jülich GmbH, Institute of Energy and Climate Research, Materials Synthesis and Processing (IEK-1), 52425, Jülich Aachen Research Alliance:JARA-Energy, Jülich, Germany*

[b] *Institute of Mineral Engineering, RWTH Aachen University, 52064 Aachen,Germany*

[c] *Faculty of Engineering and Center for Nanointegration Duisburg-Essen, Universit¨at Duisburg-Essen, Lotharstr. 1, 47057, Duisburg, Germany*

Emails: f.al-jaljouli@fz-juelich.de, r.muecke@fz-juelich.de, p.kaghazchi@fz-juelich.de, y.sohn@fz-juelich.de, m.finsterbusch@fz-juelich.de, d.fattakhova@fz-juelich.de, o.guillon@fz-juelich.de

Abstract

All-solid-state lithium ion batteries are considered a promising future battery concept due to their high safety and energy density. However, they might suffer from mechanical fatigue upon cycling, caused by mechanical stresses due to the volume changes of the electrode active materials constrained by solid electrolyte. Based on a reconstruction of actual microstructure of a mixed cathode ($LiCoO_2$/$Li_7La_3Zr_2O_{12}$: LCO/LLZO) in a lab sized cell and using computer aided material design, we calculated the thermal stresses after manufacturing and the electrochemical stresses during cycling. This approach allows us intensively study the impact of microstructural parameters (grain size, solid volume fraction and relative density) on the mechanical stress distribution and conductivities, even for cases not easily manufactural in the lab. We found that the mechanical stresses and conductivities linearly depend on the solid volume fraction of LCO and are correlated to the relative density, whereas the grain sizes influenced neither the mechanical stresses nor the conductivities. We introduced a new factor $\boldsymbol{K_n}$ as a ratio of the relative interface area between solid phases and the volume fraction of the solid phase (n= LCO or LLZO) which represents the governing factor for the stresses. On the other hand, the volume fraction of LCO and LLZO are the governing factors of their electronic and ionic conductivities. This allows for a sound forecast and determination of an optimal cathode microstructure for maximum cell performance.

1. Introduction

All-solid-state lithium ion batteries are considered a most promising candidate to replace conventional lithium ion batteries due to their intrinsic safety and potentially high energy and power density [1-5]. However, there is a large variety of solid electrolyte materials that can be used, each having its own advantages [2,5-9]. In spite of these advantages, all-solid-state batteries are still facing challenges that require further research and development: Together with the formation of dendrites [10-13], undesired chemical reactions of the solid electrolyte with the active material at their interface [14-16], significant degradation due to mechanical fatigue during cycling remains a matter to be solved [17-19]. Mechanical stresses are induced inside the composite cathode and in turn in the full cell due to the volume change of the active material [20-22]. Owed to the large stiffness of the oxide materials commonly used, these stresses can be very substantial reaching the order of 1 GPa and, thus, cause cracks in the material and in turn a capacity fade.

Several techniques have been applied to reduce induced stresses. Zero-strain cathode active materials (NCM271 and NCM361) are still challenged by volume changes during the delithiation process [23-25]. Although the proposed mixing of positive and negative strain materials (e.g. LCO/NCM) exhibits a zero net strain on component level, the stresses on the grain level still persist [26].

Furthermore, integrating elastomer binders within the composite cathode was found to lower the induced stresses [27,28]. On the other hand, elastomer binder should be integrated in low concentration to avoid capacity loss [29,30].

Composite cathodes based only on oxide-ceramic electrolytes require sintering at high temperature. For them, adjusting the microstructural design of the composite cathode to obtain the correct position of the pores to ensure free volume change of the active material seems to be a promising way to reduce the stress while maintaining the conductivity of the system. Many researchers have calculated the lithiation-induced stress. Zero stress was assumed for the fully charged state, and electrochemical stress is introduced during the discharge of the cell [31-36]. Considering the discharge kinetics and isotropic, partially anisotropic, and fully anisotropic material properties [32,37-41]. The stresses of layered oxide active cathode materials in liquid electrolytes have been calculated. In addition, researchers calculated the induced stresses from the random alignment of the primary particles of the cathode active materials coupled together

in secondary particles for practical 2D microstructures and models to analyze complex microstructures [42-45]. Furthermore, it was found that texturing the microstructure of the secondary particles of the active material lowered the stress values using liquid electrolyte in Li-ion batteries [45]. Using isotropic material properties, researchers have calculated the stress within larger 2D and reconstructed 3D microstructures of active materials [34-36,46]. The work by Anja et al. [47] is one of the rare publications studying the effect of the volume fraction of the active material, the grain size of the active material and the porosity in the composite cathode on the electrochemical properties of the composite cathode using computer-aided design. However, the effect on mechanical stress was not included. Furthermore, this study was based on very idealized structure, utilizing a spherical shape for the active material.

Our approach is based on a reconstructed real microstructure of an oxide based all-solid-state cell, in which the active material is LiCoO2 (LCO) and the solid electrolyte is Aluminum and Tantalum doped $Li_7La_3Zr_2O_{12}$ (Ta,Al-LLZO – $Li_{6.15}Al_{0.15}La_3Zr_{1.6}Ta_{0.4}O_{12}$). LCO is characterized by a good stability and high capacity [48-52]. On the other hand, LCO undergoes a moderate volume expansion of 2% below half delithiation [53,54]. LLZO exhibits a high total ionic conductivity (>10^(-4) S/cm) at room temperature, wide electrochemical window and good compatibility with LCO [55-57]. Mücke et al. [41] studied a real microstructure but did not vary the microstructural parameters. In this work, we reconstructed the microstructure of such a real composite cathode by FIB-SEM (labelled “experimental” in the following), and subsequently mimics it with a reproduced structure using computer-aided design (GeoDict) (labelled “reproduced” in the following). Successful mimicking was judged by a sufficient match between both the physical properties (conductivity of LCO and LLZO), and the microstructural properties (chord length of LCO, LLZO and pores, the average inner diameter of LCO and LLZO and the interface area between each component of the composite cathode to the other) of the experimental and the reproduced structure. The microstructural design parameters (solid volume fraction of LCO, relative density of the solid components of the composite cathode, and grain sizes of LCO and LLZO) were varied to investigate their influence on the mechanical stress and conductivity of composite cathode. The pursued goal is to identify the governing factor of the mechanical stress and the conductivity i.e. the property that primarily determines the value of the stress and conductivity independently of other parameters. It is worth mentioning that this variation is difficult to achieve experimentally, since some parameters cannot be varied freely (e.g. porosity) or such a broad range of variations will

often not yield functioning cells (e.g. high porosity and low SE volume fraction). Additionally, we also took the residual thermal stress after sintering into account, developing during cooling down to room temperature stemming from the mismatch of the thermal expansion coefficients of LCO and LLZO [58-60]. Furthermore, the anisotropic material properties of half-delithiated LCO (Li0.5CoO2) were considered because they significantly differ from those of fully lithiated LCO [32,37-39,43,61]. The half-delithiated LCO is set as the fully charged state of the LCO cathodes, since below Li0.5 an irreversible phase transition occurs.

2. Experimental and simulation method

2.1. Sample preparation

A composite cathode consisting of $LiCoO_2$ (LCO) and Ta,Al-LLZO – $Li_{6.15}Al_{0.15}La_3Zr_{1.6}Ta_{0.4}O_{12}$, with 2:1 LCO:LLZO mass ratio, was fabricated and analyzed electrochemically; more details can be found in our previous studies [62,63]. Subsequently, focused ion beam SEM stack images of the cross section were obtained. Image processing yielded an isotropic voxel size of 50 nm. Several computer-aided processes were applied to obtain a model of the experimental structure (Fig 1 b); the processing details being explained in [41].

2.2. Microstructure parameters

The volume fraction of cathode active material (LCO) with respect to the total volume (V_{Total}) is given by

$$\bar{V}_{LCO} = \frac{nv_{LCO}}{V_{Total}} \quad (1)$$

Where n is the number of LCO grains and v_{LCO} is the volume of each grains of LCO.

Similarly, the volume fraction of the solid electrolyte (LLZO) with respect to the total volume is given by:

$$\bar{V}_{LLZO} = \frac{mv_{LLZO}}{V_{Total}} \quad (2)$$

Where m is the number of LLZO grains and v_{LLZO} is the volume of each grains of LLZO.

The percentage of LCO to the total solid phases in the composite cathode is donated by SVF_{LCO}, which can be calculated by:

$$SVF_{LCO} = \frac{\bar{V}_{LCO}}{\bar{V}_{LCO}+\bar{V}_{LLZO}} \quad (3)$$

The percentage ration of the total solid contents of the composite cathode to the total volume represents the relative density ($\bar{\rho}$), and it can calculated by:

$$\bar{\rho} = \frac{\bar{V}_{LCO}+\bar{V}_{LLZO}}{V_{Total}} \quad (4)$$

2.3. Generation of microstructure

Analysis of the SEM images (Fig. 1 a) of the experimental microstructure allowed us to estimate the particle topologies, sizes, and relative volume fractions. The majority of LCO particles have a planar hexagonal shape, with a few spherical particles of LCO, whereas LLZO particles are spherical in shape. By theoretical analysis of SEM images of the experimental microstructure, and due to GeoDict restrictions, 8 discrete values of LCO and LLZO contents are selected. The estimated initial grain shapes, sizes, and relative volume fractions are listed in (Fig. 1c). In the modelled sample, the hexagonal shaped particles were primarily aligned horizontally to match the experimental finding [41]. The values of the microstructural parameters (solid volume fraction of LCO, Relative density and grain sizes of LCO and LLZO) were adopted to match the experimental microstructure after sintering. It is worth mentioning that the starting sizes in the simulation are not necessarily equal to the experimental starting particle size. A Python script embedded in GeoDict was used to generate the final experimental microstructure (Fig. 1e). The first step was to pile (to sediment) the particles from the positive z-direction in a domain size of 400×200×300 voxels (voxel length = 50 nm) using the initial particles in (Fig. 1b). The volume averaged diameter of LCO (d_{LCO}) and of LLZO (d_{LLZO}) are 2.00 µm and 1.41 µm, respectively, while the initial solid volume fraction of LCO is 69.4 %. To obtain a representative structure, the objects should be uniformly spread throughout the volume. Therefore, the distribution step is the second part of our process, which rearranges the objects until an internally homogenous structure is achieved. But at the +z and –z faces, some solid objects may aggregate or an empty areas occupied by pores may form. As a result, a non-representative structure will form, causing the necessity of eliminating these parts by cropping 50 voxels from each positive and negative direction of the z-direction, which is our third step. At the end of the cropping step, the structure was ready to be sintered with target value of the experimental relative density (93.14%). Owing to unbalanced grain growth during sintering and the cropping process after sintering, the values of the solid volume fraction of LCO and relative

density may change. The second phase of our loop is designed to check the difference between the actual and targeted values of both the solid volume fraction of LCO and relative density.

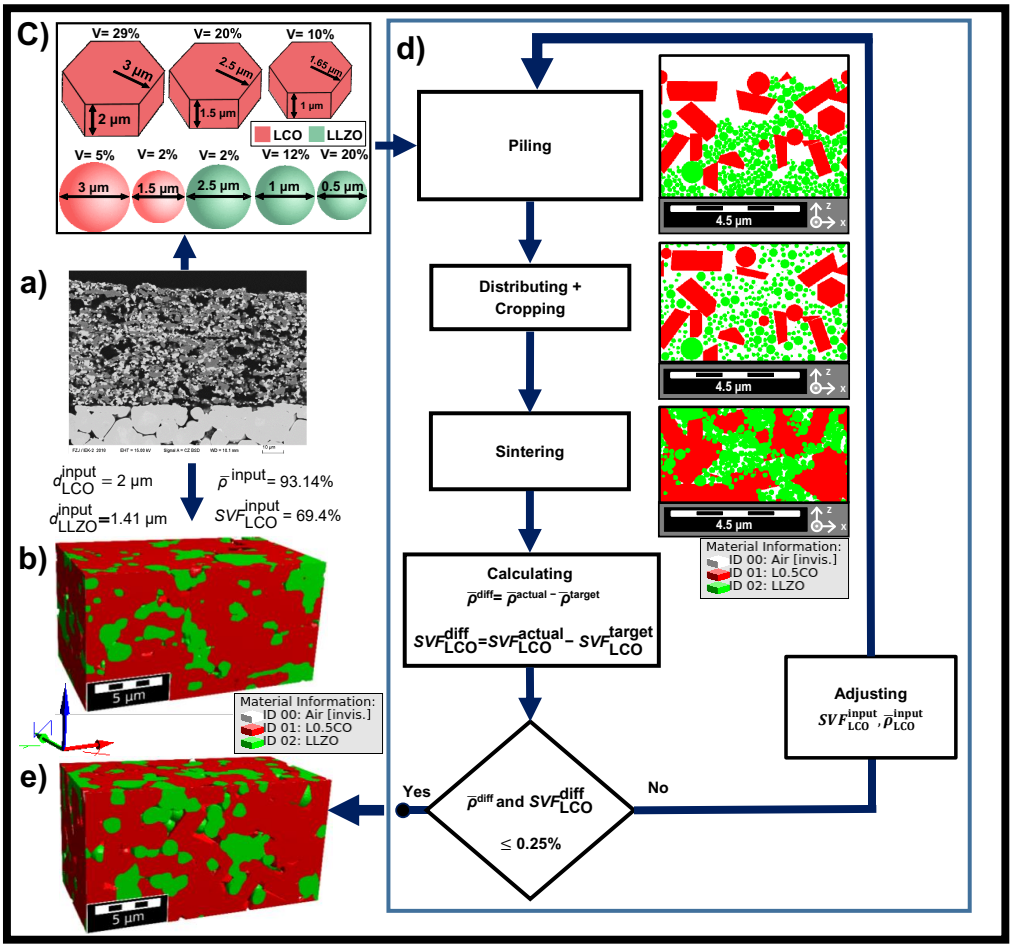

Fig. 1. a) SEM image of the experimental screen printed cathode, sintered $LiCoO_2$ (LCO - dark) $Li_7La_3Zr_2O_{12}$ (LLZO - bright) pores (black). b) Reconstructed structure. c) Initial sizes, volume fractions and types of piled grains of LCO and LLZO grains. d) The algorithm of generating a realistic microstructure. e) The regenerated microstructure, which mimic the experimental structure.

If the difference is larger than ± 0.25%, the script goes through the third phase, where the initial values of the solid volume fraction of LCO and the relative density are readjusted using DF-SANE (Derivative-Free Spectral Approach for solving nonlinear systems of equations) algorithm [64], and the process is restarted until the targeted values are achieved. The algorithm

used for the generation scripts is shown in (Fig 1 d). Figure 1e shows the regenerated structure with 400×200×200 voxels (voxel length = 50 nm).

2.4. Material parameters and constitutional equations for the simulation

In this study, we assume a homogenous delithiation process with negligible lithium concentration gradients, which corresponds to a low C-rate and a percolating network of both LCO and LLZO. The study's objectives did not encompass isolation effects, as the emphasis was on a functional battery investigation. It should be emphasized, nonetheless, that any isolated regions would exhibit minimal mechanical stress, indicating their electrochemical inactivity [65].

The mechanical calculations were based on the superimposition of electrochemically-induced and thermal strains, and were performed using a lithium concentration of 0.5 in LCO as the input parameter, as lower lithium concentrations are known to induce phase changes in LCO.

The calculations were performed taking into account the anisotropic property of LCO, with textured LCO crystals. To date, there are no experimental values for partially delithiated LCO. Thus, a stiffness matrix obtained from theoretical DFT calculations by Yamakawa et al. [43] had been adopted for our calculations.

$$C_{LCO} = \begin{bmatrix} 303.86 & 101.71 & 32.58 & 0 & 7.31 & 0 \\ 101.71 & 318.93 & 28.66 & 0 & -3.93 & 0 \\ 32.58 & 28.66 & 98.93 & 0 & 7.03 & 0 \\ 0 & 0 & 0 & 18.02 & 0 & -2.46 \\ 7.31 & -3.93 & 7.03 & 0 & 15.73 & 0 \\ 0 & 0 & 0 & -2.46 & 0 & 101.94 \end{bmatrix} \text{GPa} \quad (5)$$

LLZO does not exhibit anisotropic behavior due to its cubic crystal structure. The elastic modulus of LLZO was taken from literature as 146 GPa [66], and the experimental value for Poisson's ratio of ν_{LLZO}= 0.26 from [67,68] was used. When combining both materials in experimental sample preparation, this means that LCO shrinks anisotropic in the cooling phase after the high temperature sintering, LCO and much faster than LLZO because of the difference in thermal coefficient between LCO and LLZO [59], leading to the generation of internal thermal stresses in the final sample.

For the total electro-chemical strain, we consider all contributions mentioned above:

$$\varepsilon_{LCO} = \varepsilon_{LCO}^{Li} + \varepsilon_{LCO}^{El} + \varepsilon_{LCO}^{Th} \quad (6)$$

$$\varepsilon_{LLZO} = \varepsilon^{El}_{LLZO} + \varepsilon^{Th}_{LLZO} \quad (7)$$

Where: ε^{Li}, ε^{El} and ε^{Th} represent the total, lithiation, elastic and thermal strains of the LCO and LLZO phases, respectively.

The chemo-thermal strains ($\epsilon^{Chemo-thermal}$) (Table 1), are the sum of thermal and delithiation strains. The thermal strain values (ϵ^{Th}) of LCO and LLZO were obtained from our own experiments via in-situ high temperature X-ray diffraction (HT-XRD) between room temperature and 1000 °C are listed in Table 1.

Table 1 crystallographic strains for LCO in a-and c-axis during half delithiation and for LLZO

	Thermal ϵ^{Th}	Chemical [69] ϵ^{Li}	Chemo-thermal $\epsilon^{chemo-thermal}$
LCO (a axis)	-1.53×10^{-2}	-2.30×10^{-3}	-1.76×10^{-2}
LCO (c axis)	-2.36×10^{-2}	2.39×10^{-2}	2.38×10^{-4}
LLZO	-1.42×10^{-2}	0	-1.42×10^{-2}

During delithiation of LCO, the oxygen in the neighboring layers of the atomic structure exhibits a repulsive force, yielding a significant expansion along c-axis. In addition, LCO slightly shrink along a- and b-axis (Table1). This yields a +1.91% of volume change in good agreement with the value of +1.86% reported by Reimers et al. [53]. On the other hand, LLZO does not undergo under volume change during cycling since its Li content does not change.

The stress and conductivity computations were conducted using the ElastoDict FeelMath-LD and ConductoDict modules, respectively, within the GeoDict , Math2Market GmbH, Kaiserslautern, Germany software framework, which employs a conjugate gradient voxel-based solver [71,73] . Symmetric (Dirichlet) boundary conditions in all directions were used.

2.5. Variation of microstructural parameters

The effect of each microstructural design parameter (solid volume fraction of LCO, relative density and grain sizes of LCO and LLZO) should be studied separately, in order to obtain its individual impact on the stress distribution and the conductivity which can later be used to guide the experimental development. Therefore, we varied only one parameter each time, whereas the other parameters remained fixed. This is typically impossible to be achieved in experiments (here, e.g. a large grain size would result in lower density after the sintering process).

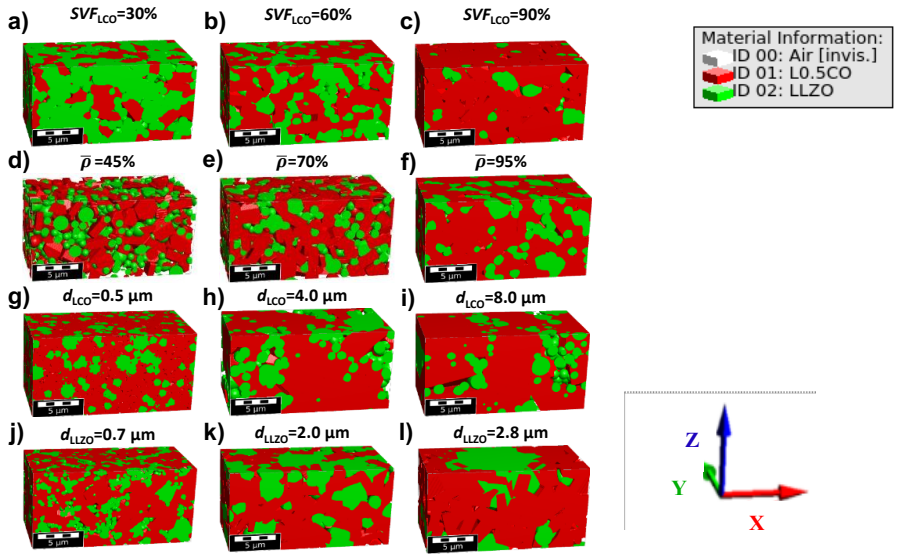

Fig. 2. a-c) variation of solid volume fraction of LCO only (30, 60 and 90%), d-f) variation of relative density only (45, 70 and 95%). g-i) variation of grain size of LCO only (0.5, 4.0 and 8.0 µm), j-l) variation of grain size of LLZO only (0.7, 2.00 and 2.8 µm).

The range for each parameter was set to cover the full range leading to reasonable cell (often already demonstrated experimentally), while also including the more extreme cases that cannot be accessed easily by experiments, allowing for predictive modelling. Fig. 2 shows some examples. The variation in the solid volume fraction of LCO ranged from 5 to 95%, while range from 33 to 66 % is the most reasonable for practical cells. The relative density was varied from 45% to 95% representing the typical values achieved for un-optimized free sintering (45–70 %) to optimized and pressure assisted sintering (80-95%). The range of variation for the grain sizes of LCO was varied by range of 4 from 0.5 µm to 8.0 µm and LLZO by range of 2 from 0.35 µm to 2.8 µm, representing the typical grain size distribution for the experimentally used powders. For each variation, we characterized each set in terms of mechanical stress and the conductivity (electronic for LCO and ionic for LLZO).

2.6. Analysis of governing parameters

In this work, we consider calculation of the following microstructural properties (chord length distribution, average inner diameter, interface area and relative conductivity) to compare between the mimicked and the experimental microstructures. Chord length distribution is considered as a measurement of the orientation of the grains. The average inner diameter of

solid phases serves as a measurement of grain size. During the volume change of the LCO, the adjacent LLZO contact area resists expansion. This drew our attention to the interface area between LCO and LLZO as a potential factor that may be the governing factor of the mechanical stresses of LCO and LLZO. Therefore, we introduce the "contact parameter *K*", which is defined as the ratio of the contact area between the two solid phases to the entire surface area of the solid content in the composite cathode. Until now, this parameter had not reported in the literature.

$$K = \frac{A_{LCO/LLZO}}{A_{LCO/Pore} + A_{LLZO/Pore} + A_{LCO/LLZO}} \quad (8)$$

Where $A_{LCO/LLZO}$ is the interface area between LCO and LLZO, $A_{LCO/pore}$ is the interface area between LCO and pore and $A_{LLZO/pore}$ is the interface area between LLZO and pore.

The volume fraction of the solid content in the composite cathode is playing a great role for reducing the stress as it going to be shown later, which is different from the effect of the contact area percentage ratio. Therefore we define the "relative contact parameters" K_{LCO} and K_{LLZO} as governing factor of the mechanical stress in LCO and LLZO respectively.

$$K_{LCO} = \frac{K}{\bar{V}_{LCO}} \quad (9)$$

$$K_{LLZO} = \frac{K}{\bar{V}_{LLZO}} \quad (10)$$

Determining the governing factors K_{LCO} and K_{LLZO} can serve to predict the stress values in the composite cathode without needs for modelling.

In addition, we inspected the physical properties of the microstructure; relative conductivity of the solid phases is to be defined as the ratio of the conductivity of the phase in the framework (LCO or LLZO) to the bulk conductivity of that phase.

$$\text{Relative conductivity} = \frac{\text{conductivity of phase framework}}{\text{bulk conductivity}} \quad (11)$$

In addition, we calculated the maximum principal stress Smax, which had been introduced by Mücke et al. [41]. In our calculations, the "error bars" represent the width of distribution.

The mechanical stress in mixed cathode is calculated by both equilibrium equation (equation 12) and kinematic equation (equation 13) [70]:

$$div\left(C(\epsilon)\right) = 0 \quad (12)$$

$$\epsilon = E + (\nabla u + (\nabla u)^T/2 \quad (13)$$

Where C is the stress tensor (GPa), ϵ is the strain tensor, E is the macroscopic strain tensor and u is the displacement vector (m)

While the electronic and ionic conductivities of LCO and LLZO respectively, are calculated by Ohm's law (equation 14) and Poisson equation (equation 15) [72]:

$$j = -\sigma\nabla\phi \quad (14)$$

$$\nabla.(\sigma_c\nabla\phi) = 0 \quad (15)$$

Where j is the current density (A/m^3), σ is the effective electrical conductivity (S/m), ϕ is the electrical potential (V) and $\sigma_c$is the local electrical conductivity (S/m).

3. Result and discussion

3.1. Validation of reproduced structure

A comparison between the reproduced and the experimental structures in terms of their physical, electrochemical and microstructural properties was performed to validate the reproduction of the experimental structure. The average inner diameters of LCO and LLZO in the reproduced structure almost matched those of the experimental structure (Fig. 3 a, b).

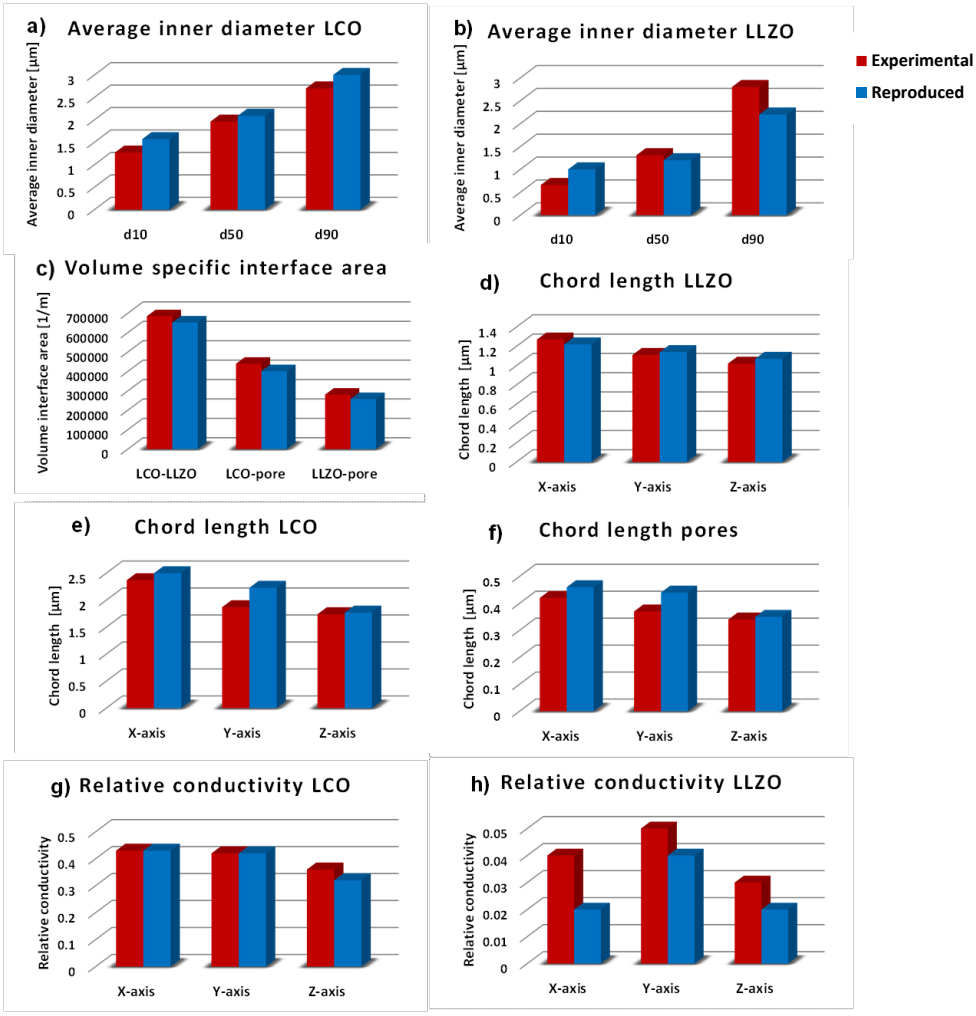

Fig. 3. Average inner diameter of LCO (a) and LLZO (b), c) volume interface area ration between the contents of the mixed cathode, chord length of LLZO (d), LCO (e) and pores (f), the relative electronic conductivity of LCO (g) and the relative ionic conductivity of LLZO (h).

The sintering process in GeoDict does not perfectly mimic a realistic sintering process. It utilizes the Voronoi tessellation process for sintering [74]. Hence, in contrast to real sintering, both phases grow until they reach an interface. This can explain the slight difference between the grain sizes of LCO and LLZO in the regenerated structure compared to the experimental structure. However, we consider the slightly differing results as a successful match regarding the grain sizes. In free standing mixed cathode of all-solid-state batteries, the presence of LLZO in the framework resists the expansion of LCO during delithiation, causing stresses in the solid

phases. The mechanical interaction between LCO and LLZO during the volume change of LCO is determined by the interface area between the contents of the microstructure, where the interface area between LCO and LLZO is the source of mechanically induced stress. The presence of pores reduces the stress magnitude. (Fig 3.c), indicates a successful match between the interface areas of the reproduced and experimental structures. The slight mismatch is ascribed to the sintering algorithm utilized in GeoDict, where LCO grains expand during the sintering process which also affect the conductivities as we will discuss later. The mechanical and electronical behaviors of a structure are affected by its texture. Particle's chord length represents the alignment of the grains in the structure. For the spherical LLZO particles, a successful match of the chord length between the regenerated and experimental structures was observed (Fig. 3 d). The chord length of LCO in the regenerated structure was higher than that in the experimental (Fig. 3 e). This indicates that the hexagonal LCO particles in the experimental structure were more oriented than the regenerated ones. It is difficult to mimic the alignment of hexagonal LCO in an experimental structure. The similar deviation trend between the pore's chord length distribution (Fig. 3 f), and chord length of LCO implies that the alignment of hexagonal LCO dictates the alignment of pores. The conductivity of the solid phases in the structure is considered as one of the important property. Conductivities in the z-direction is particularly relevant due to the major transportation of electrons and ions through the layers. We observed a perfect match between the electronic conductivity in the regenerated and experimental structure in both the x- and y-axes, whereas there was a slight difference in the z-axis (Fig.3 g). The small absolute deviation between the relative ionic conductivity of LLZO in the regenerated structure and the experimental value (Fig 3 h) is ascribed to the slightly cut of the percolation path of LLZO due to the expansion of LCO grains during sintering. Furthermore, the matching of the conductivities implies a low impact of the grain's alignment in the structure. In conclusion, we were able to achieve a successful mimicking of the experimental structure, since the physical, electrochemical and microstructural properties of the reconstructed structure are very close to those of the experimental structure.

3.2. Mechanical stress

The distribution of principal stresses with maximum absolute value is illustrated in Figure 4 a, which indicates that LCO experiences compressive stress, whereas LLZO undergoes tensile stress. Certain areas exhibit stress inversions, with LCO suffering from tensile stress and LLZO

enduring compressive stress. The results show that the in vicinity of grain boundaries higher stress levels are concentrated as there the chemo-thermal strain differences can be very high. After cooling down after sintering, LCO suffers from positive (tensile) stress, whereas LLZO suffers from negative (compressive) stress Fig. 4 b. The reverse trend is observed for the delithiation process, as LCO tends to expand and is constrained by the adjacent solid LLZO in the framework, yielding compressive stress for LCO and tensile stress for LLZO (Fig. 4 c). For the total stress (chemo-thermal), combining both contributions, the stresses from delithiation are higher than the thermal stresses hence, the total stress is compressive for LCO and tensile for LLZO (Fig. 4 d). In all three cases (thermal, chemical, and chemo-thermal), a stress inversion appears for both LCO and LLZO. It is a result of the fact that the thermal and chemical strains of LCO along the a- axis are greater than the thermal and chemical strains of LLZO (which in turn are greater than the thermal and chemical strains along its LCO in c-axis).

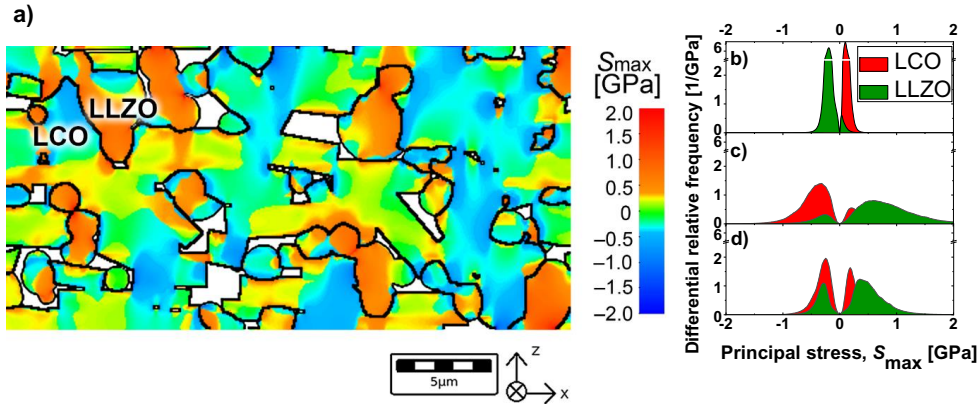

Fig. 4 a) Example slice of the stress distribution (principle stress with maximum absolute value) where d_{LCO}= 2.00 µm, d_{LLZO}= 1.41 µm, SVF_{LCO} = 69.4 % and $\bar{\rho}$ = 90% Histograms of the maximum principal stress of the same structure for thermal (b) chemical (c) and chemo-thermal (d) stresses.

3.2.1. Solid volume fraction of LCO

The ratio of the active material to the solid electrolyte in the composite cathode is the parameter which governs the capacity of the cell. Sintering process is achieved thermally by heating up to 1050°C.

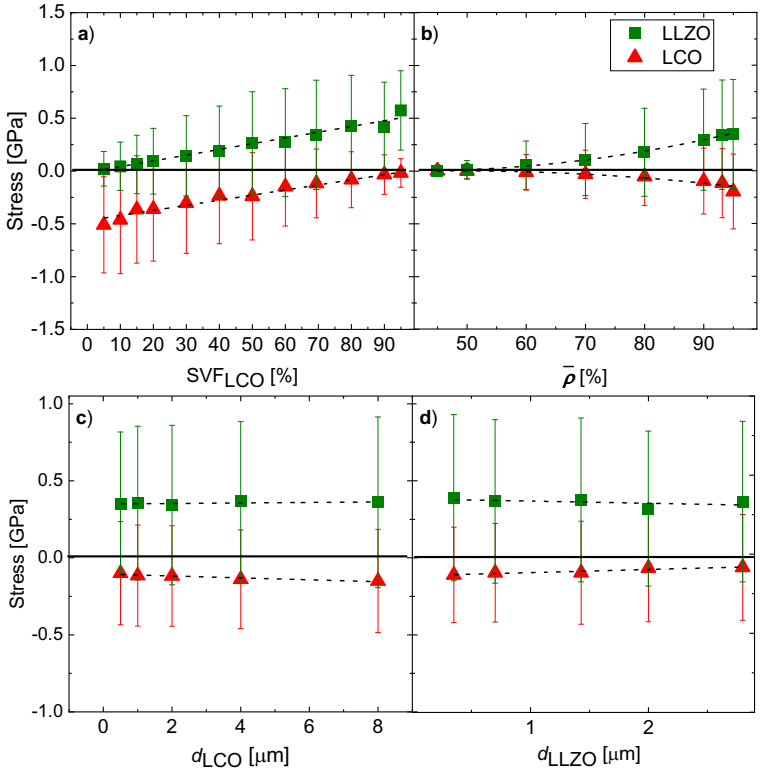

Fig.5. Principal stress values (chemo-thermal) for LCO and LLZO as a function of: a) solid volume fraction of LCO, b) relative density, c) initial grain size of LCO and d) initial grain size of LLZO. Error bars represent the width of distribution. The not varied parameters values were as follow: SVF_{LCO} = 69.4%, $\bar{\rho}$ = 39.14%, d_{LCO} = 2.00µm and d_{LLZO} = 1.41µm

When the solid volume fraction of LCO is 0%, bulk LLZO is formed; hence, no stress on LLZO occurs. When the solid volume fraction of LCO is slightly higher than 0% (SVF_{LCO} = 5%), a compressive chemo-thermal stress of 510 MPa starts to appear (Fig. 5 a). On the other hand, the LLZO experiences low tensile stress of about 20 MPa. The compressive stress in LCO gradually decreases to 18 MPa while the solid volume fraction of LCO approaches 100 %. In turn, the tensile stress in LLZO gradually increases and reaches its highest value 574 MPa ascribed to the expansion of LCO through the delithiation process. When the Solid fraction of LCO is 100%, bulk LCO emerges, hence no constraint in the cathode, leading to vanishing of compressive stress in LCO. In general, the stress curves with respect to variation of solid volume fraction of LCO are showing the same linear progression for LCO and LLZO. The direct relationship between the solid volume fraction of LCO and the stresses values will be

explained with a simple physical model showing that the stress in LCO is depends directly to the volume fraction of LLZO. On the other hand, the stress in LLZO directly depends on the volume fraction of LCO, which agree with the simulated results (Fig. S1 b).

3.2.2. Relative density

When the structure is highly porous ($\bar{\rho}$ = 45%), a very low chemo-thermal principal stresses (–0.64 MPa and 2.5 MPa for LCO and LLZO, respectively) appears (Fig. 5 b). The presence of pores lowers the particle coordination number. Hence, the volume of the LCO can freely change during delithiation. On the other hand, for a very dense structure, the chemo-thermal principal stresses in LCO and LLZO increase (–197 and 348MPa for LCO and LLZO, respectively). Subsequently, higher particle coordination number values increase the degree of constraint that hinders the expansion of LCO, causing a progressive increase in the absolute values of stresses in LCO and LLZO. Increasing the density reduces the strain tolerance of the microstructure owing to a lack of pores. However, the stress values are less sensitive to varying relative density compared to the variation in the solid volume fraction of LCO.

3.2.3. Grain size

Our investigation found that the stress is not much dependent on the grain sizes of LCO and of LLZO. A slight increase in the chemo-thermal principal stresses is observed for LCO (–100 to –150 MPa), whereas almost no effect on the chemo-thermal principal stresses of LLZO (350 to 360 MPa) is seen with increasing LCO grain size while fixing the other parameters fixed (SVFLCO= 69.4%, $\bar{\rho}$= 93.14% and D_{LLZO}= 1.41µm) (Fig. 5 c). For smaller LCO grain sizes, the population of LCO grains has been increased to maintain the solid volume fraction of LCO at 69.4%. This gives them more freedom to expand during delithiation and hence reduces the stress on the LCO grains. Vice versa, increasing the grain size of LCO decreases its grain population. Hence, the LCO particles expands only toward LLZO, causing an increase in stress. This is already a first guideline for a possible optimization strategy for mixed cathodes, providing some internal pore space for LCO expansion. Varying the grain size of LCO did not affect the fraction of the LLZO area, which in turn keep the stress on LLZO almost constant.

By increasing the grain size of LLZO while fixing the other parameters fixed (SVFLCO= 69.4%, $\bar{\rho}$= 93.14% and D_{LCO}= 2.00 µm), a slight decrease in the chemo-thermal principal stresses for both LCO (–132 to –84 MPa) and LLZO (357 to 332 MPa) is observed (Fig. 5 d). The smaller the grain size of LLZO, the greater the population of LLZO, which constrains the

expansion of LCO during delithiation. Hence, higher compressive and tensile stresses are observed for LCO and LLZO, respectively. However, while increasing the grain size of LLZO, its population is reduced, leaving more area for LCO to expand freely. This, in turn, decreases the stress of both solid phases in the composite cathode. In conclusion, larger LLZO particles and smaller LCO particles are providing a slight advantage in terms of mechanical stress distribution.

Based on the aforementioned, it can be deduced that any gradients in grain size over the thickness of wet chemical layers, which may occur due to sedimentation during the drying process after tape casting, do not alter the stress and strain distribution as long as the phase ratio of the two powder components in the composite cathode does not change over the thickness. If the phase ratio is not constant, a stress gradient can be expected.

3.2.4. Impact of the relative contact parameter K

- ***Impact of K_{LLZO}***

K_{LLZO} gradually increases for varying both the solid volume fraction of LCO and the relative density. Increasing the grain size of LCO and LLZO slightly increases and decreases the values of K_{LLZO}, respectively (Fig. S2). When plotting the mean tensile stress of LLZO vs. K_{LLZO} ratio (Fig. 6 a), a common trend can be observed for all microstructural parameters. The lower value of the volume fraction of LLZO while increasing the solid volume fraction of LCO increases K_{LLZO}, which yields larger tensile stress on LLZO even for lower contact area ratio between LCO and LLZO when the solid volume fraction of LCO is greater than 50%.

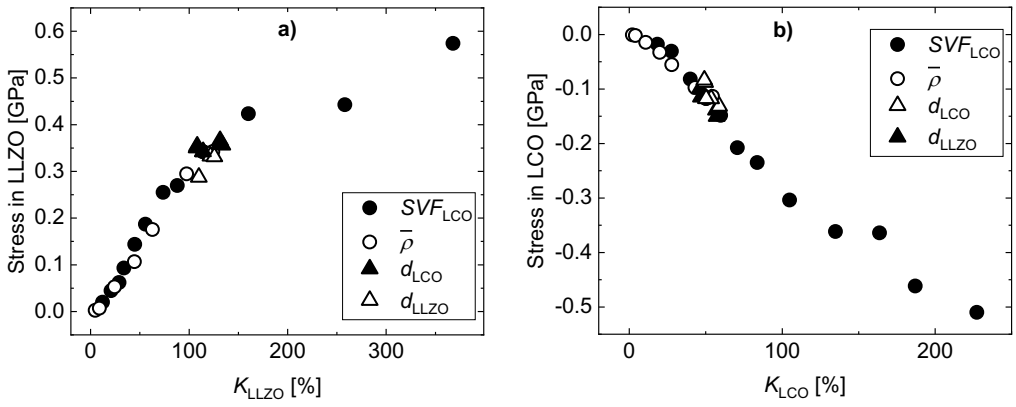

Fig. 6. Principal stress (chemo-thermal) as a function of: K_{LLZO} (a) and K_{LCO} (b) for solid volume fraction of LCO, relative density, grain size of LCO and grain size of LLZO.

Increasing the volume fraction of LLZO while increasing the relative density was not able to overcome the effect of the higher particle coordination number and under similar condition of low volume fraction of LLZO. Which in turn increases the value of K_{LLZO} and hence, increases the tensile stress in LLZO. With constant volume fraction of LLZO while varying the grain sizes of LCO and LLZO, the slight change in the contact area ration between LCO and LLZO was not sufficient enough to cause a significant change on the K_{LLZO} values, and hence non observable variation on the tensile stress values in LLZO.

- ***Impact of K_{LCO}***

K_{LCO} is gradually and slightly decreased while increasing the solid volume fraction of LCO and the grain size of LLZO respectively. But it gradually and slightly increases while varying the relative density and the grain size of LCO, respectively (Fig. S2).

The common trend is also observed for the variation of all the microstructural design parameters when plotting the mean compressive stress of LCO vs. K_{LCO} (Fig. 6 b). The higher volume fraction and lower contact area between LCO and LLZO were the main reason of decreasing K_{LCO} and hence lowering the compressive stress in LCO while increasing the solid volume fraction of LCO. Higher values of K_{LCO} while varying the relative density is ascribed to the higher coordination number, and hence, increasing the compressive stress in LCO. Once again, the slight change of the contact area between LCO and LLZO was not significant enough to affect the values of K_{LCO} while varying the grain size of LCO and LLZO. Hence, less observable effect on the compressive stress in LCO.

For all variations of microstructural parameters (solid volume fraction of LCO, relative density and grain sizes of LCO and LLZO), relative contact area K_{LCO} and K_{LLZO} were calculated. Instead of plotting the stresses against the individual microstructural parameters, they were plotted together against these relative contact parameters, as the points fall on a common line, the stresses solely depend on these introduced parameters, which hence can be considered as governing factors.

3.3. Conductivity

3.3.1. Solid volume fraction of LCO

As the solid volume fraction of LCO increases, continuous path LCO phase forms at the expense of the percolation path through LLZO, which suffers from discontinuities. Hence, the relative electronic conductivity of LCO in the z-direction increased from 0.00 to 0.78 (Fig. 7a), whereas the relative ionic conductivity of LLZO in the z-direction decreased from 0.76 to 0.00 (Fig. 7a). However, even for the almost bulk LCO, it cannot reach full conductivity since the composite cathode still exhibits a porosity about 7% ($\bar{\rho}$ ≅93%). The reverse behavior occurs for lower values of the solid volume fraction of LCO, where almost bulk LLZO forms. The symmetry of the curve of the relative conductivity of LLZO with respect to the LCO curve indicates that the microstructures of the LLZO and LCO phases behave similarly with respect to conductivity.

The electronic conductivity of LCO is 1×10^{-3} S/cm [75], while the ionic conductivity of LLZO is about 1×10^{-4} S/cm [76]. Hence the performance will be limited by LLZO.

3.3.2. Relative density

Increasing the relative density while keeping the values of the solid volume fraction of LCO and grain sizes of LCO and LLZO fixed (69.4%, 2.00 µm and 1.41 µm respectively), enhanced the relative electronic conductivity of LCO from 0.003 to 0.43, whereas the relative ionic conductivity of LLZO only increased from 0.0 to 0.03 (Fig. 7b).

The increase in the electronic conductivity of LCO is attributed to the increase in both the particle coordination number and volume ratio for both phases, which are positively affected by the relative density and, in turn, increase the effective cross-sectional area for ionic and electronic conductivity. However, the low conductivity of LLZO is considered as a bottleneck, which is ascribed to the formation of ionically insulated islands of the cathode active material (LCO). Therefore, the relative density cannot be used for stress-reduction in the considered LCO: LLZO = 2:1 composite without losing the ionic conductivity.

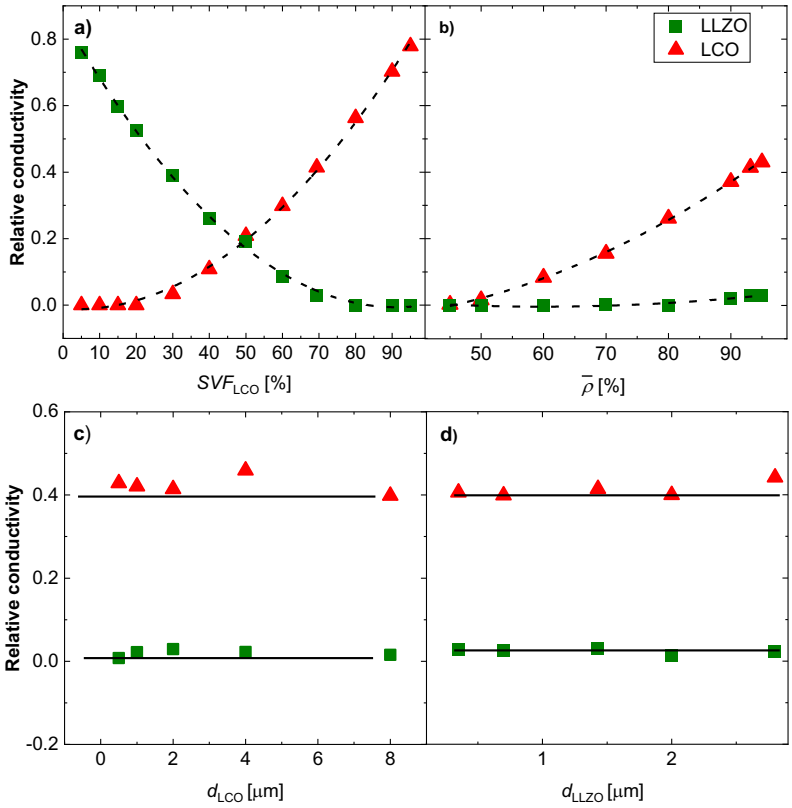

Fig.7. Relative electronic conductivity of LCO and relative ionic conductivity of LLZO as a function of: solid volume fraction of LCO (a), relative density (b), grain size of LCO (c) and grain size of LLZO (d). The not varied parameters values were as follow: SVF_{LCO} = 69.4%, $\bar{\rho}$ = 39.14%, d_{LCO} = 2.00µm and d_{LLZO} = 1.41µm

3.3.3. Grain size

Both relative electronic and ionic conductivities of LCO and LLZO, respectively, were not affected by varying the grain size of LCO (from 0.43 to 0.40 for LCO and from 0.01 to 0.02 for LLZO) (Fig. 7c). In section 3.2.3, we showed that the contact area between LCO and LLZO was almost unaffected by varying the grain size of LCO. Hence, there was no expected effect on either the electronic conductivity of LCO or the relative ionic conductivity of LLZO. Froboese et al. [77] concluded that larger active material increases the ionic conductivity, they explained this behavior by a blockage of ions pathways when the grain size of the active material is lower since these smaller grains will be more distributed in the system. We believe that this explanation is insufficient. For large active material grains, a low number of conduction pathways having a large area exist, leading to certain total resistance value. However, the same value for the total resistance can be achieved also for smaller particle sizes, having smaller

areas, if the number of pathways is increased, i.e. not changing the solid volume fraction of LCO. This explanation applies also on varying the grain size of LLZO (from 0.42 to 0.44 for LCO and from 0.03 to 0.02 for LLZO) (Fig. 7d).

3.3.4. G*overning factor*

The volume fractions of LCO and LLZO are the major factors affecting the relative conductivity (Fig. 8). All individual values obtained by the different variations fall on a single line, which shows that by varying the solid volume fraction of LCO and relative density, the change in the relative volume fraction of LCO to the total volume is the determining factor. Hence, we can consider the volume fractions of LCO and LLZO as the governing factors for the relative conductivities of LCO and LLZO, respectively.

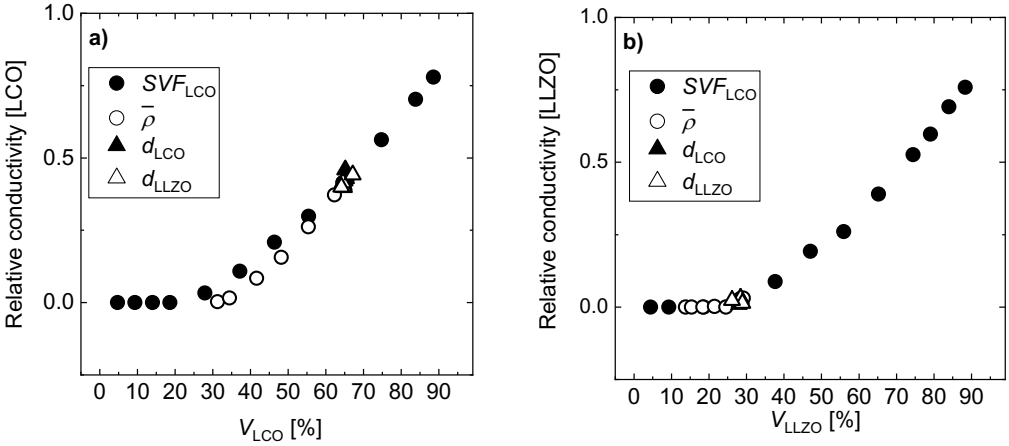

Fig.8. a) relative electronic conductivity of LCO as a function of volume fraction of LCO, b) relative ionic conductivity of LLZO as a function of volume fraction of LLZO, both a) and b) include the variation of solid volume fraction of LCO, relative density, and the grain size.

4. Conclusions

This work was based on the generation and validation of a realistic composite cathode microstructure for all-solid-state lithium-ion batteries. The distribution of chord lengths is sensitive to the orientation and shape of the grains. Moreover, the shape and orientation of the non-spherical grains dictate the orientation and shape of the pores in the system. This Agrees well with reconstructed microstructures from experimental all-soli-state cells.

We studied the effect of four microstructural design parameters (solid volume fraction of LCO, relative density, and grain sizes of LCO and LLZO) on the mechanical stresses (thermal, mechanical, and chemo-thermal) and conductivities. Consideration of the anisotropic properties of LCO is crucial for investigating the realistic behavior of layered structures. In our model, LCO and LLZO based composite cathodes were considered free-standing. The key factor in such free-standing composite cathodes is the presence of LLZO, which constrains the volume change of LCO. During cool down after high temperature sintering, the mismatch in thermal expansion coefficient between LCO and LLZO created tensile stress in LCO and compressive stress in LLZO. During the delithiation process of LCO, the stress profiles of LCO and LLZO were inverted and approximately two times greater than the thermal stresses. Thus, the resulting net chemo-thermal stress was half the chemical stress. A linear relationship was observed between the stresses of the composite cathode contents (LCO and LLZO) and their conductivities with the variation in the LCO/LLZO ratio, whereas they progressively varied with the relative density. Furthermore, we did not observe any effect on either the stress values or the conductivities by varying the grain sizes of LCO and LLZO while keeping fixed values of other parameters (solid volume fraction of LCO and relative density). The ratio between the contact area between the solid phases in the system to the summation of their total area and their volume fraction (relative contact parameters K_{LCO} and K_{LLZO}), were found to be the governing factor that controlled the stress values when varying the microstructural design parameters. The volume fractions of the solid contents were considered as the governing factors for the conductivities under the variation of all microstructural design parameters. In addition, varying the relative density did not lower the stresses in the composite cathode of 2:1 LCO: LLZO because it cause a breakdown in the ionic conductivity of the LLZO phase.

In this research, we did not take into account the effect of the grain boundaries for the calculation of conductivities which should be taken in account in future.

Further work should focus on the effect of particle morphology on the stresses and their conductivities. We suggest utilizing LLZO fibers in the system to enhance effective ionic conductivity. Furthermore, an investigation of the effect of combining LLZO as a solid electrolyte and other layered-structure active materials (NMC) on the composite cathode properties should be conducted and the experimentally feasible variations of microstructural parameters studied.

Conflicts of interest

The author declare no known competing financial interests or personal relationships that could have appeared to influence the work reported in this paper.

Acknowledgements

The financial support provided by the Federal Ministry of Education and Research of Germany in the framework of the Palestinian-German Science Bridge (PGSB) (BMBF Grant Number 01DH16027), FestBatt2-Oxide (grant no. 13XP0434A) and Meet-HiEnD III (grant no. 03XP0258C) is gratefully acknowledged.

References

[1] B. B. Owens and P. M. Skarstad, Ambient-Temperature Solid-State Batteries, Solid State Ionics 53 (1992) 665-72. https://doi.org/10.1016/0167-2738(92)90444-T.

[2] X. Y. Yao, B. X. Huang, J. Y. Yin, G. Peng, Z. Huang, C. Gao, D. Liu, and X. X. Xu, All-solid-state lithium batteries with inorganic solid electrolytes: Review of fundamental science, Chinese Physics B 25[1] (2016). https://doi.org/10.1088/1674-1056/25/1/018802.

[3] J. Janek and W. G. Zeier, A Solid Future for Battery Development, Nat Energy 1 (2016) 16141. https://doi.org/10.1038/nenergy.2016.141.

[4] Z. Gao, H. Sun, L. Fu, F. Ye, Y. Zhang, W. Luo, and Y. Huang, Promises, challenges, and recent progress of inorganic solid-state electrolytes for all-solid-state lithium batteries, Adv. Mater. (Weinheim, Ger.) 30[17] (2018) 1705702. https://doi.org/10.1002/adma.201705702.

[5] C. W. Sun, J. Liu, Y. D. Gong, D. P. Wilkinson, and J. J. Zhang, Recent advances in all-solid-state rechargeable lithium batteries, Nano Energy 33 (2017) 363-86. https://doi.org/10.1016/j.nanoen.2017.01.028.

[6] V. Thangadurai and W. Weppner, Recent progress in solid oxide and lithium ion conducting electrolytes research, Ionics 12[1] (2006) 81-92. https://doi.org/10.1007/s11581-006-0013-7.

[7] J. G. Kim, B. Son, S. Mukherjee, N. Schuppert, A. Bates, O. Kwon, M. J. Choi, H. Y. Chung, and S. Park, A review of lithium and non-lithium based solid state batteries, J. Power Sources 282 (2015) 299-322. https://doi.org/10.1016/j.jpowsour.2015.02.054.

[8] Y. Kato, S. Hori, T. Saito, K. Suzuki, M. Hirayama, A. Mitsui, M. Yonemura, H. Iba, and R. Kanno, High-power all-solid-state batteries using sulfide superionic conductors, Nat Energy 1[4] (2016) 1-7. https://doi.org/10.1038/nenergy.2016.30.

[9] J. Wu, L. Shen, Z. Zhang, G. Liu, Z. Wang, D. Zhou, H. Wan, X. Xu, and X. Yao, All-solid-state lithium batteries with sulfide electrolytes and oxide cathodes, Electrochemical Energy Reviews 4 (2021) 101-35. https://doi.org/10.1007/s41918-020-00081-4.

[10] T. Yang, J. Zheng, Q. Cheng, Y. Y. Hu, and C. K. Chan, Composite Polymer Electrolytes with $Li_7La_3Zr_2O_{12}$ Garnet-Type Nanowires as Ceramic Fillers: Mechanism of Conductivity Enhancement and Role of Doping and Morphology, ACS Appl. Mater. Interfaces 9[26] (2017) 21773-80. https://doi.org/10.1021/acsami.7b03806.

[11] F. Aguesse, W. Manalastas, L. Buannic, J. M. Lopez del Amo, G. Singh, A. Llordés, and J. Kilner, Investigating the dendritic growth during full cell cycling of garnet electrolyte in direct contact with Li metal, ACS Appl. Mater. Interfaces 9[4] (2017) 3808-16. https://doi.org/10.1021/acsami.6b13925.

[12] R. H. Basappa, T. Ito, T. Morimura, R. Bekarevich, K. Mitsuishi, and H. Yamada, Grain boundary modification to suppress lithium penetration through garnet-type solid electrolyte, J. Power Sources 363 (2017) 145-52. https://doi.org//10.1016/j.jpowsour.2017.07.088.

[13] A. Sharafi, H. M. Meyer, J. Nanda, J. Wolfenstine, and J. Sakamoto, Characterizing the Li–$Li_7La_3Zr_2O_{12}$ interface stability and kinetics as a function of temperature and current density, J. Power Sources 302 (2016) 135-39. https://doi.org/10.1016/j.jpowsour.2015.10.053.

[14] S. Wenzel, T. Leichtweiss, D. Krüger, J. Sann, and J. Janek, Interphase formation on lithium solid electrolytes—An in situ approach to study interfacial reactions by photoelectron spectroscopy, Solid State Ionics 278 (2015) 98-105. https://doi.org/10.1016/j.ssi.2015.06.001.

[15] P. Bron, B. Roling, and S. Dehnen, Impedance characterization reveals mixed conducting interphases between sulfidic superionic conductors and lithium metal electrodes, J. Power Sources 352 (2017) 127-34. https://doi.org//10.1016/j.jpowsour.2017.03.103.

[16] S. Wenzel, S. Randau, T. Leichtweiß, D. A. Weber, J. Sann, W. G. Zeier, and J. r. Janek, Direct observation of the interfacial instability of the fast ionic conductor Li10GeP2S12 at the lithium metal anode, Chem. Mater. 28[7] (2016) 2400-07. https://doi.org//10.1021/acs.chemmater.6b00610.

[17] A. Bates, S. Mukherjee, N. Schuppert, B. Son, J. G. Kim, and S. Park, Modeling and simulation of 2D lithium-ion solid state battery, Int J Energ Res 39[11] (2015) 1505-18. https://doi.org/10.1002/er.3344.

[18] G. Bucci, T. Swamy, S. Bishop, B. W. Sheldon, Y.-M. Chiang, and W. C. Carter, The effect of stress on battery-electrode capacity, J. Electrochem. Soc. 164[4] (2017) A645. https://doi.org//10.1149/2.0371704jes.

[19] G. Bucci, T. Swamy, Y.-M. Chiang, and W. C. Carter, Modeling of internal mechanical failure of all-solid-state batteries during electrochemical cycling, and implications for battery design, J Mater Chem A 5[36] (2017) 19422-30. https://doi.org/10.1039/C7TA03199H.

[20] A. Mukhopadhyay and B. W. Sheldon, Deformation and stress in electrode materials for Li-ion batteries, Progress in Materials Science 63 (2014) 58-116. https://doi.org/10.1016/j.pmatsci.2014.02.001.

[21] Y. He, C. Lu, S. Liu, W. Zheng, and J. Luo, Interfacial Incompatibility and Internal Stresses in All-Solid-State Lithium Ion Batteries, Adv Energy Mater 9[36] (2019) 1901810. https://doi.org/10.1002/aenm.201901810.

[22] P. Li, Y. B. Zhao, Y. X. Shen, and S. H. Bo, Fracture behavior in battery materials, J Phys-Energy 2[2] (2020). https://doi.org//10.1088/2515-7655/ab83e1.

[23] K. Mukai, Zero-Strain Insertion Materials for All-Solid-State Li-Ion Batteries, pp. 219-40. in Solid Electrolytes for Advanced Applications. Springer, 2019.

[24] F. Strauss, L. de Biasi, A. Y. Kim, J. Hertle, S. Schweidler, J. Janek, P. Hartmann, and T. Brezesinski, Rational Design of Quasi-Zero-Strain NCM Cathode Materials for Minimizing Volume Change Effects in All-Solid-State Batteries, Acs Mater Lett 2[1] (2020) 84-88. https://doi.org/10.1021/acsmaterialslett.9b00441.

[25] K. Mukai, Pseudo zero-strain insertion materials for Li-ion batteries: cross-sectional observations of $LiNi_{1/2}Co_{1/2}O_2$, $LiNi_{1/3}Co_{1/3}Mn_{1/3}O_2$, and $LiNi_{0.8}Co_{0.15}Al_{0.05}O_2$, Ionics 24[8] (2018) 2181-86. https://doi.org/10.1007/s11581-017-2385-2.

[26] R. Koerver, W. Zhang, L. de Biasi, S. Schweidler, A. O. Kondrakov, S. Kolling, T. Brezesinski, P. Hartmann, W. G. Zeier, and J. Janek, Chemo-mechanical expansion of lithium electrode materials–on the route to mechanically optimized all-solid-state batteries, Energ Environ Sci 11[8] (2018) 2142-58. https://doi.org//10.1039/C8EE00907D

[27] Y. Wang, D. Dang, D. Li, J. Hu, and Y.-T. Cheng, Influence of polymeric binders on mechanical properties and microstructure evolution of silicon composite electrodes during electrochemical cycling, J. Power Sources 425 (2019) 170-78. https://doi.org/10.1016/j.jpowsour.2019.04.006.

[28] D. Li, Y. Wang, J. Hu, B. Lu, D. Dang, J. Zhang, and Y.-T. Cheng, Role of polymeric binders on mechanical behavior and cracking resistance of silicon composite electrodes during

electrochemical cycling, J. Power Sources 387 (2018) 9-15. https://doi.org/10.1016/j.jpowsour.2018.03.048.

[29] G. Liu, H. Zheng, S. Kim, Y. Deng, A. Minor, X. Song, and V. S. Battaglia, Effects of various conductive additive and polymeric binder contents on the performance of a lithium-ion composite cathode, J. Electrochem. Soc. 155[12] (2008) A887. https://doi.org/10.1149/1.2976031.

[30] B. Ludwig, Z. Zheng, W. Shou, Y. Wang, and H. Pan, Solvent-free manufacturing of electrodes for lithium-ion batteries, Sci Rep-Uk 6[1] (2016) 1-10. https://doi.org/10.1038/srep23150.

[31] D. Hung-Cuong, M. Sun-il, and Y. In-Hyeong, Electrochemical Analysis of Conductive Polymer-Coated LiFePO4 Nanocrystalline Cathodes with Controlled Morphology, Electroanalysis 23[9] (2011) 2079-86. https://doi.org/10.1002/elan.201100222.

[32] V. Malave, J. R. Berger, H. Y. Zhu, and R. J. Kee, A Computational Model of the Mechanical Behavior within Reconstructed Li_xCoO_2 Li-ion Battery Cathode Particles, Electrochim. Acta 130 (2014) 707-17. https://doi.org/10.1016/j.electacta.2014.03.113.

[33] R. E. Garcıa, Y.-M. Chiang, W. C. Carter, P. Limthongkul, and C. M. Bishop, Microstructural modeling and design of rechargeable lithium-ion batteries, J. Electrochem. Soc. 152[1] (2004) A255. https://doi.org/10.1149/1.1836132.

[34] L. Wu, Y. Wen, and J. Zhang, Three-Dimensional Finite Element Study on Li Diffusion Induced Stress in FIB-SEM Reconstructed $LiCoO_2$ Half Cell, Electrochim. Acta 222 (2016) 814-20. https://doi.org/10.1016/j.electacta.2016.11.042.

[35] L. Wu, X. Xiao, Y. Wen, and J. Zhang, Three-dimensional finite element study on stress generation in synchrotron X-ray tomography reconstructed nickel-manganese-cobalt based half cell, J. Power Sources 336 (2016) 8-18. https://doi.org/10.1016/j.jpowsour.2016.10.052.

[36] H. Mendoza, S. A. Roberts, V. E. Brunini, and A. M. Grillet, Mechanical and Electrochemical Response of a $LiCoO_2$ Cathode using Reconstructed Microstructures, Electrochim. Acta 190 (2016) 1-15. https://doi.org//10.1016/j.electacta.2015.12.224.

[37] C. Lim, B. Yan, L. L. Yin, and L. K. Zhu, Simulation of diffusion-induced stress using reconstructed electrodes particle structures generated by micro/nano-CT, Electrochim. Acta 75 (2012) 279-87. https://doi.org/10.1016/j.electacta.2012.04.120.

[38] J. H. Seo, M. Chung, M. Park, S. W. Han, X. C. Zhang, and A. M. Sastry, Generation of Realistic Particle Structures and Simulations of Internal Stress: A Numerical/AFM Study of $LiMn_2O_4$ Particles, J. Electrochem. Soc. 158[4] (2011) A434-A42. https://doi.org/10.1149/1.3552930.

[39] W. Mai, M. Yang, and S. Soghrati, A particle-resolved 3D finite element model to study the effect of cathode microstructure on the behavior of lithium ion batteries, Electrochim. Acta 294 (2019) 192-209. https://doi.org/10.1016/j.electacta.2018.10.072.

[40] L. Mu, R. Lin, R. Xu, L. Han, S. Xia, D. Sokaras, J. D. Steiner, T.-C. Weng, D. Nordlund, M. M. Doeff, Y. Liu, K. Zhao, H. L. Xin, and F. Lin, Oxygen Release Induced Chemomechanical Breakdown of Layered Cathode Materials, Nano Lett. 18[5] (2018) 3241-49. https://doi.org/10.1021/acs.nanolett.8b01036.

[41] R. Mücke, M. Finsterbusch, P. Kaghazchi, D. Fatakowa-Rohlfing, and O. Guillon, Modelling Electro-Chemical Induced Stresses in All-Solid-State Batteries: Anisotropy Effects in Cathodes and Cell Design Optimisation, J. Power Sources 489 (2021) 229430. https://doi.org/10.1016/j.jpowsour.2020.229430

[42] S. A. Roberts, V. E. Brunini, K. N. Long, and A. M. Grillet, A Framework for Three-Dimensional Mesoscale Modeling of Anisotropic Swelling and Mechanical Deformation in Lithium-Ion Electrodes, J. Electrochem. Soc. 161[11] (2014) F3052-F59. https://doi.org/10.1149/2.0081411jes.

[43] S. Yamakawa, N. Nagasako, H. Yamasaki, T. Koyama, and R. Asahi, Phase-field modeling of stress generation in polycrystalline $LiCoO_2$, Solid State Ionics 319 (2018) 209-17. https://doi.org/10.1016/j.ssi.2018.02.013.

[44] U.-H. Kim, H.-H. Ryu, J.-H. Kim, R. Mücke, P. Kaghazchi, C. S. Yoon, and Y.-K. Sun, Microstructure-Controlled Ni-Rich Cathode Material by Microscale Compositional Partition for Next-Generation Electric Vehicles, Adv Energy Mater 0[0] (2019) 1803902. https://doi.org/10.1002/aenm.201803902.

[45] H. H. Ryu, N. Y. Park, J. H. Seo, Y. S. Yu, M. Sharma, R. Mücke, P. Kaghazchi, C. S. Yoon, and Y. K. Sun, A highly stabilized Ni-rich NCA cathode for high-energy lithium-ion batteries, Mater Today 36 (2020) 73-82. https://doi.org/10.1016/j.mattod.2020.01.019.

[46] R. E. Garcia, Y. M. Chiang, W. C. Carter, P. Limthongkul, and C. M. Bishop, Microstructural modeling and design of rechargeable lithium-ion batteries, J. Electrochem. Soc. 152[1] (2005) A255-A63. https://doi.org/10.1149/1.1836132.

[47] A. Bielefeld, D. A. Weber, and J. r. Janek, Microstructural modeling of composite cathodes for all-solid-state batteries, The journal of physical chemistry C 123[3] (2018) 1626-34. https://doi.org/10.1021/acs.jpcc.8b11043.

[48] J. Auborn and Y. Barberio, Lithium Intercalation Cells Without Metallic Lithium: and, J. Electrochem. Soc. 134[3] (1987) 638. https://doi.org/10.1149/1.2100521.

[49] T. Nagaura and K. Tozawa, Progress in batteries and solar cells, JEC Press 9 (1990) 209. https://doi.org/10.1541/ieejfms1990.115.4_349

[50] B. Wang, J. Bates, F. Hart, B. Sales, R. Zuhr, and J. Robertson, Characterization of thin-film rechargeable lithium batteries with lithium cobalt oxide cathodes, J. Electrochem. Soc. 143[10] (1996) 3203. https://doi.org/10.1149/1.1837188.

[51] A. Kannan, L. Rabenberg, and A. Manthiram, High capacity surface-modified LiCoO2 cathodes for lithium-ion batteries, Electrochem Solid St 6[1] (2002) A16. https://doi.org//10.1149/1.1526782.

[52] Y. J. Kim, H. Kim, B. Kim, D. Ahn, J.-G. Lee, T.-J. Kim, D. Son, J. Cho, Y.-W. Kim, and B. Park, Electrochemical stability of thin-film LiCoO2 cathodes by aluminum-oxide coating, Chem. Mater. 15[7] (2003) 1505-11. https://doi.org/10.1021/cm0201403.

[53] J. N. Reimers and J. R. Dahn, Electrochemical and In Situ X-Ray Diffraction Studies of Lithium Intercalation in Li_xCoO_2, J. Electrochem. Soc. 139[8] (1992) 2091-97. https://doi.org/10.1149/1.2221184.

[54] R. Koerver, W. Zhang, L. de Biasi, S. Schweidler, A. O. Kondrakov, S. Kolling, T. Brezesinski, P. Hartmann, W. G. Zeier, and J. Janek, Chemo-mechanical expansion of lithium electrode materials – on the route to mechanically optimized all-solid-state batteries, Energ Environ Sci 11[8] (2018) 2142-58. https://doi.org/10.1039/C8EE00907D.

[55] Y. Ren, T. Liu, Y. Shen, Y. Lin, and C.-W. Nan, Chemical compatibility between garnet-like solid state electrolyte $Li_{6.75}La_3Zr_{1.75}Ta_{0.25}O_{12}$ and major commercial lithium battery cathode materials, Journal of Materiomics 2[3] (2016) 256-64. https://doi.org/10.1016/j.jmat.2016.04.003.

[56] C. Wang, K. Fu, S. P. Kammampata, D. W. McOwen, A. J. Samson, L. Zhang, G. T. Hitz, A. M. Nolan, E. D. Wachsman, and Y. Mo, Garnet-type solid-state electrolytes: materials, interfaces, and batteries, Chem. Rev. (Washington, DC, U. S.) 120[10] (2020) 4257-300. https://doi.org/10.1021/acs.chemrev.9b00427.

[57] W. D. Richards, L. J. Miara, Y. Wang, J. C. Kim, and G. Ceder, Interface Stability in Solid-State Batteries, Chem. Mater. 28[1] (2016) 266-73. https://doi.org/10.1021/acs.chemmater.5b04082.

[58] J. N. Reimers and J. Dahn, Electrochemical and in situ X-ray diffraction studies of lithium intercalation in Li x CoO2, J. Electrochem. Soc. 139[8] (1992) 2091. https://doi.org/10.1149/1.2221184.

[59] E. J. Cheng, N. J. Taylor, J. Wolfenstine, and J. Sakamoto, Elastic properties of lithium cobalt oxide ($LiCoO_2$), Journal of Asian Ceramic Societies 5[2] (2017) 113-17. https://doi.org/10.1016/j.jascer.2017.03.001.

[60] A. A. Hubaud, D. J. Schroeder, B. J. Ingram, J. S. Okasinski, and J. T. Vaughey, Thermal expansion in the garnet-type solid electrolyte $(Li_{7-x}Al_{x/3})La_3Zr_2O_{12}$ as a function of Al content, J. Alloys Compd. 644 (2015) 804-07. https://doi.org/10.1016/j.jallcom.2015.05.067.

[61] S. A. Roberts, V. E. Brunini, K. N. Long, and A. M. Grillet, A framework for three-dimensional mesoscale modeling of anisotropic swelling and mechanical deformation in lithium-ion electrodes, J. Electrochem. Soc. 161[11] (2014) F3052. https://doi.org//10.1149/2.0081411jes.

[62] C. L. Tsai, Q. L. Ma, C. Dellen, S. Lobe, F. Vondahlen, A. Windmuller, D. Gruner, H. Zheng, S. Uhlenbruck, M. Finsterbusch, F. Tietz, D. Fattakhova-Rohlfing, H. P. Buchkremer, and O. Guillon, A garnet structure-based all-solid-state Li battery without interface modification: resolving incompatibility issues on positive electrodes, Sustain Energ Fuels 3[1] (2019) 280-91. https://doi.org/10.1039/c8se00436f.

[63] M. Finsterbusch, T. Danner, C. L. Tsai, S. Uhlenbruck, A. Latz, and O. Guillon, High Capacity Garnet-Based All-Solid-State Lithium Batteries: Fabrication and 3D-Microstructure Resolved Modeling, ACS Appl. Mater. Interfaces 10[26] (2018) 22329-39. https://doi.org/10.1021/acsami.8b06705.

[64] R. Varadhan and P. Gilbert, BB: An R package for solving a large system of nonlinear equations and for optimizing a high-dimensional nonlinear objective function, Journal of statistical software 32 (2010) 1-26. https://doi.org/10.18637/jss.v032.i04.

[65] A. Y. Hou, C. Y. Huang, C. L. Tsai, C. W. Huang, R. Schierholz, H. Y. Lo, H. Tempel, H. Kungl, R. A. Eichel, and J. K. Chang, All-Solid-State Garnet-Based Lithium Batteries at Work–In Operando TEM Investigations of Delithiation/Lithiation Process and Capacity Degradation Mechanism, Advanced Science 10[5] (2023) 2205012. https://doi.org/10.1002/advs.202205012.

[66] A. N. Wang, J. F. Nonemacher, G. Yan, M. Finsterbusch, J. Malzbender, and M. Kruger, Mechanical properties of the solid electrolyte Al-substituted $Li_7La_3Zr_2O_{12}$ (LLZO) by utilizing micro-pillar indentation splitting test, J. Eur. Ceram. Soc. 38[9] (2018) 3201-09. https://doi.org/10.1016/j.jeurceramsoc.2018.02.032.

[67] J. E. Ni, E. D. Case, J. S. Sakamoto, E. Rangasamy, and J. B. Wolfenstine, Room temperature elastic moduli and Vickers hardness of hot-pressed LLZO cubic garnet, J. Mater. Sci. 47[23] (2012) 7978-85. https://doi.org/10.1007/s10853-012-6687-5.

[68] S. Yu, R. D. Schmidt, R. Garcia-Mendez, E. Herbert, N. J. Dudney, J. B. Wolfenstine, J. Sakamoto, and D. J. Siegel, Elastic Properties of the Solid Electrolyte $Li_7La_3Zr_2O_{12}$ (LLZO), Chem. Mater. 28[1] (2016) 197-206. https://doi.org/10.1021/acs.chemmater.5b03854.

[69] Y. Takahashi, N. Kijima, K. Dokko, M. Nishizawa, I. Uchida, and J. Akimoto, Structure and electron density analysis of electrochemically and chemically delithiated $LiCoO_2$ single crystals, J. Solid State Chem. 180[1] (2007) 313-21. https://doi.org/10.1016/j.jssc.2006.10.018.

[70] H. Moulinec and P. Suquet, A numerical method for computing the overall response of nonlinear composites with complex microstructure, Comput. Meth. Appl. Mech. Eng. 157[1-2] (1998) 69-94. https://doi.org/10.1016/S0045-7825(97)00218-1.

[71] M. Kabel, D. Merkert, and M. Schneider, Use of composite voxels in FFT-based homogenization, Comput. Meth. Appl. Mech. Eng. 294 (2015) 168-88. https://doi.org/https://doi.org/10.1016/j.cma.2015.06.003.

[72] A. Wiegmann and A. Zemitis, EJ-HEAT: A fast explicit jump harmonic averaging solver for the effective heat conductivity of composite materials, (2006). https://doi.org/1027387837

[73] G. S. Ohm, Die galvanische kette: mathematisch. TH Riemann, (1827).

[74] M. Tanemura, T. Ogawa, and N. Ogita, A new algorithm for three-dimensional Voronoi tessellation, J. Comput. Phys. 51[2] (1983) 191-207. https://doi.org/10.1016/0021-9991(83)90087-6.

[75] H. Tukamoto and A. West, Electronic conductivity of LiCoO2 and its enhancement by magnesium doping, J. Electrochem. Soc. 144[9] (1997) 3164. https://doi.org/10.1149/1.1837976.

[76] M. Huang, A. Dumon, and C.-W. Nan, Effect of Si, In and Ge doping on high ionic conductivity of Li7La3Zr2O12, Electrochem. Commun. 21 (2012) 62-64. https://doi.org/10.1016/j.elecom.2012.04.032.

[77] L. Froboese, J. F. van der Sichel, T. Loellhoeffel, L. Helmers, and A. Kwade, Effect of microstructure on the ionic conductivity of an all solid-state battery electrode, J. Electrochem. Soc. 166[2] (2019) A318. https://doi.org/10.1149/2.0601902jes.

Supplementary material

Microstructural parameters governing the mechanical stress and conductivity of All-solid-state lithium-ion-battery cathodes

Fadi Al-Jaljouli [a,b], Robert Mücke [a], Payam Kaghazchi [a], Yoo Jung Sohn [a], Martin Finsterbusch [a], Dina Fattakhova-Rohlfing [a, c] and Olivier Guillon [a,b]

[a] *Forschungszentrum Jülich GmbH, Institute of Energy and Climate Research, Materials Synthesis and Processing (IEK-1), 52425, Jülich Aachen Research Alliance:JARA-Energy, Jülich, Germany*

[b] *Institute of Mineral Engineering, RWTH Aachen University, 52064 Aachen,Germany*

[c] *Faculty of Engineering and Center for Nanointegration Duisburg-Essen, Universit˙at Duisburg-Essen, Lotharstr. 1, 47057, Duisburg, Germany*

Emails: f.al-jaljouli@fz-juelich.de, r.muecke@fz-juelich.de, p.kaghazchi@fz-juelich.de, y.sohn@fz-juelich.de, m.finsterbusch@fz-juelich.de, d.fattakhova@fz-juelich.de, o.guillon@fz-juelich.de

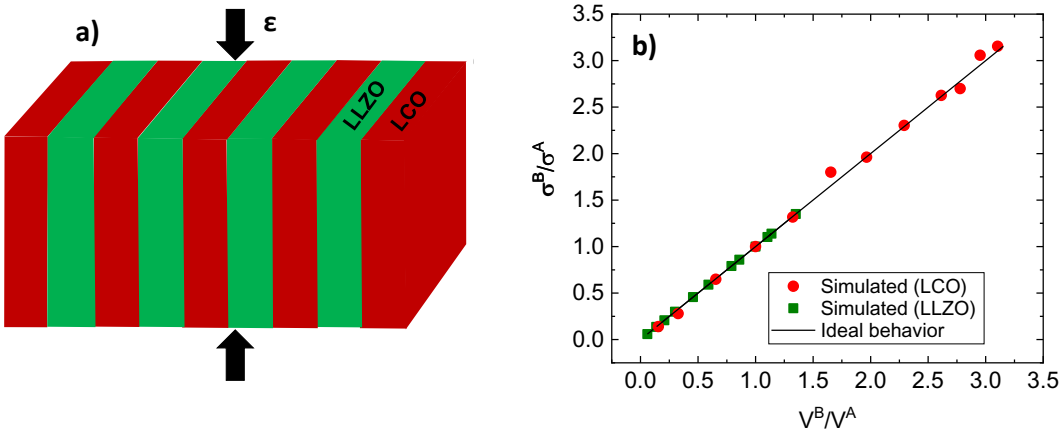

Fig. S1. a) The iso-strain condition where the force is parallel to layers b) modelled stress vs. simulated stress

A representative volume element of a 3-D composite that has the general properties of a basic microstructure and material texture is shown in Figure S1 a. To investigate its response, we considered it as a multiple group of parallel laminate subgroups. The mass ratio of the active material to the solid electrolyte in each laminate subgroup is equal to the mass ratio of the active material to the solid electrolyte in the entire composite structure yeilding to :

$$\overline{V}_{LCO} + \overline{V}_{LLZO} = \text{constant} \qquad (1)$$

In our case, the resulting strains were a consequence of the volume change in the active material, which was responsible for inducing stress. Thus, we assume a uniform distribution of the strains (Thermal and chemical) among several laminate subgroups.

$\boldsymbol{\varepsilon_{LCO}^{Th}}, \boldsymbol{\varepsilon_{LCO}^{Li}}, \boldsymbol{\varepsilon_{LCO}^{Th}}$, and $\boldsymbol{\varepsilon_{LLZO}^{Th}}$ = constants. (2)

In this case, we can apply the iso-strain model [1-3], which provides an estimation of the upper bound.

The absolute values of stress in LCO and LLZO grow with increasing corresponding surface area ratio.

For electro-chemical strain:

$$\varepsilon_{LCO} = \varepsilon_{LCO}^{Li} + \varepsilon_{LCO}^{El} + \varepsilon_{LCO}^{Th} \quad (3)$$

$$\varepsilon_{LLZO} = \varepsilon_{LLZO}^{El} + \varepsilon_{LLZO}^{Th} \quad (4)$$

Where: ε_{LCO} , ε_{LCO}^{Li}, ε_{LCO}^{El} and ε_{LCO}^{Th} are constants representing the total, lithiation, elastic and thermal strains of LCO respectively.

For iso-strain composite material (Fig. S1 a):

$$\varepsilon_{LCO}^{Li} + \varepsilon_{LCO}^{El} + \varepsilon_{LCO}^{Th} = \varepsilon_{LLZO}^{El} + \varepsilon_{LLZO}^{Th} = \varepsilon \quad (5)$$

Where: ε_{LLZO} , ε_{LLZO}^{El}, ε_{LLZO}^{Th} are constants representing the total, elastic and thermal strain of LLZO

In addition, for the equilibrium of forces:

$$\sigma_{LCO}\, A_{LCO} + \sigma_{LLZO}\, A_{LLZO} = 0 \quad (6)$$

Where A_{LCO} and A_{LLZO} are the areas of LCO layer and LLZO layer respectively, and σ_{LCO} and σ_{LLZO} are the stress in LCO and LLZO respectively.

But $= \frac{V}{d}$, where d is the depth of the layer and it is equal, So, $A \sim V$

As a result, Eq (6) can be written as:

$$\sigma_{LCO}\,\bar{V}_{LCO} + \sigma_{LLZO}\,\bar{V}_{LLZO} = 0 \qquad (7)$$

$\bar{V}_{LCO}$ and $\bar{V}_{LLZO}$ are the volume fraction of LCO and LLZO in the structure.

Applying Hook's law σ = E*ε in (7) yields:

$$E_{LCO}\varepsilon_{LCO}^{El}\bar{V}_{LCO} + E_{LLZO}\varepsilon_{LLZO}^{El}\,\bar{V}_{LLZO} = 0 \qquad (8)$$

Evaluate ε_{LCO}^{El} and ε_{LLZO}^{El} from (1) and (2) respectively and substitute them in (8) then evaluate ε

$$\epsilon = \frac{\bar{V}_{LCO}\left(\varepsilon_{LCO}^{Li} + \varepsilon_{LCO}^{Th}\right) + \bar{V}_{LLZO}\left(\varepsilon_{LLZO}^{Th}\right)}{\bar{V}_{LCO} + \bar{V}_{LLZO}} \qquad (9)$$

Again from Hook's Law

$$\sigma_{LCO} = E_{LCO}\,[\varepsilon - (\varepsilon_{LCO}^{Li} + \varepsilon_{LCO}^{Th})] \qquad (10)$$

$$\sigma_{LLZO} = E_{LLZO}\,(\varepsilon - \varepsilon_{LLZO}^{Th}) \qquad (11)$$

Substituting (9) in (10) and (11) yields the dependence of the stresses

$$\sigma_{LCO} = \frac{\bar{V}_{LLZO}}{\bar{V}_{LCO} + \bar{V}_{LLZO}}\,[\varepsilon_{LLZO}^{Th} - (\varepsilon_{LCO}^{Li} + \varepsilon_{LCO}^{Th})] \qquad (12)$$

$$\sigma_{LLZO} = \frac{\bar{V}_{LCO}}{\bar{V}_{LCO} + \bar{V}_{LLZO}}\,[\varepsilon_{LCO}^{Li} + \varepsilon_{LCO}^{Th} - \varepsilon_{LLZO}^{Th}] \qquad (13)$$

We define σ^A and σ^B as the stress of the reproduced structure (with reference parameters) and of the structure after variation of the solid volume fraction of LCO (Relative density and grain sizes of LCO and LLZO are constant), respectively. Using (12) and (13) yields:

$\frac{\sigma^B_{LCO}}{\sigma^A_{LCO}} = \frac{\bar{V}^B_{LLZO}}{\bar{V}^A_{LLZO}}$ and $\frac{\sigma^B_{LLZO}}{\sigma^A_{LLZO}} = \frac{\bar{V}^B_{LCO}}{\bar{V}^A_{LCO}}$

The modelled results agree with the simulated results (Fig. S1 b). Eq (12) and (13) indicate a direct proportional relationship between stress and the solid volume fraction of LCO and the solid volume fraction of LLZO. This was also observed in the dependency of the mean stress on the solid volume fraction of LCO (Fig. 5a).

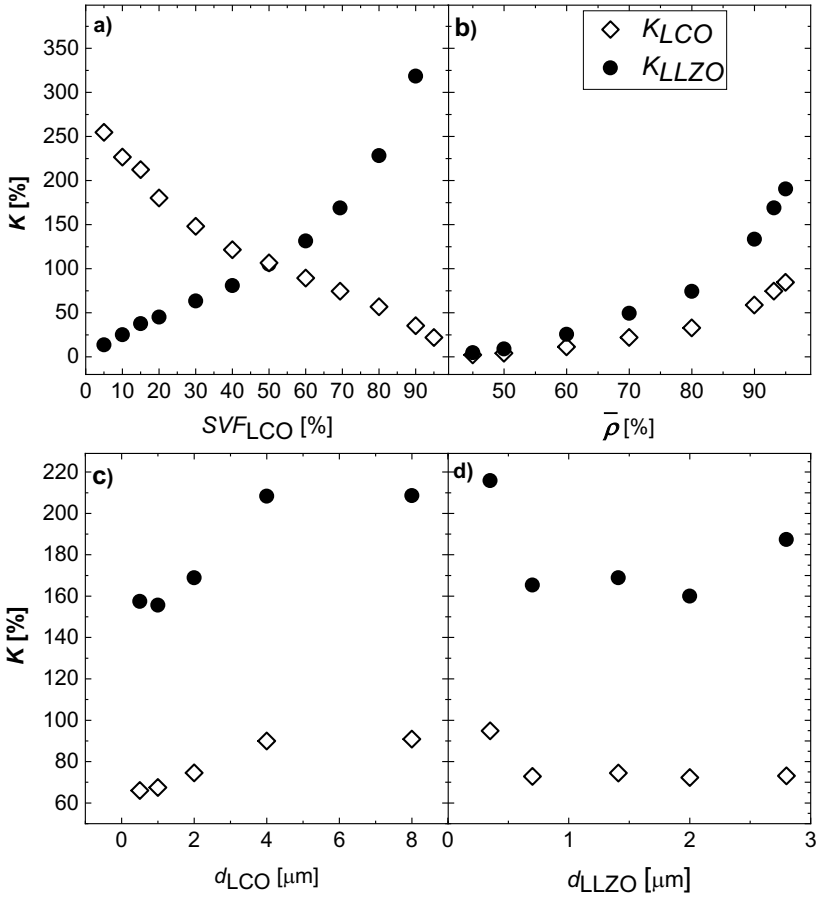

Fig. S2. K_{LCO} and K_{LLZO} as a function of solid volume fraction of LCO (a), relative density (b), grain size of LCO (c) and grain size of LLZO (d).

When the solid volume fraction of LCO increases with fixed values of the grain sizes of the solid phases and domain size, the LLZO grains are replaced by an equivalent amount of LCO grains, which leads to higher volume fraction of LCO on expense of the volume fraction of LLZO. This in turn yields to a smaller contact area between the LCO grains and the remaining LLZO grains.

K_{LCO} decreased with increasing solid volume fraction of LCO (Fig. S2 a). For a low solid volume fraction of LCO, the few LCO particles are almost completely surrounded by LLZO particles; hence, the surface of LCO is almost fully covered with LLZO and surrounded by a few pores. With increasing solid volume fraction of LCO, the LCO grain is more surrounded by other LCO grains forming the pore surface and not so frequently by LLZO grains; thus, the interface area ratio decreases. K_{LLZO} follows analogous the opposite trend with increasing solid volume fraction of LCO (Fig. S2 a). In other words, for varying solid volume fraction of LCO, K_{LCO}, and K_{LLZO}, is governed by the number of grains of one solid phase that surround the grains of the other solid phase at a constant grain size.

While increasing the relative density (Fig. S2 b) with fixed solid volume fraction of LCO, grain sizes of the solid contents and the domain size, the volume fraction of LCO and LLZO increased attributed to lower volume fraction of pores. This in turn, increases the coordination number, yielding to higher contact area between LCO and LLZO, but lower contact area between solid phases and pores. As a result, both K_{LCO} and K_{LLZO} increased.

As the grain size of LCO increases (Fig. S2 c) with fixed domain size solid volume fraction of LCO and the relative density, lower number of LCO grains formed, yielding significant decrease in the surface area between LCO and LLZO and between LCO and pores. On the other hand, higher number of LLZO are formed in order to compensate the loss of LCO grains in order to maintain the value of solid volume fraction of LCO, which in turn increase the surface area between LLZO and pores. Furthermore, increasing the grain size of LCO doesn't affect the volume fraction of neither LCO nor LLZO. As a result, both K_{LCO} and K_{LLZO} are slightly increased. On the other hand, as the grain size of LLZO increase (Fig. S2 d) with fixed domain size, solid volume fraction of LCO and the relative density, no effect on the volume fraction of LCO and LLZO was observed. Finally, the contact area between LLZO and both LCO and pores start to decrease due to lower LLZO grains. In contrast, the contact area between LCO and pores tends to increase, which in turn decreases both K_{LCO} and K_{LLZO}.

References

[1] T.-W. Chou, Textile Structural Composites, Composite Materials Seris 3 (1989). https://doi.org/, https://cir.nii.ac.jp/crid/1571980074666455552.

[2] D. W. Whyte, Structure and properties of 3-D braid reinforced composites. in. Drexel Univ., Philadelphia, PA (USA), 1986.

[3] C. M. Pastore and Y. A. Gowayed, A self-consistent fabric geometry model: modification and application of a fabric geometry model to predict the elastic properties of textile composites, Journal of Composites, Technology and Research 16[1] (1994) 32-36. https://doi.org/10.1520/CTR10392J

3.2. Paper II: Chemo-Thermal Stress in All-Solid-State Batteries: Impact of Cathode Active Materials and Microstructure

Authors	Fadi Al-Jaljouli, Robert Mücke, Christoph Roitzheim, Yoo Jung Sohn, Najma Yaqoob, Martin Finsterbusch, Payam Kaghazchi and Olivier Guillon
Journal	Journal of power sources
Volume	644
Pages	237136
Published on	April 2025
DOI	10.1016/j.jpowsour.2025.237136

The following constitute my sole contributions:

- Generation of microstructures with different CAMs while varying the microstructural design parameters.
- Calculating the chemo-thermal strains of utilized CAMs
- Mechanical characterization of the regenerated samples.
- Analyzing and explaining the stresses types appeared on CAMs and LLZO during thermal, chemical and chemo-thermal phases.
- Comparing between the induced mechanical stresses for utilized CAMs and LLZO during thermal, chemical and chemo-thermal phases.
- Writing the entire manuscript except for the subsection ’Calculation of stiffness matrix of NCM955’
- Authoring the complete supporting information except for the part of HT-XRD.
- Creation of all figures in the manuscript and supporting information.

Chemo-Thermal Stress in All-Solid-State Batteries: Impact of Cathode Active Materials and Microstructure

Fadi Al-Jaljouli [a,b], Robert Mücke [a], Christoph Roitzheim [a] Yoo Jung Sohn [a]

Najma Yaqoob [a,d], Martin Finsterbusch [a,e], Payam Kaghazchi [a,d] and Olivier Guillon [a,b,c,e]

[a] *Forschungszentrum Jülich GmbH, Institute of Energy Materials and Devices, Materials Synthesis and Processing (IMD-2), 52425, Jülich, Germany*

[b] *Institute of Mineral Engineering, RWTH Aachen University, 52064 Aachen,Germany*

[c] *Jülich Aachen Research Alliance: JARA-Energy, Jülich, 52425, Germany*

[d] *MESA+ Institute for Nanotechnology, University of Twente, P. O. Box 217, Enschede, 7500AE, The Netherlands*

[e] *Helmholtz Institute Münster: Ionics in Energy Storage (IMD-4 / HI MS), Münster 48149, Germany*

Emails: f.al-jaljouli@fz-juelich.de, r.muecke@fz-juelich.de, c.roitzheim@fz-juelich.de, y.sohn@fz-juelich.de, n.yaqoob@fz-juelich.de, m.finsterbusch@fz-juelich.de, p.kaghazchi@fz-juelich.de, o.guillon@fz-juelich.de

Abstract

The transition from conventional lithium-ion to all-solid-state lithium batteries (ASSBs) promises enhanced safety and higher energy density but also gives rise to new challenges, like capacity degradation due to enhanced mechanical stresses. This study addresses the often-overlooked residual (thermal) mechanical stress arising during manufacturing, which can significantly contribute to the overall mechanical stress. While stress evolution during battery operation is often only associated with the de-/lithiation-induced stresses from the active material, we introduce a "chemo-thermal stress" description. By this integration of thermal and chemical stresses, we developed a more accurate level to simulate real-life conditions, especially for all-solid-state batteries. This holistic approach demonstrated for the first time, that thermal stresses from manufacturing can reduce the induced mechanical stress in $LiCoO_2$ (LCO) during delithiation, resulting in the total chemo-thermal stress being approximately 43% lower. In contrast, residual thermal stress exacerbates chemical stress in $Li_{0.5}$NCM955 and $Li_{0.1}$NCM955, leading to a principal stress increases of approximately 42% and 15%, respectively. We also examine the impact of microstructural design parameters, particularly the solid volume fraction of the cathode active material (CAM) and relative density, on the induced mechanical stresses within CAM and the solid electrolyte (SE). Our investigation reveals that the volume change in cathode active materials, a primary contributor to induced mechanical stress in ASSBs, is not a reliable factor for predicting final stresses in actual full battery cells. Additionally, our findings highlight LCO's superior mechanical behavior compared to

$Li_{0.5}$NCM955 and $Li_{0.1}$NCM955, attributed to lower overall stress and prevalent compressive stress, which mitigates failure risks in oxide materials.

Keywords: All-solid-state lithium batteries, Thermal stress, Chemo-thermal stress, Composite cathodes, Microstructural design parameters.

2. Introduction

The transition from liquid lithium-ion batteries (LIBs) to all-solid-state lithium batteries (ASSBs) by replacing the conventional liquid electrolyte with a ceramic, is a promising way to enhance safety and energy density [1-4]. However, challenges such as dendrite formation [5-8], undesirable chemical reactions which occur along the interface between cathode active material (CAM) and solid electrolyte (SE) [9-11], and the mechanical fatigue during cycling results in significant degradation [12-14] persist in impeding the progress of ASSBs. Mechanical stresses induced within the system are primarily due to the rigid constraint imposed by the SE on the volume changes of CAMs [15-17].

CAMs composed of layered transition metal oxides have garnered significant attention from researchers. $LiCoO_2$ (LCO) is renowned for its electrochemical cyclability and high capacity [18-22]. However, LCO is marred by drawbacks stemming from its toxicity and high cost. Furthermore, its inherent structural instability results in a reduced experimental capacity, with a maximum achievable value of 140 mAh/g compared to theoretical 280 mAh/g.[23,24]. This spurred the exploration of nickel-rich materials. Lithium nickel manganese cobalt oxide $LiNi_{1-x-y}Co_xMn_yO_2$ (NCM), is currently regarded as most promising active material attributed to its higher voltage plateau [25,26], higher energy density and lower cost [27-34]. However, it is important to note that during cycling, NCM also generates more heat and is more prone to structural degradation leading to diminished capacity retention [35-38]. Among NCM family, NCM955 is distinguished by its highest specific capacity of 215 mAh/g and affordability. This increased reversible capacity is attributed to its increased nickel content [39].

From the wide variety of solid Li ion conductors, garnet type $Li_7La_3Zr_2O_{12}$ (LLZO) attracts particular attention. LLZO provides a high room temperature ionic conductivity of more than 1 $mScm^{-1}$, low electronic conductivity, broad electrochemical stability window, and a unique chemical and electrochemical stability towards Li metal [40-44]. Stoichiometric LLZO ($Li_7La_3Zr_2O_{12}$) undergoes a volume change during the transition from the tetragonal to the cubic

phase, this transition is primarily temperature-dependent. Buschmann *et al*. observed that a reversible tetragonal-to-cubic transition can be induced upon heating above ~ 100–150 °C [42]. However, the associated volume change is minimal. Geiger *et al*. reported that tetragonal $Li_7La_3Zr_2O_{12}$ has lattice parameters a = 13.134(2) Å and c = 12.663(2) Å, while the cubic form has a = 12.943(1) Å, indicating only a slight volumetric variation [45]. Defect generation, such as hydration, can also induce minor volume changes in stoichiometric LLZO. Larraz *et al*. investigated the effect of hydration on tetragonal LLZO and reported a slight, reversible volume expansion (~0.78%) when transitioning from the tetragonal phase (2173 $Å^3$) to the cubic phase (2190 $Å^3$) [46]. These minor volume fluctuations can be avoided by doping LLZO with elements such as Al and Ta, which stabilize the cubic phase. Besides a Li metal anode, the cathode will be decisive for the areal capacity and energy density of an ASSB. In order to realize such high energy density ASSBs, a thick composite cathode composed of intertwined SE (LLZO) and CAM particles to provide percolating pathways for ion and electron transport is needed. The fabrication of such LLZO garnet based composite cathodes is challenging. High temperature co-sintering step of SE and CAM at temperatures above 1000 °C is necessary. Material compatibility issues and residual thermal stress are the consequences of the required thermal treatment. The thermodynamic stability issue of LLZO/CAM mixtures was already intensively investigated by several groups [47-54]. Out of the different CAMs known from LIBs, only $LiCoO_2$ (LCO) was shown to be thermodynamically stable in combination with LLZO elevated temperatures, while other CAMs like NCM, $LiNi_{0.8}Co_{0.15}Al_{0.05}O_2$ (NCA), $LiMn_2O_4$ (LMO) and $LiFePO_4$ (LFP) were shown to react already at moderate temperatures between 400 °C and 800 °C.

Significant effort has been devoted to investigate the induced mechanical stress in composite cathodes of ASSBs during delithiation. However, the residual mechanical stress resulting from manufacturing processes, particularly thermal sintering, has often been disregarded. Yet, neglecting this aspect could compromise the accuracy of real-life calculations. In this study, we highlight the critical role of residual mechanical stress resulting from thermal strain mismatch between the CAM and SE during cooling after sintering (thermal stress). This residual stress significantly impacts the overall mechanical stress when combined with the stress induced by the delithiation process (chemical stress). Therefore, we introduce the concept of "chemo-thermal stress" which encompasses both thermal and chemical stresses, to better reflect real-life

conditions. Additionally, we examine the influence of microstructural design parameters (solid volume fraction of CAM and the relative density) on the thermal, chemical, and chemo-thermal stresses within the cathode active material and solid electrolyte. Our investigation reveals that the volume change of the cathode active material, a key contributor to induced mechanical stress in ASSBs, does not serve as a reliable criterion for comparing stresses across various materials or types of stress.

This research deliberately excludes the effect of grain sizes of both the cathode active material and the solid electrolyte on mechanical stress, as our previous study demonstrated that induced mechanical stress is independent of the grain sizes of the microstructural components [55].

2. Experimental and simulation methods

- ***Synthesis of experimental structure***

The composite cathode consists of $LiCoO_2$ (LCO) and aluminum and tantalum-substituted LLZO (nominal composition: $Li_{6.45}Al_{0.05}La_3Zr_{1.6}Ta_{0.4}O_{12}$), abbreviated as LLZO, was synthesized with a mass ratio of 2:1 LCO to LLZO, via a modified solid-state reaction (SSR) method as previously described [56,57]. The cathode active materials LCO and NCM955 were purchased from the commercial suppliers MTI Corporation, Richmond, CA, USA and MSE Supplies LLC, Tucson, AZ, USA, respectively.

- ***Characteristics of the Microstructure***

The percentage of cathode active material to the total solid phases in the composite cathode denoted by SVF_{CAM} is given by:

$$SVF_{CAM} = \frac{\bar{V}_{CAM}}{\bar{V}_{CAM}+\bar{V}_{LLZO}} \quad (1)$$

Similarly, the ratio of solid electrolyte to the total solid components in the composite cathode denoted by SVF_{LLZO} is given by:

$$SVF_{LLZO} = \frac{\bar{V}_{LLZO}}{\bar{V}_{CAM}+\bar{V}_{LLZO}} \quad (2)$$

Where $\bar{V}_{CAM}$ and $\bar{V}_{LLZO}$ are the volume fraction of cathode active material (LCO, $Li_{0.5}$NCM955and $Li_{0.1}$NCM955) and the volume fraction of the solid electrolyte (LLZO) with respect to the total volume respectively.

The volumetric fraction of the composite cathode's total solid components to the total volume represents the relative density ($\bar{\rho}$), which is given by:

$$\bar{\rho} = \bar{V}_{CAM} + \bar{V}_{LLZO} \quad (3)$$

- ***Generation of representative volume element***

Focused Ion Beam Scanning Electron Microscopy (FIB-SEM) was employed to acquire a stack of SEM images of the cross section with a 50 nm of voxel size. Subsequently, specially developed assorted computer-aided methodologies were applied to construct a model representing the experimental configuration. Further exhaustive details regarding this procedural approach can be found in alternative sources [58,59]. During the analysis, a focused examination of material impact was carried out, specifically assessing LCO and NCM955 using identical microstructures. Roitzheim et al.[53] utilized microstructures of NCM/LLZO cathodes, which demonstrated similar porosity to LCO/LLZO cathodes. Their findings showed that replacing LCO with NCM has minimal impact on the cathode microstructure, owing to their similar hexagonal layered structures. Both exhibit size and shape attributes comparable to those of commercially sourced powders.

The composite cathode microstructures were generated using GeoDict software, incorporating a Python script, following a series of steps outlined in [55]. Initially, grains of composite components (CAM and LLZO) were stacked to fill a domain measuring 400×200×300 voxels (voxel length = 50 nm) from the positive z-direction. To align with experimental findings [59], hexagonal grains were horizontally oriented (parallel to the Y-axis) within the modelled sample The initial SVF_{CAM} was set at 69.4%, with average grain diameters of 2.00 µm for CAM and 1.41 µm for LLZO. Subsequently, the distribution step was initiated, ensuring the attainment of a homogenous representative structure. Regions displaying deviations in SVFCAM or lower back densities were removed in the third step, reducing the domain size to 400×200×200 voxels. The structure was then subjected to sintering using the Voronoi tessellation algorithm implemented in GeoDict [60] to achieve the targeted density value of 93.14%. If necessary, the first four steps were iterated with adjusted input values for the SVF_{CAM} and the $\bar{\rho}$ to ensure maximum deviations of 0.25% from the target values. This achieved by utilizing the DFSANE algorithm derivative-free spectral approach for solving nonlinear systems of equations) [61]. Figure 1 shows the regenerated modelled microstructure consisting of CAM (LCO, $Li_{0.5}$NCM955 or $Li_{0.1}$NCM955) and LLZO.

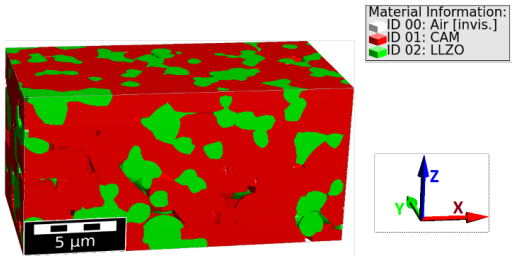

Figure 23. Regenerated modelled microstructure utilizing cathode active materials (CAM), LCO, $Li_{0.5}$NCM955 or $Li_{0.1}$NCM955. SVF_{CAM} = 69.4%, initial average grain size of CAM and LLZO are 2.00 µm and 1.43 µm respectively and $\bar{\rho}$= 93.14%.

- ***Calculation of stiffness matrix of NCM955***

Spin-polarized DFT calculations were then performed using the projector augmented wave (PAW) potential method [62] implemented in the Vienna *Ab Initio* Simulation Package (VASP) code [63]. Generalized gradient approximation (GGA) within the scheme of Perdew–Burke–Ernzerhof (PBE) [64] was chosen as the exchange-correlation functional. To perform DFT calculations for discharged and charged systems, we modelled $Li_xNi_{0.9}Co_{0.05}Mn_{0.05}O_2$ (Li_xNCM955) structure (space group: R-3m) using 4×4×1 supercells. A gamma-centred *k*-point mesh of 2×2×2 was applied. An energy cut off of 800 eV as well as electronic and force convergence criteria of 10^{-5} eV and 10^{-3} eV/Å, respectively, were used. For calculating elastic constants *Cij*, we fixed the magnetic moment and atomic coordinates to the optimized ones obtained for the equilibrium lattice parameters. C_{ij} matrix was computed using the strain values of 0, ±0.5%, and ±1%.

- ***Materials Parameters***

This study had been performed using half lithium concentration of LCO as the input parameter. While LCO, consistent with the behavior of most active materials, exhibits maximum strain at this concentration, NCM955 behaves differently, in which a higher degree of delithiation is required to achieve maximum strain. Hence, $Li_{0.1}$NCM955 was selected. Additionally, at half the lithium concentration of NCM955, its anisotropic lattice strain shows the largest deviation. The stiffness matrices of the anisotropic materials, Young's moduli and Poisson ratios of the isotropic materials are presented in Table 1. During the cooling stage subsequent to the sintering process, both the cathode active material and LLZO undergo contraction in all directions. Notably, LCO and NCM955 exhibit distinct anisotropic behaviors during this phase. Therefore, an internal thermal stress would be induced ascribed to the difference in coefficient of (α^{Th})

between CAM and LLZO. In-situ high temperature X-ray diffraction (HT-XRD), was utilized to determine the lattice parameters thereby quantifying the thermal strains (ϵ^{Th}) of LCO, NCM955 and LLZO. Temperature variations range from 0 to 1000 °C for LCO and LLZO powders, while for NCM955 the range is limited to 0–900 °C, as our experimental observations revealed decomposition of NCM955 beyond this temperature. This distinction was essential to accurately represent realistic chemo-thermal stress conditions specific to each material. The temperature change rate was maintained at 5 K min^{-1} to ensure precise experimental conditions. Additional information regarding this process is provided in the Supplementary information. The extraction of positive lithium ions during the delithiation of cathode active materials induces chemical strains ($\epsilon^{Chemical}$). For LCO and $Li_{0.5}$NCM955, substantial expansion in c-axis is observed ascribed to the repulsive force between the resulted negative charged layers. Conversely, $Li_{0.1}$NCM955 exhibits contraction along the c-axis.

Table 2 Elastic parameters including the anisotropic stiffness matrix C, Young's modulus E, and Poisson ratio ν for the cathode active materials LCO, NCM955, $Li_{0.5}CO$, $Li_{0.5}$NCM955, $Li_{0.1}$NCM955 and the electrolyte material LLZO.

Material	Elastic parameter	Ref
LCO	$C = \begin{bmatrix} 339.79 & 101.6 & 65.78 & -6.39 & 0 & 0 \\ & 339.79 & 65.78 & 0 & 0 & 0 \\ & & 214.67 & 0 & 0 & 0 \\ & sym. & & 51.47 & 0 & 0 \\ & & & & 51.47 & 0 \\ & & & & & 119.095 \end{bmatrix}$ GPa	**[65]**
NCM955	$C = \begin{bmatrix} 282.62 & 153.1 & 40.75 & 0 & 0 & 0 \\ & 282.62 & 40.75 & 0 & 0 & 0 \\ & & 354.67 & 0 & 0 & 0 \\ & sym. & & 98.79 & 0 & 0 \\ & & & & 98.79 & 0 \\ & & & & & 64.76 \end{bmatrix}$ GPa	
$Li_{0.5}CO_2$	$C = \begin{bmatrix} 303.86 & 101.71 & 32.58 & 0 & 7.31 & 0 \\ & 318.93 & 28.66 & 0 & -3.93 & 0 \\ & & 98.93 & 0 & 7.03 & 0 \\ & sym. & & 18.02 & 0 & -2.46 \\ & & & & 15.73 & 0 \\ & & & & & 101.94 \end{bmatrix}$ GPa	**[65]**
$Li_{0.5}$NCM955		**[66]**

$$C = \begin{bmatrix} 279.1 & 117.8 & 107.7 & 0 & 0 & 0 \\ & 279.1 & 107.7 & 0 & 0 & 0 \\ & & 184.6 & 0 & 0 & 0 \\ & sym. & & 75.2 & 0 & 0 \\ & & & & 75.2 & 0 \\ & & & & & 80.6 \end{bmatrix} \text{GPa}$$

$Li_{0.1}$NCM955

$$C = \begin{bmatrix} 278 & 91.5 & 114.2 & 0 & 0 & 0 \\ & 278 & 114.2 & 0 & 0 & 0 \\ & & 158.7 & 0 & 0 & 0 \\ & sym. & & 70.6 & 0 & 0 \\ & & & & 70.6 & 0 \\ & & & & & 93.2 \end{bmatrix} \text{GPa}$$

[66]

LLZO — $E = 146$ GPa, $\nu = 0.26$ — **[67-69]**

Furthermore, cathode active materials with layered structure, exhibit contraction along both a and b-axes, which in turn leads to a net volume change of 1.91%, 0.35% and -11.0% for LCO, $Li_{0.5}$NCM955 and $Li_{0.1}$NCM955 respectively. Doped LLZO doesn't exhibit any volume change during delithiation due to the stability of its phase and Li content. The combination of thermal and chemical strains leads to the emergence of chemo-thermal strains ($\epsilon^{Chemo-thermal}$). Its significance lies in its representation of realistic behavior, taking into account both cooling after sintering and delithiation steps. The values of thermal, chemical and chemo-thermal strains for cathode active materials and LLZO are listed in Table 2.

Table 3 crystallographic strains for LCO, $Li_{0.5}$NCM955 and $Li_{0.1}$NCM955 in a-and c-axes and for LLZO, in the as-manufactured state, fully lithiated (ϵ^{Th}), chemically sub-stoichiometric lithium (ϵ^{Li}) and chemo-thermal ($\epsilon^{chemo-thermal}$)

Material	ϵ^{Th}	ϵ^{Li}	$\epsilon^{chemo-thermal}$
$Li_{0.5}CO_2$	$\epsilon^a = -1.53 \times 10^{-2}$ $\epsilon^c = -2.36 \times 10^{-2}$ **($Li_{1.0}CoO_2$)**	$\epsilon^a = -2.3 \times 10^{-3}$ $\epsilon^c = 2.39 \times 10^{-2}$ **[59,70,71]**	$\epsilon^a = -1.76 \times 10^{-2}$ $\epsilon^c = 2.38 \times 10^{-4}$
$Li_{0.5}$NCM955	$\epsilon^a = -1.91 \times 10^{-2}$ $\epsilon^c = -1.76 \times 10^{-2}$ **($Li_{1.0}$NCM955)**	$\epsilon^a = -1.23 \times 10^{-2}$ $\epsilon^c = 2.81 \times 10^{-2}$ **[66]**	$\epsilon^a = -3.14 \times 10^{-2}$ $\epsilon^c = 1.04 \times 10^{-2}$

$Li_{0.1}$NCM955	Same as $Li_{0.5}$NCM955	ϵ^a=-3.95×10^{-2} ϵ^c=-3.09×10^{-2} **[66]**	ϵ^a=-5.86×10^{-2} ϵ^c=-4.85×10^{-2}
LLZO (LCO as CAM)	-1.42×10^{-2}	0	-1.42×10^{-2}
LLZO (NCM955 as CAM)	-1.32×10^{-2}	0	-1.32×10^{-2}

In this study, stress histograms are used to display the differential relative frequency as a function of principal stress values, providing a detailed representation of stress distribution. More information can be found in [66]. The average of the principal stress $\overline{\boldsymbol{S}}_{\boldsymbol{all}}$, was calculated using the ElastoDict FeelMath-LD module within GeoDict, developed by Math2Market GmbH [72,73]. While the standard deviation Δ**S** represents the width of distribution. Symmetric (Dirichlet) boundary conditions were applied in all directions. Small deformations were considered, as all deformations were within the small-scale range ≤ 5%, thereby justifying the use of linear superposition for the calculation of chemo-thermal stress. Phase transformations are implicitly incorporated through the strain-based formulation. Although interfacial reactions may induce the formation of secondary phases, their influence is considered negligible due to their limited extent and the lack of well-characterized material properties for the resulting phases. Consequently, it is reasonable to assume that the initial stress distribution within the grains is not significantly affected by such interfacial phenomena.

- ***Definition of induced mechanical stress***

The principal cause of induced mechanical stress in composite cathodes of ASSBs arise from the volume change of the CAM during delithiation, as well as the volume change in both the CAM and LLZO during the cooling down after sintering. In both instances, LLZO hinders the volume change of the CAM within the system, consequently leading to induced mechanical stress. The determination of volume change relies on the strain values of these components. For CAM, the total strain (ϵ_{CAM}) in one direction (a, b and c-axes) is given by:

$$(\epsilon_{CAM})_i = (\epsilon_{CAM}^{Li})_i + (\epsilon_{CAM}^{Th})_i + (\epsilon_{CAM}^{El})_i \qquad (i = a, b, c) \qquad (4)$$

Where ϵ_{CAM}^{Li}, ϵ_{CAM}^{Th} and ϵ_{CAM}^{El} are the lithiation, thermal and elastic strains of CAM.

On other hand, LLZO has no volume change during cycling, hence, the total strain of LLZO (ϵ_{LLZO}) in given direction (a, b and c-axes) is given by:

$$(\epsilon_{LLZO})_i = (\epsilon_{LLZO}^{Th})_i + (\epsilon_{LLZO}^{El})_i \quad (5)$$

Where ϵ_{LLZO}^{Th} and ϵ_{LLZO}^{El} are the thermal and elastic strains of LLZO phases, respectively.

The elastic strain of CAM and LLZO is linked to the stresses by Hook's law:

$$(\sigma_{CAM})_j = C_{ij}^{CAM} (\epsilon_{CAM}^{El})_i \quad (6)$$

For LLZO:

$$\sigma_{LLZO}^{i} = E(\epsilon_{LLZO}^{El})_i \quad (7)$$

- ***Varying microstructural design parameters***

One of the primary objectives of this study is to systematically investigate the impact of microstructural design parameters, including SVF_{CAM}, and the porosity on the distribution of mechanical stress in different scenarios (thermal, chemical, and chemo-thermal). Accordingly, each parameter is deliberately adjusted independently while fixing the others, employing a methodology similar to that described in [65]. Figure 2 illustrates examples of each variation. The SVF_{CAM} ranges from 5 to 95%, while the percentage of porosity varies from 5% to 60%. Subsequently, each set undergoes mechanical characterization. It is noteworthy that the selected range for each parameter exceeds the values observed in experimental cells, extending to extreme values unattainable in real-life scenarios**.** The practical range of SVF_{CAM} typically falls between 33% and 66%. In contrast, the porosity values achieved through unoptimized free sintering range from 30% to 55%, whereas for optimized and pressure-assisted sintering, it falls between 5% and 20%. The approach used to investigate the effect of a singular microstructural parameter highlights the significant advantages of modeling over experimentation in such research.

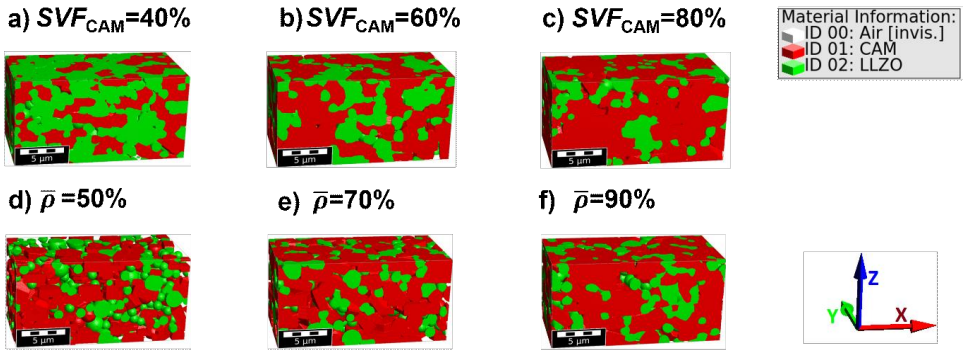

Figure 24. a-c) Variation of SVF_{CAM} only (40, 60 and 80%), d-f) variation of $\bar{\rho}$ only (50, 70 and 90%). The fixed parameters values were as follow: SVF_{CAM} = 69.4%, $\bar{\rho}$ = 93.14%, d_{CAM} = 2.00 µm and d_{LLZO} = 1.41 µm.

3. Results and discussion

- ***Impact of microstructural design parameters on induced mechanical stress***

The influence of microstructural design parameters on mechanical stresses in composite cathodes of ASSBs was investigated. These parameters included SVF_{CAM} and $\bar{\rho}$. The study investigated thermal, chemical, and chemo-thermal stresses, considering scenarios with LCO, $Li_{0.5}CO$, $Li_{0.5}NCM955$, and $Li_{0.1}NCM955$ as CAMs

The parameter governing the cell's capacity is the ratio of active material to solid electrolyte within the composite cathode. Bulk LLZO materializes when SVF_{CAM} is absent. Hence, stress-free state for LLZO occurred. As the SVF_{CAM} increases, the number of adjacent LLZO grains constraining the volume change of CAM grains decreases, being substituted by CAM grains. This substitution facilitates the volume change of CAM grains, resulting in reduced induced mechanical stress within CAM (Figure 3 a-i). However, the sensitivity of CAM stress to the increase in SVF_{CAM} is relatively low in the range of 5–20%, ascribed to the insignificant increase in the number of CAM grains within this range due to their relatively larger volume compared to LLZO grains. A notable increase in the number of CAM grains begins at SVF_{CAM} = 30%, leading to higher stress sensitivity to the increase in SVF_{CAM} This is reflected in a significant linear reduction in stress values observed beyond SVF_{CAM} = 20%.

Meanwhile, as SVF_{CAM} increases, the number of LLZO grains significantly decreases. This reduction leads to greater sensitivity of LLZO stress to variations in SVF_{CAM}, characterized by a significant increase in LLZO stress following a continuous linear trend under these conditions (Figure 3 a-i). Bulk CAM is present when the solid volume fraction of solid electrolyte reaches

0%, leading to the disappearance of LLZO in the framework. Therefore, the constraints of LLZO vanishes leading to stress-free state for aligned CAM.

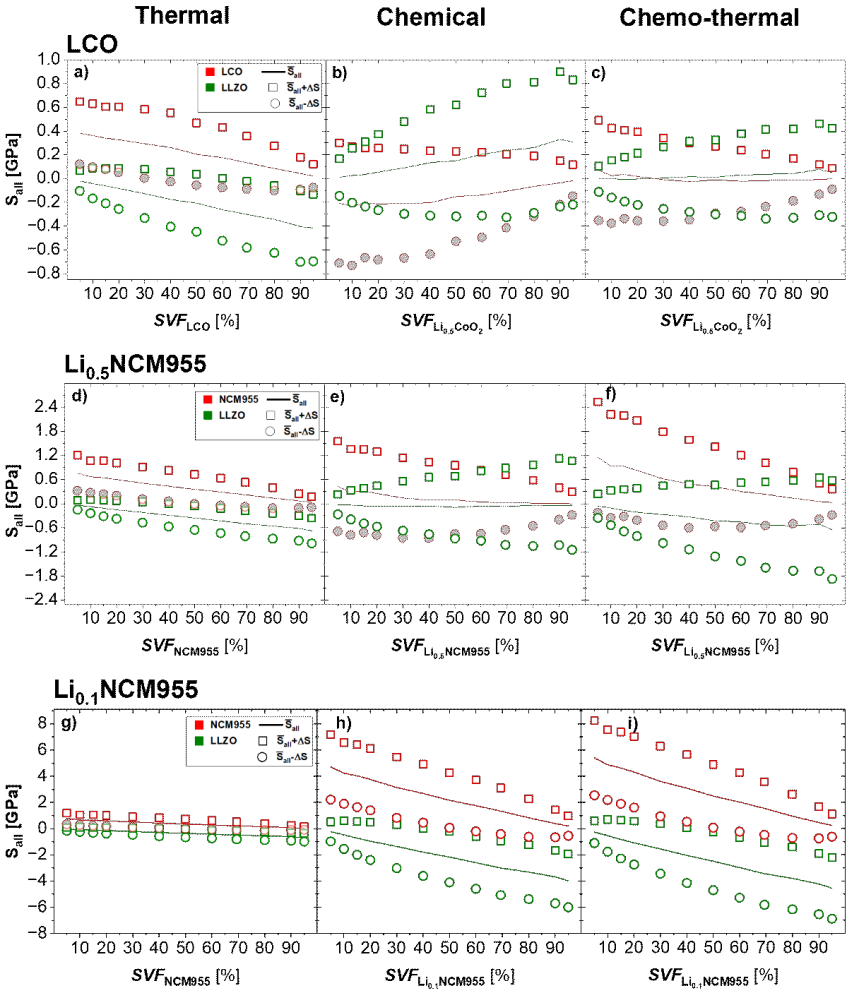

Figure *25*. The impact of SVF_{CAM} on the principal stresses for CAM (LCO a-c, $Li_{0.5}NCM955$ d-f and $Li_{0.1}NCM955$ g-i) and LLZO in case of: a, d and g) thermal, b, e, and h) chemical and c, f and i) chemo-thermal stress. The fixed parameters values were as follow: SVF_{CAM} = 69.4%, $\bar{\rho}$ = 93.14%, d_{CAM} = 2.00 µm and d_{LLZO} = 1.41 µm.

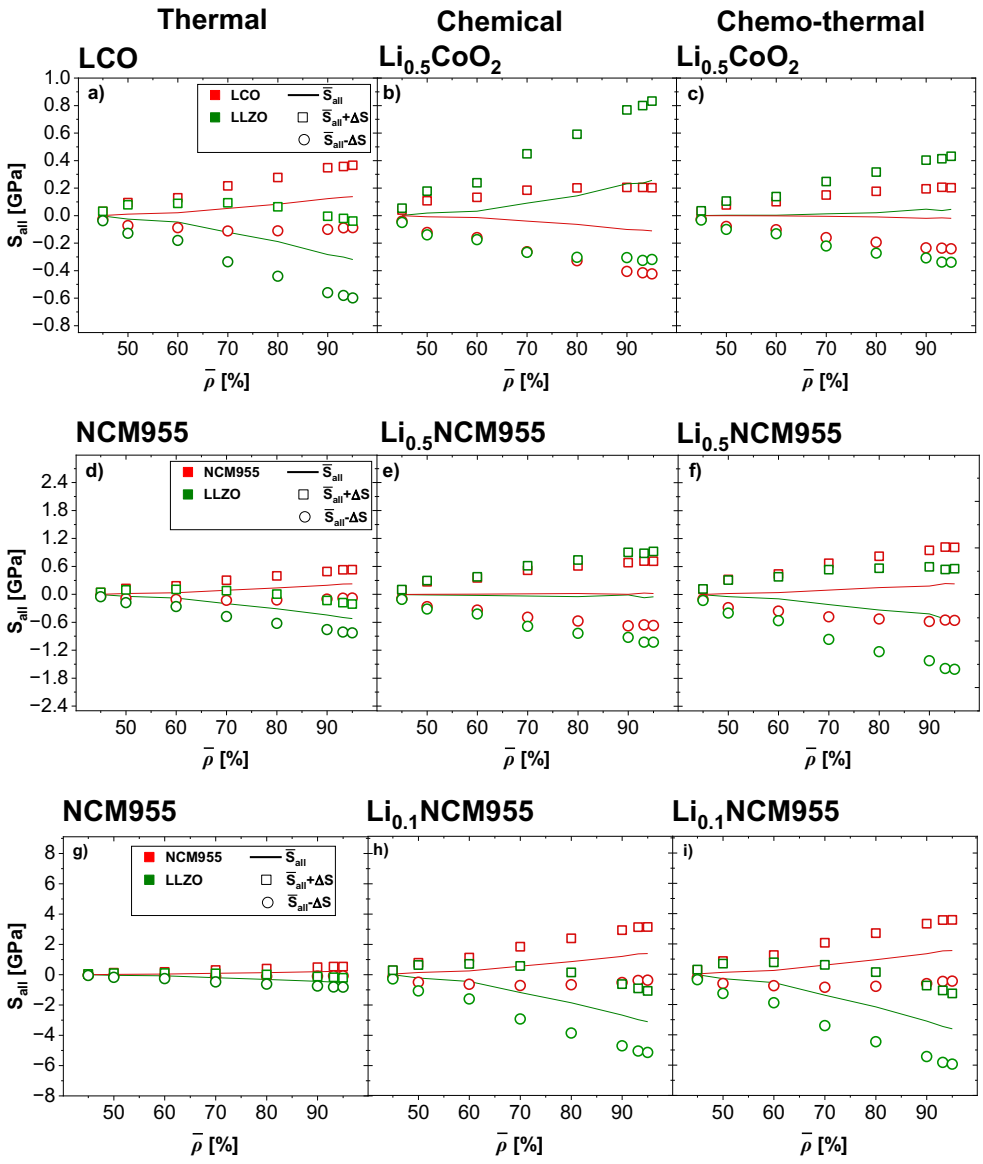

Figure 4. The impact of $\bar{\rho}$ on the principal stresses for CAM (LCO a-c, $Li_{0.5}NCM955$ d-f and $Li_{0.1}NCM955$ g-i) and LLZO in case of: a, d and g) thermal, b, e and h) chemical and c, f and i) chemo-thermal stress. The fixed parameters values were as follow: SVF_{CAM} = 69.4%, $\bar{\rho}$ = 93.14%, d_{CAM} = 2.00 µm and d_{LLZO} = 1.41 µm.

The percentage of porosity in the structure is represented by $\bar{\rho}$. The existence of residual porosity in the microstructure is essential, as it facilitates the volume change in the cathode active material and introduces a strain tolerance. In the context of a highly porous structure ($\bar{\rho}$ =

45%), LLZO exerts lower constraints on CAM, due to lower coordination number of particles. As a result, a notably diminished mechanical stress is observed.

By increasing $\bar{\rho}$, the mechanical stress of CAM and LLZO exhibits a progressive augmentation due to reduced degree of freedom in volume change for both CAM and LLZO (Figure 4).

During the thermal scenario, CAM and LLZO experience tensile and compressive stresses, respectively, due to the higher contraction strains of CAM compared to LLZO (Figure 3 a, d and g) and (Figure 4 a, d and g). In contrast, during delithiation, both $Li_{0.5}CO$ and LLZO exhibit stress inversion, with LCO undergoing compressive stress and LLZO experiencing tensile stress (Figure 3 b, e and h) and (Figure 4 b, e and h). On the other hand, $Li_{0.5}NCM955$ continues to experience tensile stress despite its volume expansion, while LLZO undergoes compressive stress during delithiation. This behavior will be discussed in detail in section (3.2.2).

Meanwhile, $Li_{0.1}NCM955$ and LLZO remain under tensile and compressive stresses, respectively, attributed to the higher volume contraction of $Li_{0.1}NCM955$ compared to LLZO.

The stress inversion observed in the $Li_{0.5}CO$/LLZO system persists under chemo-thermal conditions (Figure 3 c, f and i) and (Figure 4 c, f and i), ascribed to the greater volume expansion of $Li_{0.5}CO$ relative to the volume contraction of LLZO. In contrast, both $Li_{0.5}NCM955$/LLZO and $Li_{0.1}NCM955$/LLZO systems maintain their respective stress types during the chemo-thermal case, due to the higher volume contraction of both $Li_{0.5}NCM955$ and $Li_{0.1}NCM955$ compared to that of LLZO.

3.2. Effect of residual thermal stress on the total induced mechanical stress

3.2.1. Thermal stress

During cooling down after sintering, the composite components undergo a contraction along distinct crystallographic axes (a, b, and c-axes), inducing multidirectional shrinkage. Which in turn forming a thermal strain (ϵ^{Th}), with the thermal expansion coefficient serving as a critical parameter.

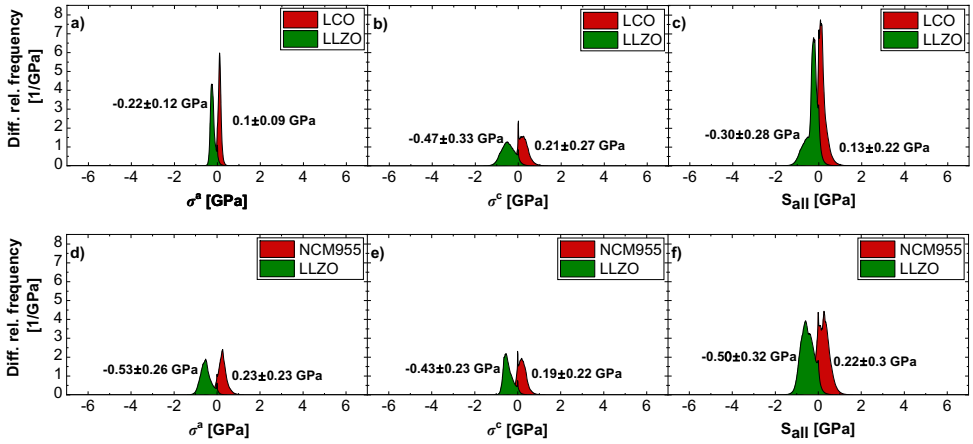

Figure 5. Thermal principal stress (S_{all}) of LCO and NCM955 in the regenerated modelled microstructure a and d) in a-axis, b and e) in c-axis, c and f) the net principal stress.

Thermal strains observed in both LCO and NCM955 are higher than those in LLZO, ascribed to the higher thermal expansion coefficients of LCO and NCM955 compared to LLZO. In essence, LCO and NCM955 exhibit higher sensitivity to thermal treatment relative to LLZO. Consequently, LLZO appears to impede the shrinking of LCO and NCM955, exhibiting a smaller negative volume change compared to the cathode active materials. While this trend is general, it is particularly pronounced in the LCO/LLZO system along the c-axis compared to the a and b-axes. Conversely, in the case of NCM955/LLZO, the effect is more noticeable along both the a and b-axes. Within this framework, both ϵ_{LCO}^{c} and $\epsilon_{LCO}^{a,b}$ exhibit negative sign due to the shrinking process. Resulting a net tensile principal stresses in LCO and compressive principal stress in LLZO along theses axes (Figure 5 a-c). Similar trend and explanation apply for NCM955 (Figure 5 d-f). In our modelled regenerated structure, the overall induced thermal stress of NCM955 S_{all}^{NCM955} is higher than that of LCO S_{all}^{LCO} (0.220± 0.30 GPa and 0.13 ± 0.22 GPa), respectively. (Figure 5 f, c).

3.2.2. Chemical stress

The dissipation of LLZO-induced strains during delithiation of the composite cathode is attributed to the absence of volume change within the LLZO phase.

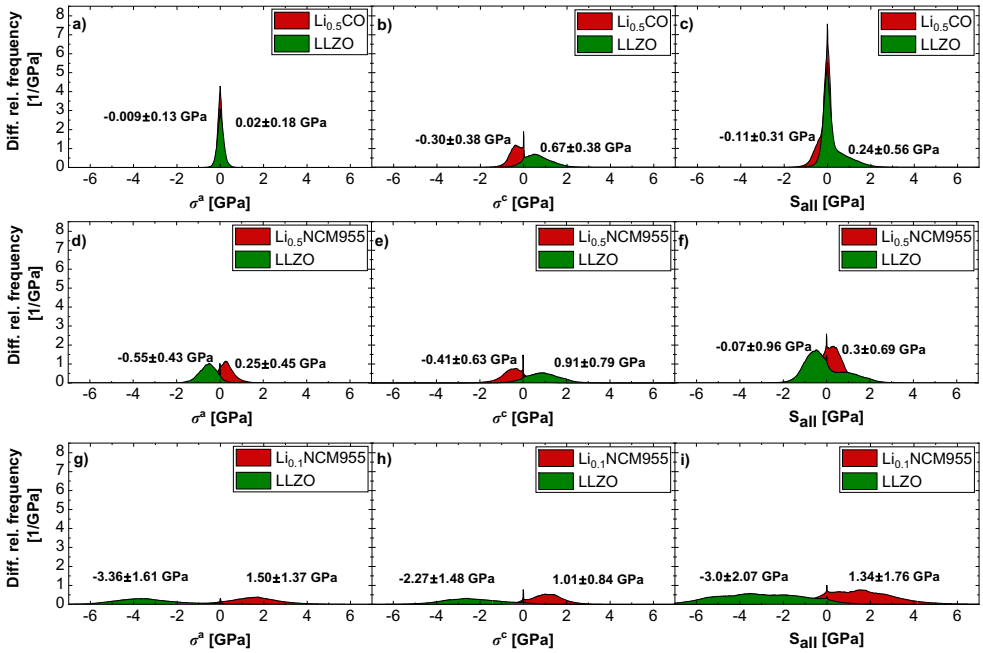

Figure 6. Chemical principal stress (S_{all}) histogram of LCO $Li_{0.5}NCM955$and $Li_{0.1}NCM955$ in the regenerated modelled microstructure, a, d and g) in a-axis, b, e and h) in c-axis, c, f and i) the net principal stress.

$Li_{0.5}CO$ tends to shrink along a and b-axes inducing mechanical stress ascribed to the constrained LLZO phase which hinders the contraction of $Li_{0.5}CO$ along these axes. The value of the strain change increases with distance from the interface between the cathode active material and LLZO. Leading to positive sign of $\sigma_{LCO}^{a,b}$ indicating very mild tensile principal stresses, while on other hand $\sigma_{LLZO}^{a,b}$ will have negative sign, indicating slight compressive principal stress. (Figure 6a). The scenario in the c-axis undergoes a complete inversion. Where, LLZO phase restricts the expansion of LCO along this axis, the total strain values of LCO are gradually increased as we move away of the interface between cathode active materials and LLZO, allowing the cathode active materials to freely expand. A similar trend is observed in LLZO. Where, the strain values decrease gradually as we move away from the interface. In this context, ϵ_{LCO}^{c} exhibits positive sign due to the expansion process. Consequently, the sign of σ_{LCO}^{c} will be negative indicating to a compressive principal stress, while the sign of σ_{LLZO}^{c} LLZO will be positive indicating tensile principal stresses in this direction (Figure 6b). The sign of net principal stress is determined by both the strain in each direction and by the resistance to deformation in each direction. In the LCO/LLZO system, ϵ_{LCO}^{c} is tenfold greater than $\epsilon_{LCO}^{a,b}$. This

leads to higher value of σ_{LCO}^{c} compared to $\sigma_{LCO}^{a,b}$, in spite of that C_{LCO}^{C} is about 0.33 times lower than C_{LCO}^{a}. Resulting in a negative sign of S_{all}^{LCO}, indicative of a net compressive principal stress, while S_{all}^{LLZO} will exhibit a positive sign, indicating a net tensile principal stress (Figure 6c). In our modelled regenerated structure, LCO exhibits a compressive stress of -0.11 ± 0.31 GPa.

Similar behavior is observed in the $Li_{0.5}$NCM955/LLZO system, where the material contracts along both the a and b axes. This contraction induces mechanical stress due to the adjacent LLZO, which impedes the contraction of $Li_{0.5}$NCM955 along these axes. Leading to positive sign of $\sigma_{Li_{0.5}NCM955}^{a,b}$ indicating tensile principal stresses. Conversely, $\sigma_{LLZO}^{a,b}$ exhibits a negative sign, indicating compressive principal stresses. (Figures 6d). Along the c-axis, the scenario is reversed. The LLZO phase restricts the expansion of $Li_{0.5}$NCM955 along this axis. The strain values in $Li_{0.5}$NCM955 gradually increase with distance from the interface between the cathode active material and LLZO, allowing for free expansion of the cathode material. Similarly, in LLZO, strain values gradually decrease with increasing distance from the interface, leading to negative sign of $\sigma_{Li_{0.5}NCM955}^{c}$ indicating to a compressive principal stress, while the sign of σ_{LLZO}^{c} LLZO is positive indicating to a tensile principal stress in this direction (Figure 6e). Despite the value of $\epsilon_{Li_{0.5}NCM955}^{C}$ is about 2.3 times higher than $\epsilon_{Li_{0.5}NCM955}^{a,b}$, which in turn leads to a positive volume change in $Li_{0.5}$NCM955 yet, it is not sufficient enough to overcome the partially tensile stress, ascribed to 0.6 times lower $C_{Li_{0.5}NCM955}^{C}$ compared to $C_{Li_{0.5}NCM955}^{a}$, leaving the induced tensile stress along both a and b-axes to be dominant in the system. Consequently, $S_{all}^{Li_{0.5}NCM955}$ will exhibit a positive sign, indicating a net tensile principal stress of 0.32± 0.69 GPa, while S_{all}^{LLZO} will have a negative sign, indicating a net compressive principal stress (Figure 6f). In the $Li_{0.1}$NCM955/LLZO system, $Li_{0.1}$NCM955 shows similar behavior as NCM955 in the thermal case, where it has a negative volume change owed to the contraction of $Li_{0.1}$NCM955 in all directions leading to an induced tensile principal stress in all direction as well (Figure 6g and h). Consequently, $S_{all}^{Li_{0.1}NCM955}$ will exhibit a positive sign, indicating a net tensile principal stress of 1.34 ± 1.76 GPa for our modelled structure, while S_{all}^{LLZO} exhibits a negative sign, indicating a net compressive principal stress (Figure 6i).

3.2.3. Chemo-thermal stress

The chemo-thermal stress integrates both thermal and chemical contributions and considers the residual stress from cooling after sintering as well as due to electrochemical cycling.

In the LCO/LLZO system, negative strains are induced in both LCO and LLZO due to contraction during cooling after sintering. These negative strains partially offset the positive strains developed in LCO during delithiation, thus reducing the overall strain and minimizing the strain difference between LCO and LLZO in the chemo-thermal phase. Our simulation calculations demonstrate that the net induced compressive stress in $Li_{0.5}CO$ during the delithiation process surpasses the net induced tensile stress during post-sintering cooling. This results in a reduced overall compressive stress within LCO. Similarly, for LLZO, the net induced tensile stress is reduced (Figure 3 a-c and Figure 4 a-c). Our computational model quantifies the chemo-thermal stress in $Li_{0.5}CO$ as -0.02 ± 0.22 GPa (Figure 7a), approximately 43% lower than the induced principal stress during delithiation. The behavior differs markedly in systems using $Li_{0.5}$NCM955 and $Li_{0.1}$NCM955 as cathode active materials with LLZO as the solid electrolyte. For $Li_{0.5}$NCM955, our results show that the negative strains induced during cooling down after sintering amplified the dominant negative strains in a and b-axes during delithiation. While on other hand, it reduces the positive strain along the c-axis induced during delithiation, leading to higher strain differences between $Li_{0.5}$NCM955 and LLZO in the chemo-thermal case. While for $Li_{0.1}$NCM955, the negative strains in NCM955 induced during cooling down after sintering amplifies the negative strains induced during delithiation in all axes. Resulting in a higher net strain and, therefore, a greater strain difference between $Li_{0.1}$NCM955 and LLZO in the chemo-thermal case. In these configurations, both the thermal and chemical stresses in the cathode materials are tensile. Consequently, the net tensile chemo-thermal stress in $Li_{0.5}$NCM955 and $Li_{0.1}$NCM955 is substantially higher than the individual thermal or chemical stresses alone (Figure 3 d-i and Figure 4 d-i). Specifically, our models show chemo-thermal stress values of 0.23 ± 0.78 GPa for $Li_{0.5}$NCM955 and 1.50 ± 2.0 GPa for $Li_{0.1}$NCM955 (Figure 7 b, c). The induced principal stress in $Li_{0.5}$NCM955 and $Li_{0.1}$NCM955 during the chemo-thermal case is approximately 42% and 15% higher, respectively, than during delithiation. This dominant tensile stress environment within these cathode materials aligns with the higher tensile stresses observed during both electrochemical and thermal processes. While for LLZO, in these systems, the net compressive principal stresses are higher than the thermal and chemical stresses (Figure 3 d-i and Figure 4 d-i).

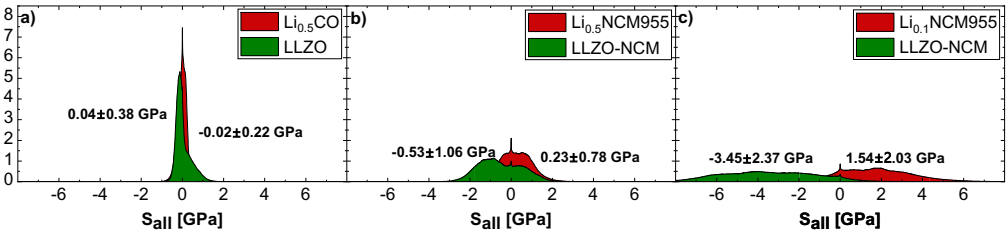

Figure 7. Chemo-thermal net principal stress (S_{all}) histogram in the regenerated modelled microstructure of a) LCO b) $Li_{0.5}$NCM955, and c) $Li_{0.1}$NCM955.

4. Conclusion

In this paper, we emphasize the critical significance of residual stress after sintering on the overall mechanical stress in all-solid-state batteries (ASSBs), while previous researches primarily focused on chemically-induced mechanical stress during delithiation. Our study addresses this gap by accounting for what we term "chemo-thermal" stress. Our findings demonstrate that for LCO, thermal stress significantly reduces the stress induced during delithiation, resulting in a chemo-thermal stress is approximately **43% lower** than the delithiation stress alone. In contrast, for both $Li_{0.5}$NCM955 and $Li_{0.1}$NCM955, the chemo-thermal principal stress in $Li_{0.5}$NCM955 approximately 42% higher when considering delithiation only, ($Li_{0.1}$NCM955 being around 15% higher). This allows us to introduce the chemo-thermal stress as the worst-case scenario which should be addressed. The use of LCO is more reliable than both $Li_{0.5}$NCM955 and $Li_{0.1}$NCM955 regarding to the mechanical properties. This is not only attributed to its lower chemo-thermal stress, but also to the fact that compressive stresses are less likely to cause failure in oxide materials compared to tensile stresses [66]. Moreover, our results show that CAM volume change is not a reliable indicator for comparing mechanical stresses across materials or stress types. Despite $Li_{0.5}$NCM955 exhibiting a lower positive volume change compared to $Li_{0.5}$CO during delithiation, the induced tensile mechanical stress is even higher than the induced compressive mechanical stress in $Li_{0.5}$CO. Our results confirm the findings from our previous study [55] regarding the effect of microstructural design parameters (SVF_{CAM} and $\bar{\rho}$) on mechanical stress. Specifically, the mechanical stress in composite components is inversely proportional to their SVF and directly proportional to their $\bar{\rho}$.

While this study is limited to numerical modeling, different composite cathode samples will be experimentally fabricated and cycled, followed by ex situ XRD measurements to assess their mechanical stresses and validate the modeling approach

Conflicts of interest

The author declares no known competing financial interests or personal relationships that could have appeared to influence the work reported in this paper.

Acknowledgements

The financial support provided by the Federal Ministry of Education and Research of Germany in the framework of the Palestinian-German Science Bridge (PGSB) (BMBF Grant Number 01DH16027), FestBatt2-Oxide (grant no. 13XP0434A), AdamBatt2 (grant no. 13XP0558A) and the financial contributions of Dr. Mariam Al-Jaljouli and Mr. Khalil Abu Ayyash are gratefully acknowledged.

References

[1] M. Finsterbusch, T. Danner, C.-L. Tsai, S. Uhlenbruck, A. Latz, and O. Guillon, High capacity garnet-based all-solid-state lithium batteries: fabrication and 3D-microstructure resolved modeling, ACS applied materials & interfaces 10[26] (2018) 22329-39. https://doi.org/10.1021/acsami.8b06705.

[2] R. Miyazaki, G. Yamaguchi, E. Yagi, T. Yoshida, and T. Tomita, Enhancement of the Li+ Conductivity of Li_3AlF_6 for Stable All-Solid-State Lithium-Ion Batteries, Acs Appl Energ Mater 7[6] (2024) 2533-41. https://doi.org/10.1021/acsaem.4c00115.

[3] K. Kerman, A. Luntz, V. Viswanathan, Y.-M. Chiang, and Z. Chen, Review—Practical Challenges Hindering the Development of Solid State Li Ion Batteries, J. Electrochem. Soc. 164[7] (2017) A1731. https://doi.org/10.1149/2.1571707jes.

[4] J. Janek and W. G. Zeier, A solid future for battery development, Nature energy 1[9] (2016) 1-4. https://doi.org/10.1038/nenergy.2016.141.

[5] T. Yang, J. Zheng, Q. Cheng, Y. Y. Hu, and C. K. Chan, Composite Polymer Electrolytes with $Li_7La_3Zr_2O_{12}$ Garnet-Type Nanowires as Ceramic Fillers: Mechanism of Conductivity Enhancement and Role of Doping and Morphology, ACS Appl. Mater. Interfaces 9[26] (2017) 21773-80. https://doi.org/10.1021/acsami.7b03806.

[6] F. Aguesse, W. Manalastas, L. Buannic, J. M. Lopez del Amo, G. Singh, A. Llordés, and J. Kilner, Investigating the dendritic growth during full cell cycling of garnet electrolyte in direct contact with Li metal, ACS Appl. Mater. Interfaces 9[4] (2017) 3808-16. https://doi.org/10.1021/acsami.6b13925.

[7] R. H. Basappa, T. Ito, T. Morimura, R. Bekarevich, K. Mitsuishi, and H. Yamada, Grain boundary modification to suppress lithium penetration through garnet-type solid electrolyte, J. Power Sources 363 (2017) 145-52. https://doi.org//10.1016/j.jpowsour.2017.07.088.

[8] A. Sharafi, H. M. Meyer, J. Nanda, J. Wolfenstine, and J. Sakamoto, Characterizing the Li–$Li_7La_3Zr_2O_{12}$ interface stability and kinetics as a function of temperature and current density, J. Power Sources 302 (2016) 135-39. https://doi.org/10.1016/j.jpowsour.2015.10.053.

[9] S. Wenzel, T. Leichtweiss, D. Krüger, J. Sann, and J. Janek, Interphase formation on lithium solid electrolytes—An in situ approach to study interfacial reactions by photoelectron spectroscopy, Solid State Ionics 278 (2015) 98-105. https://doi.org/10.1016/j.ssi.2015.06.001.

[10] P. Bron, B. Roling, and S. Dehnen, Impedance characterization reveals mixed conducting interphases between sulfidic superionic conductors and lithium metal electrodes, J. Power Sources 352 (2017) 127-34. https://doi.org//10.1016/j.jpowsour.2017.03.103.

[11] S. Wenzel, S. Randau, T. Leichtweiß, D. A. Weber, J. Sann, W. G. Zeier, and J. r. Janek, Direct observation of the interfacial instability of the fast ionic conductor Li10GeP2S12 at the lithium metal anode, Chem. Mater. 28[7] (2016) 2400-07. https://doi.org//10.1021/acs.chemmater.6b00610.

[12] A. Bates, S. Mukherjee, N. Schuppert, B. Son, J. G. Kim, and S. Park, Modeling and simulation of 2D lithium-ion solid state battery, Int J Energ Res 39[11] (2015) 1505-18. https://doi.org/10.1002/er.3344.

[13] G. Bucci, T. Swamy, S. Bishop, B. W. Sheldon, Y.-M. Chiang, and W. C. Carter, The effect of stress on battery-electrode capacity, J. Electrochem. Soc. 164[4] (2017) A645. https://doi.org//10.1149/2.0371704jes.

[14] G. Bucci, T. Swamy, Y.-M. Chiang, and W. C. Carter, Modeling of internal mechanical failure of all-solid-state batteries during electrochemical cycling, and implications for battery design, J Mater Chem A 5[36] (2017) 19422-30. https://doi.org/10.1039/C7TA03199H.

[15] A. Mukhopadhyay and B. W. Sheldon, Deformation and stress in electrode materials for Li-ion batteries, Progress in Materials Science 63 (2014) 58-116. https://doi.org/10.1016/j.pmatsci.2014.02.001.

[16] Y. He, C. Lu, S. Liu, W. Zheng, and J. Luo, Interfacial Incompatibility and Internal Stresses in All-Solid-State Lithium Ion Batteries, Adv Energy Mater 9[36] (2019) 1901810. https://doi.org/10.1002/aenm.201901810.

[17] P. Li, Y. B. Zhao, Y. X. Shen, and S. H. Bo, Fracture behavior in battery materials, J Phys-Energy 2[2] (2020). https://doi.org//10.1088/2515-7655/ab83e1.

[18] J. Auborn and Y. Barberio, Lithium Intercalation Cells Without Metallic Lithium: and, J. Electrochem. Soc. 134[3] (1987) 638. https://doi.org/10.1149/1.2100521.

[19] T. Nagaura and K. Tozawa, Progress in batteries and solar cells, JEC Press 9 (1990) 209. https://doi.org/10.1541/ieejfms1990.115.4_349

[20] B. Wang, J. Bates, F. Hart, B. Sales, R. Zuhr, and J. Robertson, Characterization of thin-film rechargeable lithium batteries with lithium cobalt oxide cathodes, J. Electrochem. Soc. 143[10] (1996) 3203. https://doi.org/10.1149/1.1837188.

[21] A. Kannan, L. Rabenberg, and A. Manthiram, High capacity surface-modified LiCoO2 cathodes for lithium-ion batteries, Electrochem Solid St 6[1] (2002) A16. https://doi.org//10.1149/1.1526782.

[22] Y. J. Kim, H. Kim, B. Kim, D. Ahn, J.-G. Lee, T.-J. Kim, D. Son, J. Cho, Y.-W. Kim, and B. Park, Electrochemical stability of thin-film LiCoO2 cathodes by aluminum-oxide coating, Chem. Mater. 15[7] (2003) 1505-11. https://doi.org/10.1021/cm0201403.

[23] C. Daniel, D. Mohanty, J. Li, and D. L. Wood, Cathode materials review, AIP Conference Proceedings 1597[1] (2014) 26-43. https://doi.org/10.1063/1.4878478.

[24] C. Wang, G. Bai, X. Liu, and Y. Li, Favorable electrochemical performance of $LiMn_2O_4$/$LiFePO_4$ composite electrodes attributed to composite solid electrolytes for all-solid-state lithium batteries, Langmuir 37[7] (2021) 2349-54. https://doi.org/10.1021/acs.langmuir.0c03274.

[25] S. Klein, P. Bärmann, T. Beuse, K. Borzutzki, J. E. Frerichs, J. Kasnatscheew, M. Winter, and T. Placke, Exploiting the Degradation Mechanism of NCM523 Graphite Lithium-Ion Full Cells Operated at High Voltage, ChemSusChem 14[2] (2021) 595-613. https://doi.org/10.1002/cssc.202002113.

[26] J.-P. Hu, H. Sheng, Q. Deng, Q. Ma, J. Liu, X.-W. Wu, J.-J. Liu, and Y.-P. Wu, High-rate layered cathode of lithium-ion batteries through regulating three-dimensional agglomerated structure, Energies 13[7] (2020) 1602. https://doi.org/10.3390/en13071602.

[27] L. de Biasi, A. O. Kondrakov, H. Geßwein, T. Brezesinski, P. Hartmann, and J. r. Janek, Between scylla and charybdis: balancing among structural stability and energy density of layered NCM cathode materials for advanced lithium-ion batteries, The Journal of Physical Chemistry C 121[47] (2017) 26163-71. https://doi.org/10.1021/acs.jpcc.7b06363.

[28] Y.-K. Sun, High-Capacity Layered Cathodes for Next-Generation Electric Vehicles, ACS Energy Letters 4[5] (2019) 1042-44. https://doi.org/10.1021/acsenergylett.9b00652.

[29] X. Yan, L. Zhang, and J. Lu, Improve safety of high energy density $LiNi_{1/3}Co_{1/3}Mn_{1/3}O_2$ graphite battery using organosilicon electrolyte, Electrochimica Acta 296 (2019) 149-54. https://doi.org/10.1016/j.electacta.2018.11.036.

[30] J.-H. Kim, K.-J. Park, S. J. Kim, C. S. Yoon, and Y.-K. Sun, A method of increasing the energy density of layered Ni-rich $Li[Ni_{1-2x}Co_xMn_x]O_2$ cathodes (x = 0.05, 0.1, 0.2), Journal of Materials Chemistry A 7[6] (2019) 2694-701. https://doi.org/10.1039/C8TA10438G.

[31] Z. Lu, D. D. MacNeil, and J. R. Dahn, Layered Cathode Materials $Li[Ni_x Li_{(1/3-2x/3)} Mn_{(2/3-x/3)}]O_2$ for Lithium-Ion Batteries, Electrochemical and Solid-State Letters 4[11] (2001) A191. https://doi.org/10.1149/1.1407994.

[32] N. Yabuuchi and T. Ohzuku, Novel lithium insertion material of $LiCo_{1/3}Ni_{1/3}Mn_{1/3}O_2$ for advanced lithium-ion batteries, J. Power Sources 119-121 (2003) 171-74. https://doi.org/10.1016/S0378-7753(03)00173-3.

[33] W. Li, B. Song, and A. Manthiram, High-voltage positive electrode materials for lithium-ion batteries, Chem Soc Rev 46[10] (2017) 3006-59. https://doi.org/10.1039/C6CS00875E.

[34] A. Manthiram, J. C. Knight, S. T. Myung, S. M. Oh, and Y. K. Sun, Nickel-rich and lithium-rich layered oxide cathodes: progress and perspectives, Advanced Energy Materials 6[1] (2016) 1501010. https://doi.org/10.1002/aenm.201501010.

[35] Y. Xi, Y. Liu, D. Zhang, S. Jin, R. Zhang, and M. Jin, Comparative study of the electrochemical performance of $LiNi_{0.5}Co_{0.2}Mn_{0.3}O_2$ and $LiNi_{0.8}Co_{0.1}Mn_{0.1}O_2$ cathode materials for lithium ion batteries, Solid State Ionics 327 (2018) 27-31. https://doi.org/10.1016/j.ssi.2018.10.020.

[36] J. Gong, Q. Wang, and J. Sun, Thermal analysis of nickel cobalt lithium manganese with varying nickel content used for lithium ion batteries, Thermochim. Acta 655 (2017) 176-80. https://doi.org/10.1016/j.tca.2017.06.022.

[37] X. Liu, X. Wang, B. Yue, G. Liu, W. Yu, X. Dong, and J. Wang, Preparation of hierarchical $LiNi_xCo_yMn_zO_2$ from solvothermal $[Ni_xCo_yMn_z](OH)_2$ via regulating the ratio of Ni, Co, and Mn and its excellent properties for lithium-ion battery cathode, Journal of the Chinese Chemical Society 67[11] (2020) 2062-70. https://doi.org/10.1002/jccs.202000051.

[38] J. Oh, J. Kim, Y. M. Lee, D. O. Shin, J. Y. Kim, Y.-G. Lee, and K. M. Kim, High-rate cycling performance and surface analysis of $LiNi_{1-x}Co_{x/2}Mn_{x/2}O_2$ (x=2/3, 0.4, 0.2) cathode materials, Mater. Chem. Phys. 222 (2019) 1-10. https://doi.org/10.1016/j.matchemphys.2018.09.076.

[39] Y. Duan, S.-P. Chen, L. Zhang, L. Guo, and F.-N. Shi, Review on Oxygen Release Mechanism and Modification Strategy of Nickel-Rich NCM Cathode Materials for Lithium-Ion Batteries: Recent Advances and Future Directions, Energy & Fuels 38[7] (2024) 5607-31. https://doi.org/10.1021/acs.energyfuels.3c04636.

[40] R. Murugan, V. Thangadurai, and W. Weppner, Fast lithium ion conduction in garnet-type $Li_7La_3Zr_2O_{12}$, Angewandte Chemie-International Edition, 46[41] (2007) 7778. https://doi.org/10.1002/anie.200701144.

[41] C.-L. Tsai, E. Dashjav, E.-M. Hammer, M. Finsterbusch, F. Tietz, S. Uhlenbruck, and H. P. Buchkremer, High conductivity of mixed phase Al-substituted $Li_7La_3Zr_2O_{12}$, Journal of Electroceramics 35[1] (2015) 25-32. https://doi.org/10.1007/s10832-015-9988-7.

[42] H. Buschmann, J. Dölle, S. Berendts, A. Kuhn, P. Bottke, M. Wilkening, P. Heitjans, A. Senyshyn, H. Ehrenberg, and A. Lotnyk, Structure and dynamics of the fast lithium ion

conductor "$Li_7La_3Zr_2O_{12}$", Phys. Chem. Chem. Phys. 13[43] (2011) 19378-92. https://doi.org/10.1039/C1CP22108F

[43] C.-L. Tsai, V. Roddatis, C. V. Chandran, Q. Ma, S. Uhlenbruck, M. Bram, P. Heitjans, and O. Guillon, $Li_7La_3Zr_2O_{12}$ Interface Modification for Li Dendrite Prevention, ACS Applied Materials & Interfaces 8[16] (2016) 10617-26. https://doi.org/10.1021/acsami.6b00831.

[44] F. Yonemoto, A. Nishimura, M. Motoyama, N. Tsuchimine, S. Kobayashi, and Y. Iriyama, Temperature effects on cycling stability of Li plating/stripping on Ta-doped $Li_7La_3Zr_2O_{12}$, J. Power Sources 343 (2017) 207-15. https://doi.org/10.1016/j.jpowsour.2017.01.009.

[45] C. A. Geiger, E. Alekseev, B. Lazic, M. Fisch, T. Armbruster, R. Langner, M. Fechtelkord, N. Kim, T. Pettke, and W. Weppner, Crystal Chemistry and Stability of "$Li_7La_3Zr_2O_{12}$" Garnet: A Fast Lithium-Ion Conductor, Inorg. Chem. 50[3] (2011) 1089-97. https://doi.org/10.1021/ic101914e.

[46] G. Larraz, A. Orera, and M. Sanjuán, Cubic phases of garnet-type $Li_7La_3Zr_2O_{12}$: the role of hydration, J Mater Chem A 1[37] (2013) 11419-28. https://doi.org/10.1039/C3TA11996C

[47] L. Miara, A. Windmüller, C.-L. Tsai, W. D. Richards, Q. Ma, S. Uhlenbruck, O. Guillon, and G. Ceder, About the Compatibility between High Voltage Spinel Cathode Materials and Solid Oxide Electrolytes as a Function of Temperature, ACS Appl. Mater. Interfaces 8[40] (2016) 26842-50. https://doi.org/10.1021/acsami.6b09059.

[48] Y. Ren, T. Liu, Y. Shen, Y. Lin, and C.-W. Nan, Chemical compatibility between garnet-like solid state electrolyte $Li_{6.75}La_3Zr_{1.75}Ta_{0.25}O_{12}$ and major commercial lithium battery cathode materials, Journal of Materiomics 2[3] (2016) 256-64. https://doi.org/10.1016/j.jmat.2016.04.003.

[49] S. Uhlenbruck, J. Dornseiffer, S. Lobe, C. Dellen, C.-L. Tsai, B. Gotzen, D. Sebold, M. Finsterbusch, and O. Guillon, Cathode-electrolyte material interactions during manufacturing of inorganic solid-state lithium batteries, Journal of Electroceramics 38[2] (2017) 197-206. https://doi.org/10.1007/s10832-016-0062-x.

[50] L. J. Miara, W. D. Richards, Y. E. Wang, and G. Ceder, First-Principles Studies on Cation Dopants and Electrolyte|Cathode Interphases for Lithium Garnets, Chemistry of Materials 27[11] (2015) 4040-47. https://doi.org/10.1021/acs.chemmater.5b01023.

[51] N. Zhang, X. Long, Z. Wang, P. Yu, F. Han, J. Fu, G. Ren, Y. Wu, S. Zheng, W. Huang, C. Wang, H. Li, and X. Liu, Mechanism Study on the Interfacial Stability of a Lithium Garnet-Type Oxide Electrolyte against Cathode Materials, ACS Applied Energy Materials 1[11] (2018) 5968-76. https://doi.org/10.1021/acsaem.8b01035.

[52] K. J. Kim, M. Balaish, M. Wadaguchi, L. Kong, and J. L. M. Rupp, Solid-State Li–Metal Batteries: Challenges and Horizons of Oxide and Sulfide Solid Electrolytes and Their Interfaces, Adv Energy Mater 11[1] (2021) 2002689. https://doi.org/10.1002/aenm.202002689.

[53] C. Roitzheim, Y. J. Sohn, L.-Y. Kuo, G. Häuschen, M. Mann, D. Sebold, M. Finsterbusch, P. Kaghazchi, O. Guillon, and D. Fattakhova-Rohlfing, All-Solid-State Li Batteries with NCM–Garnet-Based Composite Cathodes: The Impact of NCM Composition on Material Compatibility, Acs Appl Energ Mater 5[6] (2022) 6913-26. https://doi.org/10.1021/acsaem.2c00533.

[54] A. Bauer, C. Roitzheim, S. Lobe, Y. J. Sohn, D. Sebold, W. S. Scheld, M. Finsterbusch, O. Guillon, D. Fattakhova-Rohlfing, and S. Uhlenbruck, Impact of Ni–Mn–Co–Al-Based Cathode Material Composition on the Sintering with Garnet Solid Electrolytes for All-Solid-State Batteries, Chem. Mater. 35[21] (2023) 8958-68. https://doi.org/10.1021/acs.chemmater.3c01573.

[55] F. Al-Jaljouli, R. Mücke, P. Kaghazchi, Y. J. Sohn, M. Finsterbusch, D. Fattakhova-Rohlfing, and O. Guillon, Microstructural parameters governing the mechanical stress and conductivity of all-solid-state lithium-ion-battery cathodes, Journal of Energy Storage 68 (2023) 107784. https://doi.org/10.1016/j.est.2023.107784.

[56] M. Mann, M. Küpers, G. Häuschen, M. Finsterbusch, D. Fattakhova-Rohlfing, and O. Guillon, The influence of hafnium impurities on the electrochemical performance of tantalum substituted

$Li_7La_3Zr_2O_{12}$ solid electrolytes, Ionics 28[1] (2022) 53-62. https://doi.org/10.1007/s11581-021-04300-w.

[57] M. Mann, M. Küpers, G. Häuschen, M. Finsterbusch, D. Fattakhova-Rohlfing, and O. Guillon, Evaluation of Scalable Synthesis Methods for Aluminum-Substituted Li7La3Zr2O12 Solid Electrolytes, Materials 14[22] (2021) 6809. https://doi.org/10.3390/ma14226809.

[58] Z. D. Hood, Y. Zhu, L. J. Miara, W. S. Chang, P. Simons, and J. L. M. Rupp, A sinter-free future for solid-state battery designs, Energy & Environmental Science 15[7] (2022) 2927-36. https://doi.org/10.1039/D2EE00279E.

[59] R. Mücke, M. Finsterbusch, P. Kaghazchi, D. Fattakhova-Rohlfing, and O. Guillon, Modelling electro-chemical induced stresses in all-solid-state batteries: Anisotropy effects in cathodes and cell design optimisation, J. Power Sources 489 (2021) 229430. https://doi.org/10.1016/j.jpowsour.2020.229430.

[60] M. Tanemura, T. Ogawa, and N. Ogita, A new algorithm for three-dimensional Voronoi tessellation, J. Comput. Phys. 51[2] (1983) 191-207. https://doi.org/10.1016/0021-9991(83)90087-6.

[61] R. Varadhan and P. Gilbert, BB: An R package for solving a large system of nonlinear equations and for optimizing a high-dimensional nonlinear objective function, Journal of statistical software 32 (2010) 1-26. https://doi.org/10.18637/jss.v032.i04.

[62] P. E. Blöchl, Projector augmented-wave method, Phys Rev B 50[24] (1994) 17953-79. https://doi.org/10.1103/PhysRevB.50.17953.

[63] G. Kresse and J. Furthmüller, Efficient iterative schemes for ab initio total-energy calculations using a plane-wave basis set, Phys Rev B 54[16] (1996) 11169-86. https://doi.org/10.1103/PhysRevB.54.11169.

[64] J. P. Perdew, K. Burke, and M. Ernzerhof, Generalized Gradient Approximation Made Simple, Phys. Rev. Lett. 77[18] (1996) 3865-68. https://doi.org/10.1103/PhysRevLett.77.3865.

[65] S. Yamakawa, N. Nagasako, H. Yamasaki, T. Koyama, and R. Asahi, Phase-field modeling of stress generation in polycrystalline $LiCoO_2$, Solid State Ionics 319 (2018) 209-17. https://doi.org/10.1016/j.ssi.2018.02.013.

[66] R. Mücke, N. Yaqoob, M. Finsterbusch, F. Al-Jaljouli, P. Kaghazchi, D. Fattakhova-Rohlfing, and O. Guillon, Modelling electro-chemically induced stresses in all-solid-state batteries: screening electrolyte and cathode materials in composite cathodes, J Mater Chem A 11[35] (2023) 18801-10. https://doi.org/10.1039/D3TA01729J.

[67] A.-N. Wang, J. F. Nonemacher, G. Yan, M. Finsterbusch, J. Malzbender, and M. Krüger, Mechanical properties of the solid electrolyte Al-substituted $Li_7La_3Zr_2O_{12}$ (LLZO) by utilizing micro-pillar indentation splitting test, J. Eur. Ceram. Soc. 38[9] (2018) 3201-09. https://doi.org/10.1016/j.jeurceramsoc.2018.02.032.

[68] J. E. Ni, E. D. Case, J. S. Sakamoto, E. Rangasamy, and J. B. Wolfenstine, Room temperature elastic moduli and Vickers hardness of hot-pressed LLZO cubic garnet, J. Mater. Sci. 47[23] (2012) 7978-85. https://doi.org/10.1007/s10853-012-6687-5.

[69] S. Yu, R. D. Schmidt, R. Garcia-Mendez, E. Herbert, N. J. Dudney, J. B. Wolfenstine, J. Sakamoto, and D. J. Siegel, Elastic Properties of the Solid Electrolyte $Li_7La_3Zr_2O_{12}$ (LLZO), Chemistry of Materials 28[1] (2016) 197-206. https://doi.org/10.1021/acs.chemmater.5b03854.

[70] X. Wang, I. Loa, K. Kunc, K. Syassen, and M. Amboage, Effect of pressure on the structural properties and Raman modes of $LiCoO_2$, Phys Rev B 72[22] (2005) 224102. https://doi.org/10.1103/PhysRevB.72.224102.

[71] Y. Takahashi, N. Kijima, K. Dokko, M. Nishizawa, I. Uchida, and J. Akimoto, Structure and electron density analysis of electrochemically and chemically delithiated $LiCoO_2$ single crystals, J. Solid State Chem. 180[1] (2007) 313-21. https://doi.org/10.1016/j.jssc.2006.10.018.

[72] H. Moulinec and P. Suquet, A numerical method for computing the overall response of nonlinear composites with complex microstructure, Comput. Meth. Appl. Mech. Eng. 157[1-2] (1998) 69-94. https://doi.org/10.1016/S0045-7825(97)00218-1.

[73] M. Schneider, F. Ospald, and M. Kabel, Computational homogenization of elasticity on a staggered grid, International Journal for Numerical Methods in Engineering 105[9] (2016) 693-720. https://doi.org/10.1002/nme.5008.

Supplementary material

Chemo-Thermal Stress in All-Solid-State Batteries: Impact of Cathode Active Materials and Microstructure

Fadi Al-Jaljouli [a,b], Robert Mücke [a], Christoph Roitzheim [a] Yoo Jung Sohn [a]

Najma Yaqoob [a,d], Martin Finsterbusch [a,c], Payam Kaghazchi [a,d] and Olivier Guillon [a,b,c,e]

[a] *Forschungszentrum Jülich GmbH, Institute of Energy Materials and Devices, Materials Synthesis and Processing (IMD-2), 52425, Jülich, Germany*

[b] *Institute of Mineral Engineering, RWTH Aachen University, 52064 Aachen,Germany*

[c] *Jülich Aachen Research Alliance: JARA-Energy, Jülich, 52425, Germany*

[d] *MESA+ Institute for Nanotechnology, University of Twente, P. O. Box 217, Enschede, 7500AE, The Netherlands*

[e] *Helmholtz Institute Münster: Ionics in Energy Storage (IMD-4 / HI MS), Münster 48149, Germany*

Emails: f.al-jaljouli@fz-juelich.de, r.muecke@fz-juelich.de, c.roitzheim@fz-juelich.de, y.sohn@fz-juelich.de, n.yaqoob@fz-juelich.de, m.finsterbusch@fz-juelich.de, p.kaghazchi@fz-juelich.de, o.guillon@fz-juelich.de

• Calculating input parameters of thermal stress

Fabrication process of composite cathode of all-solid-state lithium-ion batteries involve co-sintering process at high temperature above 1000 °C, followed by cooling down to room temperature. A residual induced mechanical stress arises ascribed to thermal mismatch between cathode active material (CAM) and solid electrolyte (SE), due to difference between coefficient of thermal expansion between theses two components in the system.[1]

During cooling down after sintering both CAM and SE are expected to shrink, in our research, LLZO which is characterized by a cubic crystallographic microstructure had been utilized as SE. Hence. it will only exhibit an isotropic behavior. On other hand, LCO and NCM_{955} which are serving as CAM in the system have layered atomic structure. Hence, they will anisotropically shrink. The resulted thermal induced mechanical stress can be evaluated by:

$$(\sigma_{SE})^{Th} = E(\epsilon_{SE})^{Th}$$

$$\left(\sigma_{CAM}^{i}\right)^{Th} = \sum_{i=1}^{6} C_{ij}\left(\epsilon_{CAM}^{i}\right)^{Th} \qquad (i = a, b, c)$$

Where, E is the elastic modulus of solid electrolyte, $\left(\epsilon_{CAM}^{i}\right)^{Th}$ and $(\epsilon_{SE})^{Th}$ are the thermal strains of cathode active material and solid electrolyte respectively and C_{ij} is the stiffness tensor of the cathode active material.

The lattice parameters at different temperatures of LLZO:Ta, LCO, and NCM_{955} powders were determined based on in-situ high temperature XRD (HT-XRD) at an Empyrean (Malvern Panalytical Ltd, Malvern, UK) with Cu-K_α radiation.The sample was in the heating chamber with Kapton window, and heated from room temperature to 1000°C for LCO while to 900°C for NCM955 in every 100°C step. The in-situ measurements were performed in air for isotherms at the selected temperatures of 25, 100, 200, 300, 400, 500, 600, 700, 800, 900 and 1000°C. The applied heating rate for reaching the next temperature was 5 $Kmin^{-1}$. An interval of 10–80 2θ, a step width of 0.026° and an accumulation time of 200 s by using a 255 channel PIXcel detector were chosen so that the resulting holding time at the selected temperatures during the in-situ measurement was roughly 37 min. The pattern recorded were further investigated by Rietveld analysis within the software package Topas V 4.2 (Bruker Corporation, Billerica, MA, USA) [2]. Thermal strains and calculated coefficients of thermal expansion of LCO and LLZO are presented in Table S1, while the results for NCM955 are presented in Table S2

Table S4. Strain measurements and resultant secant coefficients of thermal expansion for LCO in a and c direction and of LLZO, as a function of temperature.

T [°C]	ϵ^a_{LCO}	α^a_{LCO} $[K^{-1}]$	ϵ^c_{LCO}	α^c_{LCO} $[K^{-1}]$	ϵ_{LLZO}	α_{LLZO} $[K^{-1}]$
25	0		0		0	
600	0.00603	1.05E-05	0.01159	2.02E-05	0.00826	1.44E-05
700	0.00781	1.16E-05	0.01415	2.10E-05	0.00997	1.48E-05
800	0.00958	1.24E-05	0.01657	2.14E-05	0.01166	1.50E-05
900	0.01278	1.46E-05	0.02091	2.39E-05	0.01325	1.51E-05
950	0.01526	1.64E-05	0.02361	2.54E-05	0.01405	1.52E-05
1000	0.01775	1.82E-05	0.02632	2.70E-05	0.01486	1.52E-05

Table S5. Strain measurements and resultant secant coefficients of thermal expansion for NCM_{955} in a and c direction, as a function of temperature.

T [°C]	ϵ^{a}_{NCM955}	$\alpha^{a}_{NCM955}[K^{-1}]$	ϵ^{c}_{NCM955}	$\alpha^{c}_{NCM955}[K^{-1}]$
25	0		0	
100	0.000695	9.27E-06	0.00162	2.16E-05
200	0.002086	1.19E-05	0.003873	2.21E-05
300	0.003476	1.26E-05	0.006197	2.25E-05
400	0.004866	1.30E-05	0.008592	2.29E-05
500	0.006257	1.32E-05	0.010986	2.31E-05
600	0.007994	1.39E-05	0.013099	2.28E-05
700	0.01008	1.49E-05	0.015352	2.27E-05
800	0.013208	1.70E-05	0.017606	2.27E-05
900	0.019117	2.18E-05	0.017606	2.01E-05

- # References

[1] E.J. Cheng, N.J. Taylor, J. Wolfenstine, J. Sakamoto, Journal of Asian Ceramic Societies, 5 (2017) 113-117.
[2] B.A. Topas, User's Manual, Bruker AXS, Karlsruhe, Germany, (2008).

3.3. Paper III: Modeling Chemo-Thermal Mechanical Stresses in All-Solid-State Lithium Batteries: Influence of Grain Morphology and Alignment

Authors	**Fadi Al-Jaljouli**, Robert Mücke, Martin Finsterbusch, Payam Kaghazchi and Olivier Guillon
Journal	Journal of power sources
Volume	653
Pages	237539
Published on	July 2025
DOI	10.1016/j.jpowsour.2025.237539

The following constitute my sole contributions:

- Generation of microstructures with different component's morphologies while varying the SVF_{LCO} and $\bar{\rho}$.
- Generation of microstructures with different fiber's alignments while varying SVF_{LCO}.
- Mechanical characterization of the regenerated samples.
- Analyzing and explaining the impact of grains alignments on mechanical stresses.
- Analyzing and explaining the impact of facet-specific contact interface between LCO and LLZO grains on mechanical stresses.
- Writing the entire manuscript.
- Authoring the complete supporting information.
- Creation of all figures in the manuscript and supporting information.

Modeling Chemo-Thermal Mechanical Stresses in All-Solid-State Lithium Batteries: Influence of Grain Morphology and Alignment

Fadi Al-Jaljouli,[*[a,b]] Robert Mücke,[[a]] Martin Finsterbusch,[[a,e]] Payam Kaghazchi,[[a,d]] and Olivier Guillon[[a,b,c,e]]

[a] *Forschungszentrum Jülich GmbH, Institute of Energy Materials and Devices, Materials Synthesis and Processing (IMD-2), 52425, Jülich, Germany*

[b] *Institute of Mineral Engineering, RWTH Aachen University, 52064 Aachen, Germany*

[c] *Jülich Aachen Research Alliance: JARA-Energy, Jülich, 52425, Germany*

[d] *MESA+ Institute for Nanotechnology, University of Twente, P. O. Box 217, Enschede, 7500AE, The Netherlands*

[e] *Helmholtz Institute Münster: Ionics in Energy Storage (IMD-4 / HI MS), Münster 48149, Germany;*

Emails: f.al-jaljouli@fz-juelich.de, r.muecke@fz-juelich.de, m.finsterbusch@fz-juelich.de, p.kaghazchi@fz-juelich.de, o.guillon@fz-juelich.de

Abstract

All-solid-state batteries (ASSBs) are gaining attraction as a safer and more efficient alternative to traditional liquid lithium-ion batteries due to their use of solid electrolytes. However, the advancement of ASSBs is hindered by challenges such as mechanical stress induced by volume changes in the cathode active material (CAM) during cycling. This study investigates the impact of composite cathode grain morphology on the induced mechanical stress within the composite cathode, specifically focusing on the configurations involving spherical and hexagonal $LiCoO_2$ (LCO) paired with spherical and fiber-shaped garnet-type $Li_7La_3Zr_2O_{12}$ (LLZO) electrolytes. Four distinct systems are analyzed: spherical LCO-spherical LLZO, spherical LCO-fiber LLZO, hexagonal LCO-spherical LLZO, and hexagonal LCO-fiber LLZO. By generating modeled microstructures, we investigate the effects of the solid volume fraction of LCO and porosity on the induced chemo-thermal mechanical stress, reflecting real-life scenarios considering induced stresses after sintering. Our findings reveal that fiber LLZO in conjunction with textured hexagonal LCO reduces the induced mechanical stress in both components by 11.0% for LCO and 9.0% for LLZO. In contrast, the use of randomly oriented spherical LCO in the composite leads to higher induced mechanical stresses in both LCO and LLZO. The alignment of fiber LLZO critically influences the stress type within the system due to facet-specific contact interfaces, underscoring the importance of grain morphology in optimizing the mechanical performance of ASSBs.

Keywords: All-solid-state lithium batteries, Grain morphology, Garnet electrolyte, Cathode active material, Microstructural design parameters.

1. Introduction

All-solid-state batteries (ASSBs) have attracted considerable research attention as a promising alternative to conventional liquid lithium-ion batteries (LIBs). Due to the use of solid electrolytes replacing liquid electrolytes, ASSBs offer enhanced safety and higher energy density [1-3] by enabling the coupling of high-capacity electrode materials like Li metal, they contribute to higher energy densities. However, the advancement of ASSBs is still impeded by critical challenges, including the formation of detrimental chemical reactions at the interface between the cathode active material and the solid electrolyte [4-6]. Moreover, the formation of dendrites under high current continues to pose a significant and persistent challenge for researchers. [7-10]. The significant degradation observed during cycling, attributed to mechanical fatigue [11-13], also remains an unresolved challenge.

The cathode plays a critical role in determining the areal capacity and energy density in ASSBs. To achieve high energy ASSBs, a thick composite cathode is utilized, consisting of intertwined solid electrolyte and cathode active material (CAM) particles. This configuration ensures percolating pathways for efficient ion and electron transport. However, the application of stiff solid electrolytes introduces a significant drawback, as their rigidity constrains the volume changes of the active material during cycling, which is the primary cause of mechanical stress within the composite cathode, potentially inducing microcracks propagating throughout the entire cell [14-16], which in turn leads to capacity fade.

Researchers have applied various strategies to mitigate induced mechanical stresses, emphasizing the development of CAMs. The introduction of so-called “zero-strain” CAMs (NCM271 and NCM361) is one such approach. However, these materials do not keep a constant volume and are anisotropic during the delithiation process. [17-19]. While the mixing of CAMs with opposite strain signs (e.g., LCO with NCM) achieves a net zero strain at the component level, it continues to induce stresses at the grain level. [20]. The scope of efforts has broadened to include the incorporation of additives as an additional approach. Researchers have found that integrating elastomer binders into the composite cathode can reduce induced mechanical stresses, but this reduction is accompanied by a decrease in capacity, which limits the use of

elastomer binders to low concentrations [21,22]. He, YaoLong, et al. reported a capacity fade of the graphite and silicon anodes ascribed to stresses within the solid electrolyte interphase [23]. $LiCoO_2$ (LCO) is particularly noted for its remarkable stability and high capacity among CAMs composed of layered transition metal oxides [24-28]. It exhibits a hexagonal layered α-$NaFeO_2$ structure where the layers of octahedra CoO_6 are aligned perpendicular to the c-axis, corresponding to the {001} facets. In contrast, the hexagonal crystal's six-sided facets, indexed as {010} facets, are oriented perpendicular to the {001} planes (Figure 1). Nevertheless, LCO is associated with several negative aspects, including toxicity and high materials costs. Furthermore, its inherent structural instability detrimentally impacts its electrochemical performance, resulting in a practical capacity that is only approximately 50% of its theoretical potential [29,30].

Garnet-type $Li_7La_3Zr_2O_{12}$ (LLZO) with different dopants such as Al and Ta has garnered considerable attention from researchers within the broad spectrum of solid lithium-ion conductors. This material is distinguished by its high ionic conductivity, which can exceed 1 mS/cm at room temperature, and its inherently low electronic conductivity. Furthermore, LLZO possesses a broad electrochemical stability window and exhibits exceptional chemical and electrochemical stability when interfaced with lithium metal.[31-35].

The thermodynamic stability of LLZO/CAM mixtures is driven by the necessity of high-temperature co-sintering of the solid electrolyte (SE) and cathode active material (CAM) at temperatures above 1000 °C. This high-temperature requirement poses significant challenges, primarily due to material compatibility issues and formation of interdiffusion layers as a result of undesirable side reactions among interface between LLZO and LCO which might lead to degradation of the cell’s electrochemical performance ascribed to hindering of the de-/lithiation process. Which have been widely studied by various research groups [36-38].

Among the various CAMs used in LIBs, LCO has demonstrated thermodynamic stability when combined with LLZO at elevated temperatures. In contrast, other CAMs such as NCM, $LiNi_{0.8}Co_{0.15}Al_{0.05}O_2$ (NCA), $LiMn_2O_4$ (LMO) and $LiFePO_4$ (LFP) react with LLZO at moderate temperatures between 400 °C and 800 °C.

Grain morphologies have been the focus of limited research. Jeon et al. concluded that the shape and facet design of CAMs significantly influence solid-solid ion migration, suggesting that

single-crystalline octahedral NCM particles enhance Li-ion diffusion at the interface between the solid electrode and solid electrolyte in ASSBs [39]. Meanwhile, Wu et al. found that LCO flakes exhibit high specific capacity, excellent rate performance, and remarkable cycling stability over a wide range of operating temperatures [40].

Despite various studies investigating the effect of fiber LLZO in the solid electrolyte [41-45], none of the previous researches has addressed the impact of component grain morphologies on the induced mechanical stress in ASSBs.

In this research, we investigate the effect of composite cathode grain morphology on the induced mechanical stress within the composite cathode. Model microstructures were generated, incorporating spherical and hexagonal shapes of LCO alongside spherical and fiber-shaped LLZO. This approach leads to the formation of four distinct systems: spherical LCO-spherical LLZO, spherical LCO-fiber LLZO, hexagonal LCO-spherical LLZO, and hexagonal LCO-fiber LLZO. For each configuration, we analyze the effects of the solid volume fraction of LCO and the porosity on the induced chemo-thermal mechanical stress, which accurately reflects real-life scenarios, as it considers the mechanical stress induced by cooling down to room temperature after sintering. Additionally, we examine the impact of the random orientation of spherical LCO and the alignment of fiber LLZO on the type and magnitude of the induced mechanical stress. Notably, this research excludes the effects of grain sizes for both the CAM and SE, since our previous study demonstrated that the induced mechanical stress is independent from the grain size of the microstructural components [46].

2. Methods

2.1. Synthesis and acquisition of experimental structure

The composite cathode, consisting of $LiCoO_2$ (LCO) and Ta, Al-doped LLZO (abbreviated as LLZO, $Li_{6.45}Al_{0.05}La_3Zr_{1.6}Ta_{0.4}O_{12}$) in a mass ratio of 2:1, was synthesized through a modified solid-state reaction (SSR) method, as described previously [47,48]. Subsequently, focused ion beam (FIB) SEM stack images of the cross section were acquired, yielding an isotropic voxel size of 50 nm. These images were then subjected to a sequence of computational methods to generate a model of the experimental structure. The processing details are thoroughly explained in [49].

2.2. Characteristics of the microstructure

Solid volume fraction of LCO (SVF_{LCO}) can be defined as the ratio of LCO to the relative density $\bar{\rho}$,which is defined as the sum of volume ratio of LCO ($\bar{V}_{LCO}$) with the volume fraction of LLZO ($\bar{V}_{LLZO}$) in the composite cathode.

$$SVF_{LCO} = \frac{\bar{V}_{LCO}}{\bar{\rho}} \quad (1)$$

$$\bar{\rho} = \bar{V}_{LCO} + \bar{V}_{LLZO} \quad (2)$$

$$\bar{V}_{LCO} = \frac{nv_{LCO}}{V_{Total}} \quad (3)$$

$$\bar{V}_{LLZO} = \frac{mv_{LLZO}}{V_{Total}} \quad (4)$$

Where n and m are the number of LCO and LLZO grains respectively, while v_{LCO} and v_{LLZO} are the volume of each grain of LCO and LLZO respectively.

2.3. Generation of model microstructure

The composite cathode microstructure was generated using GeoDict software, utilizing a Python script, as described in [46]. Initially, populating a domain of 400×200×300 voxels (voxel length = 50 nm) with LCO and LLZO grains. The initial solid volume fraction of LCO was set at 69.4%. In the generated systems utilizing hexagonal-shaped LCO, the hexagonal grains were horizontally aligned (parallel to the XY-plane) (Figure 1) within the modeled sample to align with experimental observations [49] . The average grain diameters and fiber dimensions are listed in Figure 1. Thereafter, a distribution step was implemented to ensure a homogeneous distribution of the microstructural components within the system. In order to ensure the representativeness of the generated structure, regions exhibiting inhomogeneity in either solid components or pores were eliminated. Followed by sintering process utilizing the Voronoi tessellation algorithm in GeoDict [50] to achieve the targeted density value of 93.14%. The initial values of the solid volume fraction of LCO and relative density may be readjusted to ensure that the resulting values for both parameters exhibit a maximum deviation of 0.25% from the target values. Figure 1 shows the generated structures.

2.4. Materials parameters

To capture realistic behavior, our mechanical calculations were based on the induced chemo-thermal strains. These strains result from the superposition of thermal strains, generated after sintering due to the mismatch in the thermal expansion coefficients between LCO and LLZO [51] and electrochemically-induced strains. Furthermore, the calculations considered the input parameters of Li_xCO with half lithium concentration (x=0.5).

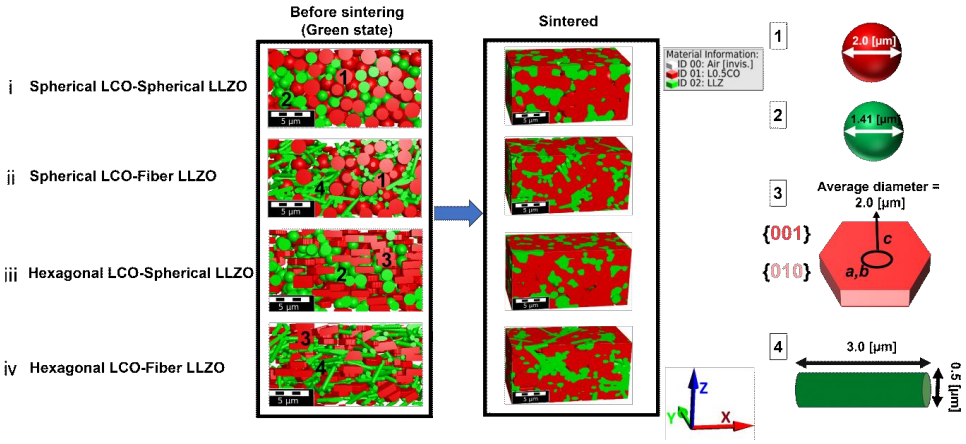

Figure 1. Generated modelled microstructure utilizing different LCO and LLZO morphologies: (i) spherical LCO–spherical LLZO, (ii) spherical LCO–fiber LLZO, (iii) hexagonal LCO-spherical LLZO, and (iv) hexagonal LCO-fiber LLZO. The assigned lattice facets of hexagonal LCO are indicated. The initial average grain sizes of LCO and LLZO 2.00 µm and 1.41 µm, respectively. fiber LLZO length and diameters 3µm and 0.5µm respectively, SVF_{LCO} = 69.4% and $\bar{\rho}$= 93.14%.

Theoretical DFT calculations by Yamakawa et al. [52] of the stiffness matrix of half delithiated LCO were adopted for our calculations due to the absence of experimental data. The stiffness matrix of $Li_{0.5}CoO_2$, as well as the Young's modulus and Poisson's ratios for LLZO, are summarized in Table 1.

Table 1 Anisotropic stiffness matrix C, Young's modulus E, and Poisson ratio ν for LCO, LLZO.

Material	Elastic parameter	Ref
$Li_{0.5}CoO_2$	$C = \begin{bmatrix} 303.86 & 101.71 & 32.58 & 0 & 7.31 & 0 \\ & 318.93 & 28.66 & 0 & -3.93 & 0 \\ & & 98.93 & 0 & 7.03 & 0 \\ & & sym. & 18.02 & 0 & -2.46 \\ & & & & 15.73 & 0 \\ & & & & & 101.94 \end{bmatrix}$ GPa	**[52]**
LLZO	E = 146 GPa, ν = 0.26	**[53-55]**

From chemo-thermal strain calculations, the layered structure of LCO exhibits an expansion along c-axis, while contracting in both a and b-axes. Meanwhile, LLZO undergoes uniform contraction in all directions. The chemo-thermal strain values for $Li_{0.5}CO$ and LLZO are listed in Table 2.

Table 2 crystallographic chemo-thermal strains for $L_{0.5}CoO_2$ in a-and c-axes and for LLZO.

Material	$\epsilon^{chemo-thermal}$	Ref
$Li_{0.5}CoO_2$	$\epsilon^a = -1.76 \times 10^{-2}$ $\epsilon^c = 2.38 \times 10^{-4}$	[46]
LLZO	-1.42×10^{-2}	[46]

The average principal stress $\overline{\boldsymbol{S}}_{\mathbf{all}}$ and the standard deviation **ΔS,** which represents the distribution's width, were calculated through a MATLAB script specifically developed to process output data from the ElastoDict FeelMath-LD module within GeoDict, developed by Math2Market GmbH. [56,57]. Symmetric (Dirichlet) boundary conditions were imposed in all directions. The calculations assumed small deformation, as all observed deformations are less than 5%. Furthermore, we assumed a homogenous charging (low C-rate), which in turn leads to a homogenous stress distribution across the microstructure. The geometric microstructures are found to be representative with a margin of error 2% for LCO and 5% for LLZO (Figure S1).

2.5. Varying microstructural design parameters

To investigate the effect of grain morphology on the induced mechanical stress in the composite cathode, it is crucial to analyze how each modeled structure with different grain morphologies behaves while varying the environment of the structure specifically in this case, the solid volume fraction of LCO and the relative density. A similar approach was employed in [46], where one parameter of interest was varied while fixing the other, followed by mechanical characterization for each variation set. This method clearly reveals the effect of the investigated parameter by isolating the impact of the fixed parameters. The reference for our comparison in this research is the hexagonal LCO-spherical LLZO configuration, as it represents the experimentally achieved microstructure. The solid volume fraction of LCO lies between 20 and 95% (Figure 2), while relative density is within 40-95% (Figure 3). Worth mentioning is that the practical range of solid volume fraction for CAM in experimental cells generally falls between 33% and 66%. While through optimized and pressure-assisted sintering, relative density values are typically achieved within the range of 80% to 95%. In case of unoptimized free sintering, the relative density values typically range from 45% to 70%. this comparison shows how simulation can enlarge the range of investigated parameters.

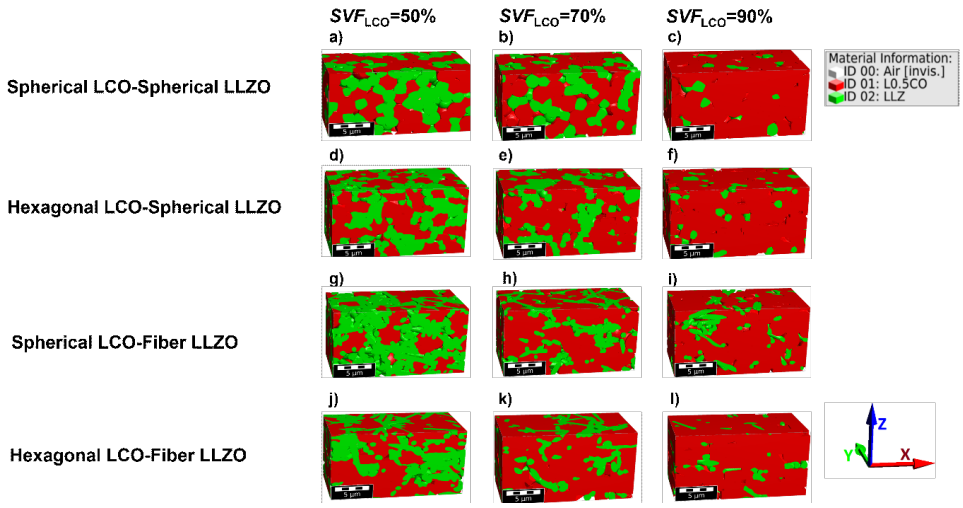

Figure 2. Variation of SVF_{LCO} only (50, 70 and 90%), a-c) spherical LCO-Spherical LLZO d-f) hexagonal LCO-spherical LLZO g-i) Spherical LCO-fiber LZO j-l) hexagonal LCO-fiber LLZO. The fixed parameters values were as follow: $\bar{\rho} = 93.14\%$, average grain size of LCO and LLZO 2.00 µm and 1.43 µm, respectively, fiber LLZO length and diameters 3µm and 0.5µm, respectively.

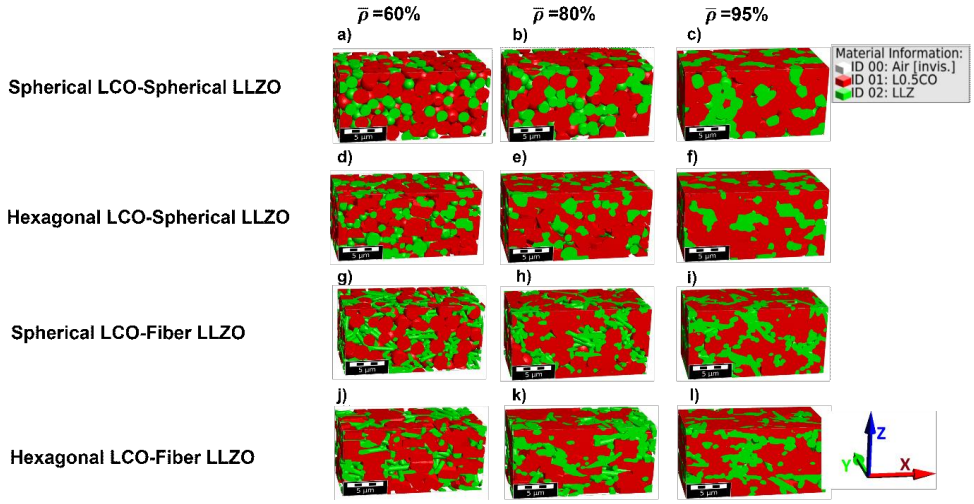

Figure 3. Variation of $\bar{\rho}$ only (60, 80 and 95%), a-c) spherical LCO-Spherical LLZO. d-f) hexagonal LCO-spherical LLZO. g-i) Spherical LCO-fiber LZO. j-l) hexagonal LCO-fiber LLZO. The fixed parameters values were as follow: SVF_{LCO}= 69.4%, average grain size of LCO and LLZO 2.00 µm and 1.43 µm, respectively, fiber LLZO length and diameters 3µm and 0.5µm, respectively.

2.2. Mathematical formula of induced mechanical stress

The main contributor to induced mechanical stress in composite cathodes of ASSBs is the volume change which occurs during the cooling phase after sintering for both LCO and LLZO, as well as during the de-/lithiation phase for LCO. In both instances, the volume change in LCO is constrained by the neighboring LLZO, leaving the components of the microstructure to suffer from induced mechanical stress. Consequently, strain values are critical in determining the volume changes of the composite cathode components.

The total strain of LCO (ϵ_{LCO}) in given direction (a, b and c-axes) can be expressed as:

$$(\epsilon_{LCO})_i = (\epsilon_{LCO}^{Li})_i + (\epsilon_{LCO}^{Th})_i + (\epsilon_{LCO}^{El})_i \ (i = a, b, c) \quad (5)$$

Where, ϵ_{LCO}^{Li}, ϵ_{LCO}^{Th} and ϵ_{LCO}^{El} are the lithiation, thermal and elastic strains of LCO.

In contrast, no volume change is observed in LLZO during cycling. Thus, the total strain of LLZO (ϵ_{LLZO}) in given direction (a, b and c-axes) can be expressed as:

$$(\epsilon_{LLZO})_i = (\epsilon_{LLZO}^{Th})_i + (\epsilon_{LLZO}^{El})_i \quad (6)$$

Where ϵ_{LLZO}^{Th} and ϵ_{LLZO}^{El} are the thermal and elastic strains of LLZO phases, respectively.

The elastic strains of LCO and LLZO are related to the stresses according to Hooke's law:

$$\sigma^{i}_{LCO} = \sum_j C^{ij} \left(\epsilon^{El}_{LCO}\right)_j \quad (7)$$

$$\sigma^{i}_{LLZO} = E\left(\epsilon^{El}_{LLZO}\right)_i \quad (8)$$

In this research, we did not consider any interface zones between CAM/SE due to lack of intrinsic mechanical parameters of formed interface zone.

3. Result and discussion

3.2. Effect of grain morphology with varying solid volume fraction of LCO

3.1.1. Spherical Vs. Hexagonal LCO-Spherical LLZO

Increasing the solid volume fraction of LCO reduces the presence of LLZO grains in the microstructure, which are then replaced by LCO grains. The primary advantage of increasing the LCO solid volume fraction is the reduction of mechanical stress in the LCO, as fewer constraints from the LLZO grains allow the LCO to undergo volume changes more freely. On the other hand, the remained LLZO grain content suffers from an induced tensile mechanical stress [46]. However, when spherical LCO particles are randomly oriented, the induced mechanical stress of LCO is entirely reversed, that is, it increases in parallel with the rise in SVF_{LCO} (Figure 4.).

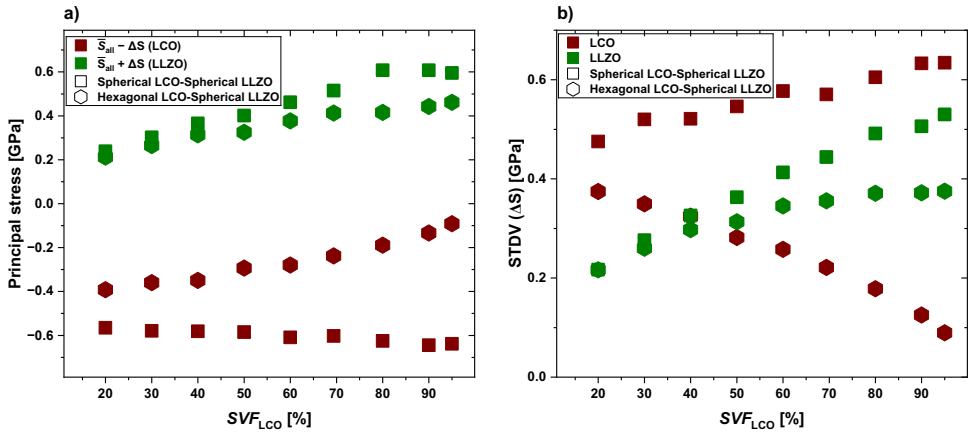

Figure 4. a) Chemo-thermal principal stress as a function of the solid volume fraction of LCO for random oriented spherical LCO-spherical LLZO and textured hexagonal LCO-spherical LLZO. b) The standard deviation, which represents the width of the distribution.

The orientation of spherical LCO grains cannot be precisely controlled. Figure 5b shows the orientation of spherical LCO grains from the x-axis, closely reflecting real-life conditions, while Figure 5a depicts a similar structure with aligned orientations of spherical LCO grains. It is worth noting that the LLZO grains are aligned at 0° with respect to the x-axis, due to their isotropic structure. We investigated the mechanical stress induced in both configurations. In the case of aligned LCO spheres, the LCO grains can expand freely as the solid volume fraction increases, which lowers the induced compressive mechanical stress in LCO, while the remaining LLZO grains experience higher tensile stress (Figure 5c). However, in randomly oriented spherical LCO grains, the axes of neighboring LCO grains may conflict (e.g., the c-axis of one LCO grain may oppose the a- or b-axis of another LCO grain), restricting LCO's ability to expand. As a result, LCO grains will suffer from an induced compressive mechanical stress (Figure 5d). The induced compressive mechanical stress in LCO grains continues to increases with rising solid volume fraction of LCO since the LCO grains which substitute the LLZO ones have similar shrinking behavior of LLZO (Figure 4). Furthermore, the compressive mechanical stress induced in LCO due to random LCO grain orientations is higher than that induced by LLZO, which is attributed to the larger strain values along the a- and b-axes of LCO compared to LLZO.

On the other hand, the behavior of the induced mechanical stress in LLZO follows the trend influenced by the increasing solid volume fraction of LCO. As spherical LLZO grains are gradually replaced by randomly oriented spherical LCO grains, the remaining LLZO grains exhibit an induced tensile mechanical stress, which intensifies as the LCO volume fraction increases (Figure 4). When aligned spherical LCO is used, LLZO grains are surrounded by LCO grains. Parts of LLZO grains are in contact with the c-axis of neighboring LCO, which is expanding, thereby inducing tensile mechanical stress in the LLZO. Meanwhile, other parts of the LLZO grains contact to a surface parallel to a- or b-axis of LCO, which are under contraction, inducing compressive mechanical stress that counteracts the tensile stress (Figure 5c). In contrast, when randomly oriented spherical LCO is present, the LLZO grains are in contact the expanding surface parallel to c-axis of LCO, leading to amplified tensile stress in LLZO (Figure 5d).

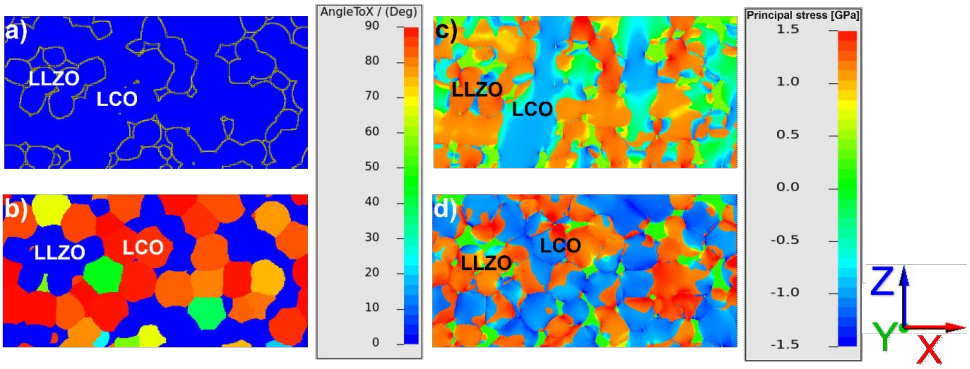

Figure 5. a and b) Distribution of the angle to x-axis of LCO and LLZO grains for aligned spherical LCO-spherical LLZO and random oriented spherical LCO-spherical LLZO respectively. c and d) distribution of principal stress of tailored spherical LCO-spherical LLZO and random oriented spherical LCO-spherical LLZO respectively.

When LCO grains with textured hexagonal planar structures are used, most LCO grains exhibit similar orientations where {001} facets are perpendicular to the c-axis. This sufficiently reduce the effect of random grain orientations on the induced mechanical stress. As a result, LCO can undergo volume changes freely, without constraints from neighboring grains, as the solid volume fraction of LCO increases. Consequently, the expected reduction in the induced compressive mechanical stress in LCO grains is observed (Figure 4). However, the remaining LLZO grains experience higher induced tensile mechanical stress as the LCO volume fraction increases (Figure 4).

Compared to the random oriented spherical LCO-spherical LLZO structure, the textured hexagonal LCO-spherical LLZO system exhibits lower induced mechanical stress, which is attributed to the absence of the impact of the random orientation of spherical LCO grains. It is worth mentioning that the key distinction between spherical and hexagonal LCO grains lies not in their shape but in the ability of flat hexagonal particles to be aligned during fabrication. If both grain types could be texturally aligned, they would exhibit similar mechanical results.

3.1.2. Effect of fiber LLZO

In this section, we investigated the influence of incorporating fiber LLZO on the induced mechanical stress in the system, considering variations in the LCO grain shape between random oriented spherical and textured hexagonal forms.

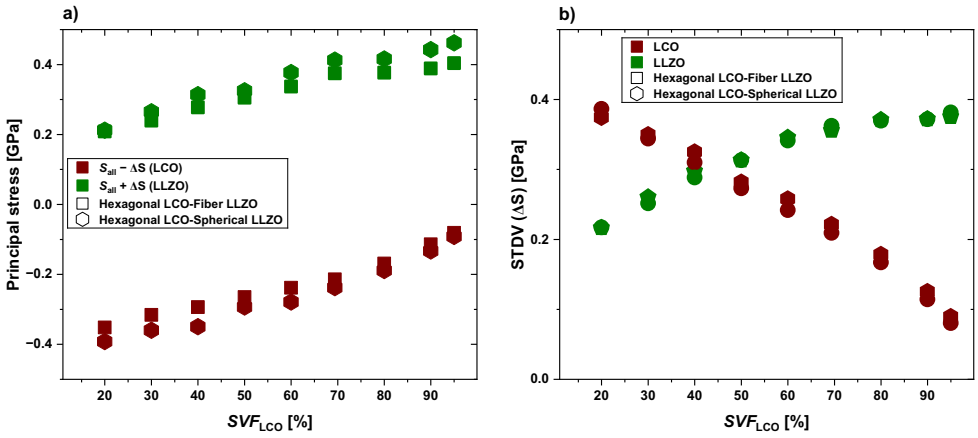

Figure 6. a) Chemo-thermal principal stress as a function of the solid volume fraction of LCO for textured hexagonal LCO-spherical LLZO and textured hexagonal LCO-fiber LLZO. b) The standard deviation, which represents the width of the distribution.

As the solid volume fraction of LCO increases in both the hexagonal LCO-spherical LLZO and hexagonal LCO-fiber LLZO systems, the mechanical stresses induced in LCO decreases while those in LLZO increase. Nevertheless, the hexagonal-fiber system exhibits reduced induced mechanical stresses for both LCO and LLZO compared to the hexagonal-spherical system (Figure 6).

LCO exhibits anisotropic lattice change and is in textured alignment. Hence, an effect of the alignment of fiber LLZO on the mechanical stresses can be expected. Therefore, we generated a series of hexagonal-LCO-fiber LLZO microstructures, maintaining the hexagonal LCO grains in a textured orientation while systematically varying the alignment of the LLZO fibers at 0°, 45°, and 90° relative to the x-axis Figure 7 a, b and c respectively.

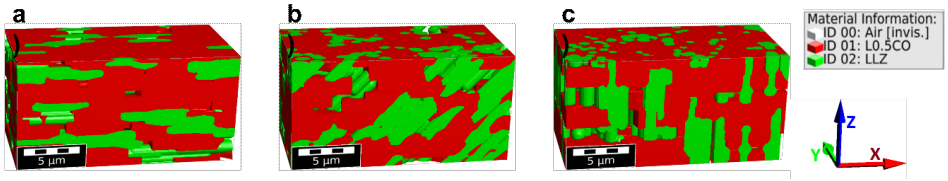

Figure 7. Generated modelled microstructure utilizing textured hexagonal LCO and fiber LLZO while varying the alignment angles to the x-axis of fibers. a) 0°, b) 45°, c) 90°. SVF_{LCO} = 69.4%, initial average grain size of LCO and LLZO 2.00 µm, the length and the diameter of fiber LLZO 3µm and 0.5µm respectively, and $\bar{\rho}$= 93.14%.

For each set, we analyzed the effect of increasing the solid volume fraction of LCO on the induced mechanical stresses in both LCO and LLZO. When the fiber LLZO was aligned horizontally, parallel to the x-axis, LCO exhibited higher induced tensile mechanical stress, while LLZO experienced higher induced compressive mechanical stress compared to the system which utilizes fiber LLZO with random orientation (Figure 8 a,e), indicating a stress inversion compared to the system with randomly aligned fibers. In this case, the fiber LLZO has greater contact with the {001} facets of hexagonal LCO, where the a- and b-axes undergo significant contractions with higher strain compared to LLZO. As a result, LLZO impedes the contraction of LCO, leading to induced tensile mechanical stress in LCO and compressive mechanical stress in LLZO. Conversely, fewer fiber's bases contact the {010} facets of hexagonal LCO grains, where the c-axis expands more actively, resulting in lower induced compressive mechanical stress in LCO and correspondingly lower tensile mechanical stress in LLZO.

A completely inverted behavior, with higher induced mechanical stresses, was observed when the fiber LLZO was aligned vertically, parallel to the z-axis. In this configuration, the LLZO fibers primarily contact the {010} facets of the hexagonal LCO grains, where the c-axis expansion is active, inducing compressive mechanical stress in LCO and tensile mechanical stress in LLZO (Figure 8 b,e). Conversely, fewer LLZO fiber bases come into contact with the {001} facets of the hexagonal LCO grains, resulting in lower induced tensile mechanical stress in LCO and lower compressive mechanical stress in LLZO.

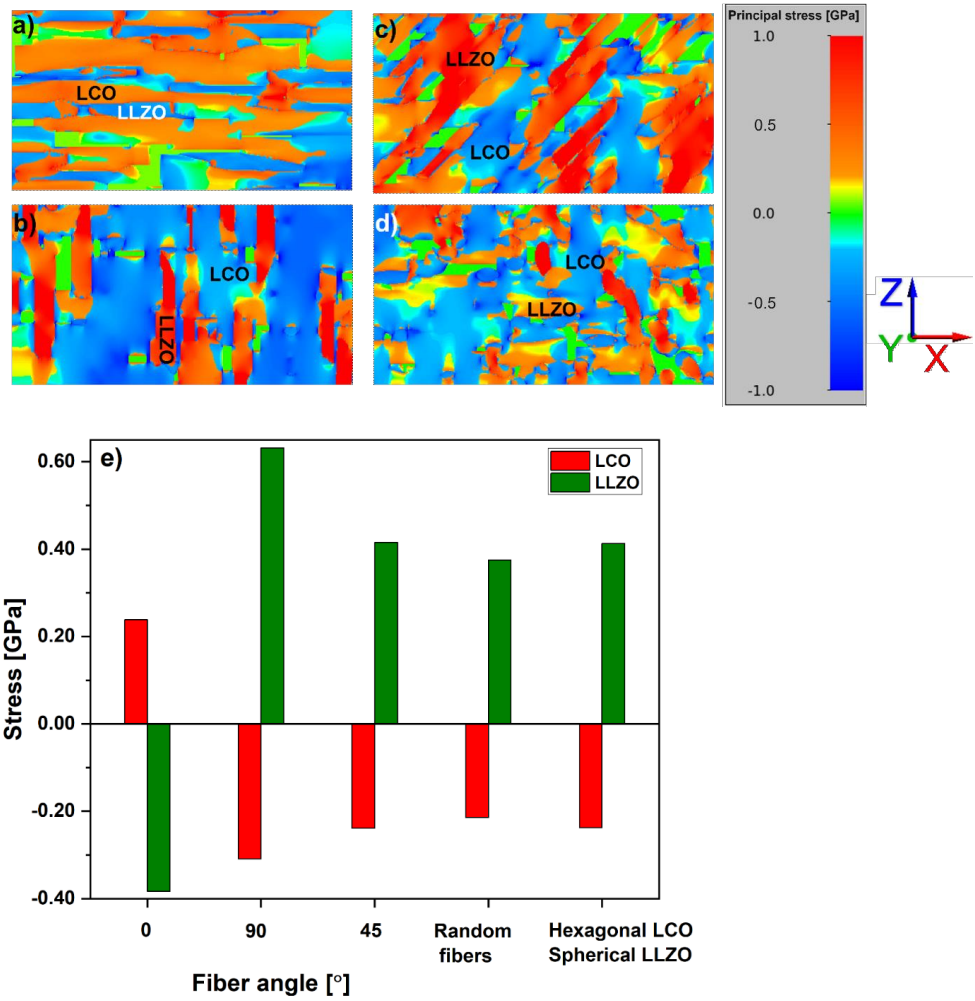

Figure 8. Distribution of principal stress of textured hexagonal LCO-fiber LLZO while varying the alignment angles to the x-axis of fibers. a) 0°, b) 45°, c) 90° and d) randomly aligned. e) Bar chart illustrating the induced mechanical stress in LCO (red) and LLZO (green) as a function of fiber orientation (0°, 45°, 90° and random) and LLZO morphology (fibers vs. spherical). The results highlight the influence of fiber alignment and LLZO morphology on the induced mechanical stress within the composite cathode. SVF_{LCO} = 69.4%, initial average grain size of LCO and LLZO 2.00 µm and 1.43 µm respectively, fiber LLZO length and diameters 3µm and 0.5µm respectively, and $\bar{\rho}$= 93.14%.

The system in which LLZO fibers are aligned 45° from x-axis, exhibits a similar behavior to the system in which the LLZO fibers are vertically aligned. However, in this case, more fiber bases are in contact with the {001} facets of the hexagonal LCO, leading to higher induced tensile mechanical stress in LCO and compressive mechanical stress in LLZO in both a and b-axes.

This, in turn, contributes to a reduction in the higher induced compressive and tensile mechanical stresses in both LCO and LLZO, particularly along the c-axis attributed to increased contact between the fibers and the {010} facets of the hexagonal LCO grains, where c-axis expansion is active. Consequently, this leads to lower net induced compressive and tensile mechanical stresses in both LCO and LLZO, respectively (Figure 8 c,e).

In the previous three sets, although a similar number of hexagonal LCO and fiber LLZO grains were utilized, each configuration exhibited not only different behavior but also varying levels of induced mechanical stresses in both LCO and LLZO. Consequently, the facet-specific interface between LCO and LLZO grains is a key factor controlling the mechanical stresses observed in the system containing fiber LLZO. When LLZO fibers engage with the {001} facets of the hexagonal LCO grains, tensile mechanical stress in LCO and compressive mechanical stress in LLZO are induced. This configuration helps to reduce the induced compressive and tensile mechanical stresses of LCO and LLZO, respectively.

While utilizing textured hexagonal LCO grains, fiber LLZO with random alignment exhibits lower induced mechanical stresses for both LCO and LLZO by 11.0% and 9.0% respectively, compared to the system utilizing spherical LLZO (Figure 6, 8e). This behavior can be attributed to the lower number of spherical grains that can come into contact with the {001} facets of hexagonal LCO. Consequently, this results in less reduction of the induced compressive and tensile mechanical stresses in both LCO and LLZO, which are mainly driven by the higher contact with the {010} facets of the hexagonal LCO grains. Furthermore, it is important to note that the results from the system where LLZO fibers are aligned at 45° from the x-axis are matching those of the spherical LLZO system (Figure 8e), suggesting that these two systems exhibit equivalent mechanical behavior.

Despite the benefits of utilizing fiber LLZO, the orientation of LCO grains also plays a crucial role in limiting or even negating these advantages. This effect is more pronounced in systems using fiber LLZO combined with randomly oriented spherical LCO. In such cases, fiber LLZO predominantly contacts the regions of LCO where the c-axis is actively expanding, with fewer opportunities to engage with areas where the a- or b-axes are shrinking. As a result, the potential for reducing the induced mechanical stresses in the system is reduced, leading to higher induced tensile stress in LLZO as the solid volume fraction of LCO increases. On other hand, LCO grains exhibit higher induced mechanical stresses while increasing SVF_{LCO} (Figure 9). The

induced compressive mechanical stresses in LCO exhibit a behavior similar to that of the previously discussed system utilizing spherical LCO and spherical LLZO. Therefore, a similar explanation for this behavior is applicable.

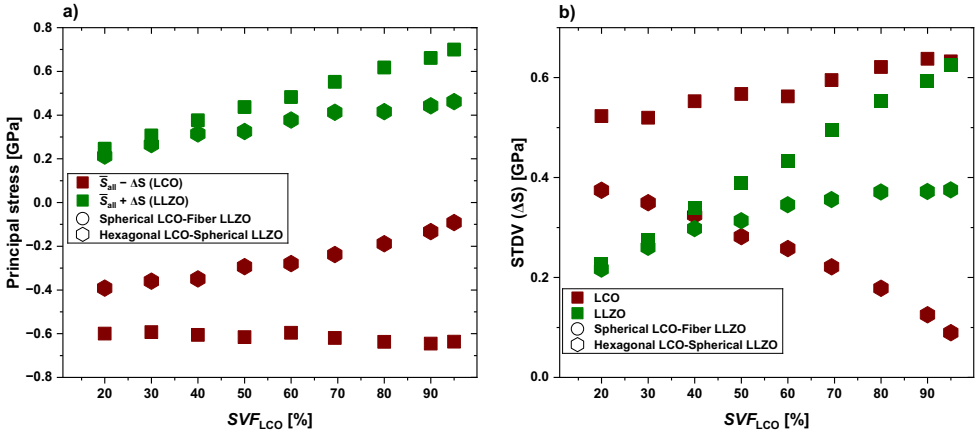

Figure 9. Chemo-thermal principal stress as a function of the solid volume fraction of LCO for textured hexagonal LCO-spherical LLZO and random oriented spherical LCO-fiber LLZO. b) The standard deviation, which represent the width of distribution.

3.2. Grain morphology behavior with varying the relative density

The induced mechanical stress in both LCO and LLZO is exhibiting the convenient trend of varying the values of relative density [46]. In which the induced mechanical stress in LCO and LLZO are directly proportional to $\bar{\rho}$, ascribed to the higher coordination number (Figure S2-S3).

In systems utilizing tailored hexagonal LCO, the induced mechanical stress in LCO is lower than that in LLZO (Figure S2 a,b), which can be attributed to the low volume fraction of LLZO in the system. On the other hand, systems which utilize random oriented spherical LCO exhibit higher induced stresses in both LCO and LLZO compared to those with tailored hexagonal LCO (Figure S2,S3), a result of the previously discussed effect of random orientation in LCO. Due to this effect, the sensitivity of mechanical stress in LCO to the variation of $\bar{\rho}$ is higher than the one in LLZO. Which in turn leads to higher induced mechanical stress in LCO than in LLZO (Figure S3 a,b) despite low volume fraction of LLZO in the system. Furthermore, while utilizing randomly oriented spherical LCO, the stress values in both LCO and LLZO are slightly higher for fiber LLZO compared to spherical LLZO, ascribed to the higher surface area of fiber LLZO.

4. Conclusions

In this study, we investigated the effect of the grain morphology in a composite cathode on the induced mechanical stress. Our finding shows that utilizing LLZO fiber with random alignments combined with textured hexagonal LCO reduced the induced mechanical stress in both LCO and LLZO by 11.0% and 9.0% respectively, compared to the systems utilizing spherical LLZO. The alignment of LLZO fibers significantly impacted the stress type in the system, due to the facet-specific contact interface between the LLZO and LCO grains. When fiber LLZO are in contact with the {001} facets of textured hexagonal LCO, tensile and compressive mechanical stresses in LCO and LLZO, respectively, are expected. On other hand, stresses are inverted when the LLZO fiber is in contact with the {010} facets of hexagonal LCO. Furthermore, we showed the preferable anisotropic expansion-contraction behavior in the CAM, which could be utilized to lower the induced mechanical stress in the system. This was more pronounced by utilizing fiber LLZO. However, the advantages which could gained by utilizing the impact of facet-specific contact interface between the solid electrolyte and the cathode active material grains are limited by the behavior of the cathode active material. Furthermore, it is not favorable to utilize spherical LCO, since its orientation cannot be guaranteed. The randomly oriented spherical LCO-spherical LLZO exhibits the highest induced mechanical stresses compared to the other investigated systems. Currently, all stress values presented in this study are obtained through theoretical calculations. A comprehensive experimental validation of the modeling methodology is underway using synchrotron measurements at the European Synchrotron Radiation Facility (ESRF) in Grenoble, France; however, the process remains highly challenging. Moreover, the experimental validation of the stiffness tensors, is not yet achievable. Accurate representation of microstructural features, including voxel size and interface resolution, plays a critical role in ensuring the reliability of property simulations. A detailed discussion of these aspects is provided in our previous work [65]. The impact of the morphology of the component's grains on the electronic and ionic conductivities of LCO and LLZO respectively will be the topic of investigation in the future work.

Conflicts of interest

The author declares no known competing financial interests or personal relationships that could have appeared to influence the work reported in this paper.

Acknowledgements

The financial support provided by the Federal Ministry of Education and Research of Germany in the framework of the Palestinian-German Science Bridge (PGSB) (BMBF Grant Number 01DH16027), FestBatt2-Oxide (grant no. 13XP0434A) and Meet-HiEnD III (grant no. 03XP0258C) is gratefully acknowledged.

References

[1] M. Finsterbusch, T. Danner, C.-L. Tsai, S. Uhlenbruck, A. Latz, and O. Guillon, High Capacity Garnet-Based All-Solid-State Lithium Batteries: Fabrication and 3D-Microstructure Resolved Modeling, *ACS applied materials & interfaces* 10[26] (2018) 22329-39. https://doi.org/10.1021/acsami.8b06705.

[2] R. Miyazaki, G. Yamaguchi, E. Yagi, T. Yoshida, and T. Tomita, Enhancement of the Li+ Conductivity of Li_3AlF_6 for Stable All-Solid-State Lithium-Ion Batteries, *ACS Appl. Energ. Mater*. 7[6] (2024) 2533-41. https://doi.org/10.1021/acsaem.4c00115.

[3] K. Kerman, A. Luntz, V. Viswanathan, Y.-M. Chiang, and Z. Chen, Review—Practical Challenges Hindering the Development of Solid State Li Ion Batteries, *J. Electrochem. Soc.* 164[7] (2017) A1731. https://doi.org/10.1149/2.1571707jes.

[4] S. Wenzel, T. Leichtweiss, D. Krüger, J. Sann, and J. Janek, Interphase formation on lithium solid electrolytes—An in situ approach to study interfacial reactions by photoelectron spectroscopy, *Solid State Ionics* 278 (2015) 98-105. https://doi.org/10.1016/j.ssi.2015.06.001.

[5] P. Bron, B. Roling, and S. Dehnen, Impedance characterization reveals mixed conducting interphases between sulfidic superionic conductors and lithium metal electrodes, *J. Power Sources* 352 (2017) 127-34. https://doi.org//10.1016/j.jpowsour.2017.03.103.

[6] S. Wenzel, S. Randau, T. Leichtweiß, D. A. Weber, J. Sann, W. G. Zeier, and J. r. Janek, Direct observation of the interfacial instability of the fast ionic conductor $Li_{10}GeP_2S_{12}$ at the lithium metal anode, *Chem. Mater*. 28[7] (2016) 2400-07. https://doi.org//10.1021/acs.chemmater.6b00610.

[7] T. Yang, J. Zheng, Q. Cheng, Y. Y. Hu, and C. K. Chan, Composite Polymer Electrolytes with $Li_7La_3Zr_2O_{12}$ Garnet-Type Nanowires as Ceramic Fillers: Mechanism of Conductivity Enhancement and Role of Doping and Morphology, *ACS Appl. Mater. Interfaces* 9[26] (2017) 21773-80. https://doi.org/10.1021/acsami.7b03806.

[8] F. Aguesse, W. Manalastas, L. Buannic, J. M. Lopez del Amo, G. Singh, A. Llordés, and J. Kilner, Investigating the dendritic growth during full cell cycling of garnet electrolyte in direct contact with Li metal, *ACS Appl. Mater. Interfaces* 9[4] (2017) 3808-16. https://doi.org/10.1021/acsami.6b13925.

[9] R. H. Basappa, T. Ito, T. Morimura, R. Bekarevich, K. Mitsuishi, and H. Yamada, Grain boundary modification to suppress lithium penetration through garnet-type solid electrolyte, *J. Power Sources* 363 (2017) 145-52. https://doi.org//10.1016/j.jpowsour.2017.07.088.

[10] A. Sharafi, H. M. Meyer, J. Nanda, J. Wolfenstine, and J. Sakamoto, Characterizing the Li–$Li_7La_3Zr_2O_{12}$ interface stability and kinetics as a function of temperature and current density, *J. Power Sources* 302 (2016) 135-39. https://doi.org/10.1016/j.jpowsour.2015.10.053.

[11] A. Bates, S. Mukherjee, N. Schuppert, B. Son, J. G. Kim, and S. Park, Modeling and simulation of 2D lithium-ion solid state battery, *Int. J. Energ. Res.* 39[11] (2015) 1505-18. https://doi.org/10.1002/er.3344.

[12] G. Bucci, T. Swamy, S. Bishop, B. W. Sheldon, Y.-M. Chiang, and W. C. Carter, The effect of stress on battery-electrode capacity, *J. Electrochem. Soc.* 164[4] (2017) A645. https://doi.org//10.1149/2.0371704jes.

[13] G. Bucci, T. Swamy, Y.-M. Chiang, and W. C. Carter, Modeling of internal mechanical failure of all-solid-state batteries during electrochemical cycling, and implications for battery design, *J. Mater. Chem* A 5[36] (2017) 19422-30. https://doi.org/10.1039/C7TA03199H.

[14] A. Mukhopadhyay and B. W. Sheldon, Deformation and stress in electrode materials for Li-ion batteries, *Progress in Materials Science* 63 (2014) 58-116. https://doi.org/10.1016/j.pmatsci.2014.02.001.

[15] Y. He, C. Lu, S. Liu, W. Zheng, and J. Luo, Interfacial Incompatibility and Internal Stresses in All-Solid-State Lithium Ion Batteries, *Adv. Energy Mater.* 9[36] (2019) 1901810. https://doi.org/10.1002/aenm.201901810.

[16] P. Li, Y. B. Zhao, Y. X. Shen, and S. H. Bo, Fracture behavior in battery materials, *J. Phys. Energy* 2[2] (2020). https://doi.org//10.1088/2515-7655/ab83e1.

[17] K. Mukai, Zero-Strain Insertion Materials for All-Solid-State Li-Ion Batteries, pp. 219-40. in Solid Electrolytes for Advanced Applications: Garnets and Competitors. Edited by R. Murugan and W. Weppner. Springer International Publishing, Cham, 2019.

[18] F. Strauss, L. de Biasi, A. Y. Kim, J. Hertle, S. Schweidler, J. Janek, P. Hartmann, and T. Brezesinski, Rational Design of Quasi-Zero-Strain NCM Cathode Materials for Minimizing Volume Change Effects in All-Solid-State Batteries, *ACS Mater. Lett.* 2[1] (2020) 84-88. https://doi.org/10.1021/acsmaterialslett.9b00441.

[19] K. Mukai, Pseudo zero-strain insertion materials for Li-ion batteries: cross-sectional observations of $LiNi_{1/2}Co_{1/2}O_2$, $LiNi_{1/3}Co_{1/3}Mn_{1/3}O_2$, and $LiNi_{0.8}Co_{0.15}Al_{0.05}O_2$, *Ionics* 24[8] (2018) 2181-86. https://doi.org/10.1007/s11581-017-2385-2.

[20] R. Koerver, W. Zhang, L. de Biasi, S. Schweidler, A. O. Kondrakov, S. Kolling, T. Brezesinski, P. Hartmann, W. G. Zeier, and J. Janek, Chemo-mechanical expansion of lithium electrode materials–on the route to mechanically optimized all-solid-state batteries, *Energ. Environ. Sci.* 11[8] (2018) 2142-58. https://doi.org//10.1039/C8EE00907D

[21] G. Liu, H. Zheng, S. Kim, Y. Deng, A. Minor, X. Song, and V. S. Battaglia, Effects of various conductive additive and polymeric binder contents on the performance of a lithium-ion composite cathode, *J. Electrochem. Soc*. 155[12] (2008) A887. https://doi.org/10.1149/1.2976031.

[22] B. Ludwig, Z. Zheng, W. Shou, Y. Wang, and H. Pan, Solvent-free manufacturing of electrodes for lithium-ion batteries, *Sci Rep.* 6[1] (2016) 1-10. https://doi.org/10.1038/srep23150.

[23] Y. He, P. Xu, D. Jiang, H. Hu, D. Li, and S. Shi, Quantifying the solid electrolyte interphase stress induced capacity fading of lithium-ion batteries via a multiscale mechanical-electrochemical coupling model, *Science China Technological Sciences* 67[10] (2024) 3168-81. https://doi.org/10.1007/s11431-024-2711-7.

[24] J. Auborn and Y. Barberio, Lithium Intercalation Cells Without Metallic Lithium: MoO_2 and $WO_2/LiCoO_2$, J. Electrochem. Soc. 134[3] (1987) 638. https://doi.org/10.1149/1.2100521.

[25] T. Nagaura and K. Tozawa, Progress in batteries and solar cells, JEC Press 9 (1990) 209. https://doi.org/10.1541/ieejfms1990.115.4_349

[26] B. Wang, J. Bates, F. Hart, B. Sales, R. Zuhr, and J. Robertson, Characterization of thin-film rechargeable lithium batteries with lithium cobalt oxide cathodes, *J. Electrochem. Soc.* 143[10] (1996) 3203. https://doi.org/10.1149/1.1837188.

[27] A. Kannan, L. Rabenberg, and A. Manthiram, High capacity surface-modified $LiCoO_2$ cathodes for lithium-ion batteries, *Electrochem. Solid-State Lett.* 6[1] (2002) A16. https://doi.org//10.1149/1.1526782.

[28] Y. J. Kim, H. Kim, B. Kim, D. Ahn, J.-G. Lee, T.-J. Kim, D. Son, J. Cho, Y.-W. Kim, and B. Park, Electrochemical stability of thin-film $LiCoO_2$ cathodes by aluminum-oxide coating, *Chem. Mater.* 15[7] (2003) 1505-11. https://doi.org/10.1021/cm0201403.

[29] C. Daniel, D. Mohanty, J. Li, and D. L. Wood, Cathode materials review, *AIP Conf. Proc.* 1597[1] (2014) 26-43. https://doi.org/10.1063/1.4878478.

[30] C. Wang, G. Bai, X. Liu, and Y. Li, Favorable electrochemical performance of $LiMn_2O_4$/$LiFePO_4$ composite electrodes attributed to composite solid electrolytes for all-solid-state lithium batteries, *Langmuir* 37[7] (2021) 2349-54. https://doi.org/10.1021/acs.langmuir.0c03274.

[31] R. Murugan, V. Thangadurai, and W. Weppner, Fast lithium ion conduction in garnet-type $Li_7La_3Zr_2O_{12}$, *Angewandte chemie-international edition in english*- 46[41] (2007) 7778. https://doi.org/10.1002/anie.200701144.

[32] C.-L. Tsai, E. Dashjav, E.-M. Hammer, M. Finsterbusch, F. Tietz, S. Uhlenbruck, and H. P. Buchkremer, High conductivity of mixed phase Al-substituted $Li_7La_3Zr_2O_{12}$, *J. of Electroceramics* 35[1] (2015) 25-32. https://doi.org/10.1007/s10832-015-9988-7.

[33] H. Buschmann, J. Dölle, S. Berendts, A. Kuhn, P. Bottke, M. Wilkening, P. Heitjans, A. Senyshyn, H. Ehrenberg, and A. Lotnyk, Structure and dynamics of the fast lithium ion conductor "$Li_7La_3Zr_2O_{12}$", *Phys. Chem. Chem. Phys.* 13[43] (2011) 19378-92. https://doi.org/10.1039/C1CP22108F.

[34] C.-L. Tsai, V. Roddatis, C. V. Chandran, Q. Ma, S. Uhlenbruck, M. Bram, P. Heitjans, and O. Guillon, $Li_7La_3Zr_2O_{12}$ Interface Modification for Li Dendrite Prevention, *ACS Appl. Mater & Interfaces* 8[16] (2016) 10617-26. https://doi.org/10.1021/acsami.6b00831.

[35] F. Yonemoto, A. Nishimura, M. Motoyama, N. Tsuchimine, S. Kobayashi, and Y. Iriyama, Temperature effects on cycling stability of Li plating/stripping on Ta-doped $Li_7La_3Zr_2O_{12}$, *J. Power Sources* 343 (2017) 207-15. https://doi.org/10.1016/j.jpowsour.2017.01.009.

[36] L. Miara, A. Windmüller, C.-L. Tsai, W. D. Richards, Q. Ma, S. Uhlenbruck, O. Guillon, and G. Ceder, About the Compatibility between High Voltage Spinel Cathode Materials and Solid Oxide Electrolytes as a Function of Temperature, *ACS Appl. Mater. Interfaces* 8[40] (2016) 26842-50. https://doi.org/10.1021/acsami.6b09059.

[37] K. H. Kim, Y. Iriyama, K. Yamamoto, S. Kumazaki, T. Asaka, K. Tanabe, C. A. J. Fisher, T. Hirayama, R. Murugan, and Z. Ogumi, Characterization of the interface between $LiCoO_2$ and $Li_7La_3Zr_2O_{12}$ in an all-solid-state rechargeable lithium battery, *J. Power Sources* 196[2] (2011) 764-67. https://doi.org/10.1016/j.jpowsour.2010.07.073.

[38] W. D. Richards, L. J. Miara, Y. Wang, J. C. Kim, and G. Ceder, Interface Stability in Solid-State Batteries, *Chem. Mater.* 28 (2016) 266-73. https://doi.org/10.1021/acs.chemmater.5b04082.

[39] H. Jeon, D.-H. Kwon, H. Kim, J.-H. Lee, Y. Jun, J.-W. Son, and S. Park, Tailoring shape and exposed crystal facet of single-crystal layered-oxide cathode particles for all-solid-state batteries, *Chem. Eng. J.* 445 (2022) 136828. https://doi.org/10.1016/j.cej.2022.136828.

[40] N. Wu, Y. Zhang, Y. Guo, S. Liu, H. Liu, and H. Wu, Flakelike $LiCoO_2$ with Exposed {010} Facets As a Stable Cathode Material for Highly Reversible Lithium Storage, *ACS Appl. Mater. Interfaces* 8[4] (2016) 2723-31. https://doi.org/10.1021/acsami.5b10977.

[41] M. J. Counihan, D. J. Powers, P. Barai, S. Hu, T. Zagorac, Y. Zhou, J. Lee, J. G. Connell, K. S. Chavan, I. S. Gilmore, L. Hanley, V. Srinivasan, Y. Zhang, and S. Tepavcevic, Understanding the Influence of $Li_7La_3Zr_2O_{12}$ Nanofibers on Critical Current Density and Coulombic Efficiency in Composite Polymer Electrolytes, *ACS Appl. Mater. Interfaces* 15[21] (2023) 26047-59. https://doi.org/10.1021/acsami.3c04262.

[42] Z. Wan, D. Lei, W. Yang, C. Liu, K. Shi, X. Hao, L. Shen, W. Lv, B. Li, Q.-H. Yang, F. Kang, and Y.-B. He, Low Resistance–Integrated All-Solid-State Battery Achieved by $Li_7La_3Zr_2O_{12}$ Nanowire Upgrading Polyethylene Oxide (PEO) Composite Electrolyte and PEO Cathode Binder, *Adv. Funct. Mater.* 29[1] (2019) 1805301. https://doi.org/10.1002/adfm.201805301.

[43] D. O. Shin, K. Oh, K. M. Kim, K.-Y. Park, B. Lee, Y.-G. Lee, and K. Kang, Synergistic multi-doping effects on the $Li_7La_3Zr_2O_{12}$ solid electrolyte for fast lithium ion conduction, *Sci Rep.Uk* 5[1] (2015) 18053. https://doi.org/10.1038/srep18053.

[44] L. Zhong, J. Li, Z.-x. Chen, L.-p. Zhou, H.-x. Liu, X.-q. Shen, and M.-x. Jing, A LLZO Fibers/ PPO polymeric matrix solid electrolyte for high voltage solid-state lithium batteries, *Appl. Phy. A* 130[9] (2024) 662. https://doi.org/10.1007/s00339-024-07815-x.

[45] W. He, H. Ding, X. Chen, and W. Yang, Three-dimensional LLZO/PVDF-HFP fiber network-enhanced ultrathin composite solid electrolyte membrane for dendrite-free solid-state lithium metal batteries, *J. Membr. Sci.* 665 (2023) 121095. https://doi.org/10.1016/j.memsci.2022.121095.

[46] F. Al-Jaljouli, R. Mücke, P. Kaghazchi, Y. J. Sohn, M. Finsterbusch, D. Fattakhova-Rohlfing, and O. Guillon, Microstructural parameters governing the mechanical stress and conductivity of all-solid-state lithium-ion-battery cathodes, *J. Energy Storage* 68 (2023) 107784. https://doi.org/10.1016/j.est.2023.107784.

[47] M. Mann, M. Küpers, G. Häuschen, M. Finsterbusch, D. Fattakhova-Rohlfing, and O. Guillon, The influence of hafnium impurities on the electrochemical performance of tantalum substituted $Li_7La_3Zr_2O_{12}$ solid electrolytes, *Ionics* 28[1] (2022) 53-62. https://doi.org/10.1007/s11581-021-04300-w.

[48] M. Mann, M. Küpers, G. Häuschen, M. Finsterbusch, D. Fattakhova-Rohlfing, and O. Guillon, Evaluation of Scalable Synthesis Methods for Aluminum-Substituted $Li_7La_3Zr_2O_{12}$ Solid Electrolytes, *Materials* 14[22] (2021) 6809. https://doi.org/10.3390/ma14226809.

[49] R. Mücke, M. Finsterbusch, P. Kaghazchi, D. Fattakhova-Rohlfing, and O. Guillon, Modelling electro-chemical induced stresses in all-solid-state batteries: Anisotropy effects in cathodes and cell design optimisation, *J. Power Sources* 489 (2021) 229430. https://doi.org/10.1016/j.jpowsour.2020.229430.

[50] M. Tanemura, T. Ogawa, and N. Ogita, A new algorithm for three-dimensional Voronoi tessellation, *J. Comput. Phys.* 51[2] (1983) 191-207. https://doi.org/10.1016/0021-9991(83)90087-6.

[51] E. J. Cheng, N. J. Taylor, J. Wolfenstine, and J. Sakamoto, Elastic properties of lithium cobalt oxide ($LiCoO_2$), *J. Asian Ceram. Soc.* 5[2] (2017) 113-17. https://doi.org/10.1016/j.jascer.2017.03.001.

[52] S. Yamakawa, N. Nagasako, H. Yamasaki, T. Koyama, and R. Asahi, Phase-field modeling of stress generation in polycrystalline $LiCoO_2$, *Solid State Ionics* 319 (2018) 209-17. https://doi.org/10.1016/j.ssi.2018.02.013.

[53] A.-N. Wang, J. F. Nonemacher, G. Yan, M. Finsterbusch, J. Malzbender, and M. Krüger, Mechanical properties of the solid electrolyte Al-substituted $Li_7La_3Zr_2O_{12}$ (LLZO) by utilizing micro-pillar indentation splitting test, *J. Eur. Ceram. Soc.* 38[9] (2018) 3201-09. https://doi.org/10.1016/j.jeurceramsoc.2018.02.032.

[54] J. E. Ni, E. D. Case, J. S. Sakamoto, E. Rangasamy, and J. B. Wolfenstine, Room temperature elastic moduli and Vickers hardness of hot-pressed LLZO cubic garnet, *J. Mater. Sci.* 47[23] (2012) 7978-85. https://doi.org/10.1007/s10853-012-6687-5.

[55] S. Yu, R. D. Schmidt, R. Garcia-Mendez, E. Herbert, N. J. Dudney, J. B. Wolfenstine, J. Sakamoto, and D. J. Siegel, Elastic Properties of the Solid Electrolyte $Li_7La_3Zr_2O_{12}$ (LLZO), *Chem. of Mater.* 28[1] (2016) 197-206. https://doi.org/10.1021/acs.chemmater.5b03854.

[56] H. Moulinec and P. Suquet, A numerical method for computing the overall response of nonlinear composites with complex microstructure, *Comput. Meth. Appl. Mech. Eng.* 157[1] (1998) 69-94. https://doi.org/10.1016/S0045-7825(97)00218-1.

[57] M. Schneider, F. Ospald, and M. Kabel, Computational homogenization of elasticity on a staggered grid, *Int. J. Numer. Meth. Engng*. 105[9] (2016) 693-720. https://doi.org/10.1002/nme.5008.

Supplementary material

Modeling Chemo-Thermal Mechanical Stresses in All-Solid-State Lithium Batteries: Influence of Grain Morphology and Alignment

Fadi Al-Jaljouli,[*[a,b]] Robert Mücke,[[a]] Martin Finsterbusch,[[a,e]] Payam Kaghazchi,[[a,d]] and Olivier Guillon[[a,b,c,e]]

[a] *Forschungszentrum Jülich GmbH, Institute of Energy Materials and Devices, Materials Synthesis and Processing (IMD-2), 52425, Jülich, Germany*

[b] *Institute of Mineral Engineering, RWTH Aachen University, 52064 Aachen, Germany*

[c] *Jülich Aachen Research Alliance: JARA-Energy, Jülich, 52425, Germany*

[d] *MESA+ Institute for Nanotechnology, University of Twente, P. O. Box 217, Enschede, 7500AE, The Netherlands*

[e] *Helmholtz Institute Münster: Ionics in Energy Storage (IMD-4 / HI MS), Münster 48149, Germany;*

Emails: f.al-jaljouli@fz-juelich.de, r.muecke@fz-juelich.de, m.finsterbusch@fz-juelich.de, p.kaghazchi@fz-juelich.de, o.guillon@fz-juelich.de

- ***Statistical analysis***

In order to assess the producibility of our results, a set of 10 microstructures was generated with fixed SVF_{LCO}, $\bar{\rho}$ and grains dimension while varying the random seed only followed by characterizing their chemo-thermal mechanical stresses for both LCO and LLZO. We have arbitrary chosen the random seed variation in this range considering that any change of random seed will yield a completely different series of produced pseudo random numbers. Any other range of the random seed values would yield the same statistics. The standard deviation was 0.005 GPa (2%) for LCO and 0.02 GPa (5%) for LLZO (Figure S1). This indicates that the findings are well reproducible.

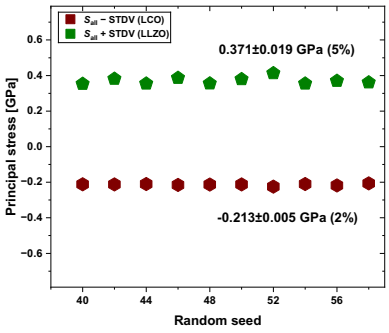

Figure S1. Chemo-thermal principal stress as a function of random seed for textured hexagonal LCO-fiber LLZO. The fixed parameters were as follow: SVF_{LCO}= 69.4%, $\bar{\rho}$ = 93.14%, average grain size of LCO 2.00 µm, fiber LLZO length and diameters 3µm and 0.5µm, respectively.

- ***Grain morphology behavior with varying the relative density***

Varying the relative density $\bar{\rho}$ effectively modifies the porosity percentage within the system, which directly impacts the coordination number. Hence, increasing the value of $\bar{\rho}$ leads to an increase of the coordination number, resulting in a decrease in the system's porosity. Under these circumstances, the volume changes of the composite cathode components (LCO and LLZO) during the chemo-thermal condition are constrained leading to a progressive increase in the induced mechanical stresses in both LCO and LLZO [1].

In systems employing textured hexagonal LCO grains, those incorporating randomly aligned fiber LLZO demonstrate slightly lower induced mechanical stresses in both LCO and LLZO compared to systems utilizing spherical LLZO (Figure S2). This slight reduction can be attributed to the artifact in the system specifically, shadowing created by the fibers.

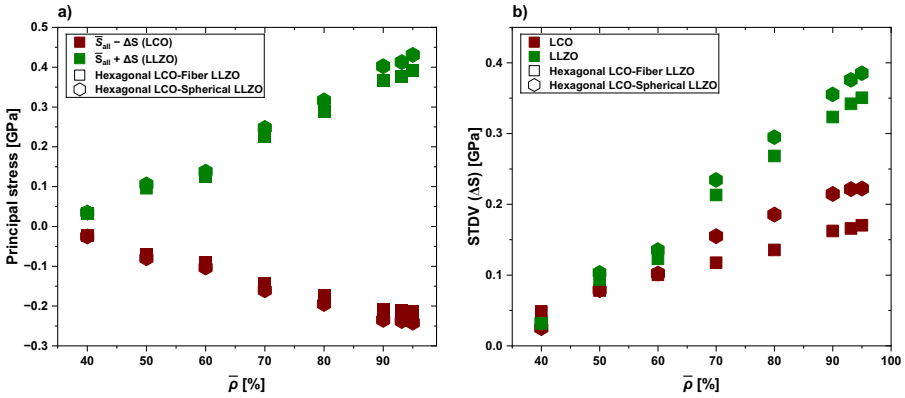

Figure S2. a) Chemo-thermal principal stress as a function of $\bar{\rho}$ for textured hexagonal LCO-spherical LLZO and textured hexagonal LCO-fiber LLZO. b) The standard deviation, which represent the width of distribution.

Conversely, in systems utilizing randomly oriented spherical LCO grains, both the increase in coordination number and the effects of these randomly oriented grains contribute to amplify the induced mechanical stresses in both LCO and LLZO. However, comparing to systems utilizing spherical LLZO, the systems which utilize fiber LLZO exhibit higher induced tensile mechanical stresses (Figure S3). This attributed to the higher interface area of each spherical LCO grains that can contact fiber LLZO. Hence, both induced compressive and tensile mechanical will arise in fiber LLZO by each single LCO grains which in contact with fiber LLZO thereby increasing the resultant induced tensile stresses.

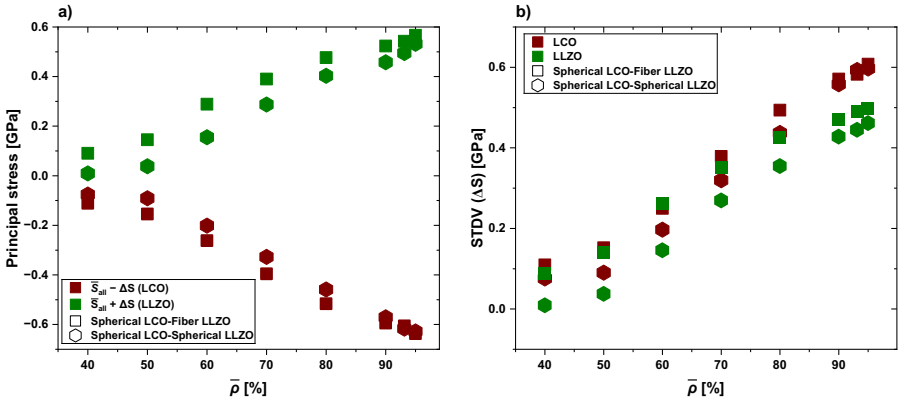

Figure S3. a) Chemo-thermal principal stress as a function of $\bar{\rho}$ for random oriented spherical LCO-spherical LLZO and random oriented spherical LCO-fiber LLZO. b) The standard deviation, which represent the width of distribution.

References

[1] F. Al-Jaljouli, R. Mücke, P. Kaghazchi, Y. J. Sohn, M. Finsterbusch, D. Fattakhova-Rohlfing, and O. Guillon, Microstructural parameters governing the mechanical stress and conductivity of all-solid-state lithium-ion-battery cathodes, *J. Energy Storage* 68 (2023) 107784. https://doi.org/10.1016/j.est.2023.107784.

3.4. Paper IV: Modelling Electro-Chemically Induced Stresses in All-Solid-State Batteries: Screening Electrolyte and Cathode Materials in Composite Cathodes

Authors	Robert Mücke, Najma Yaqoob, Martin Finsterbusch, **Fadi Al-Jaljouli**, Payam Kaghazchi, Dina Fattakhova-Rohlfing and Olivier Guillon
Journal	Journal of materials chemistry A
Volume	11
Pages	18801-18810
Published on	Aug 2023
DOI	10.1039/D3TA01729J

The following are my contributions:

- Investigate the impact of volume change on mechanical stresses values for utilized CAMs
- Investigate the impact of the electro-chemical crystallographic strain difference and the corresponding stresses on the Width of the stress distribution.
- Creation of Figure 2u,v in the manuscript.

.

Modelling Electro-Chemically Induced Stresses in All-Solid-State Batteries: Screening Electrolyte and Cathode Materials in Composite Cathodes

Robert Mücke,*[a] Najma Yaqoob,[a,b] Martin Finsterbusch,[a] Fadi Al-Jaljouli,[a,c] Payam Kaghazchi,[a,b] Dina Fattakhova-Rohlfing [a,d] and Olivier Guillon[a,c]

Abstract

All-solid-state lithium batteries (ASSBs) are gaining significant attention worldwide as one of the most promising alternatives to lithium-ion batteries due to their superior safety and potentially higher energy density. However, one of the main problems of known ASSBs remains rapid capacity degradation, which needs to be addressed before their large-scale market introduction. One important degradation mechanism is the mechanical fatigue of the cathode layer due to the volume change of the cathode active material (CAM) during cycling. Quasi-zero-strain CAMs such as $Li_xNi_{0.3}Co_{0.6}Mn_{0.1}O_2$ (NCM361) and $Li_xNi_{0.2}Co_{0.7}Mn_{0.1}O_2$ (NCM 271) could solve this problem, but their use in ASSBs has not been investigated yet. We theoretically investigate the suitability of these CAMs in composite cathodes with various solid electrolytes such as poly(ethylene oxide) (PEO), Li_3PS_4 (LPS), $Li_{1.3}Al_{0.3}Ti_{1.7}(PO_4)_3$ (LATP) and $Li_7La_3Zr_2O_{12}$ (LLZO) with respect to the mechanical stresses occurring at microscopic grain level and compare them with $Li_xNi_{0.9}Co_{0.05}Mn_{0.05}O_2$ (NCM955) and $LiCoO_2$ (LCO). Although the quasi-zero-strain materials develop stresses in the GPa range during cycling, they still exhibit the lowest stresses of all the CAMs studied and could be of particular interest when using stiff electrolytes such as LATP or LLZO. High-capacity NCMs such as NCM955 exhibit a large volume change and should preferably be used together with electrolytes with bulk modulus less than 25 GPa such as PEO and LPS. While for soft electrolytes such as PEO and LPS the difference between the lattice strains along the different axes of the active material determines the stresses, for stiff electrolytes such as LATP and LLZO the total volume change is more important. Finally, a method is introduced to determine the stresses quickly from the free macroscopic strain mismatch without stress simulations.

Introduction

All-solid-state batteries (ASSB) are gaining a lot of attention worldwide as one of the most promising alternatives to lithium-ion batteries (LIBs) due to an expected improvement in cell properties in terms of safety, energy density and operating temperature range. Various solid electrolytes are currently being considered for ASSB

fabrication, mostly of the oxide, sulfide, halide or polymer type, each with its advantages and disadvantages.

Although important breakthroughs have been reached in various systems, such as an exceptional ionic conductivity of sulfide electrolytes or high current densities with Li metal anodes obtained with oxide electrolytes, the performance of liquid-free ASSB still lags behind that of LIBs. In particular, the fabrication of cathodes with high energy density and high cycling stability remains one of the most pressing problems of known ASSBs, which needs to be solved before large-scale market introduction.

To achieve competitive energy and power densities, the cathode layers should contain a large amount of high energy density cathode active material distributed in the solid electrolyte, similar to the three-dimensional composite cathode architecture in LIBs. Layered oxides of the quasi-ternary phase diagram $LiCoO_2$ – $LiNiO_2$ – $LiMnO_2$ ($Li_xNi_{1-y-z}Co_yMn_zO_2$, NCM) are state-of-the-art cathode active materials to achieve high energy densities and enable high currents. However, all these oxides suffer from degradation during cycling, and the fracture of cathode particles due to non-negligible volume changes during lithiation and delithiation plays a crucial role.[1-10] Nickel-rich NCMs such as $Li_xNi_{0.9}Co_{0.05}Mn_{0.05}O_2$ (NCM955) are very attractive cathode active materials because they yield very good energy density and avoid cobalt for economic, security, and ethical reasons. However, this comes with a drawback of a rather high chemical lattice strain of up-to –4%. Attempts have been undertaken to develop quasi-zero-strain NCM materials with minimised volume change, such as $Li_xNi_{0.3}Co_{0.6}Mn_{0.1}O_2$ (NCM361) and $Li_xNi_{0.2}Co_{0.7}Mn_{0.1}O_2$ (NCM 271),[11] which have a capacity of ~160 mAh/g_{NCM} at 4.3 V and 210 mAh/g_{NCM} at 4.6 V. However, significant lattice strains also occur in these materials during lithiation and delithiation (ε_a = −1.1% and ε_c = +1.3% for NCM361). It should be noted that it is not the final stress but the maximum accompanying stress that governs the degree of mechanical degradation. The maximum stresses occur at about x=0.5 and decrease again at x=0.2 (compare Fig. 4 of [11]).

Mechanical degradation is exacerbated when solid electrolytes are used instead of liquid electrolytes in the composite cathodes, and is considered by many researchers to be the main reason for the capacity loss of ASSBs during cycling.[12] Due to the rigid structure of solid electrolytes, their ability to absorb and distribute stresses deteriorates, resulting in large local stresses throughout the entire cathode architecture and mechanical failure of

various interfaces. The stress development is affected by the anisotropy of the cathode active material lattice and the particle distribution, as well as by the type of solid electrolyte.[13-16]

Different solid electrolytes in composite cathodes exhibit a strong variation of mechanical properties and thus significantly affect the overall stress state. $Li_7La_3Zr_2O_{12}$ (LLZO) is an intensively investigated oxide ceramic with good electrochemical stability against various CAMs,[17, 18] and is so far the only ceramic electrolyte that is (electro-)chemically stable toward Li metal anodes.[19] It exhibits a rather high (isotropic) mechanical stiffness of approximately 145GPa. The NASICON-type solid electrolyte $Li_{1.3}Al_{0.3}Ti_{1.7}(PO_4)_3$ (LATP) exhibits a comparable stiffness, but with pronounced rhombohedral anisotropy. In addition to the oxides, the sulphides form another main group of ceramic electrolytes, among which the thio-phosphates have the highest conductivity.[20] They exhibit a rather low stiffness (20-30 GPa)[21] and offer good mechanical ductility. We analysed Li_3PS_4 (LPS) from this group as an example to compare it with the other electrolytes. Furthermore, polymers are another very important group of solid electrolytes for all-solid-state battery. One candidate is poly (ethylene oxide) (PEO) with extremely low stiffness (0.1 GPa) and high strain tolerance, which has already been used in composite LCO/PEO cathodes.[22]

The models for predicting stresses are important for the development of ASSBs as they allow the screening of various material composition and electrode architectures without extensive experimental studies. In our previous work, we developed a theoretical approach to study the anisotropic stress distributions in a LCO/LLZO composite cathode.[13] Using computer-generated microstructures, we further showed that for low *C* rates (equilibrium Li concentration) the grain size has no significant effect on the mechanical stresses whereas the LCO:LZZO ratio exhibited a significant linear effect, keeping the difference in the stress levels of the two phases constant, and the porosity showed a non-linear effect.[23] In the present work, we use an experimental and four computer-generated microstructures to investigate other prospective cathode active materials and solid electrolytes to explore their potential to reduce the mechanical stresses in the microstructure. We theoretically investigate the suitability of quasi-zero-strain cathode active materials such as NCM361 and NCM 271 in composite cathodes with important solid electrolytes such as PEO, LPS, LATP and LLZO with respect to the

mechanical stresses occurring at grain level and compare them with NCM955 and LCO. To study only the effect of material parameters, the same microstructure applicable for all cases was used to model the mechanical behaviour of all materials based on the experimental microstructure of LCO-LLZO cathodes, the results were confirmed by three more computer-generated microstructures with different CAM content and porosity and one reference computer-generated structure. Unknown anisotropic elastic stiffness matrices for some of cathode materials during charge/discharge ($Li_{0.5}$NCM271, $Li_{0.5}$NCM955, $Li_{0.1}$NCM955, $Li_{0.5}CoO_2$) were calculated using density functional theory (DFT). The material parameters that lead to the stresses were analysed to find the origin of the stresses and to find a common relationship between all stresses. Based on this we present an approach which allows the stress determination without complex simulations which can be useful in future material screenings.

Results and discussion

First we focus on the experimental microstructure, at the end we compare some results with the computer-generated structures. Without any electrolyte material in the cathode, the pure LCO and NCM networks develop mechanical stresses during delithiation because of their anisotropic electro-chemical strains and the random orientation of the connecting grains (Fig.1 a-d). The different crystallographic orientations lead to a mismatch of chemical strains of adjacent grains along the same macroscopic direction. It should be noted that compressive stresses of the observed order will not cause failure in oxide materials as under compression the fracture strength is extremely high. Tensile stresses are more serious. However, in absence of stress concentrators (typically large pores of tens or hundreds of microns, cracks, etc.) at the microscopic level the tensile strength of single crystals and whiskers in the micrometre range is also very high (in the GPa range, typically at least one order of magnitude lager than the tensile strength measured macroscopically for a polycrystalline ceramic). Out of this reason, well-sintered composite cathodes with low porosity prepared e.g. by field assisted sintering[24] might be more stress tolerant than traditionally sintered electrodes that show a residual porosity and cracks after cycling.[10]

The corresponding stress histograms indicate the most narrow stress distribution with the smallest stresses for NCM271, followed by NCM361 and LCO (Fig. 2a-d). $Li_{0.5}$NCM955 showed the broadest distribution with microscopic tensile stresses well above 1.5 GPa due to its

high stiffness and strain anisotropy (the stress distribution of $Li_{0.1}NCM955$ is shown in Fig. S1). As the cathodes are free-standing and can expand freely macroscopically, high chemical strains alone do not lead to high stresses in pure cathode active polycrystalline materials, but the strain difference between the two different chemical lattice strains, namely $\varepsilon_{c,ch} - \varepsilon_{a,ch}$, control the stress state together with the materials' stiffness.

Plotting the width of the stress distribution *vs*. the mere strain difference of the different materials a common trend to higher stress values for higher strain differences is observed (Fig. 2u). $Li_{0.1}NCM955$ shows the smallest stress values because of the small difference in the strain components $\varepsilon_{c,ch} - \varepsilon_{a,ch}$. However, in order to obtain this high degree of delithiation, $Li_{0.5}NCM955$ with a lower Li content has to be reached beforehand which is accompanied with the highest stresses because of the large difference in the strain components. The points (Δ_{ch}) still scatter significantly. This scattering becomes slightly smaller considering the absolute value of the developing stresses $\Sigma_{\Delta} = \left|\varepsilon_{c,ch} - \varepsilon_{a,ch}\right| / \left(c_{11}^{-1} + c_{33}^{-1}\right)$ according to an iso-strain model of two adjacent grains with a perpendicular orientation leading to maximum strain difference. The remaining scattering shows that the real situation with arbitrary grain boundary angles and non-uniform stress states is more complex.

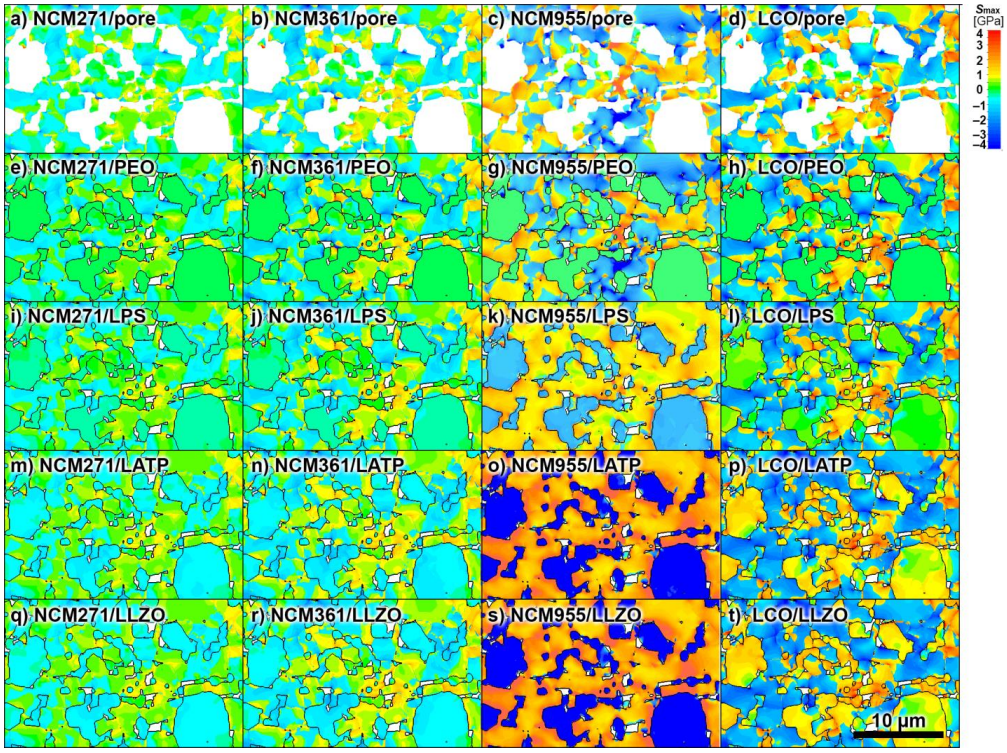

Fig. 1: Stress maps (principle stress with maximum absolute value) of a cross section of the delithiated porous/composite cathode with different cathode active materials and electrolyte materials for the configuration with the max. stresses: Li=0.1. for k,o,s and Li=0.5 for all others.

in the following, the stress results of composite cathodes with various electrolyte materials in ascending order of their stiffness are presented. PEO exhibits an extremely small Young's modulus (approx. 3 orders of magnitude lower than the cathode active material); in consequence it can compensate almost all stresses by deformation when acting as electrolyte in a composite cathode (Fig. 2e-h), the stresses inside PEO are practically zero. Furthermore, no change in the stress state in the cathode active material was observed with or without PEO (Fig 1a-h, compare Fig. 2 e-h with Fig. 2 a-d).

Using LPS as electrolyte material in the composite cathode introduces a slight shift of the stress distribution inside the cathode active materials (Fig. 2 i-l). This shift is smallest for NCM271 and NCM361, followed by LCO, and very significant for NCM955 (0.49 GPa). The stress distributions of LCO/LPS are shifted in the opposite direction than the distributions of the other three combinations as LCO is the only material that expands during delithiation. Also the shape of the distributions changed: the sharp maxima at zero stress were reduced and widened as the

cathode active material directly in contact with the electrolyte material cannot expand freely anymore but is significantly constrained. The width of the distributions remained unchanged except for the case of NCM955. In this case $Li_{0.1}$NCM955 with a smaller stress distribution width was considered as it introduces the largest stresses in the electrolyte. (The stress

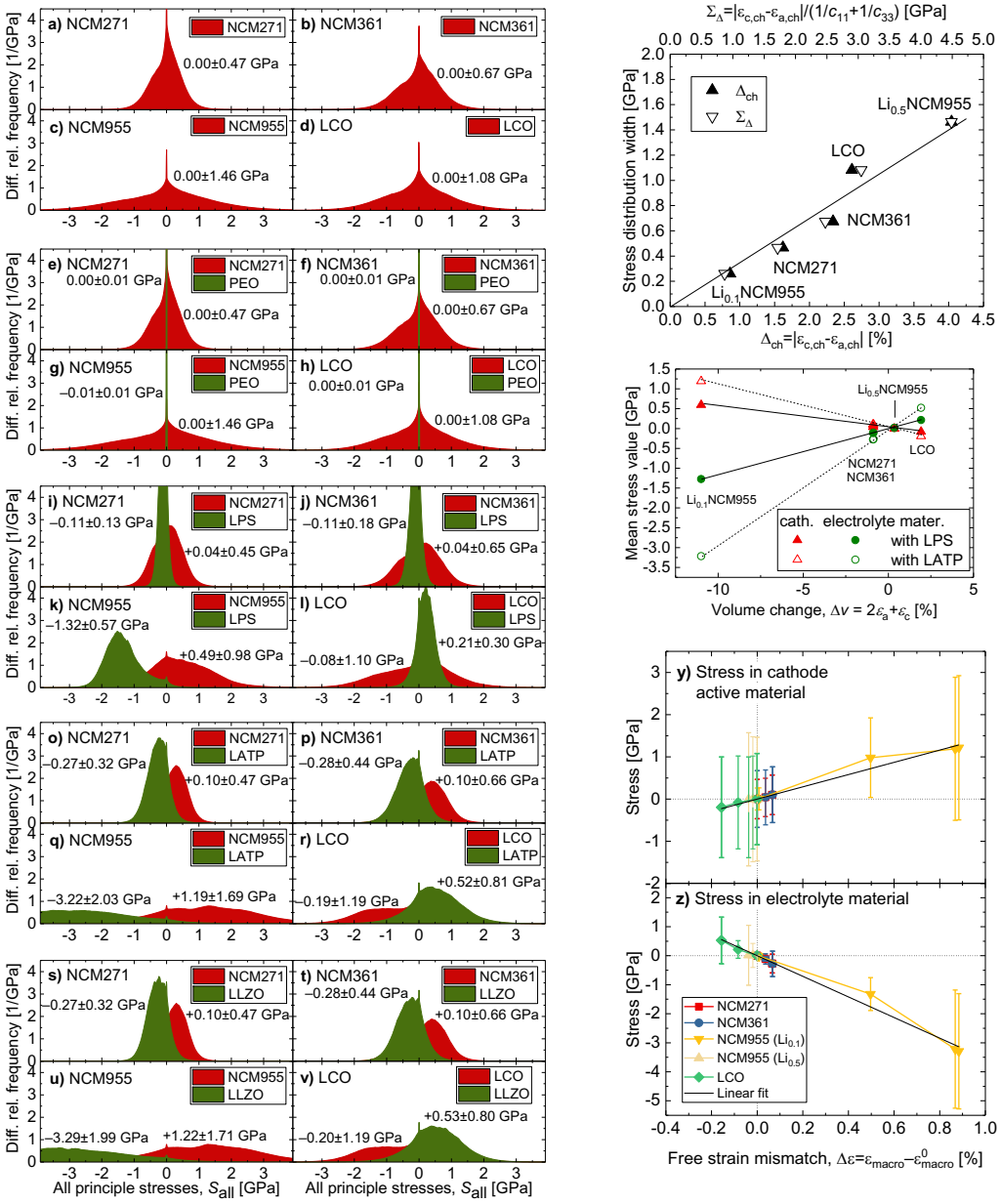

Fig. 2:a-d) Histograms of all principal stresses inside different pure polycrystalline cathode active materials with random crystallographic grain orientation, e-h) with PEO electrolyte material, i-l) with LPS electrolyte material, o)-r) with LATP as electrolyte material, s)-v) with LLZO as electrolyte material. c,g) $Li_{0.5}NMC955$, k,q,u) $Li_{0.1}NMC955$. The mean value and the width (standard deviation) of distributions are given. w) Width of the stress distribution of Fig. **Error! Reference source not found.** a-d as a function of the electro-chemical crystallographic strain difference (Δ_{ch}) and the corresponding stresses (Σ_Δ). x) Mean stress values of the cathode active and electrolyte material of the composite cathode as a function of the volume change for different electrolytes. (LLZO would behave very similar to LATP.) y,z) Stress in cathode active material (y) and electrolyte material (z) of composite cathodes as a function of the free strain mismatch for various cathode active materials. The error bars indicate the width (standard deviation) of the stress distribution.

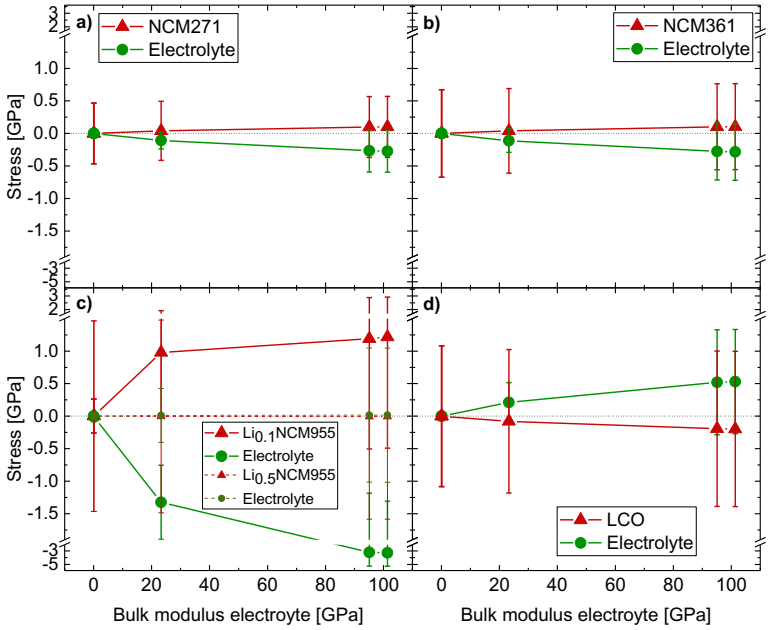

Fig. 3: Average principal stresses inside composite cathodes with different cathode active materials (a-d) as a function of the bulk modulus of the electrolyte material. The error bars indicate the width (standard deviation) of the stress distribution.

distribution of $Li_{0.5}NCM955$ is given in Fig. S1c.) NCM955 shows a significant general increase of the stress levels (Fig. 3g, k) which is caused by the very high absolute values of the chemical strains of NCM955 against LPS with non-negligible stiffness. Typically, cell stacks with LPS based cells are compressed e.g. with 250 MPa during operation. The final stress results with compression are given in Fig S2, they do not differ significantly from the calculations without compression.

Whereas only the difference of the anisotropic strains component mattered for the pure cathode active materials the value of the total volume change becomes more important once a more or less rigid electrolyte phase is introduced in the composite cathode. The mean principle stress value (σ_{mean}) inside the cathode material is proportional to the relative volume change (Δv) of the cathode active material (Fig. 2 x, more details in Fig. S3). The absolute value of the proportionality factor ($\sigma_{mean}/\Delta v$) increases non-linearly with increasing electrolyte stiffness (Fig. S3 c). Due to the stiffness of LPS the stresses inside the electrolyte material are not negligible anymore, but also grow with the chemical strains of the cathode material and its stiffness. The highest value is reached in combination with $Li_{0.1}NCM955$.

With LATP as electrolyte material, the shift of the stress distributions of the cathode active materials becomes more significant as for LPS as electrolyte material whereas the order of the cathode active materials from high to low shift levels remains the same (Fig. 2 o-r). The maximum value, 1.19 GPa, was reached with NCM955/LATP. For LCO and in particular for NCM955 the width of the distribution widened significantly due to higher overall stress levels (Fig. 1 o, p)

When LLZO is used as electrolyte material, the stress states (Fig. 2q–t) are almost identical to the stress states with LATP as the average stiffness is similar. The stiffness anisotropy of LATP does not change the effective principle stresses.

In order to get an overview about the mean stress values, all values together with their distribution width are plotted as a function of the bulk modulus of the electrolyte in Fig 3. This modulus governs the stiffness of the rigid electrolyte framework against which the cathode active material has to expand or shrink. The absolute mean stresses inside the cathode active material and the electrolyte material of the composite cathode first grow quickly with increasing bulk modulus of the electrolyte material. This increase slows down for bulk moduli bigger than 24 GPa. Therefore a soft electrolyte with a bulk modulus smaller than approx. 25 GPa is preferable in particular for large strain cathode active materials. The quasi zero strain NCM materials (NCM271, NCM 361) develop the smallest stresses considering also the width of the distribution. The magnitude of the stress level inside the active material is comparable to that for LCO. The stresses inside the electrolyte material are much smaller in composite cathodes with NCM271 and NCM361 compared to cathodes with LCO.

A common relationship for the stress values of all combinations analysed is found when plotting the strain vs. the difference of the average macroscopic strain with and without electrolyte material (Fig. 2 y,z). The expansion of the pure cathode active material, $\varepsilon^{0}_{\mathrm{macro}}$, can be calculated and the expansion of the composite cathode, $\varepsilon_{\mathrm{macro}}$, can be measured. Then, the mean values of the stresses can be obtained easily. Tab. S1 shows that for not too low CAM content (CAM:Electrolyte material ≥ 1:1) the known mean lattice strains $(2\varepsilon_a+\varepsilon_b)/3$ can be used for $\varepsilon^{0}_{\mathrm{macro}}$

The slope of a linear fit is (+1.5±0.1) GPa/% for the stress inside the cathode active material, and (−3.5±0.4) GPa/% for the stress inside the electrolyte material. Once the dependency of these slopes on the microstructure is found, a very general model for the stresses inside composite cathodes can be given without the necessity of stress simulations. Tab. 1 summarises

the slopes also for four modelled microstructures with different cathode active material contents and porosity. The difference in both slopes ($\sigma_{CAM}/\Delta\varepsilon$ and $\sigma_{ELC}/\Delta\varepsilon$) between the experimental and the same modelled microstructure is mainly that the point of $Li_{0.1}$NCM955/LPS deviates in the opposite direction of the proportionality fit line. However, considering the margin of error the slopes are in agreement. Whereas the CAM content did not change the slope $\sigma_{CAM}/\Delta\varepsilon$ it significantly affects $\sigma_{ELC}/\Delta\varepsilon$. The porosity changes both slopes.

Tab. 1: Slopes of the stress-free strain difference curves of (Fig. **Error! Reference source not found.** y,z) and of more modelled microstructures (Fig. S4-S7). Exp./Mod.=experimental/modelled microstructure The volume ratio between CAM:electrolyte material (ELC) and the porosity (%) is given.

Exp./Mod.	CAM:ELC	Por.,%	$\sigma_{CAM}/\Delta\varepsilon$, GPa/%	$\sigma_{ELC}/\Delta\varepsilon$, GPa/%
Exp.	2:1	7	+1.5±0.2	−3.5±0.4
Mod.	2:1	7	+1.3±0.2	−2.8±0.3
Mod.	1:1	7	+1.2±0.2	−1.2±0.2
Mod.	1:2	7	+1.5±0.3	−0.7±0.2
Mod.	2:1	20	+0.8±0.1	−1.8±0.2

Conclusions

There are four reasons for the mechanical stresses in all solid composite cathodes occurring during electrochemical cycling: (1) The difference of anisotropic lattice expansion in pure cathode active materials. This introduces already stresses in pure active materials with sintered randomly oriented polycrystals. (2) With a rigid and stiff electrolyte the overall volume change of cathode active material becomes more important, the mean values of the stresses are proportional to the volume change. (3) In particular the stiffness (bulk modulus) of the electrolyte material. It determines the proportionality factor between mean stress and volume change. (4) The stiffness of the active material (they differ not much, however).

Applied to the materials screened it follows: The quasi zero strain NCM materials (NCM271 and NCM 361) still develop stresses in the GPa range on the grain level over the course of delithiation, but exhibit the smallest stresses among all materials investigated. This might be of particular interest when stiff electrolytes like LATP or LLZO are used. However, NCM271 and NCM361 still consist of a remarkable amount of Cobalt (60% and 70% of that of LCO, respectively) which might reduce their attractiveness for large scale application. For high-strain NCM 955 cathode material a bulk modulus of the electrolyte material of 25 GPa or less is preferable (LPS or PEO

electrolyte). Alternatively, a hybrid-electrolyte approach could be of interest, combining low and high bulk modulus materials to reduce the overall induced stresses.
Finally, all stresses depend proportionally on the free strain mismatch. This will also be the case for constrained composite cathodes layers e.g. on a thick separator. This measure can be used to predict the stresses easily. An initial general dependency of the corresponding proportionality factors on the microstructural parameters has been presented.

Experimental and simulation methods

Microstructure

The three dimensional microstructure of a sintered LLZO/LCO composite cathode was acquired by FIB-SEM and cropped to 26.5 × 16.5 × 16.5 µm (530 × 330 × 330 voxels) with a voxel size of 50 nm (Fig. 4 a). The LLZO:LCO volume ratio was 2:1. Details can be found elsewhere.[13] The same microstructure was used for different electrolyte or cathode active materials during the screening, in order to obtain the impact of the materials only. The microstructure used for modelling the mechanical behaviour in our

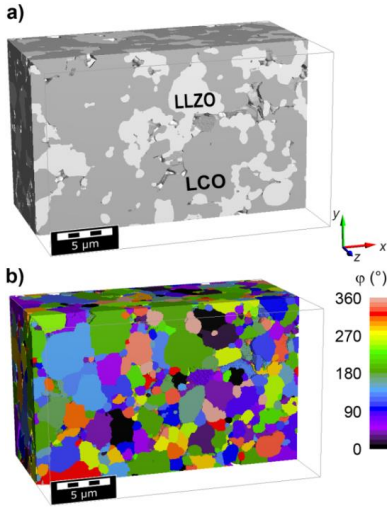

Fig. 1: a) Slice of the reconstructed 3D microstructure, b) distribution of the Euler angle φ of the randomly oriented grains after segmentation.

work is very typical for composite cathodes fabricated from powders slurries by conventional methods. This microstructure was observed experimentally for the ceramic

LCO-LLZO composite cathodes fabricated by various methods, e.g., screen-printed cathodes[25] or tape-cast free-standing cathodes.[26, 27] Similar to LCO, NCM is also a hexagonal layered oxide with comparable size and shape of the commercial powders, so replacing LCO with NCM powders should not significantly affect the microstructure of composite cathodes. This was confirmed by a very similar microstructure of screen-printed NCM-LLZO cathodes, which have comparable relative density and porosity to the LCO-LZO cathodes.[28] If PEO is infiltrated in a sintered porous cathode active network, then it will resemble the sintered LLZO phase of this study. The grains were segmented using the watershed method (GrainFind module of GeoDict, Math2Market GmbH, Kaiserslautern, Germany) and the crystallographic orientation was chosen randomly by appropriate Euler angles (φ, θ, ψ) to obtain a uniform distribution of the coordinate axes on the unit sphere (Fig. 4b). All calculations have been repeated on four computer-generated microstructures taken from Ref. 23 with varying CAM content and porosity in order to find the microstructure dependent slopes similar that of Fig. 2w and x for different microstructure parameters summarised in Tab.1.

Calculation of the strains and stiffness matrix of cathode active materials

Spin-polarized DFT calculations were performed using the projector augmented wave (PAW) potential method [29] implemented in the Vienna *Ab Initio* Simulation Package (VASP) code [30]. Generalized gradient approximation (GGA) within the scheme of Perdew–Burke–Ernzerhof (PBE) [31] was chosen as the exchange-correlation functional. To perform electrostatic energy analysis as well as DFT calculations we modelled $Li_xNi_{0.2}Co_{0.7}Mn_{0.1}O_2$ (Li_xNCM271) and $Li_xNi_{0.9}Co_{0.05}Mn_{0.05}O_2$ (Li_xNCM955) structure (space group: R-3m) using a 2×2×1 and 4×4×1 unit cell, respectively. To perform DFT calculations gamma-centred *k*-point meshes of 4×4×1 and 2x2x2 were applied for Li_xNCM271 and Li_xNCM955 structures respectively. An energy cut off of 800 eV as well as electronic and force convergence criteria of 10^{-5} eV and 10^{-3} eV/Å, respectively, were considered. For the calculation of elastic constants C_{ij}, we kept fixed the magnetic moment and atomic coordinates to the optimized ones for the equilibrium lattice parameters. C_{ij} matrix was computed using the strain values of 0, ±0.5%, and ±1%. After computing C_{ij}, we obtained the mechanical properties such as Young's, bulk and shear modulus as well as Poisson's ratio by using the Voigt-Reuss-Hill (VRH) homogenization scheme.[32] To find the position of TM (Ni, Co, and Mn) and Li ions in $Li_{1.0}$NCM271

(modelled by $Li_{12}Ni_2Co_9Mn_1O_{24}$) and $Li_{1.0}$NCM955 (modelled by $Li_{48}Ni_{44}Co_2Mn_2O_{96}$) we first modelled and calculated the Coulomb energy (E_c) of all possible structures and then performed DFT on minimum energy ones. Total Coulomb energy calculations were carried out using the so-called supercell code.[33]

$Li_xNi_{0.2}Co_{0.7}Mn_{0.1}O_2$ (Li_xNCM271). We computed E_c for $\frac{12!}{2!10!}.\frac{10!}{1!9!} = 660$ possible structures with 1 Mn, 2Ni, and 9 Co ions in 12 TM sites to find the position of TM ions in $Li_{1.0}Ni_{0.2}Co_{0.7}Mn_{0.1}O_2$. Afterwards, we kept fixed the position of TM ions in the determined lowest E_c structure among 660 configurations and obtained the position of Li ions for $Li_{0.5}Ni_{0.2}Co_{0.7}Mn_{0.1}O_2$ by calculating E_c for $\frac{12!}{6!6!} = 924$ structures with 6 Li ions in 12 Li sites. The following charges were considered for Li, TM (Ni, Co and Mn), and O ions, respectively: 1^+, 3^+ (3.5^+ for half delithiation), and 2^-. Finally, by performing DFT-PBE calculation on 5 distinguishable topmost favourable structures from electrostatic analysis on $Li_{0.5}Ni_{0.2}Co_{0.7}Mn_{0.1}O_2$ we obtained the lowest total energy structure.

$Li_xNi_{0.9}Co_{0.05}Mn_{0.05}O_2$ (Li_xNCM955). We computed E_c for $\frac{48!}{2!46!}.\frac{46!}{2!44!} = 1.17 \cdot 10^6$ structures with 2 Mn, 2 Co and 44 Ni ions in 48 TM sites to find the position of TM ions in $Li_{1.0}Ni_{0.9}Co_{0.05}Mn_{0.05}O_2$. Then, we carried out DFT-PBE calculations on 2 configurations with lowest energies: i) Mn and Co at the same layer and ii) Mn and Co at different layers. The second configuration was found to be more favourable. Finding position of Li ions in $Li_{0.5}Ni_{0.9}Co_{0.05}Mn_{0.05}O_2$ is (computationally) a formidable task due to the large number of possible configurations with 24 Li ions in 48 Li sites. For this reason, we considered the arrangement of Li ions in $Li_{0.5}Ni_{0.2}Co_{0.7}Mn_{0.1}O_2$ for $Li_{0.5}Ni_{0.9}Co_{0.05}Mn_{0.05}O_2$.

Material parameters

Tab. 2: Elastic parameters (anisotropic stiffness matrix *C*, Young's modulus *E*, Poisson ratio ν, and bulk modulus *B*) and chemical strains for different cathode active materials and electrolyte materials. Values without references were calculated with DFT. VHR values denote the Voigt-Reuss-Hill approximation from the stiffness matrix.[34-37]

Elastic parameters	Chemical strains
$Li_{0.5}NCM271$	
$C = \begin{pmatrix} 242.2 & 87.4 & 136.0 & 0 & 0 & 0 \\ & 242.2 & 136.0 & 0 & 0 & 0 \\ & & 188.0 & 0 & 0 & 0 \\ & sym. & & 146.2 & 0 & 0 \\ & & & & 146.2 & 0 \\ & & & & & 77.4 \end{pmatrix}$ GPa ($E_{VHR} = 221$ GPa, $\nu_{VHR} = 0.26$, $B_{VHR} = 155$ GPa)	$\varepsilon_a = -0.83\%$ $\varepsilon_c = +0.79\%$ [11]
$Li_{0.5}NCM361$	
same as $Li_{0.5}NCM271$	$\varepsilon_a = -1.08\%$ $\varepsilon_c = +1.26\%$ [11]
$Li_{0.5}NCM955$	
$C = \begin{pmatrix} 279.1 & 117.8 & 107.7 & 0 & 0 & 0 \\ & 279.1 & 107.7 & 0 & 0 & 0 \\ & & 184.6 & 0 & 0 & 0 \\ & sym. & & 75.2 & 0 & 0 \\ & & & & 75.2 & 0 \\ & & & & & 80.6 \end{pmatrix}$ GPa ($E_{VHR} = 195$ GPa, $\nu_{VHR} = 0.29$, $B_{VHR} = 153$ GPa)	$\varepsilon_a = -1.23\%$ $\varepsilon_c = +2.81\%$
$Li_{0.1}NCM955$	
$C = \begin{pmatrix} 278.0 & 91.5 & 114.2 & 0 & 0 & 0 \\ & 278.0 & 114.2 & 0 & 0 & 0 \\ & & 158.7 & 0 & 0 & 0 \\ & sym. & & 70.6 & 0 & 0 \\ & & & & 70.6 & 0 \\ & & & & & 93.2 \end{pmatrix}$ GPa ($E_{VHR} = 188$ GPa, $\nu_{VHR} = 0.29$, $B_{VHR} = 146$ GPa)	$\varepsilon_a = -3.95\%$ $\varepsilon_c = -3.09\%$
$Li_{0.5}CoO_2$	
$C = \begin{pmatrix} 308.6 & 78.3 & 84.9 & 0 & 0 & 0 \\ & 308.6 & 84.9 & 0 & 0 & 0 \\ & & 187.9 & 0 & 0 & 0 \\ & sym. & & 64.1 & 0 & 0 \\ & & & & 64.1 & 0 \\ & & & & & 115.2 \end{pmatrix}$ GPa ($E_{VHR} = 212$ GPa, $\nu_{VHR} = 0.25$, $B_{VHR} = 141$ GPa)	$\varepsilon_a = -0.23\%$ $\varepsilon_c = +2.38\%$ [13, 38, 39]
PEO	
$E = 0.1$ GPa, $\nu = 0.4$, $B = 0.167$ GPa	$\varepsilon = 0\%$

LPS

$$C = \begin{pmatrix} 32.1 & 10.9 & 19.7 & 0 & 0 & 0 \\ & 38.1 & 17.4 & 0 & 0 & 0 \\ & & 51.8 & 0 & 0 & 0 \\ & sym. & & 10.5 & 0 & 0 \\ & & & & 9.5 & 0 \\ & & & & & 13.7 \end{pmatrix} \text{GPa}$$ [21]

$\varepsilon = 0\%$

$(E_{VRH} = 31.2\,\text{GPa},\ \nu_{VRH} = 0.28,\ B_{VHR} = 23.3\,\text{GPa})$

LATP

$$C = \begin{pmatrix} 226.0 & 86.7 & 43.9 & 7.9 & 0 & 0 \\ & 226.0 & 43.9 & -7.9 & 0 & 0 \\ & & 116.3 & 0 & 0 & 0 \\ & sym. & & 48.6 & 0 & 0 \\ & & & & 48.6 & 7.9 \\ & & & & & 69.6 \end{pmatrix} \text{GPa}$$

$\varepsilon = 0\%$

value for $LiTi_2(PO_4)_3$ [21]

$(E_{VRH} = 146\,\text{GPa},\ \nu_{VRH} = 0.24,\ B_{VHR} = 95.1\,\text{GPa})$

LLZO

$E = 146\,\text{GPa},\ \nu = 0.26,\ B = 101\,\text{GPa}$ $\varepsilon = 0\%$

The maximum strain over the course of delithiation is crucial for the effect of mechanical fatigue. This occurs in all considered cathode active materials approximately at the point of half lithiation ($x = 0.5$), except for NCM955. For this material the largest strains are found for higher state of charges ($x < 0.5$), we selected $x = 0.1$. Notwithstanding, the largest difference in the anisotropic lattice strains is observed for $x = 0.5$ also for NMC955. As will be seen later, depending on the electrolyte stiffness, one or the other state of charge leads to the maximum stress. Hence, both cases have been considered and the results with the maximum stress are given in the main article and the other case in the supplementary information.

The stiffness matrices for the anisotropic materials and the Young's moduli and Poisson ratios for the isotropic materials are summarised together with chemical strains of the cathode active materials in Tab. 2. As no values for LATP were available, the calculated values for the similar $LiTi_2(PO_4)_3$ have been used.

Simulation setup and boundary conditions

The charging rate was assumed to be low enough that the resulting Li concentration gradients inside the cathode were negligible. This is typically the case for C rates not larger than 0.1 (sometimes 1, for low CAM content and small grain sizes). Thus, comparable benchmark

stresses are calculated emerging in a perfectly working battery (no isolated CAM regions are present).

The constitutive equation of the linear elastic chemo-mechanical calculations are given in the Supplementary information, p. S1-2. We calculated the stresses of composite cathodes of different compositions at these given state of charge (Tab. 2) and compared the different material combinations. According to the Pugh criterion, the materials with the given elastic constants do not express a significant ductility, but were assumed to behave elastically until fracture. The fracture process itself was not part of the model. Until now, there are no strength data available to conclude the exact point of failure. Still, the analyses of the resulting stresses can serve as a guideline for lowering mechanical stresses in composite cathodes of all-solid-state batteries avoiding stress concentrations detrimental to the fracture strength of the composite. Furthermore, a reliable battery should not show crack formation at all, but exhibit low stresses; the material combination which show these can be found with our screening approach. Since we study the effect of the mere delithiation in this work, no thermal mismatch stresses of the manufacturing processes were taken into account. These thermo-elastic stresses arising during cooling from the sintering temperature to room temperature simply add to the electrochemically induced stresses.

The 3D microstructure acquired by FIB-SEM and the computer-generated microstructures served as representative volume elements (RVE). Thus they represent a bulk cathode of infinitive extent using symmetric (Dirichlet) boundary conditions in all directions. The composite cathode was considered as free-standing, hence no constrains were applied. The stress calculations were carried out using the ElastoDict FeelMath-LD module of the GeoDict software with a conjugate gradient voxel based solver.[40,41] The geometry was discretised with a regular voxel grid skipping the necessity of complex meshing required by finite element solvers. As all deformations were small the small deformation theory was used.

Stress representation

Stress histograms served as the main type for stress representation in this work. They show the differential relative frequency as a function of the stress value. The differential relative frequency $\tilde{n}_k$ was determined from the absolute frequency N_k of the stress S inside the stress interval $[S_k, S_{k+1}[$ by:

$$\tilde{n}_k = \frac{N_k}{(S_{k+1} - S_k) \sum_j N_j}$$

which is independent from the interval size chosen. An interval size of $S_{k+1} - S_k = 8$ MPa was used. In this work, the frequencies for all three principal stresses were summed up to represent the overall stress state.

Author contributions

Robert Mücke: Conceptualization, Methodology, Investigation, Validation, Visualisation, Writing – original draft. Najma Yaqoob: Investigation, Writing – original draft. Martin Finsterbusch: Writing – review & editing. Fadi Al-Jaljouli: Methodology, Investigation. Payam Kaghazchi: Methodology, Supervision, Writing – review & editing. Dina Fattakhova-Rohlfing: Funding acquisition, Writing – review & editing. Olivier Guillon: Conceptualization, Supervision, Writing – review & editing.

Conflicts of interest

There are no conflicts to declare.

Acknowledgements

Financial support from the German Ministry of Education and Research (BMBF) under grant number 13XP0510A (CatSE2) and 13XP0434A (FestBatt 2 – Oxid) is gratefully acknowledged.

References

1. A. O. Kondrakov, A. Schmidt, J. Xu, H. Gesswein, R. Monig, P. Hartmann, H. Sommer, T. Brezesinski and J. Janek, *J. Phys. Chem. C*, 2017, **121**, 3286-3294.
2. T. Li, X.-Z. Yuan, L. Zhang, D. Song, K. Shi and C. Bock, *Electrochemical Energy Reviews*, 2020, **3**, 43-80.
3. W. Hua, S. Wang, M. Knapp, S. J. Leake, A. Senyshyn, C. Richter, M. Yavuz, J. R. Binder, C. P. Grey, H. Ehrenberg, S. Indris and B. Schwarz, *Nature Communications*, 2019, **10**, 5365.
4. P. Teichert, G. G. Eshetu, H. Jahnke and E. Figgemeier, *Batteries*, 2020, **6**, 8.
5. L. de Biasi, A. O. Kondrakov, H. Gesswein, T. Brezesinski, P. Hartmann and J. Janek, *J. Phys. Chem. C*, 2017, **121**, 26163-26171.
6. J. P. Pender, G. Jha, D. H. Youn, J. M. Ziegler, I. Andoni, E. J. Choi, A. Heller, B. S. Dunn, P. S. Weiss, R. M. Penner and C. B. Mullins, *ACS Nano*, 2020, **14**, 1243-1295.
7. L. Mu, R. Lin, R. Xu, L. Han, S. Xia, D. Sokaras, J. D. Steiner, T.-C. Weng, D. Nordlund, M. M. Doeff, Y. Liu, K. Zhao, H. L. Xin and F. Lin, *Nano Lett.*, 2018, **18**, 3241-3249.
8. A. Mukhopadhyay and B. W. Sheldon, *Progress in Materials Science*, 2014, **63**, 58-116.
9. Y. He, C. Lu, S. Liu, W. Zheng and J. Luo, *Adv Energy Mater*, 2019, **9**, 1901810.
10. A. Y. Hou, C. Y. Huang, C. L. Tsai, C. W. Huang, R. Schierholz, H. Y. Lo, H. Tempel, H. Kungl, R. A. Eichel, J. K. Chang and W. W. Wu, *Adv Sci*, 2022, DOI: 10.1002/advs.202205012.

11. F. Strauss, L. de Biasi, A. Y. Kim, J. Hertle, S. Schweidler, J. Janek, P. Hartmann and T. Brezesinski, *Acs Mater Lett*, 2020, **2**, 84-88.
12. Y. Y. Ren, T. Danner, A. Moy, M. Finsterbusch, T. Hamann, J. Dippell, T. Fuchs, M. Muller, R. Hoft, A. Weber, L. A. Curtiss, P. Zapol, M. Klenk, A. T. Ngo, P. Barai, B. C. Wood, R. P. Shi, L. W. F. Wan, T. W. Heo, M. Engels, J. Nanda, F. H. Richter, A. Latz, V. Srinivasan, J. Janek, J. Sakamoto, E. D. Wachsman and D. Fattakhova-Rohlfing, *Adv Energy Mater*, 2022, DOI: 10.1002/aenm.202201939.
13. R. Mücke, M. Finsterbusch, P. Kaghazchi, D. Fatakowa-Rohlfing and O. Guillon, *J. Power Sources*, 2021, **489**, 229430.
14. V. Malave, J. R. Berger, H. Y. Zhu and R. J. Kee, *Electrochim. Acta*, 2014, **130**, 707-717.
15. L. Wu, X. Xiao, Y. Wen and J. Zhang, *J. Power Sources*, 2016, **336**, 8-18.
16. H. Mendoza, S. A. Roberts, V. E. Brunini and A. M. Grillet, *Electrochim. Acta*, 2016, **190**, 1-15.
17. L. J. Miara, W. D. Richards, Y. E. Wang and G. Ceder, *Chem. Mater.*, 2015, **27**, 4040-4047.
18. F. D. Han, Y. Z. Zhu, X. F. He, Y. F. Mo and C. S. Wang, *Adv Energy Mater*, 2016, **6**, 1501590.
19. W. D. Richards, L. J. Miara, Y. Wang, J. C. Kim and G. Ceder, *Chem. Mater.*, 2016, **28**, 266-273.
20. Y. G. Lee, S. Fujiki, C. Jung, N. Suzuki, N. Yashiro, R. Omoda, D. S. Ko, T. Shiratsuchi, T. Sugimoto, S. Ryu, J. H. Ku, T. Watanabe, Y. Park, Y. Aihara, D. Im and I. T. Han, *Nat Energy*, 2020, **5**, 299-308.
21. Z. Deng, Z. B. Wang, I. H. Chu, J. Luo and S. P. Ong, *J. Electrochem. Soc.*, 2016, **163**, A67-A74.
22. Y. H. Zhang, F. Chen, D. J. Yang, W. P. Zha, J. Y. Li, Q. Shen, X. L. Zhang and L. M. Zhang, *J. Electrochem. Soc.*, 2017, **164**, A1695-A1702.
23. F. Al-Jaljouli, R. Mücke, P. Kaghazchi, Y. J. Sohn, M. Finsterbusch, D. Fattakhova-Rohlfing and O. Guillon, *Journal of Energy Storage*, 2023, **68**, 107784.
24. M. Ihrig, L.-Y. Kuo, S. Lobe, A. M. Laptev, C.-a. Lin, C.-h. Tu, R. Ye, P. Kaghazchi, L. Cressa, S. Eswara, S.-k. Lin, O. Guillon, D. Fattakhova-Rohlfing and M. Finsterbusch, *ACS Appl. Mater. Interfaces*, 2023, **15**, 4101-4112.
25. W. S. Scheld, S. Lobe, C. Dellen, M. Ihrig, G. Häuschen, L. C. Hoff, M. Finsterbusch, S. Uhlenbruck, O. Guillon and D. Fattakhova-Rohlfing, *J. Power Sources*, 2022, **545**, 231872.
26. M. Rosen, M. Finsterbusch, O. Guillon and D. Fattakhova-Rohlfing, *J Mater Chem A*, 2022, **10**, 2320-2326.
27. R. Ye, M. Ihrig, E. Figgemeier, D. Fattakhova-Rohlfing and M. Finsterbusch, *ACS Sustainable Chemistry & Engineering*, 2023, **11**, 5184-5194.
28. C. Roitzheim, Y. J. Sohn, L.-Y. Kuo, G. Häuschen, M. Mann, D. Sebold, M. Finsterbusch, P. Kaghazchi, O. Guillon and D. Fattakhova-Rohlfing, *Acs Appl Energ Mater*, 2022, **5**, 6913-6926.
29. P. E. Blöchl, *Phys Rev B*, 1994, **50**, 17953-17979.
30. G. Kresse and J. Furthmüller, *Phys Rev B*, 1996, **54**, 11169-11186.
31. J. P. Perdew, K. Burke and M. Ernzerhof, *Phys. Rev. Lett.*, 1996, **77**, 3865-3868.
32. D. H. Chung and W. R. Buessem, *J. Appl. Phys.*, 1967, **38**, 2010-2012.
33. K. Okhotnikov, T. Charpentier and S. Cadars, *Journal of Cheminformatics*, 2016, **8**.
34. W. Voigt, *Lehrbuch der Kristallphysik (mit Ausschluß der Kristalloptik)*, B.G. Teubner, Leipzig, Berlin, 1910.
35. A. Reuss, *ZAMM - Journal of Applied Mathematics and Mechanics / Zeitschrift für Angewandte Mathematik und Mechanik*, 1929, **9**, 49-58.
36. R. Hill, *Proceedings of the Physical Society. Section A*, 1952, **65**, 349-354.
37. O. L. Anderson, *J. Phys. Chem. Solids*, 1963, **24**, 909-917.
38. X. Wang, I. Loa, K. Kune, K. Syassen and M. Amboage, *Phys Rev B*, 2005, **72**.
39. Y. Takahashi, N. Kijima, K. Dokko, M. Nishizawa, I. Uchida and J. Akimoto, *J. Solid State Chem.*, 2007, **180**, 313-321.
40. H. Moulinec and P. Suquet, *Comput. Meth. Appl. Mech. Eng.*, 1998, **157**, 69-94.
41. M. Schneider, F. Ospald and M. Kabel, *International Journal for Numerical Methods in Engineering*, 2016, **105**, 693-720.

Supplementary information

Modelling Electro-Chemically Induced Stresses in All-Solid-State Batteries: Screening Electrolyte and Cathode Materials in Composite Cathodes

Robert Mücke[a], Najma Yaqoob[a,b], Martin Finsterbusch[a], Fadi Al-Jaljouli[a,c], Payam Kaghazchi[a,b], Dina Fattakhova-Rohlfing[a,d], Olivier Guillon[a,c]

[a] Forschungszentrum Jülich GmbH, Institute of Energy and Climate Research, Materials Synthesis and Processing (IEK-1), 52425 Jülich, Germany;
Jülich Aachen Research Alliance: JARA-Energy, 52425 Jülich, Germany
[b] MESA+ Institute for Nanotechnology, University of Twente, P. O. Box 217, Enschede 7500AE, The Netherlands
[c] Department of Ceramics and Refractory Materials, Institute of Mineral Engineering, RWTH Aachen University, 52064 Aachen, Germany
[d] Faculty of Engineering and Center for Nanointegration Duisburg-Essen, Universität Duisburg-Essen, Lotharstr. 1, 47057 Duisburg, Germany.

Constitutive equations

A slow uniform decrease in the Li concentration *x* leads to a corresponding change in the lattice parameters of the cathode active material resulting in lattice strains ε_a^{Li}, ε_b^{Li}, ε_c^{Li} with $\varepsilon_b^{Li} = \varepsilon_a^{Li}$ as all studied cathode materials were of hexagonal crystallographic structure. The values were just called ε_a and ε_b in Tab. 1. In tensor notation the lattice strains can be we written as (the shear components are 0):

$$\underline{\varepsilon}^{Li} = \begin{pmatrix} \varepsilon_a^{Li} \\ \varepsilon_a^{Li} \\ \varepsilon_c^{Li} \\ 0 \\ 0 \\ 0 \end{pmatrix}$$

For the electrolyte materials there is no Li induced strain, and thus $\underline{\varepsilon}^{Li} = \underline{0}$. The total strain $\underline{\varepsilon}$ is the sum of the Li induced strain $\underline{\varepsilon}^{Li}$ and the elastic strain $\underline{\varepsilon}^{e}$ considering the grain orientation:

$$\underline{\varepsilon} = \underline{\underline{R}}\,\underline{\varepsilon}^{Li} + \underline{\varepsilon}^{e}$$

where $\underline{\underline{R}}$ is the grain-dependent rotation matrix. The stresses $\underline{\sigma}$ are linked by Hooks law to the elastic strains:

$$\underline{\sigma} = \underline{\underline{R}}\,\underline{\underline{C}}\,\underline{\underline{R}}^{T}\,\underline{\varepsilon}^{e}$$

where $\underline{\underline{C}}$ is the stiffness matrix, which is rotated according to the grain orientation $\underline{\underline{R}}$. $\underline{\underline{C}}$ is taken

directly from Table 1 or calculated from the Young's modulus and Poisson's ratio for the isotropic materials.

Further results on NCM955

For the sake of clearness only the configuration of NCM955 with highest stresses was given. The stresses of the other degrees of lithiation are summarised in Fig. S1. All other cathode active materials do not show this behaviour.

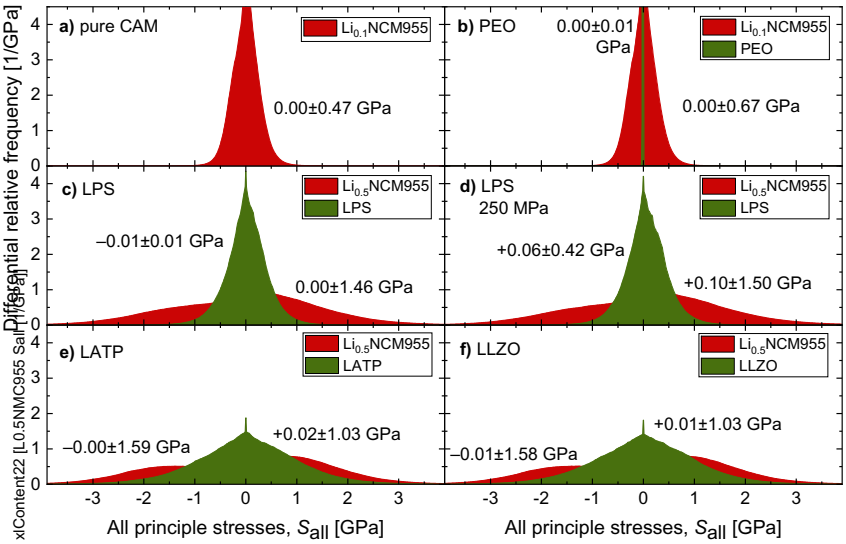

Fig. S1: Histograms all principle stresses of NCM955 at alternative lithiation states for the pure cathode active material and different electrolyte materials in mixed cathodes.

LPS based cathodes under stack compression

LPS based mixed cathodes are typically compressed upto 250 MPa in the cell stack. The resulting stresses given in Fig. S2 do not differ significantly from the stresses without cell compression given in the main text (Fig. 2i-l).

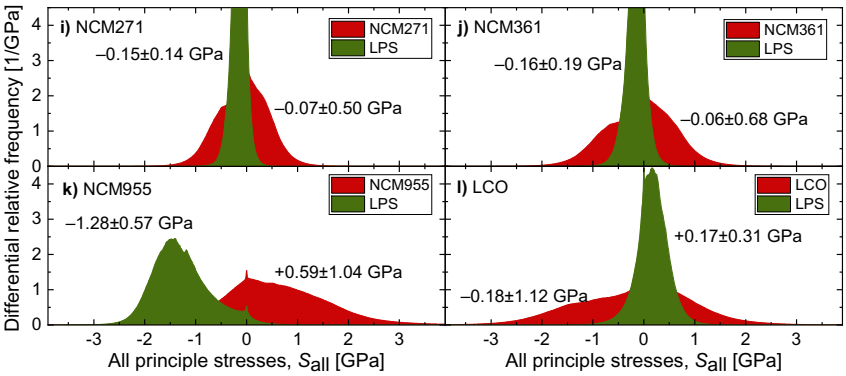

Fig. S2: Histograms of all principle stresses of LPS based mixed cathodes with different cathode active materials with a cell pressure of 250 MPa.

Means stress vs. volume change

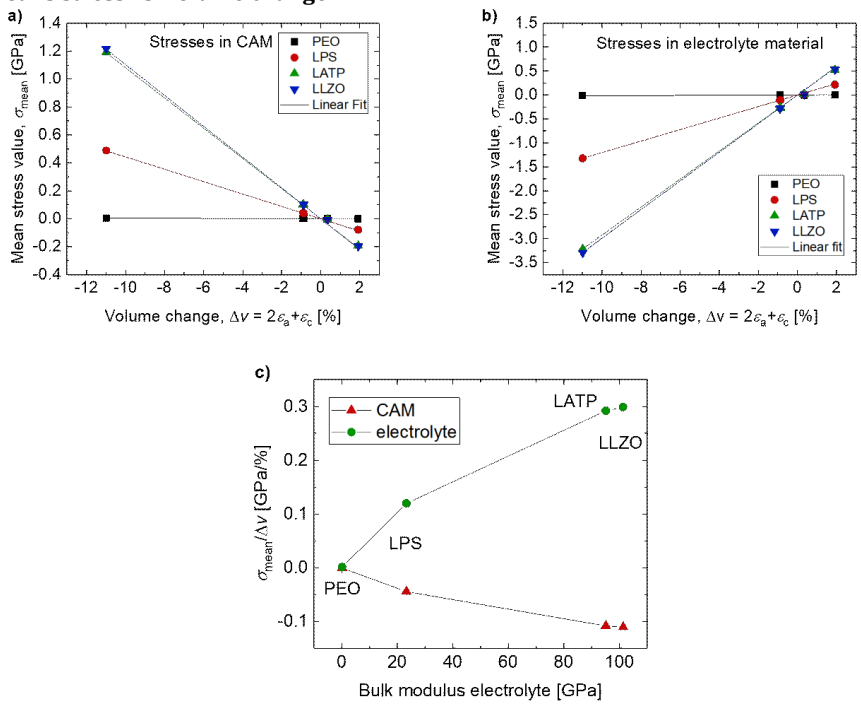

Fig. S3: a) Mean stress values σ_{mean} inside cathode active material b) inside electrolyte material as a function of volume change Δv for different electrolyte materials in the composite cathode. c) Corresponding slopes $\sigma_{mean}/\Delta v$ as a function of bulk modulus of the electrolyte material.

Further microstructures

All material combinations have also been calculated on four different modelled microstructures taken from Ref. 23 with different content of the cathode active material and density (Fig. S4-

S7). The results of the dependence of the mean stresses on the electrolyte bulk modulus (sub figures b)-e)) show the same trends as the experimental microstructure in Fig. 3 (also the other results not shown here are comparable). The stress in the CAM and electrolyte materials vs. the free strain mismatch $\Delta\varepsilon$ were plotted in the sub figures f) and g), respectively. There were used to calculate the proportionality factor in Tab. 1.

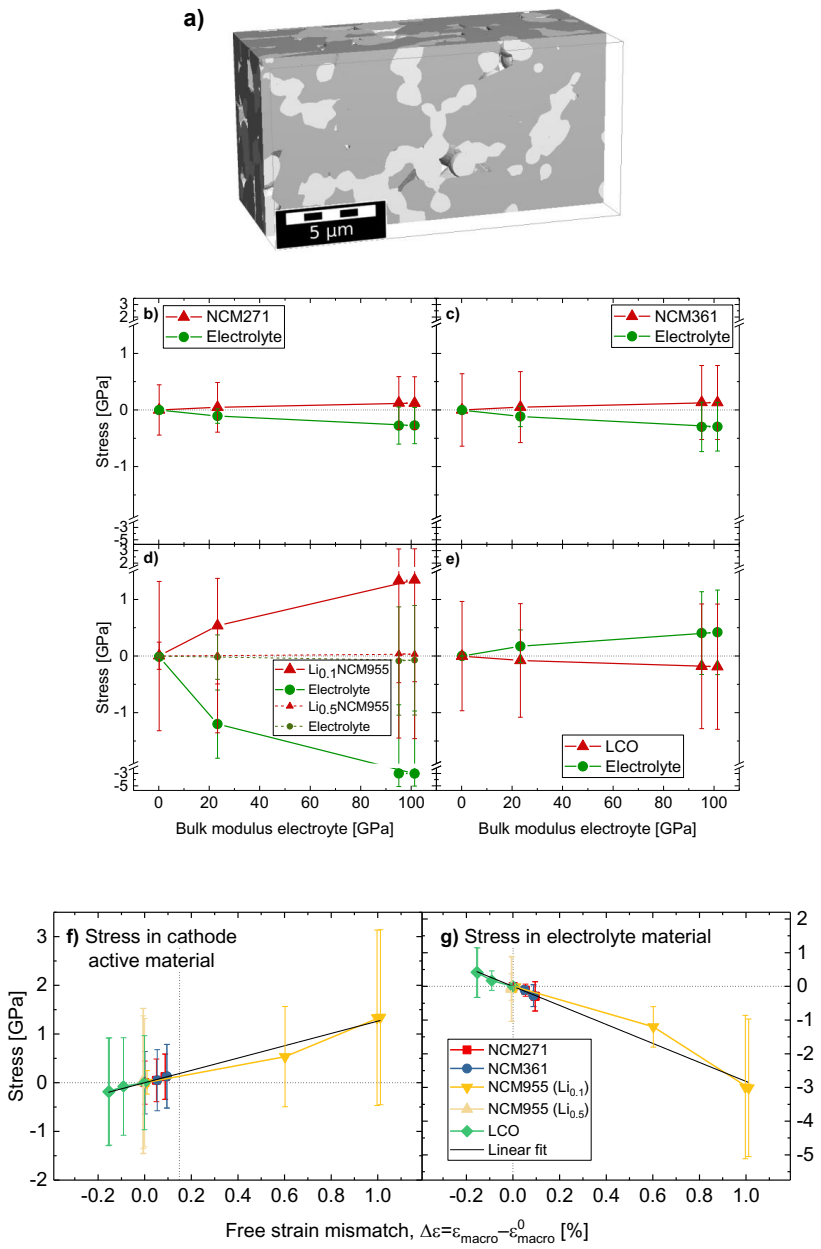

Fig. S4: a) Modelled composite cathode microstructure **CAM** (dark)**: Electrolyte** (bright) **= 2:1 with a porosity of 7%.** b-e) Average principal stresses inside composite cathodes with different cathode active materials as a function of the bulk modulus of the electrolyte material f) Corresponding stress in CAM g) and electrolyte material of composite cathodes as a function of the free strain mismatch for various cathode active materials. The error bars indicate the width (standard deviation) of the stress distribution.

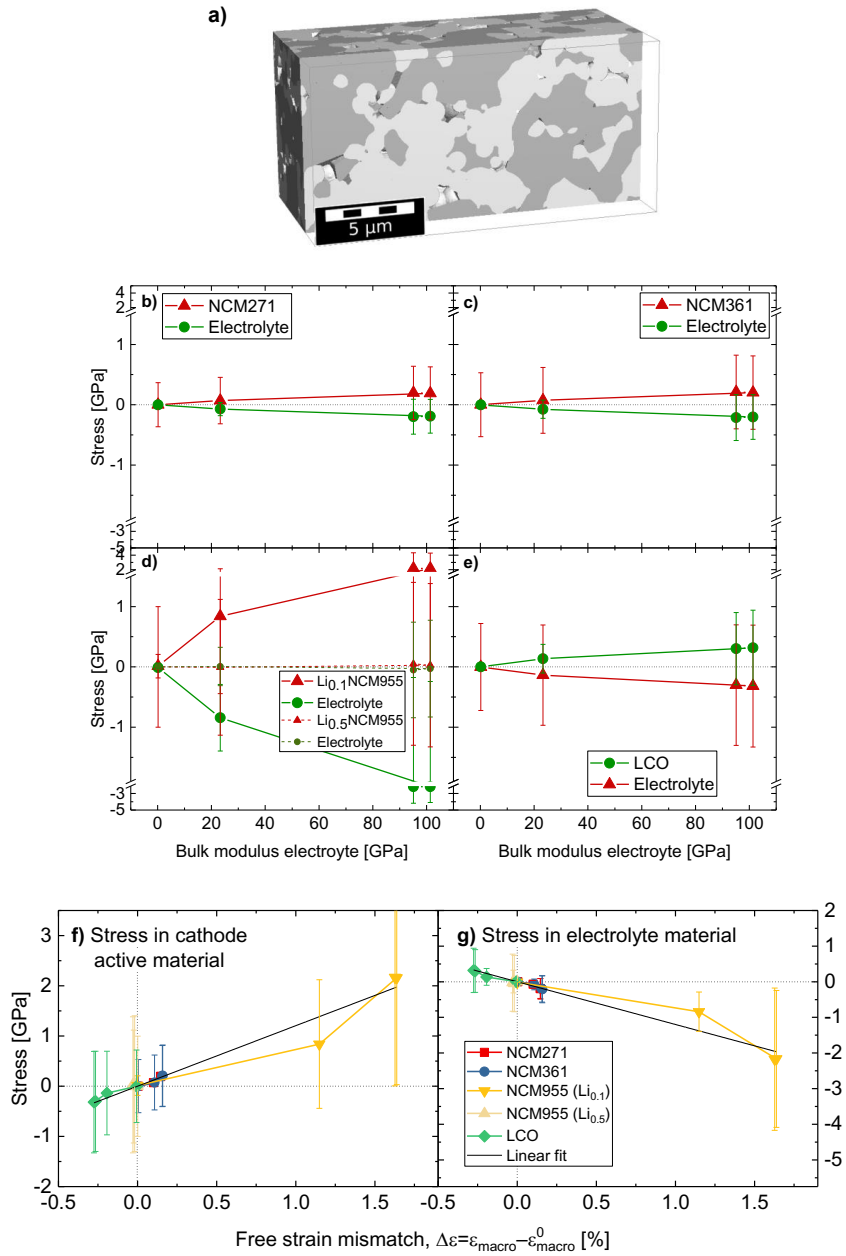

Fig. S5: a) Modelled composite cathode microstructure **CAM** (dark) **: Electrolyte** (bright) = **1:1 with a porosity of 7%.** b-e) Average principal stresses inside composite cathodes with different cathode active materials as a function of the bulk modulus of the electrolyte material f) Corresponding stress in CAM g) and electrolyte material of composite cathodes as a function of the free strain mismatch for various cathode active materials. The error bars indicate the width (standard deviation) of the stress distribution.

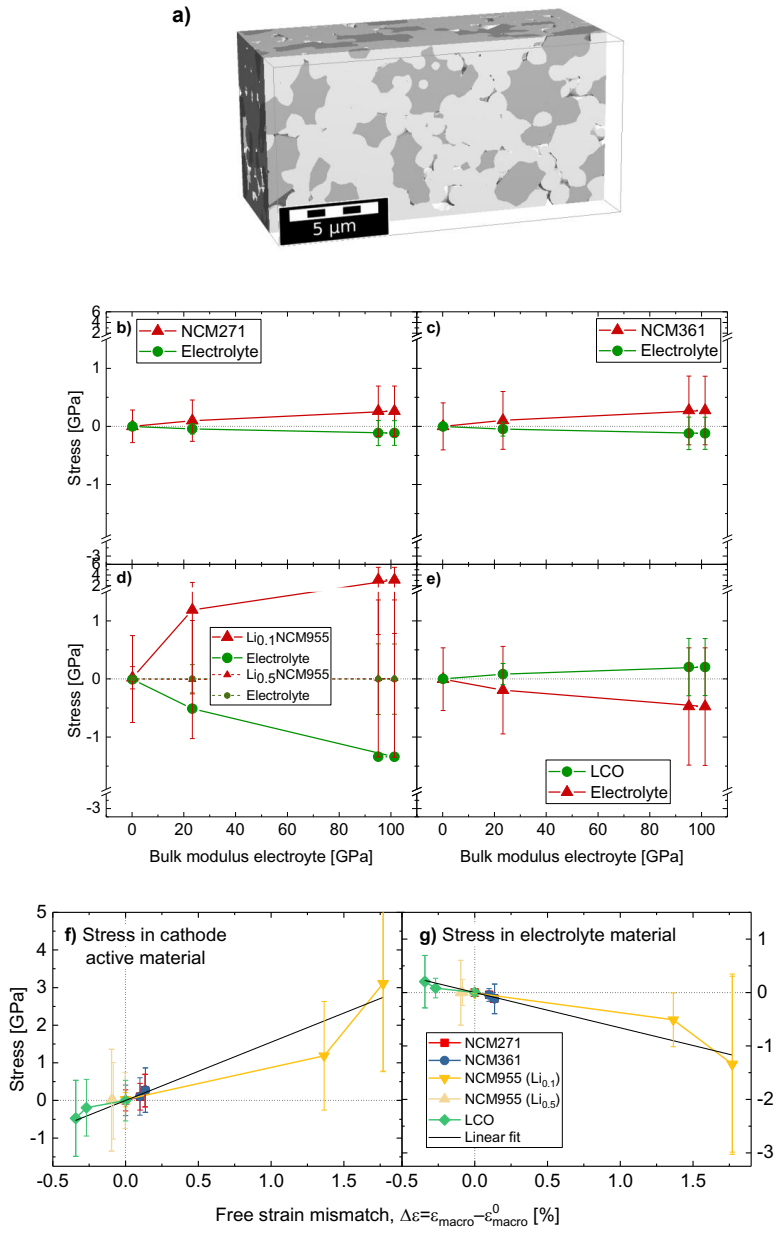

Fig. S6: a) Modelled composite cathode microstructure **CAM** (dark) **: Electrolyte** (bright) **= 1:2 with a porosity of 7%.** b-e) Average principal stresses inside composite cathodes with different cathode active materials as a function of the bulk modulus of the electrolyte material f) Corresponding stress in CAM g) and electrolyte material of composite cathodes as a function of the free strain mismatch for various cathode active materials. The error bars indicate the width (standard deviation) of the stress distribution.

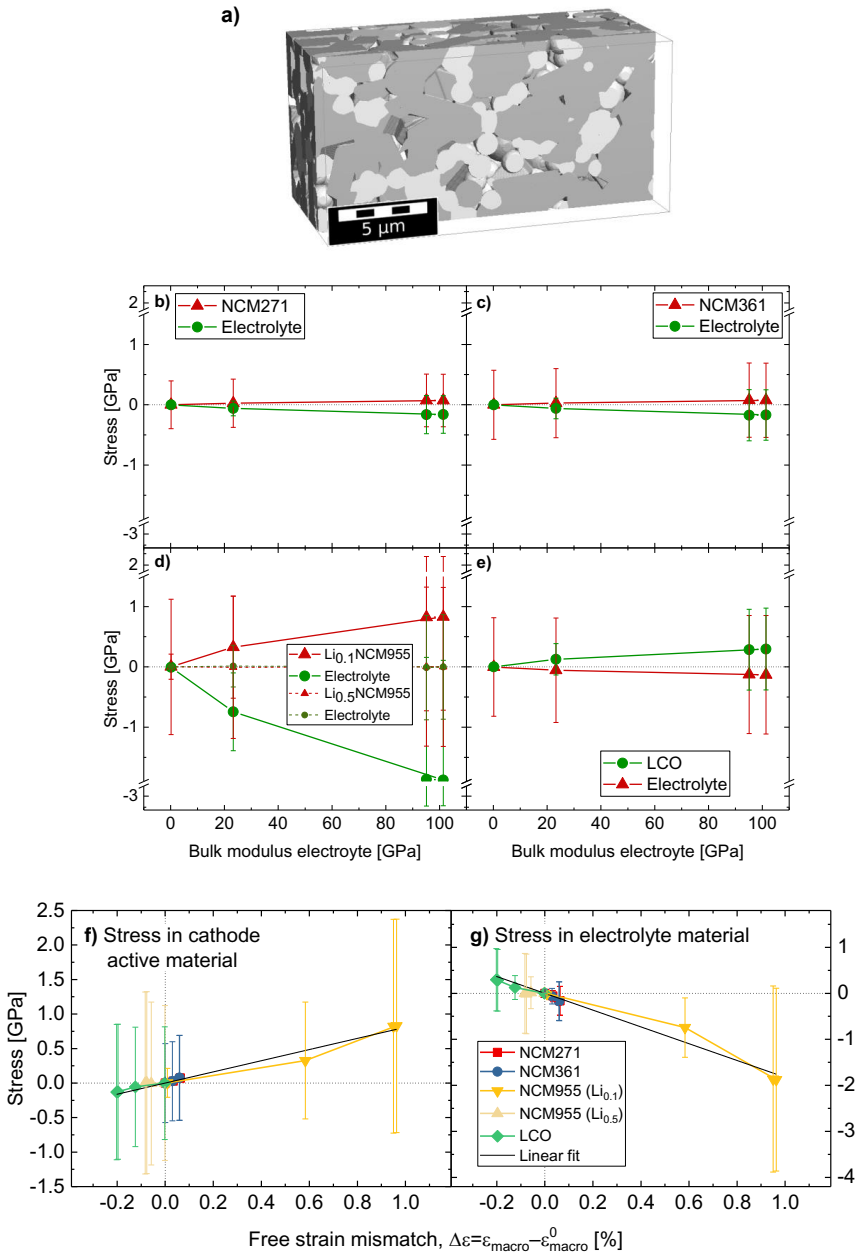

Fig. S7: a) Modelled composite cathode microstructure **CAM** (dark) **: Electrolyte** (bright) **= 2:1 with a porosity of 20%.** b-e) Average principal stresses inside composite cathodes with different cathode active materials as a function of the bulk modulus of the electrolyte material f) Corresponding stress in CAM g) and electrolyte material of composite cathodes as a function of the

free strain mismatch for various cathode active materials. The error bars indicate the width (standard deviation) of the stress distribution.

Tab. S1: Free macroscopic strains of pure randomly oriented cathode active materials $\epsilon^0_{\mathrm{macro}}$ for different microstructures compared to the mean lattice strain $\Delta v/3=(2\varepsilon_a+\varepsilon_c)/3$. For the modelled structures (Mod.) the volume ratio of CAM:Electrolyte and the porosity in % of the composite cathode are given.

	$\Delta v/3=(2\varepsilon_a+\varepsilon_c)/3$	**Exp. structure**	**Mod. 2:1, 7%**	**Mod. 1:1, 7%**	**Mod. 1:2, 7%**	**Mod. 2:1, 20%**
$Li_{0.5}NCM217$	-0.29%	-0.29%	-0.31%	-0.30%	-0.23%	-0.29%
$Li_{0.5}NCM316$	-0.30%	-0.31%	-0.32%	-0.32%	-0.24%	-0.29%
$Li_{0.5}NCM955$	0.12%	0.05%	0.01%	0.03%	0.10%	0.09%
$Li_{0.1}NCM955$	-3.66%	-3.67%	-3.67%	-3.62%	-3.01%	-3.66%
$Li_{0.5}CO_2$	0.64%	0.57%	0.56%	0.58%	0.53%	0.61%

Chapter 4 Conclusions and Outlook

The aim of this work was to study the factors and conditions which affect the induced mechanical stresses and conductivities of composite cathodes of all-solid-state lithium batteries which govern the durability and performance of ASSBs. Our research was based on an experimental composite cathode consisting of LCO and LLZO. This structure was successfully reproduced by the following steps:1) piling (sediment) the solid grains. 2) distribution the grains in order to achieve a homogenous structure. Yet, solid grains may aggregate and unfavorable pores may form, yielding formation of a non-representative volume element, hence, 3) a cropping step was necessary to remove these defects. 4) sintering process, to achieve the desired porosity and grain growth, utilizing the Voronoi tessellation algorithm, in which, the solid phases grow until they reach an interface.

A set of quantitative parameters was introduced to enable direct comparison between the experimental and reproduced structures and thus a validation of the microstructure generation process. These parameters include the chord lengths of LCO, LLZO, and pores along the x, y, and z directions; the average inner diameters of the solid components (d_{10}, d_{50}, and d_{90}); the volume-specific interfacial area between the solid phases, as well as between each solid phase and the pore phase; and the relative electronic and ionic conductivities of LCO and LLZO, respectively, along the x, y, and z axes. Our results reveal a successful reproduction of a representative volume element of the composite cathode microstructure replicating the experimental structure.

Then, we systematically analyzed the effects of four microstructural design parameters: the solid volume fraction of LCO (SVF_{LCO}), relative density ($\bar{\rho}$), and the grain sizes of LCO and LLZO (d_{LCO}, d_{LLZO}) on induced mechanical stress in cathode active materials and LLZO. The consideration of the anisotropic mechanical behavior of LCO was essential for accurately calculating stress responses in layered materials. In free-standing cathodes, LLZO constrained CAM's volumetric expansion during delithiation, establishing strong mechanical interactions between the phase.

Mechanical stresses and the conductivities exhibit a linear relationship with SVF_{LCO}. They change progressively with increasing $\overline{\boldsymbol{\rho}}$, the grain sizes of LCO and LLZO, have negligible influence on both induced mechanical stresses and conductivities when SVF_{LCO} and $\overline{\boldsymbol{\rho}}$ are fixed on the other hand.

The development of mechanical stress in both LCO and LLZO was found to be governed

primarily by the relative contact parameters K_{LCO} and K_{LLZO}, respectively, which represent the ratio of relative interface area between composite solid contents and the volume fraction of LCO and LLZO, respectively. These parameters reflect the mechanical connectivity and constraint imposed by one phase on the others. With increasing K_{LCO} and K_{LLZO} values, the mechanical coupling between LCO and LLZO is increased, leading to a larger constraint of LCO's volume change and, hence, elevated local stresses. Therefore, K_{LCO} and K_{LLZO} serve as sensitive indicators of the stress development. In contrast, ionic and electronic conductivities of LLZO and LCO were predominantly governed by their volume fractions of the respective solid phases. Furthermore, although the reducing of $\overline{\boldsymbol{\rho}}$ lowers the stress levels is considerably, it also leads to a breakdown of LLZO ionic pathways in the system, indicating that increasing porosity is not a viable strategy for stress mitigation due to a compromised conductivity.

This research further emphasized the importance of residual thermal stresses induced by the cooling down after the sintering process, in determining the total mechanical stress in ASSBs. This is typically not taken in consideration; therefore, we introduced the concept of chemo-thermal stress, which integrates both thermal stress and chemical stress induced during electro-chemical process. We showed that considering the thermal stress significantly reduced the total stress in LCO by ~43% (compared to the mere chemical stress). In contrast, thermal stress amplified the chemical stress by ~42% in $Li_{0.5}$NCM955 and ~15% in $Li_{0.1}$NCM955, thereby identifying chemo-thermal stress as a comprehensive representation of the stress state in the composite cathode. Furthermore, LCO was shown to be a mechanically more reliable cathode active material compared to both NCM derivatives due to its lower chemo-thermal stress which is of compressive type. This is less damaging to oxide materials than tensile stress. Importantly, the extent of CAM volume change did not correlate reliably with mechanical stress. This was in particular pronounced in $Li_{0.5}$NCM955, which, despite exhibiting a smaller positive volume change compared to LCO, generated higher tensile stress than the compressive stress observed in LCO.

This study also investigated the effect of grain morphology in a composite cathode on the induced mechanical stress. Our findings show that utilizing LLZO fibers with random alignments in combination with textured hexagonal LCO reduced the induced chemo-thermal stress in both LCO and LLZO by 11.0% and 9.0%, respectively, compared to systems utilizing spherical LLZO. The alignment of LLZO fibers significantly impacted the type and distribution of stress within the system due to the facet-specific contact interface between LLZO and LCO

grains. When fiber-shaped LLZO is in contact with the {001} facets of textured hexagonal LCO, the induced mechanical stress in LCO is tensile and the stress in LLZO is compressive, which is attributed to the contraction behavior of *a* and *b*-axes along {001} facets. On the other hand, the stress state is inverted when the LLZO fibers interact with the {010} facets of the hexagonal LCO, ascribed to the expansion behavior of the *c*-axis along {010} facets.

In addition, we demonstrated that the anisotropic expansion–contraction behavior of the cathode active material can be favorably exploited to reduce the induced mechanical stress in the system. This effect was more pronounced when fiber-shaped LLZO was employed aligned and in directional contact with specific LCO facets. Moreover, our results revealed that the use of spherical LCO is not favorable, as its random orientation prevents the alignment of specific crystallographic facets with the LLZO. As a result, the randomly oriented spherical LCO–spherical LLZO system exhibited the highest induced mechanical stresses among all investigated configurations.

It is worthy to emphasize that our study did not take into account the effect of grain boundary resistance. Moreover, since all stress values presented in this study are derived from theoretical calculations, an experimental validation is currently being pursued through strain measurements conducted at the European Synchrotron Radiation Facility (ESRF) in Grenoble, France. The validation is challenging due to the low X-ray absorption contrast between LCO, LLZO, and pores, which complicates phase differentiation. Precise alignment of the region of interest within the synchrotron beam demands high experimental accuracy, and refining diffraction data adds further complexity, as it is essential for reliable, spatially resolved strain measurements. Moreover, an experimental determination of stiffness tensors is not yet possible. The investigation of the impact of grain morphology on the electronic conductivity of LCO and the ionic conductivity of LLZO shall be the subject of future investigations. When combined with the current findings on the influence of grain morphology on induced mechanical stress, this will provide a comprehensive understanding of how grain morphology can be strategically engineered for the design of composite cathodes in all-solid-state lithium batteries. Such an integrated approach supports the development of cathodes that not only exhibit improved mechanical durability during cycling, thereby preserving capacity, but also enhanced electrochemical performance through improved conductivities.

Band / Volume 709
European Energy Transition – Germany in the Heart of Europe
T. Klütz, P. Dunkel, T. Busch, J. Linssen, D. Stolten (2026), V, 54 pp
ISBN: 978-3-95806-916-9 (Print)
ISBN: 978-3-95806-917-6 (E-Book)

Band / Volume 710
Development of High-Efficiency Perovskite/Silicon Tandem Solar Cells
Q. Yang (2026), 264 pp
ISBN: 978-3-95806-920-6 (Print)
ISBN: 978-3-95806-921-3 (E-Book)

Band / Volume 711
No-Regret-Maßnahmen der integrierten Netzplanung mit Fokus auf Wasserstoff
T. G. Busch (2026), xx, 325 pp
ISBN: 978-3-95806-922-0 (Print)
ISBN: 978-3-95806-923-7 (E-Book)

Band / Volume 712
Data-Driven Modeling for Digital Representations in Energy Systems
M. C. Zimmer (2026), xv, 166 pp
ISBN: 978-3-95806-926-8 (Print)
ISBN: 978-3-95806-927-5 (E-Book)

Band / Volume 713
Towards integrated PV applications: development of lightweight silicon heterojunction solar modules and their damp-heat and UV stability
K. Zhang (2026), iii, 179 pp
ISBN: 978-3-95806-928-2 (Print)
ISBN: 978-3-95806-929-9 (E-Book)

Band / Volume 714
Zinc-Based Catalysts for the Electrochemical CO_2 Reduction
I. Stamatelos (2026), vii, 136 pp
ISBN: 978-3-95806-932-9 (Print)
ISBN: 978-3-95806-933-6 (E-Book)

Band / Volume 715
Charakterisierung innovativer keramischer Materialien für Elektrolysezellen
L. P. Wehner (2026), xiv, 110 pp
ISBN: 978-3-95806-936-7 (Print)
ISBN: 978-3-95806-937-4 (E-Book)

Band / Volume 716
Process Optimization and Scale-Up for $Ba(Zr,Ce,Y)O_{3-\delta}$-Based Proton-Conducting Electrolysis Half-Cells
L.-A. Schäfer (2026), iv, 141 pp
ISBN: 978-3-95806-940-4 (Print)
ISBN: 978-3-95806-941-1 (E-Book)

Band / Volume 717
Kostenoptimale Energieausfälle in erneuerbaren Energiesystemen
D. Franzmann (2026), xix, 235 pp
ISBN: 978-3-95806-942-8 (Print)
ISBN: 978-3-95806-943-5 (E-Book)

Band / Volume 718
***Semiclassical Thermodynamics* of Metal-Solution Interfaces: A Density-Potential Functional Theory Study**
Z. Zhang (2026), 143 pp
ISBN: 978-3-95806-946-6 (Print)
ISBN: 978-3-95806-947-3 (E-Book)

Band / Volume 719
Development and Characterization of the Airborne Chemical Ionization Mass Spectrometer FunMass-C for Atmospheric Trace Gas Measurements
S. Alber (2026), xli, 265 pp
ISBN: 978-3-95806-948-0 (Print)
ISBN: 978-3-95806-949-7 (E-Book)

Band / Volume 720
Material design and stability of All-Solid-State Lithium batteries
F. H. Al-Jaljouli (2026), xv, 174 pp
ISBN: 978-3-95806-950-3 (Print)
ISBN: 978-3-95806-951-0 (E-Book)

Weitere ***Schriften des Verlags im Forschungszentrum Jülich*** unter
http://wwwzb1.fz-juelich.de/verlagextern1/index.asp

Energie & Umwelt / Energy & Environment
Band / Volume 720
ISBN 978-3-95806-951-0

Mitglied der Helmholtz-Gemeinschaft

JÜLICH
Forschungszentrum